

Compaction and Microfabric Rearrangement of Fine-Grained Siliciclastic Sediments

by

Ingo F. Matenaar

NEWCASTLE UNIVERSITY LIBRARY

301 10710 6

Thesis L7114

A thesis submitted to the University of Newcastle upon Tyne
in partial fulfilment of the requirements for the degree of
Doctor of Philosophy
in the Faculty of Science

Fossil Fuels and Environmental Geochemistry
(Postgraduate Institute): Newcastle Research Group (NRG)
University of Newcastle upon Tyne, UK

March, 2002

DECLARATION

I hereby certify that the work described in this thesis is my own, except where otherwise acknowledged and has not been submitted previously for a degree at this, or any other University

Ingo F. Matenaar

ACKNOWLEDGEMENTS

I would like to thank Professor Andrew Aplin for his advice, guidance, tolerance, support and enthusiasm throughout my PhD. Professor Steve Larter and Dr. Yunlai Yang are also gratefully acknowledged for their advice. Professor Ben van der Pluijm and John Solum (University of Michigan, Ann Arbor) are thanked for giving me the opportunity to use their HRXTG setup and to help me with the interpretation of the data.

I would also like to thank the academic members and industrial sponsors of the GeoPOP II research project for their help and financial support. Thanks especially to Dr. Richard Swarbrick, Dr. Anthony Mallon and Derek Teasdale (University of Durham), Lars Wensaas (Statoil), Sven Hansen (Norsk Hydro), Stephan Düppenbecker and James Iliffe (BP).

In addition to the above I would like to thank Trevor Whitfield for his invaluable help by showing me how to use the various machines necessary for the analysis of mudstones. I would also like to thank Rob Hunter for always helping out when something wasn't working properly.

Finally I would like to thank Sandra Ortega-Lucach, Greg Rock, Katherine Pattison, Gordon Love, Julian Moore and the other members of NRG for their help, support and perseverance during my years in Newcastle.

ABSTRACT

The main topic of this thesis is the mechanical and non-mechanical compaction and fabric rearrangement of fine-grained siliciclastic sediments. Part A concentrates on the mechanical compaction of shallow (<1000mbsf), fine-grained marine sediments, a majority of which was provided by DSDP/ODP. The used porosities and stresses were based on measurements by DSDP/ODP on fresh sample material. Results reveal, that the reduction of porosity with increasing effective stress is mainly controlled by lithology. Clay fraction (% material <2 μ m) was used as parameter for the grain size of the sample material and found the single most important control on the relationship between porosity and effective stress. However, for a given clay fraction the porosities of samples containing significant amounts of microfossils exceeded those of the fossil-poor sediments. Larger amounts of grains between 2 μ m and 8 μ m in the fossil-rich material presumably led to these differences in pore space. Deviations between the porosities measured on fresh (wet) sample material by DSDP/ODP with those determined by mercury intrusion porosimetry on the partly dried out samples used in study highlighted the sensitivity of soft, clay-rich sediments to air drying. Experimental drying of two clay samples confirmed these observations and revealed the changes in total porosity and pore size distribution during air and oven drying. Furthermore, two case studies, one located in the Mid-Norway area and one offshore New Jersey, underlined the importance of a thorough assessment of lithology and confirmed the influence of microfossils on shallow mudstone compaction. In Part B of this thesis, a novel approach was applied to correlate the petrophysical changes of fine-grained sediments during compaction and early diagenesis to alterations of the sediment microfabric. High Resolution X-ray Texture Goniometry (HRXTG) was used to quantify the alignment of phyllosilicates and results reveal, that mechanical compaction does not necessarily lead to a significant alignment of platy minerals. The analysis of the present mineralogies and grain size/shape distributions led to the conclusion, that only if both the clay and silt-fractions are dominated by platy minerals, mechanical compaction results in higher degrees of phyllosilicate alignment. On the other hand, if the silt-fraction is dominated by spherical grains (e.g. quartz, feldspar), increasing effective stress simply results in tight, poorly-aligned grain packing. Advanced stages of clay mineral diagenesis were only observed in two Gulf of Mexico wells. Here, the onset of the smectite-to-illite conversion was delayed until temperatures of at least 115°C, presumably due to the high sedimentation rates (>1000m/Ma). Although observed in other studies, an obvious influence of diagenesis on the clay mineral fabric of this sample set was not evident. It can therefore be assumed, that the mud- and siltstones from the Gulf of Mexico are still too immature to reflect diagenetic reactions in their phyllosilicate fabric.

CONTENTS

Declaration	ii
Acknowledgements	iii
Abstract	iv
Contents	v
1 Introduction.....	1
2 Samples and Methods	8
2.1 Sample locations	8
2.1.1 Leg 26 Indian Ocean: Site 250: Mozambique Basin	10
2.1.2 Leg 26 Indian Ocean: Site 257: Wharton Basin.....	11
2.1.3 Leg 36 Falkland Plateau.....	12
2.1.4 Leg 43 Bermuda Rise.....	14
2.1.5 Leg 57 Japan Trench.....	15
2.1.6 Leg 116 Bengal Fan	17
2.1.7 Leg 127 Yamato (Japan) Sea.....	19
2.1.8 Leg 150 New Jersey Slope.....	21
2.1.9 Leg 174 New Jersey Shelf.....	22
2.1.10 Leg 175 Benguela Current.....	24
2.2 Mineralogy	26
2.3 Physical properties	26
2.3.1 Grain size	26
2.3.2 Grain density	27
2.3.3 Porosities provided by ODP.....	29
2.3.4 Mercury intrusion porosimetry	30
2.3.5 Sample dehydration	30
2.3.5.1 Background	30

2.3.5.2	Sample storage and drying techniques	31
2.3.5.3	Dehydration effect on porosity and pore size distribution	36
3	Results.....	42
3.1	Grain size distribution	42
3.1.1	Fossil-poor versus fossil-rich material	44
3.1.2	Comparison with grain size data from DSDP/ODP	49
3.2	Grain density.....	50
3.3	Bulk mineralogy	51
3.4	Total organic carbon (TOC)	54
3.5	Porosimetry	54
4	Discussion	60
4.1	Compaction trends.....	60
4.1.1	Fossil-rich samples	61
4.1.2	Fossil-poor samples	63
4.1.2.1	The influence of grain size	64
4.1.2.2	The influence of temperature	65
4.1.2.3	The influence of time	65
4.1.2.4	The influence of mineralogy.....	66
4.2	Comparison with compaction models.....	66
4.2.1	Compaction trends	66
4.3	Case studies.....	75
4.3.1	Compaction trends of the shallow Norwegian North Sea sequences.....	75
4.3.1.1	Background	75
4.3.1.2	Compaction analysis of a well from offshore Mid-Norway	77
4.3.1.3	Discussion and conclusions.....	86
4.3.2	The New Jersey shelf and continental slope.....	87

4.3.2.1	Background	87
4.3.2.2	Conclusions of the compaction study of Dugan & Flemings (2000a/b) 90	
4.3.2.3	Re-examination of the compaction history at Site 1073.....	94
4.3.2.4	Summary and Conclusions	103
5	Conclusions	105
6	Samples and Methods	107
6.1	High Resolution X-ray Texture Goniometry: Background	107
6.2	Sample set.....	109
6.2.1	Well 43/386 Central Bermuda Rise	109
6.2.2	North Viking Graben (North Sea): NVG	109
6.2.3	Central Viking Graben: CVG.....	109
6.2.4	Mid-Norway area: MN.....	110
6.2.5	Bay of Bengal: BB	110
6.2.6	Caspian Sea: CS.....	110
6.2.7	Deep water Gulf of Mexico: Panis, Ikon, Diva	110
6.3	High Resolution X-ray Texture Goniometry	111
6.3.1	Sample preparation	112
6.3.2	Measurements	113
6.4	Mineralogy	118
6.5	Clay mineral diagenesis	118
6.6	Physical properties and total organic carbon content	119
7	Results.....	120
7.1	Grain size distribution/Clay fraction.....	120
7.2	Grain density.....	121
7.3	Bulk mineralogy	123
7.3.1	North Viking Graben.....	123

7.3.2	Central Viking Graben	124
7.3.3	Mid-Norway	125
7.3.4	Bay of Bengal.....	125
7.3.5	Caspian Sea.....	125
7.3.6	Central Bermuda Rise	125
7.3.7	Gulf of Mexico: Panis	126
7.3.8	Gulf of Mexico: Ikon & Diva	126
7.4	Clay mineralogy	127
7.4.1	North Sea, Mid-Norway, Caspian Sea & Bay of Bengal.....	127
7.4.2	Gulf of Mexico: Panis, Ikon & Diva	128
7.5	Total organic carbon content (TOC).....	130
7.6	Water content	133
7.7	Porosimetry	134
7.7.1	North Viking Graben	136
7.7.2	Central Viking Graben	136
7.7.3	Bay of Bengal.....	137
7.7.4	Caspian Sea.....	137
7.7.5	Gulf of Mexico: Panis , Ikon & Diva	137
7.8	Clay mineral diagenesis	138
7.8.1	North Sea, Mid-Norway, Caspian Sea & Bay of Bengal.....	138
7.8.2	Gulf of Mexico: Panis, Ikon & Diva	139
7.9	HRXTG	141
7.9.1	Central Bermuda Rise	141
7.9.2	North Viking Graben.....	142
7.9.3	Mid-Norway	144
7.9.4	Central Viking Graben	145
7.9.5	Bay of Bengal.....	146
7.9.6	Caspian Sea.....	147

7.9.7	Gulf of Mexico: Panis, Ikon & Diva	148
8	Discussion	151
8.1	Hydrodynamics and the depositional environment	151
8.2	Grain size and mineralogy	155
8.3	Clay mineral diagenesis	161
8.4	The effects of phyllosilicate alignment and clay mineral diagenesis on porosity and pore size.....	167
8.4.1	General correlation of the phyllosilicate fabric with porosity, pore size and grain size.....	168
8.4.2	Regional correlations of the phyllosilicate fabric with porosity, pore size, grain size and diagenetic grade.....	170
8.4.2.1	Gulf of Mexico.....	170
8.4.2.2	Other regions	177
9	Summary and Conclusion.....	183
10	Final Conclusions.....	185
11	Future Work	186
	References	188
	Appendix	210
	Physical Property Data: Part A DSDP/ODP core material	211
	Physical Property Data: Part B	213
	Grain Size Data: Part A	215
	Grain Size Data: Part B	218
	Mercury Intrusion Porosimetry Data: Part A Glacial Clays for Drying Tests	221
	Mercury Intrusion Porosimetry Data: Part A DSDP/ODP	225
	Mercury Intrusion Porosimetry Data: Part B Panis (cuttings)	240

Mercury Intrusion Porosimetry Data: Part B Ikon (core samples).....244

Mercury Intrusion Porosimetry Data: Part B Diva (core samples)246

Mercury Intrusion Porosimetry Data: Part B Bay of Bengal (cuttings)248

Mercury Intrusion Porosimetry Data: Part B North Viking Graben (core)249

Mercury Intrusion Porosimetry Data: Part B Caspian Sea (core)251

Mercury Intrusion Porosimetry Data: Part B Central Viking Graben (core)
.....252

HRXTG Data Part B253

1 Introduction

Fine-grained siliciclastic lithologies such as mud- and siltstones dominate sedimentary systems around the world (Füchtbauer, 1988; O'Brien & Slatt, 1990; Schieber & Zimmerle, 1998; Aplin et al., 1999). Numerous articles have been published about the processes that are involved in the deposition of these sediments (e.g. Hjulstrøm, 1955; Rieke & Chilingarian, 1974; Potter et al., 1980; Chamley, 1989; Potter, 1998; Schieber, 1998) and much work has been done to characterize the physical properties (e.g. porosity, permeability, mechanical strength) of the resulting rocks once they are lithified (e.g. Steiger & Leung, 1988; Katsube et al., 1991; Horsrud et al., 1998; Pearson, 1999). However, relatively little is known about the mechanical and chemical processes that control these properties during the transition from soft sediment to solidified rock.

It is of great significance to understand the controls on these properties and the role of the involved lithological parameters, since porosity, permeability and elastoplasticity underpin several important facets of geoscience. These include the analysis of fluid flow in basin studies and the prediction of pore pressures and fracture gradients from both seismic and wireline data (Atwater & Miller, 1965; Bredehoeft et al., 1988; Mann & Mackenzie, 1990; Neuzil, 1994; Hansen, 1996a/b; Bolton & Maltman, 1998; Giles et al., 1998; Luo et al., 1998; Dewhurst et al., 1999a; Swarbrick et al., 2000).

For siliciclastic sediments mechanical compaction is the dominant process over the first few kilometres of burial (Jones, 1994; Giles et al., 1998 and references therein). It is an elastoplastic process (Casagrande, 1936; Jones, 1994; Schneider et al., 1994; Suetnova & Vasseur, 2000) and can be defined as the stress driven rearrangement of grains which results in the loss of porosity and expulsion of pore fluid. Compaction is usually described by curves (Fig. 1) which show the relationship between porosity and burial depth (Hamilton, 1976; Sclater & Christie, 1980; Baldwin & Butler, 1985; Dzevenshir et al., 1986; Nobes et al., 1986; Ramm & Bjørlykke, 1994; Giles et al., 1998).

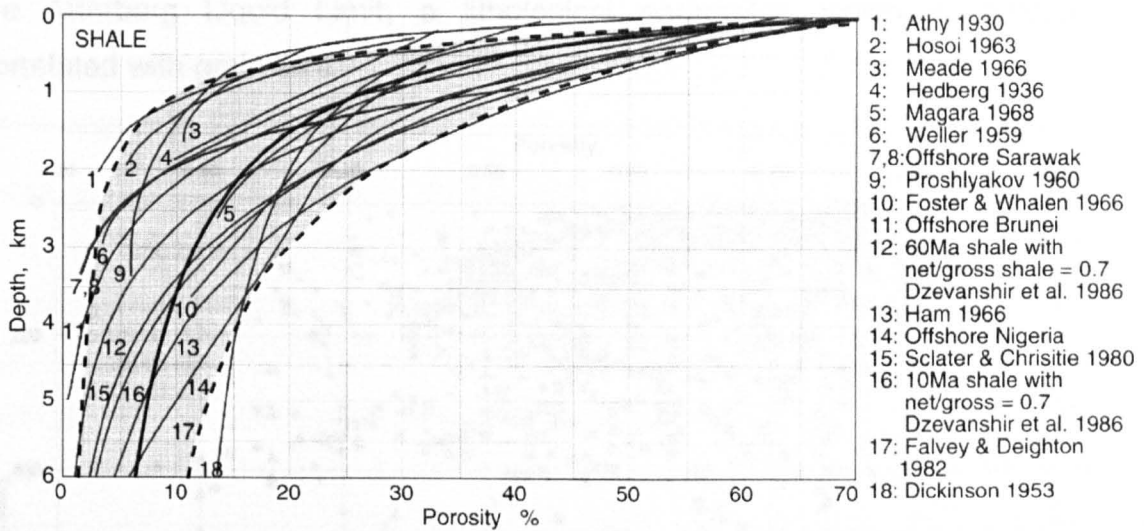


Fig. 1 Porosity versus depth trends (compaction curves) for shales from various studies (Giles et al, 1998).

Since burial depth gives no information about the driving force for compaction (effective stress), these compaction curves (Fig. 1) often show huge variations. Instead, it is more reasonable to plot porosity against vertical effective stress, as this accounts for other than hydrostatic pore pressures (Terzaghi, 1921; Gibson et al., 1967, 1981; Skempton, 1970; Burland, 1990; Schneider et al., 1994; Dewhurst et al., 1998). However, even a collection of published porosity/depth data for clay-rich sediments from the Deep Sea and Ocean Drilling Program (Fig. 2) show significant variations. Here, nearly hydrostatic pore pressures in most of these wells would justify a plot of porosity against burial depth. Nevertheless, compaction trends scatter heavily and show porosities that vary over more than 50% for a given burial depth (see also Nobes et al., 1986).

Previous investigations by Aplin et al. (1995), Dewhurst et al. (1998, 1999b) and Yang & Aplin (1998) have suggested that a critical constant in the relationship between porosity and vertical effective stress in mudstones is clay fraction (percentage of material $<2\mu\text{m}$ in spherical diameter). Their work is based on the principles of soil mechanics, where earlier studies (Skempton, 1970; Burland, 1990) revealed that the decrease of porosity in clays and muds with increasing vertical effective stress is mainly controlled by

the Atterberg Liquid Limit, a lithological parameter, which is strongly correlated with grain size.

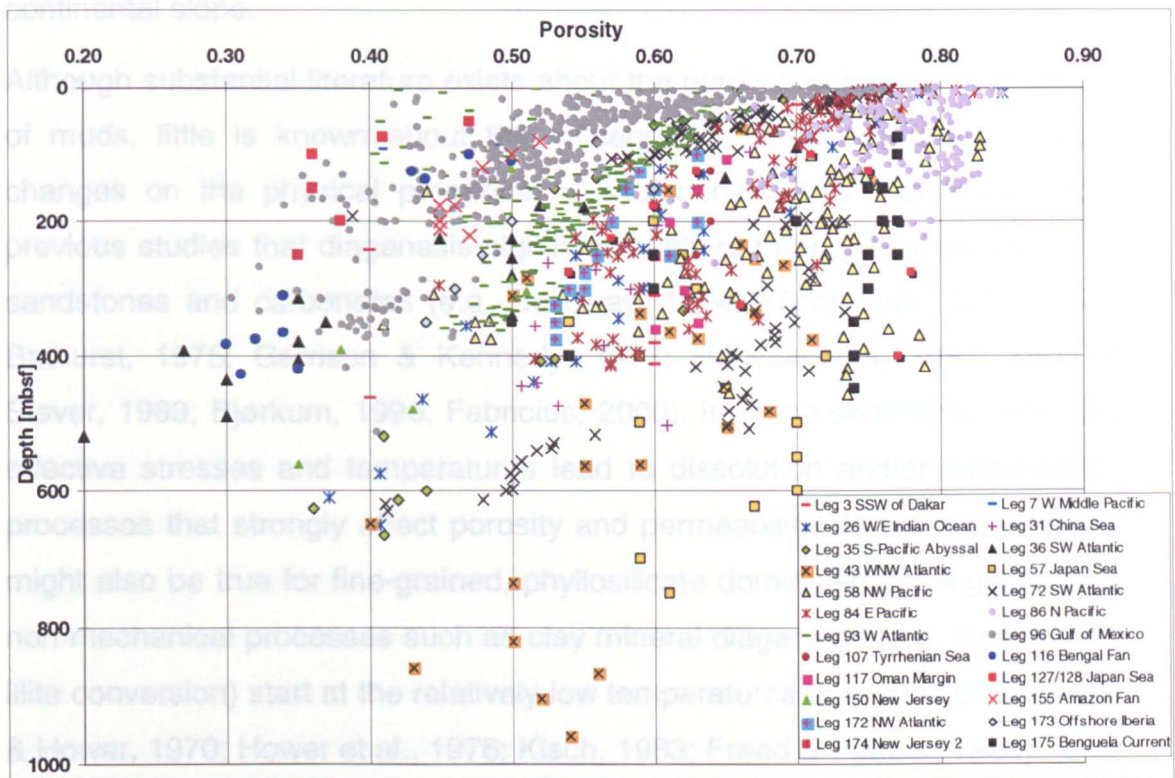


Fig. 2 Porosity/depth data for "clays" and "muds" (incl. "claystones" & "mudstones") from the Deep Sea and Ocean Drilling Program. Measured porosities can vary over more than 50% at a given depth (400mbsf) and more than 950m for a given porosity (55%).

On the basis of this work Yang & Aplin (submitted) established a compaction model for fine-grained, siliciclastic lithologies in sedimentary basins. The model was calibrated with both laboratory and geophysical well log data from the North Sea and Gulf of Mexico. The dataset mainly comprises lithological information from very shallow (<100mbsf) and deeper (>1000mbsf) sections of the sedimentary record. Data from the intermediate sequences (100-1000mbsf), where fine-grained sediments lose up to 50 percent of their initial porosity (Fig. 1 & Fig. 2) is sparse. In Part A of the present study 80 fine-grained sediment samples from the DSDP/ODP were chosen to verify Yang & Aplin's (submitted) compaction model for intermediate depths and to test its applicability in several different sedimentary environments. During this investigation the possible influence of other parameters like fossil content, mineralogy and age was also considered. Part A concludes with two case

studies where the established relationships are tested on two shallow sediment sequences from the northern North Sea and the New Jersey continental slope.

Although substantial literature exists about the purely mechanical compaction of muds, little is known about the influence of diagenetic (mineralogical) changes on the physical properties of mudstones. It is well known from previous studies that diagenesis significantly alters the physical properties of sandstones and carbonates (e.g. Galloway, 1974; Füchtbauer, 1967, 1979; Bathurst, 1975; Garrison & Kennedy, 1977; Houseknecht, 1987; Tada & Siever, 1989; Bjørkum, 1996; Fabricius, 2000). In these sediments, elevated effective stresses and temperatures lead to dissolution and/or cementation processes that strongly affect porosity and permeability. These observations might also be true for fine-grained, phyllosilicate dominated lithologies, since non-mechanical processes such as clay mineral diagenesis (e.g. smectite-to-illite conversion) start at the relatively low temperatures of around 60°C (Perry & Hower, 1970; Hower et al., 1976; Kisch, 1983; Freed & Peacor, 1989).

The key difficulty of quantifying the effect of mineralogical change on the physical properties of mudstones is their grain size. Siltstones and especially claystones are dominated by grains often smaller than a few micrometres and changes in the physical properties are very hard to correlate to visible alterations of the sediment matrix. The most obvious macro- and microscopical alterations of clay-rich sediments during lithification are observed in their phyllosilicate microtexture (e.g. Oertel, 1970; Oertel & Curtis, 1972; Page and Wenk, 1979; Curtis et al., 1980; Lee et al., 1985, 1986; Ho et al., 1995, 1999; van der Pluijm et al. 1998; Merriman and Peacor, 1999; Jacob et al. 2000). These alterations are mainly caused by two processes:

1. mechanical rotation or kinking of discrete phyllosilicate crystals within a surrounding clay matrix
2. chemical alterations, namely phyllosilicate neocrystallisation, dissolution-recrystallisation and diffusion, the latter often described as annealing.

TEM observations have shown that during the early stages of burial (diagenetic zone) and cleavage development (low-grade metamorphic zone), grain kinking and rotation prevails in low-energy environments (Sintubin, 1994; Ho et al., 1995, 1996; van der Pluijm et al., 1998). At later stages and in high-energy environments grain dissolution and neocrystallisation (e.g. smectite-to-illite or illite to phengite muscovite transformation) dominate the development of preferred particle orientation, either parallel to bedding (mainly smectite-to-illite) or parallel to cleavage (Lipshie et al, 1976; Lee et al., 1986; Merriman et al., 1990; Ho et al, 1995, 1996, 1999; van der Pluijm et al., 1998).

The work of Oertel et al. (1989), Sintubin (1994), Ho et al. (1999) and Jacob et al. (2000) revealed that the degree of preferred orientation is partly controlled by lithology (grain size). Both Oertel et al. (1989) and Sintubin (1994) observed a decrease of fabric intensity during cleavage development with increasing quartz content and Jacob et al. (2000) showed that the reorientation of phyllosilicates occurred at a lower metamorphic grade in finer-grained rocks than in silt dominated lithologies.

Many of these investigations used X-ray texture goniometry (XTG) to quantify the orientation of phyllosilicates (e.g. Baker, 1969; Oertel, 1970, 1983; Wood et al, 1976; O'Brien, 1987; Sintubin, 1994). In order to improve the traditional XTG method van der Pluijm et al. (1994) developed High Resolution X-ray Texture Goniometry (HRXTG). This method "is able to record variations in the strain state of deformed (compacted) rocks over small, mm-scale distances" (van der Pluijm et al., 1994) and its improved capabilities have been demonstrated in several studies (Ho et al., 1995, 1996, 1999, 2001; van der Pluijm et al., 1998; Jacob et al, 2000).

In one of these studies Ho et al. (1999) showed a close correlation of the smectite-to-illite diagenetic reaction with the increase in preferred orientation in phyllosilicates of some Gulf Coast mudstones. Since neither Ho et al. (1999) nor any of the other studies give an accurate description of the sediments they studied (grain size distribution, porosity), systematic relationships between lithology, phyllosilicate orientation and the physical

properties of mudstones remain to be established. Part B of this study examines the extent to which compaction alters the phyllosilicate fabric of fine-grained sediments and the role that non-mechanical processes like clay mineral diagenesis play in the reduction of pore space. Here, samples from several sedimentary basins around the world were analyzed by HRXTG to generate a first understanding of the interaction between pore space, grain size, microfabric and diagenetic grade of clay-rich sediments during compaction. 88 samples from 9 wells were chosen to represent sedimentary environments such as the continental rise (DSDP well 43/386), a lacustrine intercontinental basin (Caspian Sea) and shelf to slope petroleum basins (North Sea, Mid-Norway, deep water Gulf of Mexico and Bay of Bengal).

Thesis Outline

This study is divided into two parts. Part A deals with the purely mechanical compaction of mudstones and begins with a chapter (**2 Samples and Methods**) describing the chosen sample set and the applied analytical methods. The following chapter (**3 Results**) gives details about the results of the laboratory experiments, which are discussed in the next chapter (**4 Discussion**). Part A will finish with the conclusions that can be drawn from this investigation (**5 Conclusions**). Part B concentrates on the use of phyllosilicate fabric as compaction parameter and indicator of non-mechanical changes of the physical properties of mudstones. Its structure is very similar to Part A, beginning with a chapter about the chosen samples and applied methods (**6 Samples and Methods**). This is again followed by a detailed description of the analytical results (**7 Results**) which are then discussed in the subsequent chapter (**8 Discussion**). A summary of the main observations followed by the main conclusions will be given in the final chapter of Part B (**9 Summary and Conclusion**). The thesis ends with a few final conclusions that can be drawn from Parts A and B (**10 Final Conclusions**) and some recommendations for future work in this field (**11 Future Work**).

Part A

2 Samples and Methods

Definition

The terms used throughout this study to describe the analyzed lithologies are based on the conventions displayed in Table 1:

% particles < 2 μ m	unconsolidated soft	consolidated non-fissile	consolidated fissile
>65	clay	claystone	shale
45-65	mud	mudstone	
<45	silt	siltstone	silty shale

Table 1 The classification of fine-grained siliciclastic sediments used in this study.

2.1 Sample locations

80 samples from 10 DSDP/ODP wells were selected based on the following criteria:

1. Samples are at maximum depth (vertical effective stress), i.e. no major uplift or erosion has occurred.
2. Detailed information about the lithology (physical properties etc.) and stratigraphical age is available.
3. Maximum temperatures are below 60°C to avoid significant diagenetic reactions.
4. In situ pore pressures are hydrostatic to prevent unloading effects, i.e. effective stresses do not deviate from maximum due to elevated pore fluid pressures (good knowledge of effective stress is essential).

In order to increase the representativeness of the examined material, a variety of different geographical locations (Fig. 3) were chosen to provide a collection of different lithologies, burial depths (effective stresses), mineralogical assemblages and geological ages.

The water depths at the well sites range from 98 m (New Jersey Shelf; Table 2) to 5278 m (Wharton Basin), the age of the sediments spanning about 156 Ma (Recent to Oxfordian; Table 2). Burial depths range from 1m to 959m. The sedimentary regimes under which the sediments were deposited range

from mid-ocean ridge to continental shelf, representing deep sea basin, continental rise, slope, and upwelling conditions (Fig. 3).

The sample material from the older wells (26/250, 26/257 and 36/330), drilled in the early and mid-1970's, consisted of nearly dried-out core chips, whereas the majority of samples comprised relatively fresh, wet core plugs. The amount of material used varied between 12 and 15 g, depending on the water content.

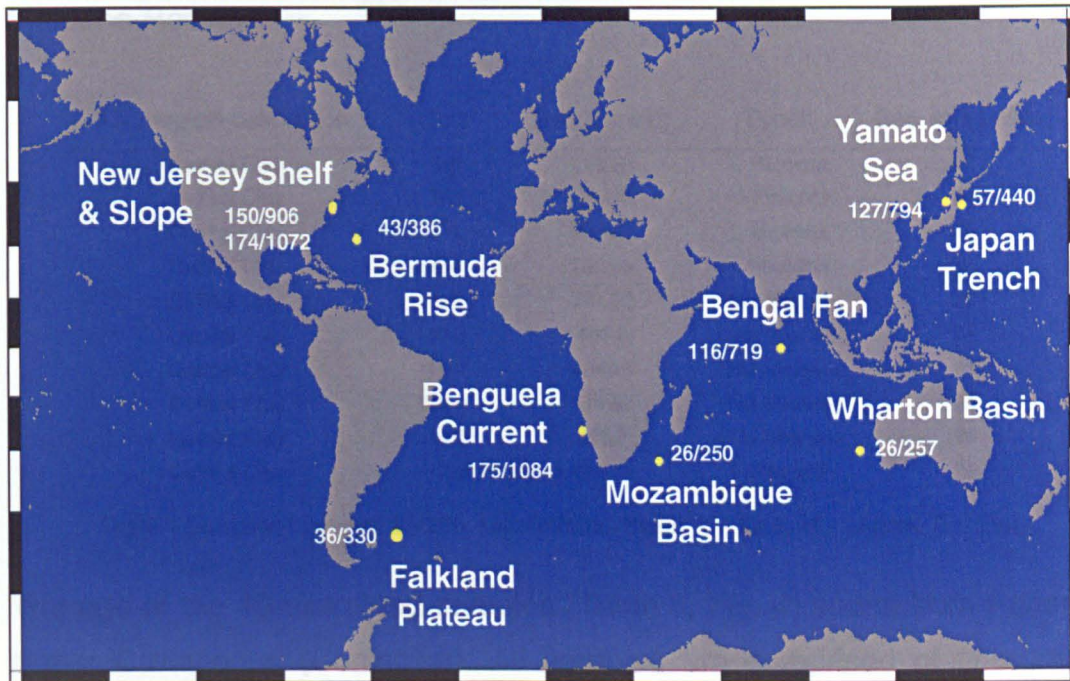


Fig. 3 Location of the sampled DSDP and ODP wells.

Well	Water Depth [m]	No of Samples	Deepest Sample [m]	Age Range	Sed. Regime
26-250	5119	10	648	Plio-Miocene	Deep Sea Basin/Ridge
26-257	5278	4	250	Pleisto-Albian	Deep Sea Basin
36-330	2626	9	520	Albian-Oxfordian	Rise
43-386	4782	14	959	Pleistocene-Albian	Rise
57-440	4509	8	748	Pleisto-Miocene	Trench Slope
116-719a	4748	9	449	Pleisto-Miocene	Deep Sea Fan
127-794a	2821	6	485	Pleisto-Miocene	Deep Sea Basin
150-906a	925	6	560	Mio-Eocene	Slope
174-1072a	110	6	250	Pleisto-Miocene	Shelf
175-1084a	2004	8	450	Pleisto-Pliocene	Coastal Upwelling

Table 2 Details of the sample set.

2.1.1 Leg 26 Indian Ocean: Site 250: Mozambique Basin

Well 26/250 is located in the southeast of the Mozambique Basin (Fig. 3) near the north flank of the Indian Ocean Ridge and was drilled in 5119 meters of water (Davies et al. 1972). The basin is bounded west and east by the north-south-trending Mozambique and Madagascar rises, respectively. Much of the sediment fill is thought to be derived from the Zambezi Canyon and Fan system which transports sediments from East Africa and Madagascar south to the Mozambique Basin. Sedimentation rates in this area are estimated to be about 25m/Ma for the Miocene and about 45m/Ma for the Pliocene-Recent.

Lithological description	Core	Depth [mbsf]	Epoch	Sed. rate [m/Ma]
Detrital Clay	4-6	119.38	L-Pliocene	47
Detrital Clay	6-3	189.6	M-Pliocene	25
Detrital Clay	7-4	238.65	L-Miocene	25
Detrital Clay	8-4	295.65	L-Miocene	25
Detrital Clay	9-3	351.22	M-Miocene	25
Detrital Clay	10-2	407.3	E-M-Miocene	25
Detrital Clay	11-2	464.97	E-M-Miocene	25
Detrital Clay	13-4	571.67	E-M-Miocene	25
Detrital Clay	14-2	606.7	E-M-Miocene	25
Detrital Clay	17-2	645.71	L-Pliocene	25

Table 3 Samples from well 26/250: Mozambique Basin; L – Late, M – Middle, E – Early.

The age of the 10 examined samples (Table 3, Fig. 4) spans from Recent to Upper Cretaceous (Coniacian). All samples are comprised of fine-grained detrital clay (Fig. 4) which sometimes contain low amounts of coccoliths.

Depth [mbsf]	Lithology	Age
0-116	Clayey coccolith ooze interbedded with detrital silty clay	Recent - Upper Pliocene
116-351	Detrital clay, very minor silty coccolith ooze, clay-rich coccolith ooze, and coccolith-rich clay	Upper Pliocene - Upper Miocene
351-568	Detrital clay	Upper Miocene - Lower/Middle Miocene
568-638	Interbedded detrital clay	L/M Miocene
638-725.3	Detrital clay	Lower Miocene - Coniac
725.3-738.5	Basalt	


 samples

Fig. 4 Lithostratigraphy of well 26/250: Mozambique Basin (Davies et al. 1972).

2.1.2 Leg 26 Indian Ocean: Site 257: Wharton Basin

Well 26/257 was drilled southwest of Australia (Fig. 3), in the south-eastern Wharton Basin, northeast of the Naturaliste Plateau (Davies et al. 1972). The lithological column at this location is represented by only a thin (262m) sedimentary sequence, which overlies oceanic crust (olivine basalt, Fig. 5). The deep water conditions at this site (5278m water depth) are reflected by the present sediments, comprised of zeolite rich or zeolite bearing, dark reddish-brown detrital clay.

Well 36/330 is located at Maurice Ewing Bank, the eastern end of the Falkland Plateau (Fig. 3). The well, drilled at a water depth of 2620m, passed through 551m of sediments and 20m of basement rock, represented by a gneiss pegmatite (Fig. 6). During the last 100Ma (Recent-Albian) about 50m of diatomaceous and nanofossil-rich clays and ooze were deposited at very low rates of about 1.6m/Ma (Barker et al. 1974). In Early Albian to Late Jurassic times sedimentation rates were calculated to be between 20m/Ma

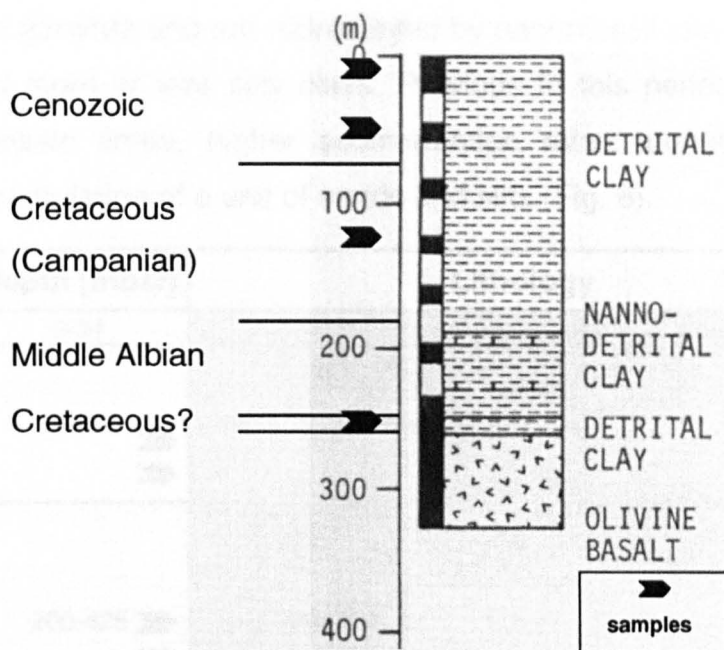


Fig. 5 Lithostratigraphy at site 26/257: Wharton Basin (Davies et al. 1972).

An absence of palaeontological data makes a stratigraphic subdivision very difficult. Therefore, sedimentation rates can only be estimated at about 2m/Ma or less for the first 199.5mbsf (Davies et al. 1972) and at least 25m/Ma for the remaining deeper sediments (>199.5mbsf). Four clay samples were selected from well 26/257 (Table 2), covering about 100Ma years of deep sea sedimentation.

Lithological description	Core	Depth [mbsf]	Epoch	Sed. rate [m/Ma]
Detrital Clay	1-5	7.2	?	~2
Detrital Clay	3-2	49.2	?	~2
Detrital Clay	5-2	124.04	Campanian	2
Detrital Clay	9-2	248.7	E-M-Albian	25

Table 4 Samples from well 26/257: Wharton Basin; L – Late, M – Middle, E – Early.

2.1.3 Leg 36 Falkland Plateau

Well 36/330 is located at Maurice Ewing Bank, the eastern end of the Falkland Plateau (Fig. 3). The well, drilled at a water depth of 2626m, passed through 551m of sediments and 26m of basement rock, represented by a gneiss pegmatite (Fig. 6). During the last 100Ma (Recent-Albian) about 50m of diatomaceous and nannofossil-rich clays and oozes were deposited at very low rates of about 1.6m/Ma (Barker et al. 1974). In Early Albian to Late Jurassic times sedimentation rates were calculated to be between 22m/Ma

and 25m/Ma and are represented by nannofossil clays, sapropelic claystones and more or less silty clays. Previous to this period, during Late to Middle Jurassic times, higher sedimentation rates around 100m/Ma led to the accumulation of a unit of sands and silts (Fig. 6).

Depth [mbsf]	Lithology	Age
0-34	Diatomaceous silty clay, clayey diatom ooze	Recent-Eocene
34-200 ➤ ➤	Nanno ooze, nanno clay	Cenomanian - Early Albian
200-425 ➤ ➤ ➤ ➤ ➤	Sapropelic claystone (and limestone)	Aptian - Oxfordian
425-540 ➤ ➤	Silty clay, clayey silt	Oxfordian - Middle Jurassic
540-551	Sand and silt	Oxfordian - Middle Jurassic
551-576	Gneiss pegamatite	Pre-Cambrian

➤
samples

Fig. 6 Lithostratigraphy of well 36/330: Falkland Plateau (Barker et al. 1974).

Erosion, nondeposition or a drastic reduction in sedimentation rate (Barker et al. 1974) resulted in a hiatus of approximately 19m between the Oxfordian sapropelic claystone and silty clay (Fig. 6). The dimension of this gap was regarded as being of low significance for the overall compaction trend of this well. However, since sampling over this interval was very dense (Table 5), any drastic change in the compaction trend would have been noticed.

Lithological description	Core	Depth [mbsf]	Epoch	Sed. rate [m/Ma]
Nannofossil Claystone	1-4	134.71	M-Albian	22
Nannofossil Claystone	2-2	177.41	M-Albian	22
Sapropelic Claystone	6-4	314.55	Aptian	22
Sapropelic Claystone	8-3	350.37	E-Kim-Oxfordian	25
Sapropelic Claystone	9-2	377.75	Oxfordian	25
Sapropelic Claystone	10-2	405.95	Oxfordian	25
Silty Claystone	11-2	434.8	Oxfordian	100
Silty Claystone	13-1	490.83	Oxfordian	100
Silty Claystone	14-2	519.88	Oxfordian	100

Table 5 Samples from well 36/330: Falkland Plateau; Kim – Kimmeridgian, L – Late, M – Middle, E – Early.

2.1.4 Leg 43 Bermuda Rise

Well 43/386 was drilled at a water depth of 4782m on the central Bermuda Rise, 140km south-southeast of Bermuda (Fig. 3). The drilled section is represented by an almost continuously deposited sediment column, ranging in age from Cretaceous (Albian) to Recent (Tucholke et al. 1975). The sediments are mainly comprised of:

1. Nannofossil ooze and clay in the upper Pleistocene-Miocene formations
2. Volcanogenic sand turbidites in the Oligocene and Upper Eocene
3. Siliceous and calcareous turbidites in the Middle Eocene
4. Cherty and radiolarian claystones in the Lower Eocene-Upper Paleocene
5. Multicolored claystone in the Cretaceous (Fig. 7).

Sedimentation rates were generally low, between 9m/Ma and 20-40m/Ma. For this study 14 samples were taken up to a depth of 957mbsf (Fig. 7, Table 6).

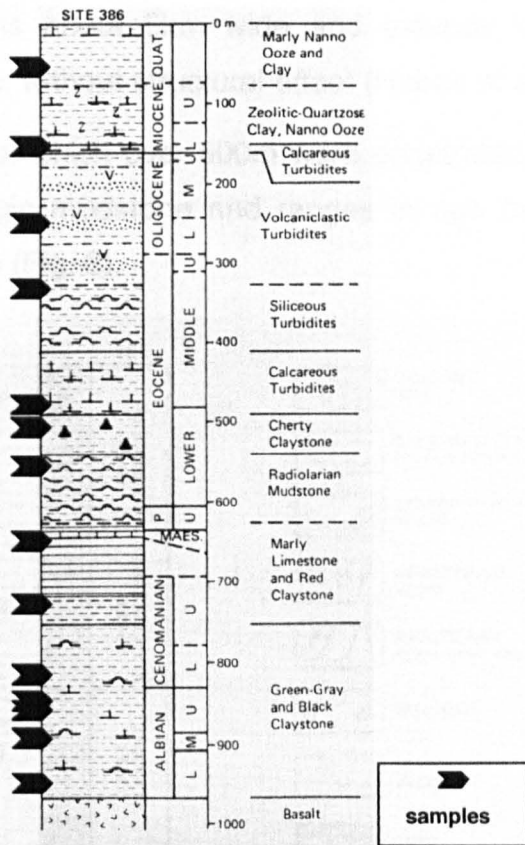


Fig. 7 Lithostratigraphy at site 43/386: Central Bermuda Rise (Tucholke et al. 1975).

Lithological description	Core	Depth [mbsf]	Epoch	Sed. rate [m/Ma]
Stiff Brown Clay	1-6	59.28	Pleistocene	8
Brown Clay	4-4	151.97	E-Miocene	1
Grey Claystone	11-2	252.94	E-Oligocene	10
Olive Silty Claystone	14-5	335.82	M-Eocene	7
Olive Claystone	26-2	480.81	E-Eocene	50
Grey Claystone	28-3	502	E-Eocene	20
Grey Claystone	32-5	562.96	E-Eocene	15
Red Claystone	36-4	646.8	L-Cretaceous	2
Black Claystone	42-4	731.8	L-Cenomanian	15
Olive Claystone	50-4	818.22	E-Cenomanian	15
Black Claystone	54-6	858.82	L-Albian	15
Black Claystone	55-4	865.05	L-Albian	15
Grey/Black Claystone	59-3	900.59	E-M-Albian	20
Black Claystone	65-2	957.37	E-Albian	20

Table 6 Samples taken from well 43/386: Bermuda Rise; L – Late, M – Middle, E – Early.

2.1.5 Leg 57 Japan Trench

Site 440 was drilled at a water depth of 4515m, 28km west of the Japan Trench, on the trench inner slope. The site lies on a prominent midslope

structural terrace that is about 5km wide and extends more than 50km parallel within the trench, without structural offset (Huene et al. 1977).

The sediment section, of which over 800m were penetrated, is comprised of fairly uniform hemipelagic mudstone and ranges in age from late Miocene through late Pleistocene (Fig. 8).

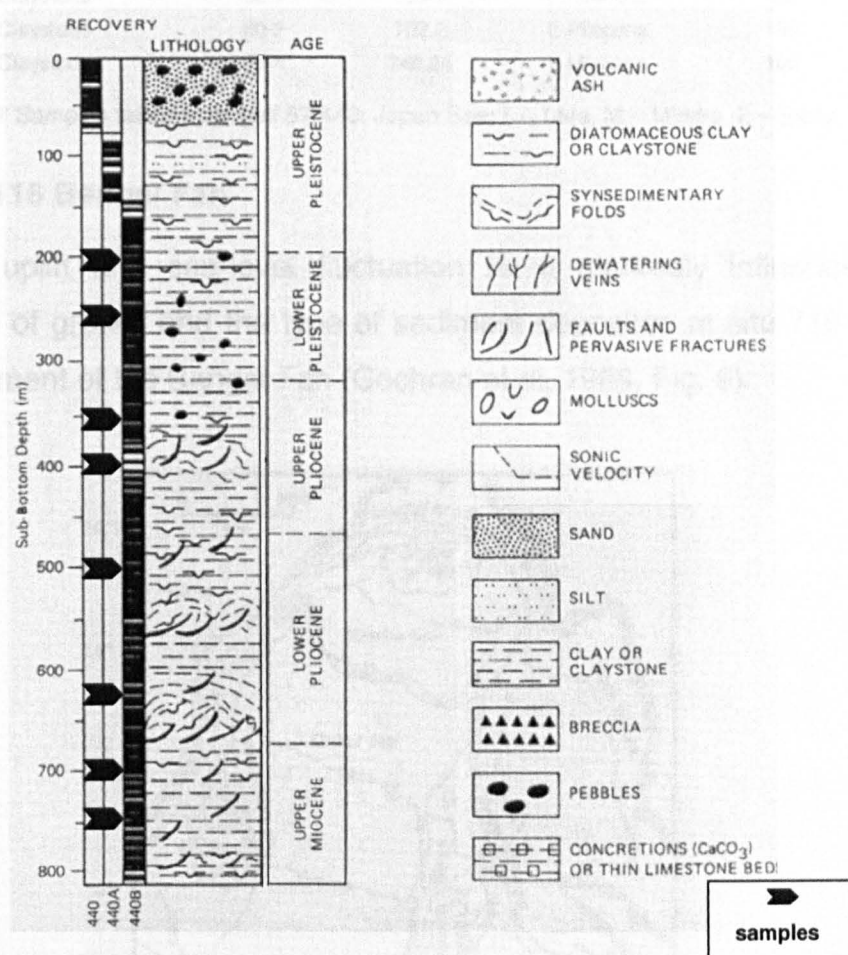


Fig. 8 Lithostratigraphic subdivision of well 57/440: Japan Trench (HUENE ET AL. 1977).

Three or more periods of slumping in the Miocene and Pliocene are the only breaks in continuous sedimentation. Sediment accumulation rates, which are uncorrected for compaction, were around 105m/Ma during the Late Miocene to Lower Pleistocene and increased more than twofold during the Upper Pleistocene, to about 270m/Ma (Huene et al. 1977).

The eight claystone samples, which were selected from this well for analysis, cover the depth between 208mbsf and 748mbsf (Table 7) and range in age from about 1Ma to 7Ma.

Lithological description	Core	Depth [mbsf]	Epoch	Sed. rate [m/Ma]
Claystone	8-2	208.2	L-Pleistocene	270
Claystone	13-3	257.23	E-Pleistocene	105
Claystone	24-1	358.74	E-Pleistocene	105
Claystone	28-3	399.7	L-Pliocene	105
Claystone	39-2	502.72	L-Pliocene	105
Claystone	52-1	624.7	E-Pliocene	105
Claystone	60-2	702.2	E-Pliocene	105
Claystone	65-1	748.24	L-Miocene	105

Table 7 Samples taken from well 57/440: Japan Sea; L – Late, M – Middle, E – Early.

2.1.6 Leg 116 Bengal Fan

Himalayan uplift and sea-level fluctuation have markedly influenced the relative rate of growth and the type of sediment deposited at site 719 during the development of the Bengal Fan (Cochran et al. 1988, Fig. 9).

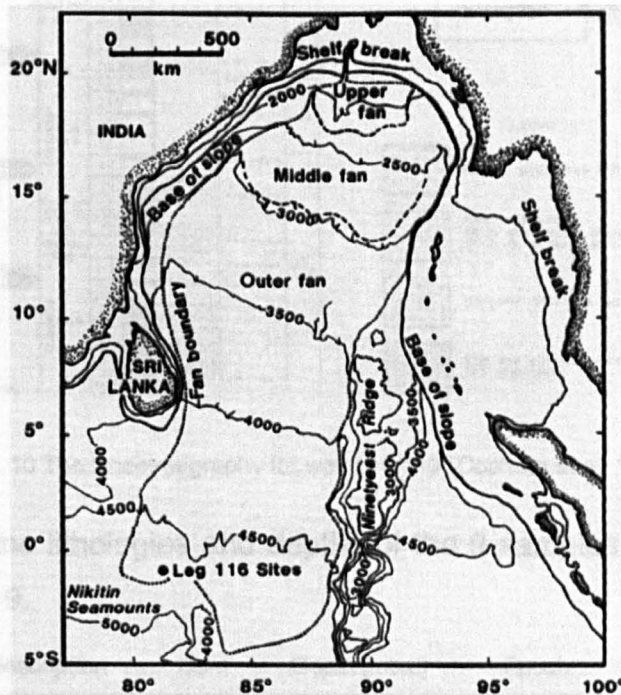


Fig. 9 The geographical position of well 116/719 on the outer Bengal Fan system (WETZEL & WIJAYANANDA 1990).

Prominent changes in sedimentation occurred when the silty turbidite sections of Miocene and Pleistocene age were disrupted by mud-rich Pliocene turbidite sequences (Fig. 10). The latter were separated by pelagic clays that accumulated at a rate of 70m/Ma. The Pleistocene mud turbidites

accumulated at a rate of 50-100m/Ma. The youngest, Late Pliocene sedimentation rates were determined as ranging between 150m/Ma and 200m/Ma. Although the state of consolidation varies between under- and overconsolidated, Cochran et al. (1988) classified most sediments to be normally consolidated.

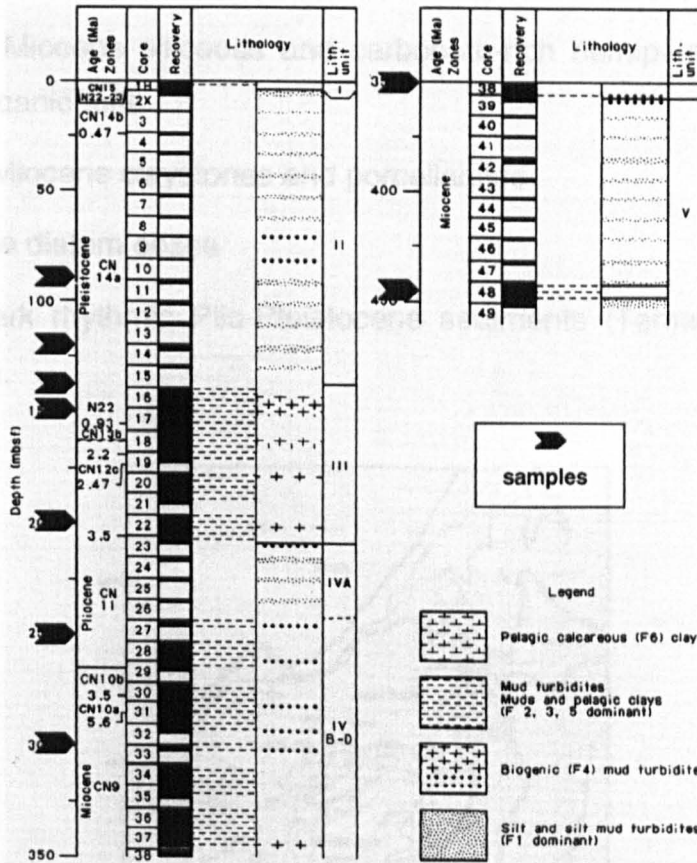


Fig. 10 The lithostratigraphy for well 116/719 (Cochran et al. 1988).

Table 8 shows the lithologies and depths of the 9 samples that were chosen from well 116/719.

Lithological description	Core	Depth [mbsf]	Epoch	Sed. rate [m/Ma]
Clay	11X-1	90.58	L-Pleistocene	175
Clayey Silt	14X-2	120.12	L-Pleistocene	175
Clay	16X-1	138.26	Pleisto-L-Pliocer	75
Clay	17X-3	150.87	Pleisto-L-Pliocer	75
Clay	22X-4	200	L-Pliocene	75
Clay	28X-1	251.55	L-Miocene	75
Clay	33X-2	300.75	L-Miocene	75
Clay	38X-3	350.3	L-Miocene	75
Clay	48X-6	448.95	L-Miocene	75

Table 8 Samples taken from well 116/719: Bengal Fan; L – Late, M – Middle, E – Early.

2.1.7 Leg 127 Yamato (Japan) Sea

The sedimentary sequence overlying the basement in the 2811m deep Yamato basin (Fig. 11) is built from five distinct lithological formations. These are:

1. Lower Miocene delta-front sands and siltstones rich in plant debris
2. Middle Miocene siliceous and carbonate-rich hemipelagic claystones and volcanic tuffs
3. Upper Miocene claystones and porcellanites
4. Pliocene diatom oozes
5. Light/dark rhythmic Plio-Pleistocene sediments (Tamaki et al. 1990, Fig. 12).

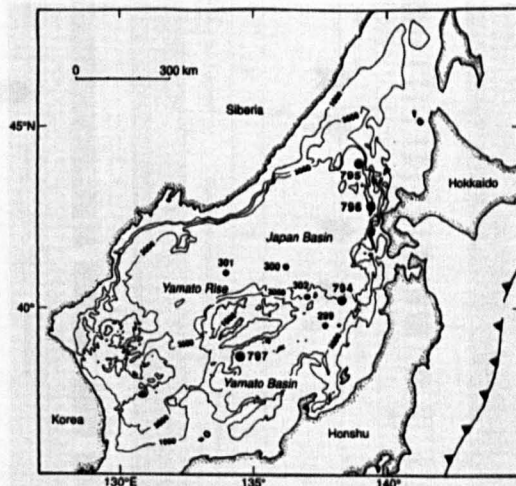


Fig. 11 The Yamato Basin and the position of well 127/794 west of the Islands of Japan (Tamaki et al. 1990).

The 6 selected samples range in depth from close to sea floor (1mbsf) down to about 485mbsf and cover various clay-rich lithologies (Table 9, Fig. 12).

2.1.8 Leg 150 New Jersey Slope

One of three sites drilled on the New Jersey continental slope during Leg 150, well 906 is located about 70km south-west of well 174/1072 (Fig. 13) at a water depth of 925m (Mountain et al. 1994). The sediments in this well cover Eocene to Holocene ages and are dominated by clays, claystones and silty clays. Sequence boundaries, which can be traced from the shelf to the slope, mark a fundamental change in depositional regime from Eocene chawks to Oligocene and younger siliciclastic sediments (Fig. 14).

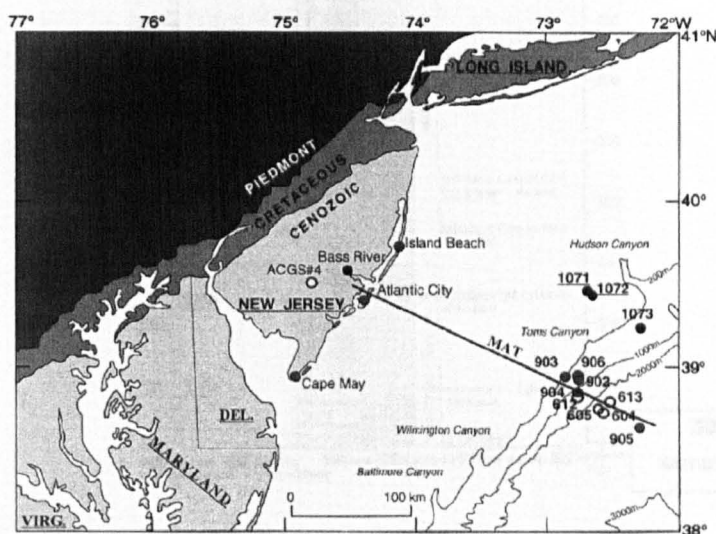


Fig. 13 Locations of wells 150/906 and 174/1072 on the outer New Jersey continental shelf and slope (Vanderaveroot 2000).

The sedimentary record shows a filled canyon which was formed between 15Ma and 12Ma (ODP-TAMU, 2001) ago. The early canyon filling consists mainly of debris from its walls and turbidites. The end of the canyon phase is marked by rapid infilling with laminated mud.

Lithological description	Core	Depth [mbsf]	Epoch	Sed. rate [m/Ma]
Silty Clay	14X-1	121.31	L-Miocene	<100*
Silty Clay	31X-1	285.6	M-Miocene	<100*
Silty Clay	33X-1	305.05	M-Miocene	<100*
Clay-Silty Clay	41X-3	384.53	E-M-Miocene	<100*
Claystone	51X-3	481.1	L-Oligocene	<100*
Silty Claystone	59X-1	554.86	L-Eocene	<100*

Table 10 Samples from well 150/906: New Jersey Slope; L – Late, M – Middle, E – Early; *) estimated from age and thickness.

The depths and lithologies of the six samples taken from this well are shown in Table 10 and Fig. 14.

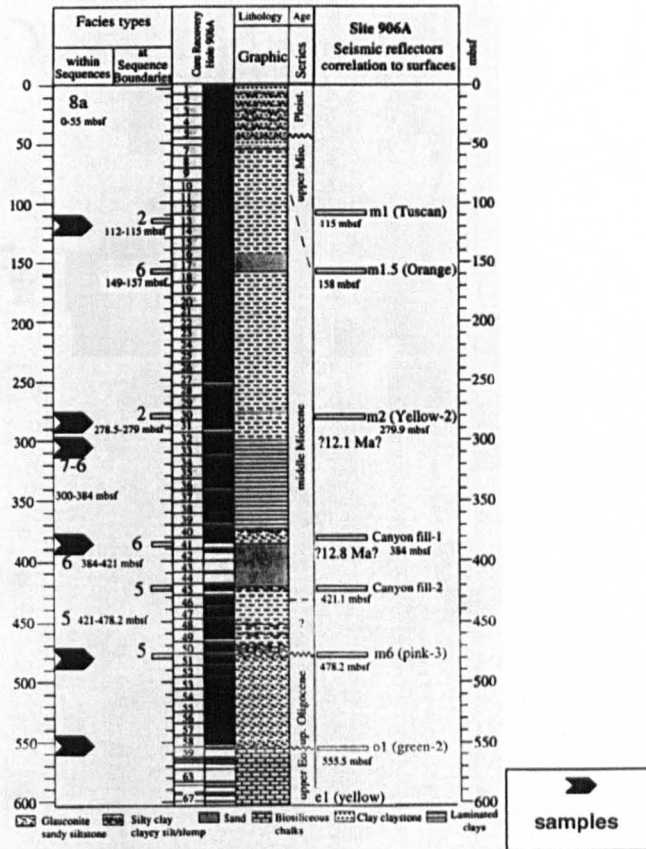


Fig. 14 Lithostratigraphy of well 150/906a (Mountain et al. 1994).

2.1.9 Leg 174 New Jersey Shelf

Site 1072 was drilled on the outer continental shelf of the New Jersey margin, about 130km east of Atlantic city (Fig. 13). The drilled formations belong to a classic passive continental margin sequence (Austin et al. 1998) and are mainly comprised of silty and muddy sands, sands and clays (Fig. 15).

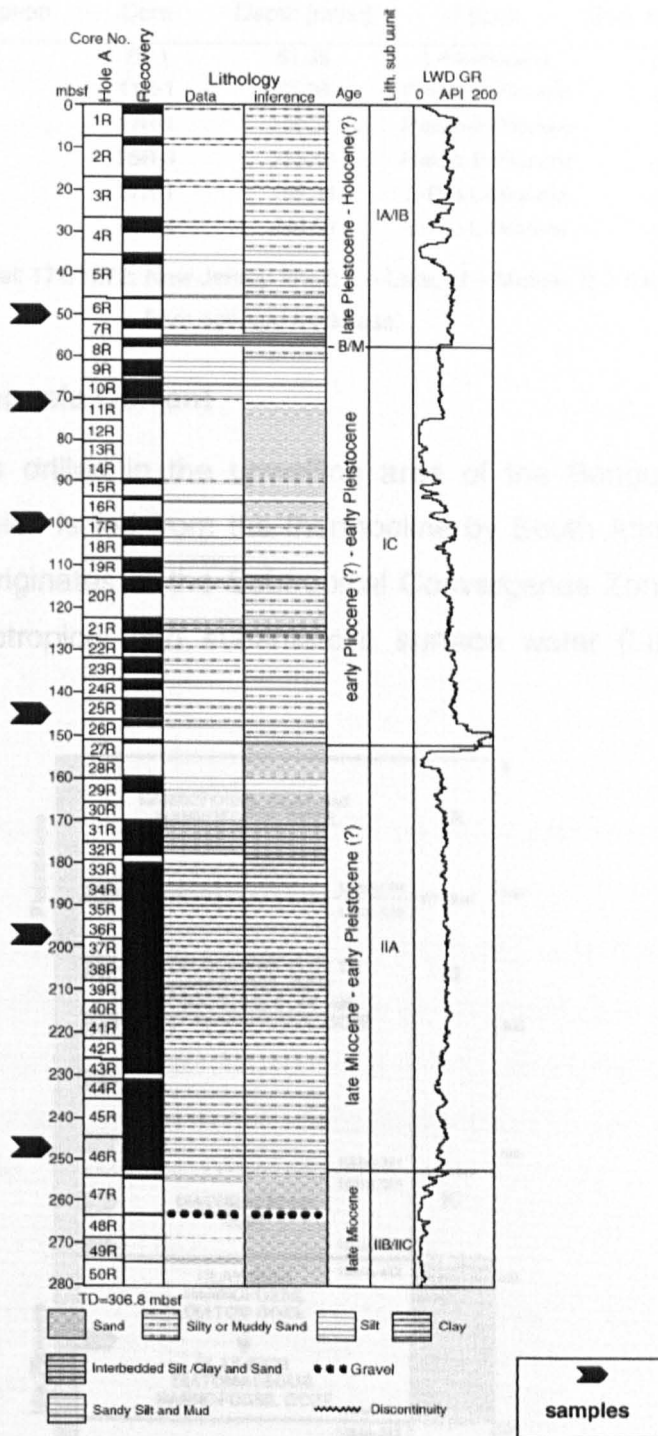


Fig. 15 Lithostratigraphy of well 174/1072 (Austin et al. 1998).

The accumulation rates at site 174/1072 are reported to be in the range of tens to hundreds of m/Ma (Austin et al. 1998). Six samples have been taken for analysis (Table 11, Fig. 15).

Lithological description	Core	Depth [mbsf]	Epoch	Sed. rate [m/Ma]
Silty Clay	7R-1	51.35	L-Pleistocene	≤150*
Silty Clay	11R-1	71.08	Pleisto-E-Pliocene	≤150*
Sandy Mud	17R-1	100.21	Pleisto-E-Pliocene	≤150*
Sandy Mud	25R-3	145.16	Pleisto-E-Pliocene	≤150*
Silty Clay	37R-1	198.34	E-Plio-L-Miocene	≤150*
Muddy Sand	46R-4	249.68	E-Plio-L-Miocene	≤150*

Table 11 Samples from well 174/1072: New Jersey Shelf; L – Late, M – Middle, E – Early; *) estimated from age and thickness.

2.1.10 Leg 175 Benguela Current

Well 175/1084 was drilled in the upwelling area of the Benguela Coastal Current (Fig. 3), which is fed from the thermocline by South Atlantic Central Water. The latter originates at the Subtropical Convergence Zone by mixing and sinking of subtropical and subantarctic surface water (Lutjeharms & Valentine 1987).

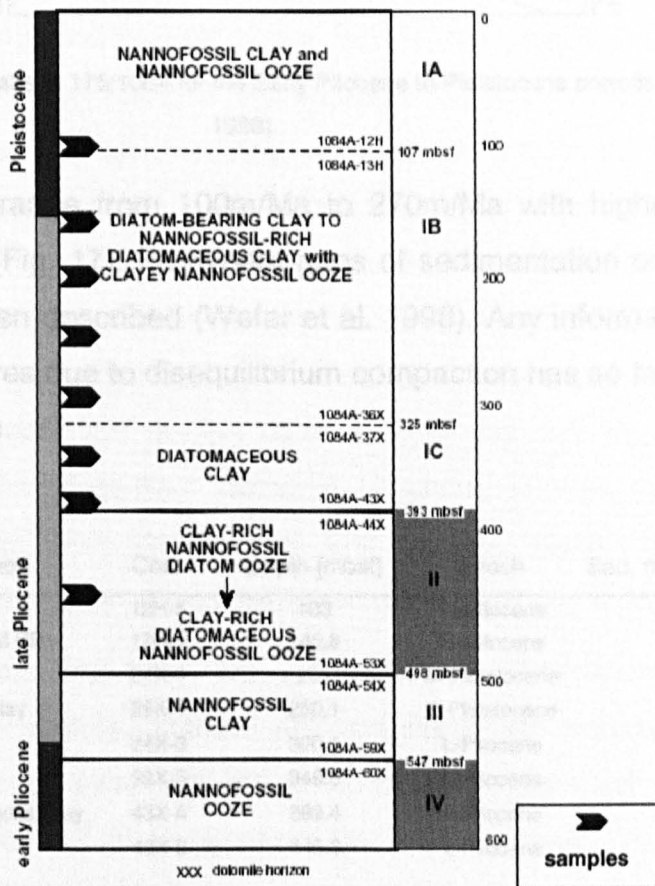


Fig. 16 Lithostratigraphy and sampled horizons of well 175/1084 (Wefer et al. 1998).

The lithostratigraphic column at site 1084 is built up mainly by hemipelagic nannofossil and diatom-bearing clays and oozes (Fig. 16), a sedimentary

facies typical for upwelling zones. The eight samples analyzed from this well were taken from the clay-rich sequences (Fig. 16, Table 12), but the fossiliferous opal content in these samples can still reach up to 27 wt% (Wefer et al. 1998).

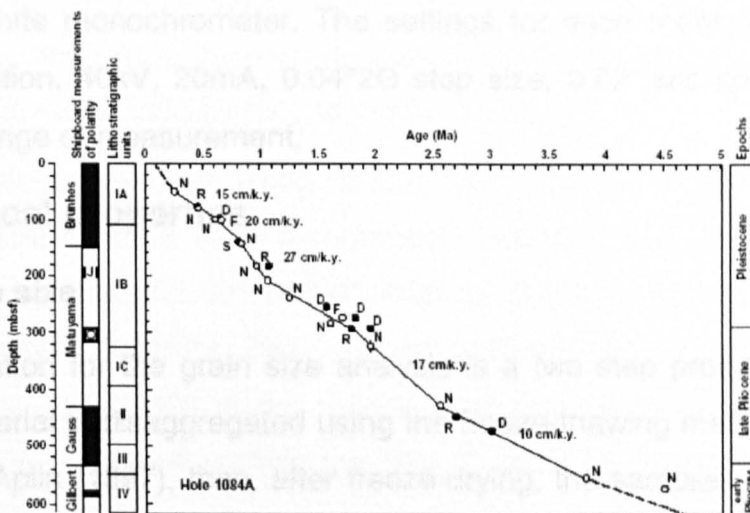


Fig. 17 Sedimentation rates at site 175/1084 for the Early Pliocene to Pleistocene periods (Wefer et al. 1998).

Sedimentation rates range from 100m/Ma to 270m/Ma with highest values within the last 1 Ma (Fig. 17). Prominent gaps of sedimentation or erosional surfaces have not been described (Wefer et al. 1998). Any information about elevated pore pressures due to disequilibrium compaction has so far not been reported from this site.

Lithological description	Core	Depth [mbsf]	Epoch	Sed. rate [m/Ma]
Nannofossil Clay	12H-5	103	Pleistocene	150
Diatomaceous Nannofossil Clay	17H-1	145.8	Pleistocene	230
Nannofossil Clay	24X-1	201	M-Pleistocene	220
Nannofossil Bearing Clay	29X-1	250.1	E-Pleistocene	120
Nannofossil Clay	34X-3	300.1	L-Pliocene	140
Diatomaceous Clay	39X-3	349.5	L-Pliocene	170
Nannofossil-Rich Diatomaceous Clay	43X-4	389.4	L-Pliocene	170
Nannofossil Clay	49X-6	449.3	L-Pliocene	120

Table 12 Samples from well 175/1084: Benguela Current; L – Late, M – Middle, E – Early.

2.2 Mineralogy

The mineralogy of the sample set was determined by X-ray powder diffractometry. The setup used was a Hiltonbrooks DG2 X-ray generator connected to a Phillips PW1050 goniometer with a Phillips PW1752 single crystal graphite monochromator. The settings for each measurement were: Cu-K α radiation, 40kV, 20mA, 0.04°2 Θ step size, 0.02°/sec speed and 2.5-80.02°2 Θ range of measurement.

2.3 Physical properties

2.3.1 Grain size

The preparation for the grain size analysis is a two step process: firstly the sample material is disaggregated using the freeze-thawing method described by Yang & Aplin (1997), then, after freeze-drying, the samples are dispersed and homogenised using an ultrasonic probe. Finally, the grain size distribution (63-0.25 μm) is determined using a *Micromeritics Sedigraph 5000ET*®. For this measurement about 1.5g of sample material are dispersed in 45ml of distilled water. 5ml of a dispersant solution (0.35M sodium metaphosphate/0.06M sodium carbonate) are then added to the sample solution to avoid any flocculation of clay minerals. During the Sedigraph measurement, X-rays pass through a cell filled with the sample solution and the X-ray intensities detected on the other side of the cell determine the settling velocity of the dispersed particles. Applying Stokes' Law, these settling velocities are then transformed into particle sizes. The weight percentage of material coarser than 63 μm is determined using a 63 μm sieve.

The particle sizes resulting from the application of Stoke's law describe values for spherical grains. These are sufficient for samples mainly comprised of quartz or other spherical minerals but do not accurately describe the grain sizes of platy minerals like phyllosilicates. To overcome these problems the Sedigraph measurements were calibrated with internal standards (London Clay) which had been previously analysed using the pipette method (British Standards 1377, part 6, 1990). The pipette method utilizes the relationship between settling time and grain size (Stoke's Law).

For this method a sediment sample is brought into suspension and sampled by pipette after pre-defined time intervals. Due to the rapid settling velocities of grains with diameters larger than $10\mu\text{m}$, only the $\leq 10\mu\text{m}$ size fraction could be calibrated using this method. Consequently, the detailed analysis of the grain size distributions in this study was limited to the $0.25\mu\text{m}$ - $10\mu\text{m}$ interval. The repeated analysis of the internal standards with the Sedigraph revealed a relatively high reproducibility for this interval.

For the Sedigraph method, every sample has a distinct value for the RATE-parameter that controls the measurement (duration, step size etc.). RATE stands for sedimentation rate and depends on the liquid viscosity and on the liquid and particle densities. The input parameters to determine RATE are the grain density, the weight of the sample material, the temperature and the volume of the dispersed sample solution. In order to estimate the errors of incorrect grain densities or temperatures, the effects of different RATE-values on the resulting clay fraction was determined using a fine-grained (76% $< 2\mu\text{m}$) sample. The results reveal, that the errors caused by deviating grain densities ($\pm 0.15 \text{ g/cm}^3$) and solution temperatures ($\pm 2 \text{ }^\circ\text{C}$) are within the reading errors caused by the thickness of the plotting line ($\pm 0.75 \text{ \% } < 2\mu\text{m}$).

2.3.2 Grain density

In reality, rocks are very inhomogeneous and comprised of many different minerals with varying densities. Different depositional environments lead to lithologies which might be classified by grain size (e.g. silts or clays), but are dominated by very different constituents. Textbooks often display lists of grain densities or grain density ranges for certain lithologies, which are then used to estimate physical properties like porosity, sonic velocity or shear strength. Table 13 shows published grain density ranges for minerals and lithologies that are typical for use in petroleum geoscience (e.g. basin modelling). Changes in mineral composition due to different sedimentary regimes (e.g. shelf or deep sea basin) are reflected by large variations in grain density (Table 14) and might limit the applicability of the published values (Table 13) significantly. Additionally, diagenesis and low-grade metamorphism during burial alter the mineral matrix and change the grain density of these

lithologies further. It is therefore very important to establish which range of grain densities can be expected for a certain lithological formation. The importance of these observations becomes more and more important due to the increased number of petroleum prospects in shallow deep sea sedimentary sequences (Ellouz-Zimmermann & Mascle, 2001).

Lithology/Mineral	Density [g/cm ³]
Sandstone	2.65
Limestone	2.71
Dolomite	2.87
Clay-shales	2.65-2.70
Salt	2.04
Gypsum	2.35
Quartz	2.65
Smectite	2.0-3.0
Kaolinite	2.40-2.69
Chlorite	2.60-3.22
Muscovite	2.76-3.1
Biotite	2.65-3.1

Table 13 Typical grain densities (matrix densities) used in petroleum geoscience (Rider, 1996).

In this study, the grain densities for a variety of marine clay-rich lithologies comprised of a wide range of different mineral phases were obtained applying the pycnometer method (British Standard 733, 1987). Some of the results are displayed in Table 14 and reveal, that under certain circumstances sediments classified as "clay" can yield grain densities around 2.1 g/cm³ whereas others reach values of up to 2.9 g/cm³. The dominance of opal-A/opal-CT in upwelling systems for example, can lead to a significant decrease in grain density whereas the abundance of smectite in other areas increases this value. Higher organic carbon contents also lead to lower grain densities.

After elimination of all samples containing significant amounts of nanno- or microfossils (diatoms, radiolaria etc.) and thus opal-A/opal-CT, the grain density average of the remaining clays and mudstones is about 2.71 g/cm³. This value closely resembles the "shale" grain density value used for most basin models (Table 13; Rider, 1996). The grain densities of the complete sample set averages about 2.61 g/cm³. Quartz standards (grain density: 2.65

g/cm^3) were included in all runs (sets of about 15 samples) and revealed a standard deviation of $\pm 0.02 \text{ g/cm}^3$ for 29 measurements (Fig. 18).

Sedimentary environment	Water depth [m]	Sample depth [m]	Grain density	% $<2\mu\text{m}$
Shelf	98	51.35	2.781	59
Coastal Upwelling	2004	250.1	2.294	59
Coastal Upwelling	2004	389.4	2.103	61
Continental Rise	2626	350.37	2.662	62
Continental Rise	4782	252.94	2.946	59
Continental Rise	4782	731.8	2.763	60
Deep Sea Fan	4748	200	2.789	63
Deep Sea Basin	2821	453.6	2.579	65

Table 14 The variety of grain densities in samples of similar grain size ("clays").

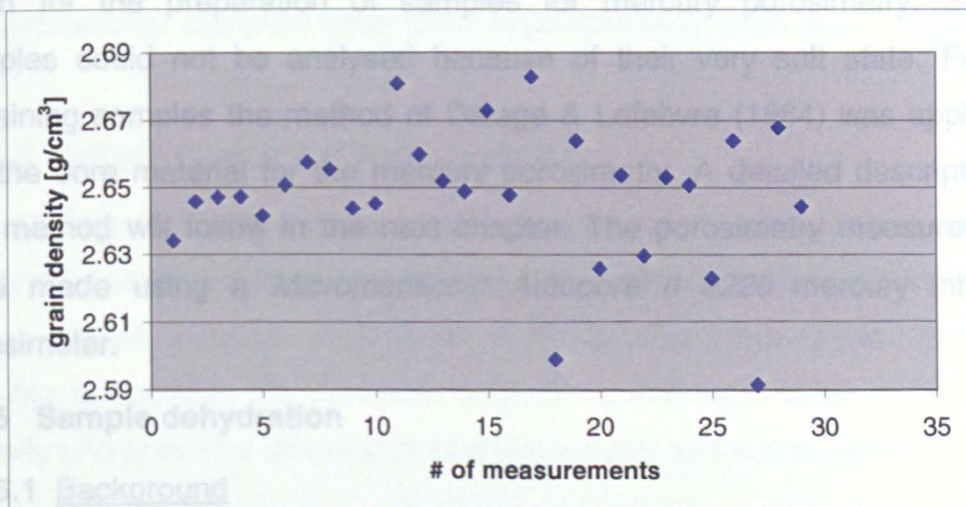


Fig. 18 Summary of grain densities determined for a quartz standard. The calculated mean and median is $2.65 \pm 0.02 \text{ g/cm}^3$.

2.3.3 Porosities provided by ODP

The majority of the porosities published by the DSDP and ODP were determined gravimetrically, using the wet bulk weight, dry weight, volume and grain densities of fresh sample material at room temperature (Boyce 1976, 1984). In few cases (26/250-7,8,10,13,14,17), only porosity data calculated with the GRAPE tool were available. The GRAPE technique utilises the attenuation of gamma ray intensity in a beam passing through a sediment sample to calculate the bulk density (Boyce 1976, 1984). This on-board

technique is very sensitive to both the quality of the core and the accuracy of the actual measurement process, and usually provides data of lower reliability. In addition, the grain density used in the GRAPE algorithms to infer the porosity is by default 2.7 g/cc (Boyce 1976) which often deviates significantly from the real values.

In some cases, sample material provided for this study originated from positions on the core which were up to 5m away from those used by the ODP for their porosity measurements. In these cases ODP porosities over the adjacent interval were averaged to diminish the uncertainties.

2.3.4 Mercury intrusion porosimetry

Due to the fragile and soft condition of most samples, special care had to be taken for the preparation of samples for mercury porosimetry. Several samples could not be analysed because of their very soft state. For the remaining samples the method of Delage & Lefebvre (1984) was applied to dry the core material for the mercury porosimetry. A detailed description of this method will follow in the next chapter. The porosimetry measurements were made using a *Micromeritics® Autopore II 9220* mercury intrusion porosimeter.

2.3.5 Sample dehydration

2.3.5.1 Background

Drilling and sampling of soils and clay-rich formations, which have not been lithified by cementation, revealed that these sediments remain relatively soft (i.e. sensitive to small physical forces) until burial depths of at least 1000m. Exposure to air leads to the evaporation of pore water of these structurally weak sediments and the surface tension forces at the air-water interface often cause significant shrinkage (e.g. Gillot 1973; Tovey & Wong 1973; Delage et al. 1982, Delage and Lefebvre 1984). To avoid these fabric changes, various methods to remove the pore fluid have been examined and the effects on the microstructure analyzed (e.g. Tovey and Wong 1973; Gillot 1973). Results revealed that the simple exposure to air under ambient conditions (Gillot 1973) has the strongest impact on clay fabric and that oven drying causes

less shrinkage than air drying (Tovey & Wong 1973). However, both methods significantly alter the sample material and must be used with caution when determining the structural or physical properties of sediments. In contrast, methods like freeze-drying or critical point drying have been found to be least destructive and are widely recommended for the pore structure analysis of soils and clays (e.g. Gillot 1973; Tovey and Wong 1973; Delage et al 1982). More recent publications (e.g. Delage and Lefebvre 1984; Griffiths and Joshi 1990; Dewhurst et al. 1998) suggest that freeze-drying is the most commonly used drying method.

Many of the samples examined in this study were provided by the DSDP/ODP and most of these had dried out during storage. In order to estimate the impact of drying on the mercury intrusion porosimetry (MIP) measurements, two glacial clay samples have been experimentally dried and analyzed by MIP.

2.3.5.2 Sample storage and drying techniques

The rationale for taking two glacial clay samples was to establish the extent to which different methods of storage and drying affect the poro-perm properties of non-lithified, clay-rich sediments. If these effects are known, it will be possible to estimate the minimum corrections that need to be made to the porosity and pore size distribution of dried-out clay and soil samples.

In this investigation two clay cores (BI and BII) were taken from an open boulder clay pit at Birtley Brickworks in Birtley, south of Newcastle upon Tyne. The cores were taken using a plastic pipe 5cm in diameter. The first core (BI) was located stratigraphically 4m lower than the second (BII). The mineralogy of both samples is dominated by kaolinite and quartz with illite and chlorite as accessory constituents. BI and BII have a grain densities and clay fractions of 2.76g/cm^3 and 67% and 2.8g/cm^3 and 56%, respectively.

Two pieces of each sample were separated directly after sampling to measure the degree of pore-water loss due to different methods of sample storage. One piece of each sample was placed in an open plastic beaker and stored in a cupboard under ambient conditions. The second piece as well as the remainder of the sample material was wrapped in aluminium foil, placed

in a plastic bag and stored in a refrigerator. The weights of all samples were measured on the day of sampling and on several later dates in order to determine the amount of pore water evaporated.

The extent of the water loss for the two methods of sample storage are displayed in Fig. 19 and Fig. 20. Exposure to air led to a reduction of sample weight by 22% and 21% after 77 days for BI and BII, respectively (Fig. 19). This accounts for a reduction of the total water content by 93% for BI and 94% for BII (Table 15). A second measurement after 238 days revealed that by then about 99% of the pore water in both samples had been lost due to evaporation. In comparison, samples stored in the refrigerator lost insignificant amounts of water (Fig. 20, Table 15). The water content after storage for 204 days was still greater than 99% of the initial value for both BI and BII. At this point the foil wrapping of the samples had to be renewed, resulting in the loss of minor amounts of sample material and thus, a relatively large decrease in weight after 238 days.

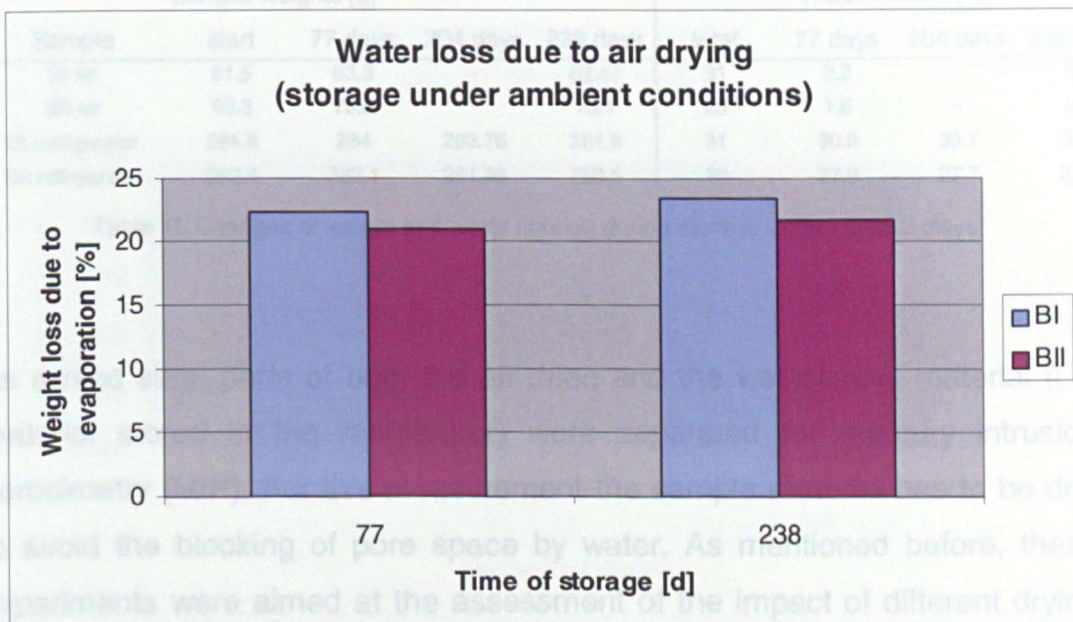


Fig. 19 The amount of pore water lost during storage of two clay samples (BI & BII) under ambient conditions. Both samples have lost most of their moisture after 77 days.

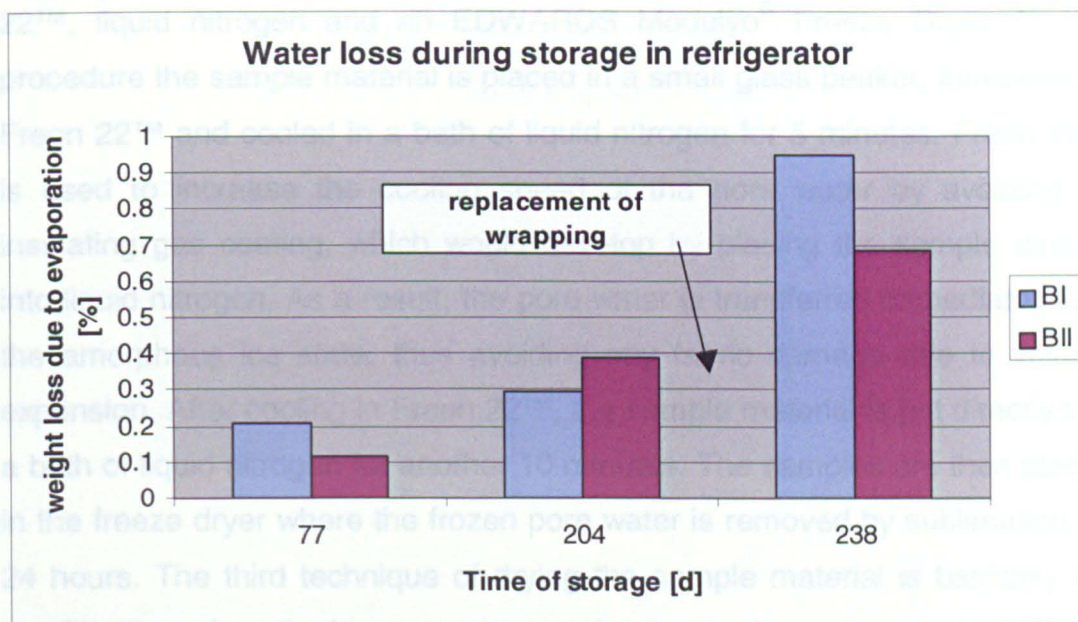


Fig. 20 The extent of evaporation during storage in a refrigerator. The amount of pore water lost during storage is minimal (less than 0.5% after 204 days) and only the replacement of the aluminium foil wrapping led to a distinct loss of sample weight.

Sample	Sample weights [g]				total	Water content [%]		
	start	77 days	204 days	238 days		77 days	204 days	238 days
BI air	81.5	63.3	-	62.47	31	2.2	-	0.3
BII air	93.3	73.8	-	73.1	28	1.6	-	0.4
BI refrigerator	284.6	284	283.76	281.9	31	30.8	30.7	30.3
BII refrigerator	262.4	262.1	261.38	260.6	28	27.9	27.7	27.7

Table 15 Changes of weight and water content during storage for two glacial clays.

As a next step, parts of both the air dried and the wet sample material (i.e. material stored in the refrigerator) were separated for mercury intrusion porosimetry (MIP). For this measurement the sample material has to be dry, to avoid the blocking of pore space by water. As mentioned before, these experiments were aimed at the assessment of the impact of different drying methods on MIP. Therefore, three different procedures were used to prepare both air dried and wet samples for MIP.

For the first method about 5g of the air dried and about 18g of the wet samples were placed in an oven at 105°C for 24 hours. For the second technique similar amounts of sample material were freeze-dried using Freon

22TM, liquid nitrogen and an EDWARDS Modulyo[®] Freeze Dryer. In this procedure the sample material is placed in a small glass beaker, immersed in Freon 22TM and cooled in a bath of liquid nitrogen for 5 minutes. Freon 22TM is used to increase the cooling speed of the pore water by avoiding an insulating gas coating, which would develop by placing the sample directly into liquid nitrogen. As a result, the pore water is transferred immediately into the amorphous ice state, thus avoiding any fabric damage due to volume expansion. After cooling in Freon 22TM, the sample material is put directly into a bath of liquid nitrogen for another 10 minutes. The samples are then placed in the freeze dryer where the frozen pore water is removed by sublimation for 24 hours. The third technique of drying the sample material is basically the combination of methods one and two, where samples are oven dried for 24 hours directly after the "Freon 22TM freeze drying" process.

The results of the measurements show (Fig. 21 & Fig. 22) that all three procedures remove approximately the same amount of pore water from the sample material.

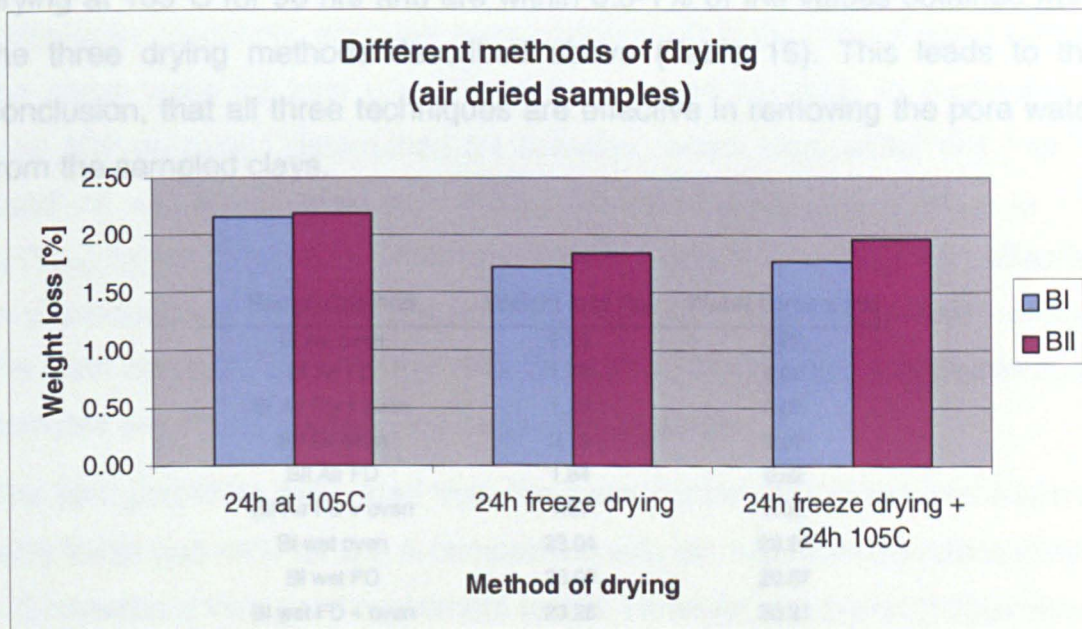


Fig. 21 The amount of pore water removed from the air dried sample material by different drying processes: 1. 24h at 105°C (oven drying); 2. 24h Freon-22TM freeze drying; 3. 24h Freon-22TM freeze drying combined with 24h at 105°C (oven drying).

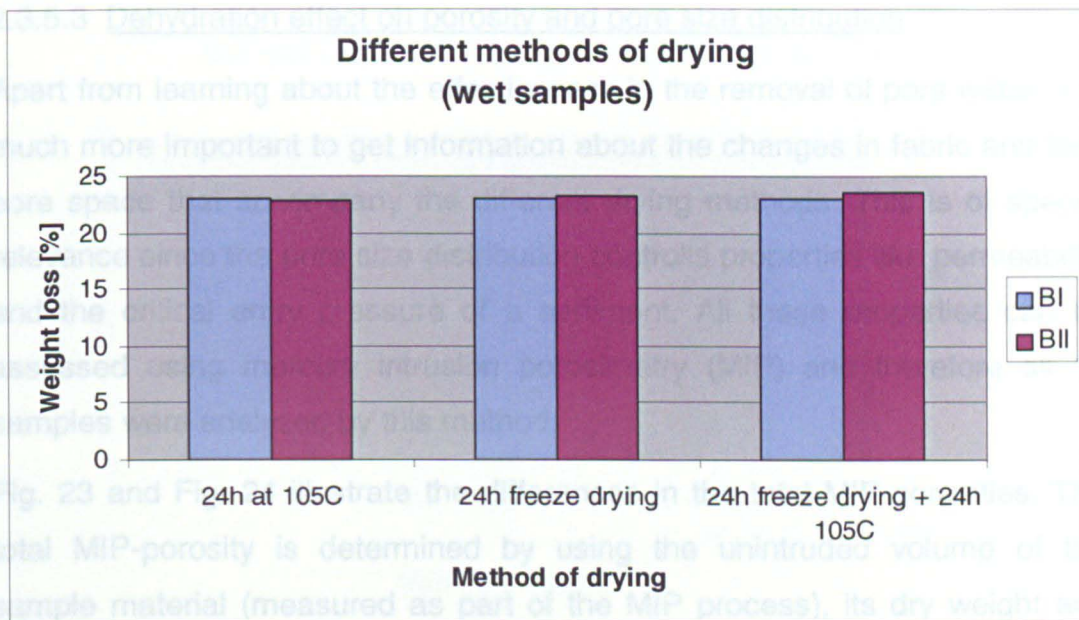


Fig. 22 The amount of pore water removed from the wet sample material by different drying processes:

1. 24h at 105°C (oven drying);
2. 24h Freon-22™ freeze drying;
3. 24h Freon-22™ freeze drying combined with 24h at 105°C (oven drying).

The total water contents of samples BI and BII were determined by oven drying at 105°C for 96 hrs and are within 0.5-1% of the values obtained from the three drying methods described above (Table 16). This leads to the conclusion, that all three techniques are effective in removing the pore water from the sampled clays.

Sample/method	Weight loss [%]	Water content [%]
BI Air oven	2.16	0.02
BI Air FD	1.73	0.02
BI Air FD + oven	1.78	0.02
BII Air oven	2.19	0.02
BII Air FD	1.84	0.02
BII Air FD + oven	1.97	0.02
BI wet oven	23.04	29.94
BI wet FD	23.00	29.87
BI wet FD + oven	23.26	30.31
BII wet oven	24.23	31.98
BII wet FD	23.17	30.15
BII wet FD + oven	23.85	31.33

Table 16 The amount of pore water removed by oven drying for 24h at 105°C (oven), freeze-drying (FD) and a combination of both methods (FD + oven).

2.3.5.3 Dehydration effect on porosity and pore size distribution

Apart from learning about the effectiveness in the removal of pore water, it is much more important to get information about the changes in fabric and thus pore space that accompany the different drying methods. This is of special relevance since the pore size distribution controls properties like permeability and the critical entry pressure of a sediment. All these properties can be assessed using mercury intrusion porosimetry (MIP) and therefore all 12 samples were analysed by this method.

Fig. 23 and Fig. 24 illustrate the differences in the total MIP-porosities. The total MIP-porosity is determined by using the unintruded volume of the sample material (measured as part of the MIP process), its dry weight and grain density. It often differs slightly from the intruded MIP-porosity since not all pores are connected or large enough to be intruded under the applied pressures.

Two main features can be observed; firstly, there is no significant difference in total porosity for the air dried samples, independent of all drying techniques. Secondly, each wet sample dried only in the oven showed exactly the same value for total porosity as the air-dried samples. In contrast, the total MIP-porosities determined for samples, which were either wet freeze-dried or wet freeze-dried and then oven dried, were 5% (15%_{rel}) to 7% (17%_{rel}) higher (Table 17). Therefore, freeze-drying seems to be very effective in preventing a significant shrinkage of the initial pore space during drying. For both clays, BI and BII, the total porosities of the freeze-dried/oven-dried samples are 1% higher than the freeze-dried samples.

The total porosities calculated from the water content of the samples reached 48% for BI and 44% for BII. A comparison with the total MIP-porosities (Table 17) reveals a very good agreement for BII. However, the porosity determined gravimetrically for BI is about 5% (10%_{rel}) greater than the one measured by MIP. Here, much smaller mean pore throat radii for BI might indicate that it was either not possible to intrude all pores with the applied pressure, or that BI contains a much higher amount of unconnected micropores.

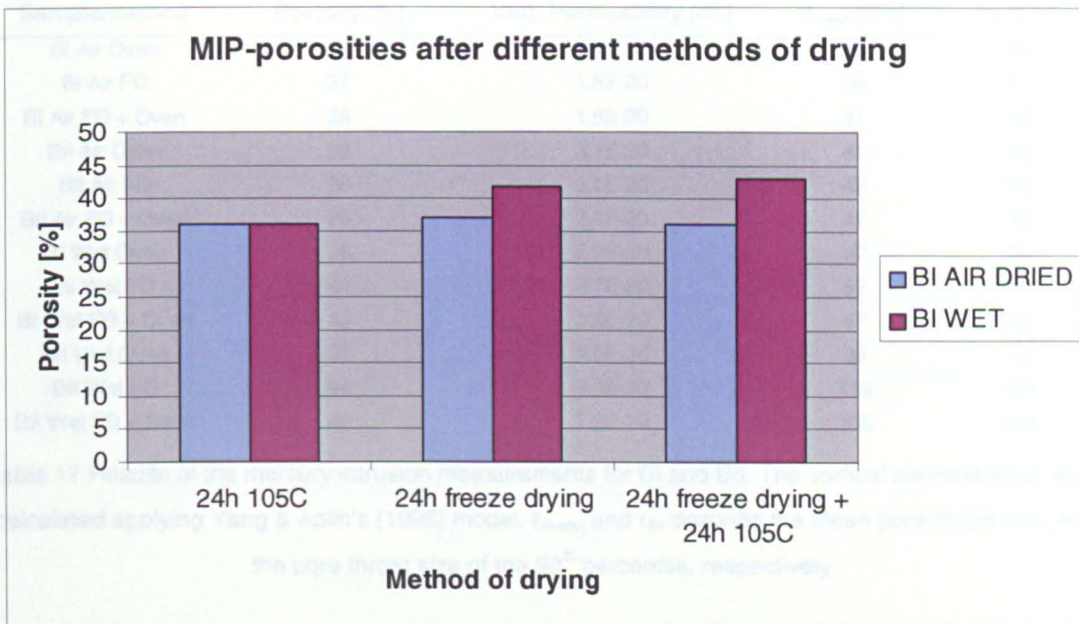


Fig. 23 The total MIP-porosities for the air-dried and wet samples of BI. Both the air-dried and the wet samples have been experimentally dried applying three different methods.

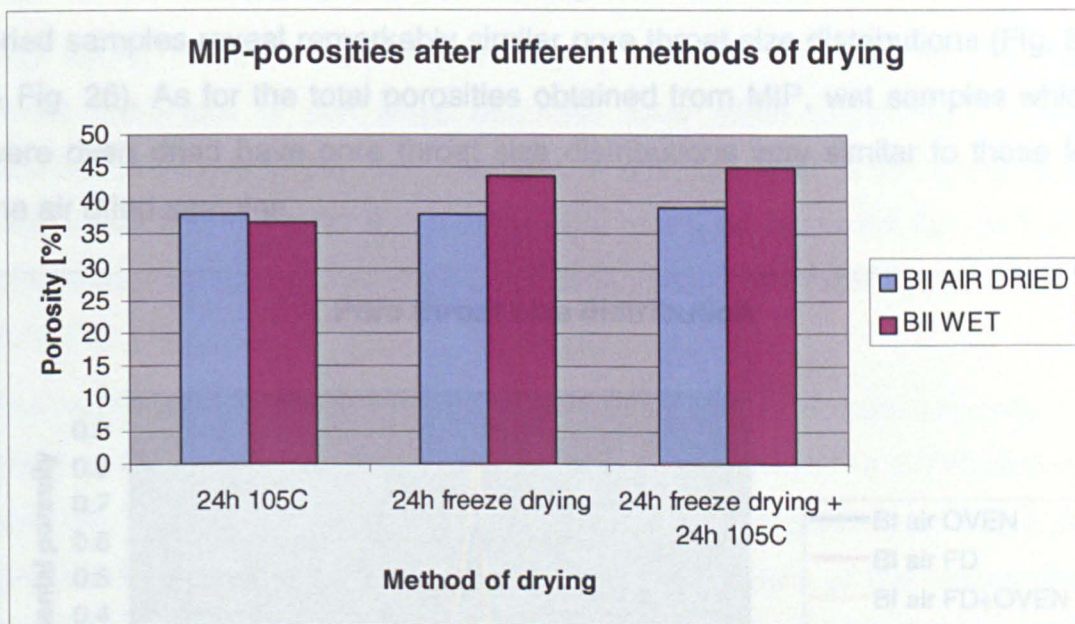


Fig. 24 The total MIP-porosities for the air-dried and wet samples of BII. Both the air-dried and the wet samples have been experimentally dried applying three different methods.

Sample/method	Porosity [%]	Vert. Permeability [m^2]	r_{mean} [nm]	r_{90} [nm]
BI Air Oven	36	1.7E-20	28	48
BI Air FD	37	1.8E-20	30	51
BI Air FD + Oven	36	1.8E-20	31	48
BII Air Oven	38	3.1E-20	41	83
BII Air FD	38	3.1E-20	42	80
BII Air FD + Oven	39	3.5E-20	47	95
BI Wet Oven	36	2.2E-20	37	56
BI Wet FD	42	3.7E-20	59	104
BI Wet FD + Oven	43	3.5E-20	57	95
BII Wet Oven	37	2.9E-20	39	77
BII Wet FD	44	9.0E-20	118	191
BII Wet FD + Oven	45	7.9E-20	106	159

Table 17 Results of the mercury intrusion measurements for BI and BII. The vertical permeabilities were calculated applying Yang & Aplin's (1998) model. r_{mean} and r_{90} describe the mean pore throat size and the pore throat size of the 90th percentile, respectively.

The influence of each drying method on the clay fabric can best be observed by analysing pore throat size distributions obtained by MIP (Fig. 25 to Fig. 28). For both samples (BI & BII), mercury intrusion measurements for the air dried samples reveal remarkably similar pore throat size distributions (Fig. 25 & Fig. 26). As for the total porosities obtained from MIP, wet samples which were oven dried have pore throat size distributions very similar to those for the air dried samples.

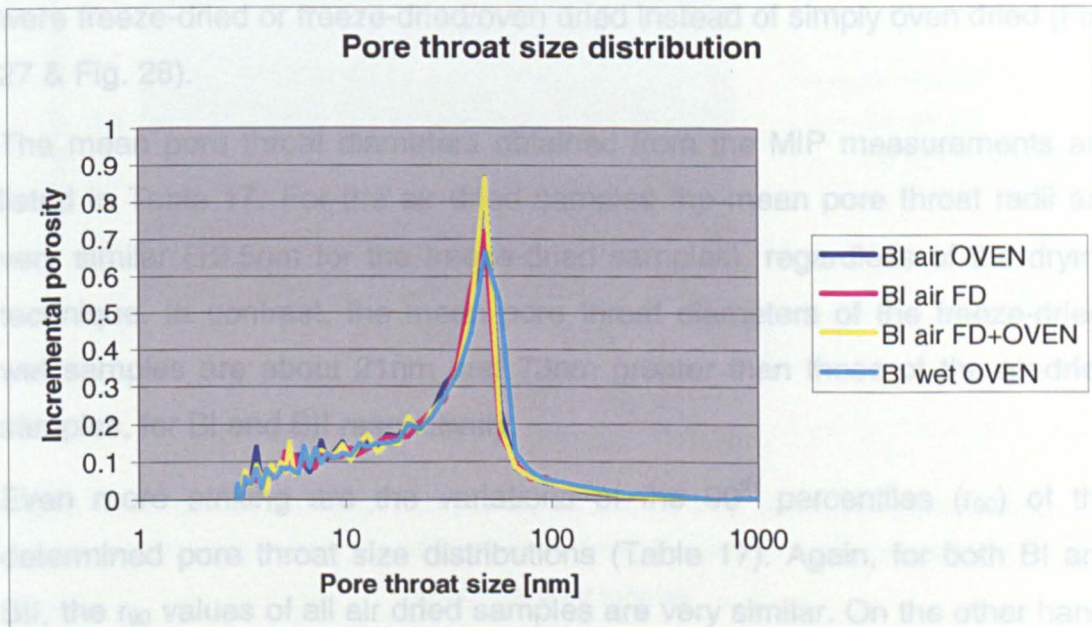


Fig. 25 Pore throat size distribution curves for the air dried samples and the wet oven dried sample of BI. All four drying methods resulted in very similar, unimodal distributions with insignificantly higher throat sizes for the wet sample.

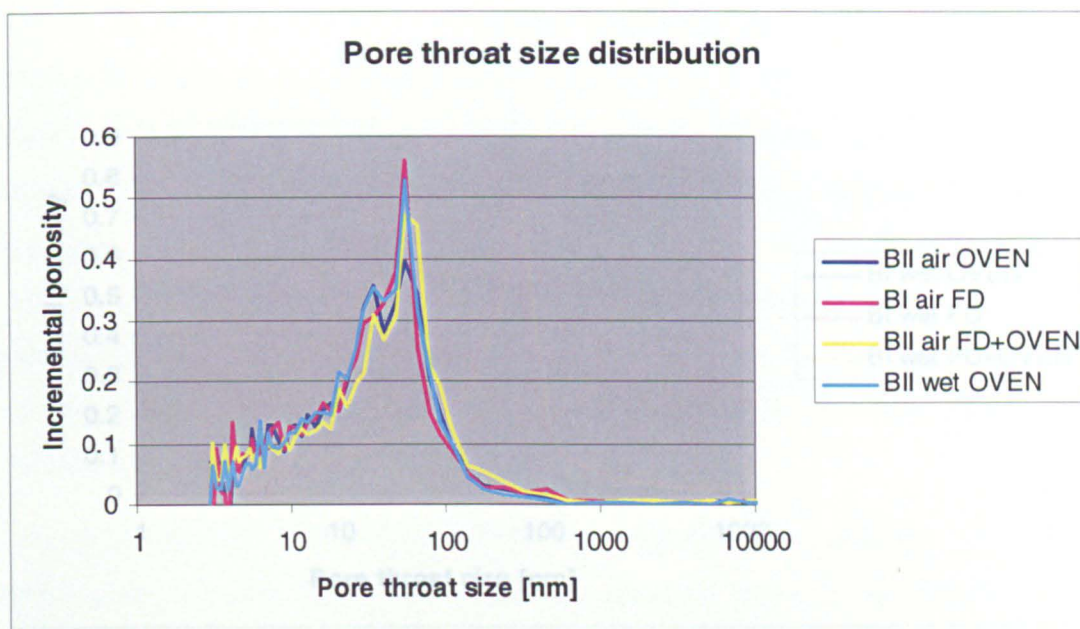


Fig. 26 Pore throat size distribution curves for the air dried samples and the wet oven dried sample of BII. Similar to BI, all four drying methods resulted in very similar, bimodal distributions.

The strong influence that different drying methods can have on the pore throat diameters of soft clays becomes clear when comparing the size distribution curves of the "wet" samples. In both cases (BI & BII) a significant shift towards larger pore throat diameters could be observed for clays that were freeze-dried or freeze-dried/oven dried instead of simply oven dried (Fig. 27 & Fig. 28).

The mean pore throat diameters obtained from the MIP measurements are listed in Table 17. For the air dried samples the mean pore throat radii are very similar ($\pm 2.5\text{nm}$ for the freeze-dried samples), regardless of the drying technique. In contrast, the mean pore throat diameters of the freeze-dried, wet samples are about 21nm and 73nm greater than those of the air-dried samples, for BI and BII respectively.

Even more striking are the variations of the 90th percentiles (r_{90}) of the determined pore throat size distributions (Table 17). Again, for both BI and BII, the r_{90} values of all air dried samples are very similar. On the other hand, the differences between the wet oven dried and wet freeze-dried samples are significant.

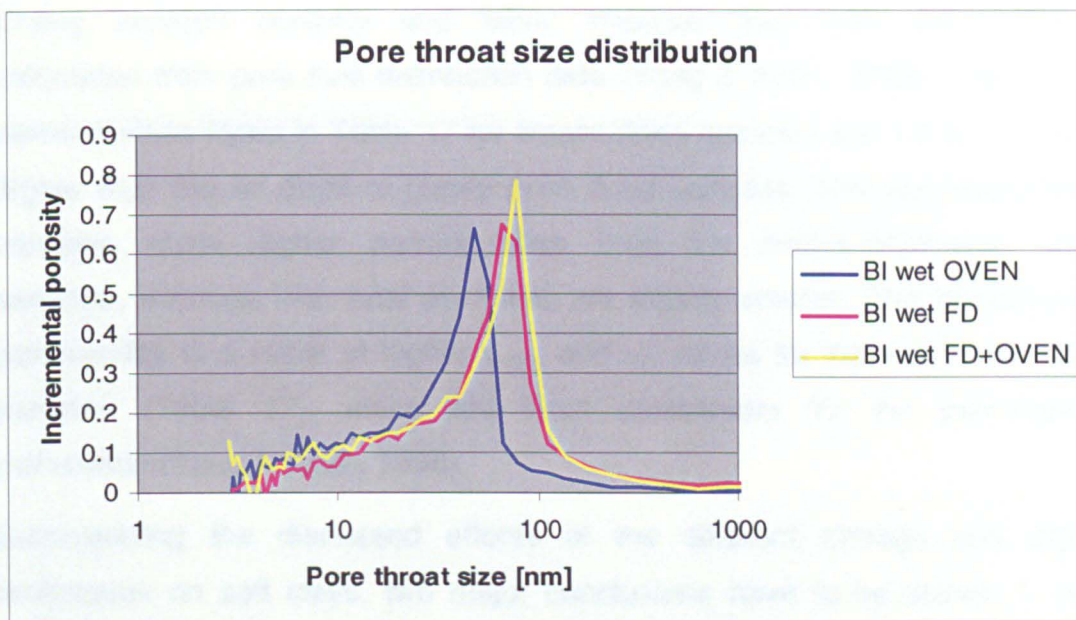


Fig. 27 Pore throat size distribution curves for the wet samples of BI. The curves are shifted significantly towards higher pore throat diameters for the freeze-dried and freeze-dried/oven dried samples.

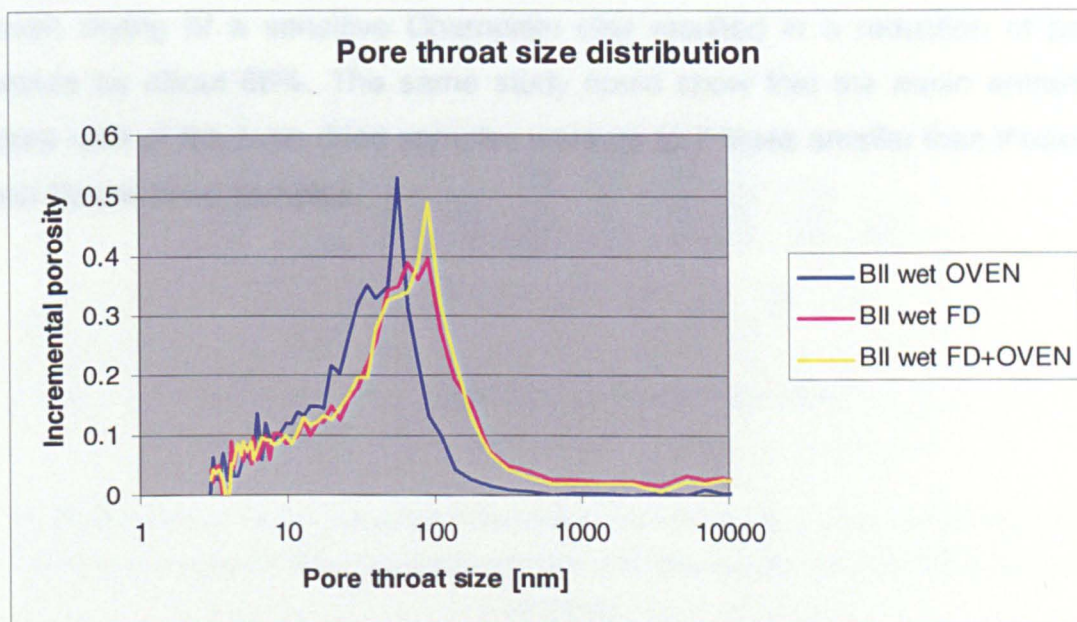


Fig. 28 Pore throat size distribution curves for the wet samples of BII. As could be observed for BI, the curves are shifted significantly towards higher pore throat diameters for the freeze-dried and freeze-dried/oven dried samples.

The r_{90} value for the wet, freeze-dried sample of BI (104nm) is about twice that of the wet, oven dried sample (56nm), and three times greater for BII.

Drying induced porosity and fabric changes also alter permeabilities calculated from pore size distribution data (Yang & Aplin, 1998). The vertical permeabilities listed in Table 17 for freeze-dried samples are 1.6 to 3.1 times higher than the air dried or purely oven dried samples. The wet freeze-dried samples show higher permeabilities than the freeze-dried/oven dried samples, although their total porosities are slightly smaller. This difference in permeability is a result of higher r_{mean} and r_{90} values for the wet freeze-dried samples (Table 17), which are input parameters for the permeability calculation (Yang & Aplin, 1998).

Summarizing the discussed effects of the different storage and drying techniques on soft clays, two major conclusions have to be drawn: 1. only fresh sample material (in-situ water content) should be used for MIP; 2. Freon 22™ freeze-drying effectively preserves the pore space and fabric of soft clays during drying. The latter observation confirms earlier experiments by Delage & Lefebvre (1984) who could show that in contrast to freeze-drying, oven drying of a sensitive Champlain clay resulted in a reduction of pore space by about 66%. The same study could show that the mean entrance pore radii of the oven dried samples were up to 7 times smaller than those of the freeze-dried samples.

3 Results

3.1 Grain size distribution

Measured clay fractions (% of mass $<2\mu\text{m}$) vary between 18% in sandy samples and 85% in deep sea clays (Table 18).

Fig. 29 to Fig. 32 show weight percentages for the $0.25\mu\text{m}$ to $10\mu\text{m}$ fraction which are representative for the sample set. The distinct characteristics of the grain size distributions reflect the various sediment types present in the sample set. For reasons explained in the previous chapter (**2 Samples and Methods**) the detailed grain size analysis was limited to the interval between $0.25\mu\text{m}$ and $10\mu\text{m}$. In Table 18 the weight percentages for the very fine-grained ($<0.25\mu\text{m}$) and coarse-grained material are listed together with the clay fraction ($<2\mu\text{m}$) and median grain size (Φ_{50} , where $\Phi = -\log_2(\text{grain size in mm})$).

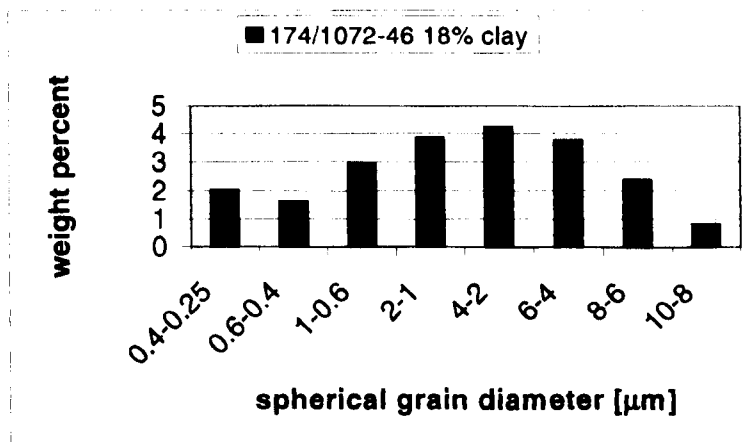


Fig. 29 Histogram of the size distribution in the $0.25\mu\text{m}$ - $10\mu\text{m}$ fraction for a sandy sample (18% $<2\mu\text{m}$). The amount of material outside this spectrum is 78% of the total sample mass (i.e. 70% $>10\mu\text{m}$ & 8% $<0.25\mu\text{m}$).

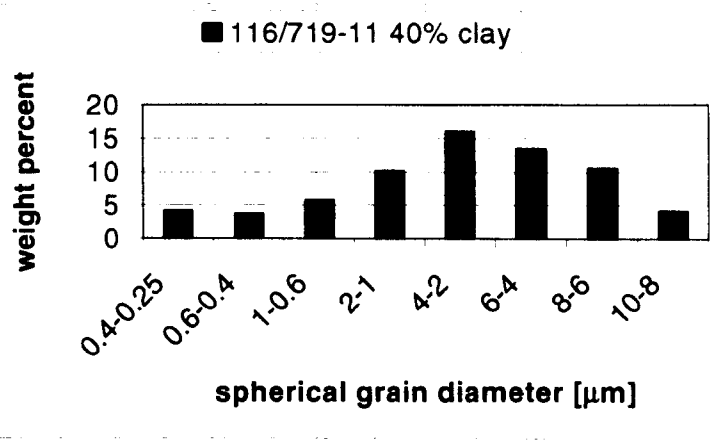


Fig. 30 Histogram of the size distribution in the $0.25\mu\text{m}$ - $10\mu\text{m}$ fraction for a fine-silt sample (40% $<2\mu\text{m}$). The amount of material outside this spectrum is 32% of the total sample mass (i.e. 16% $>10\mu\text{m}$ & 16% $<0.25\mu\text{m}$).

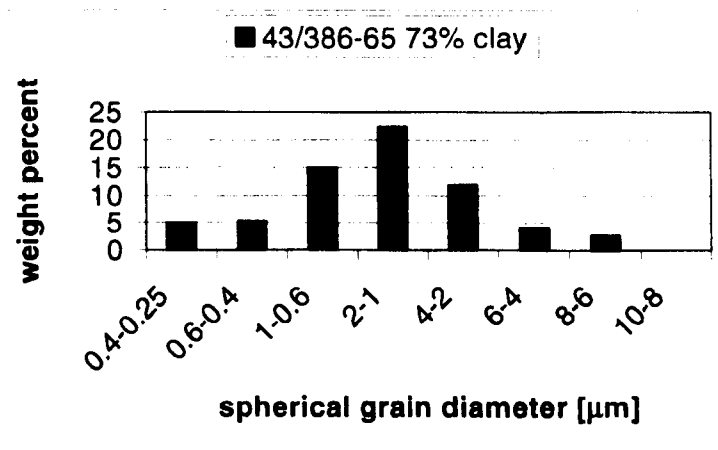


Fig. 31 Histogram of the size distribution in the $0.25\mu\text{m}$ - $10\mu\text{m}$ fraction for a clay sample (73% $<2\mu\text{m}$). The amount of material outside this spectrum is 33% of the total sample mass (i.e. 8% $>10\mu\text{m}$ & 25% $<0.25\mu\text{m}$).

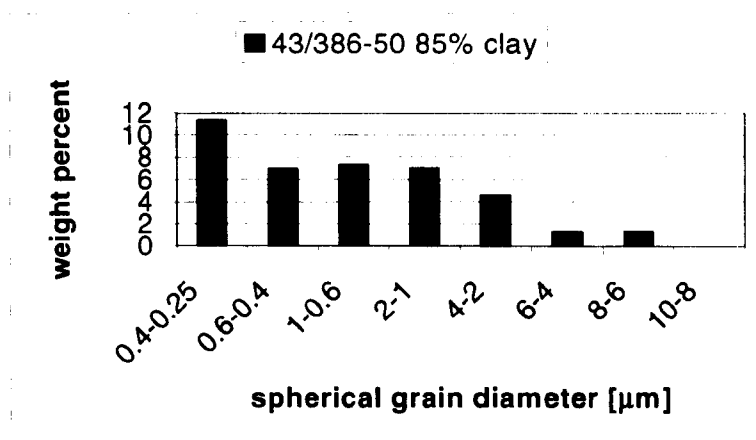


Fig. 32 Histogram of the size distribution in the 0.25 μ m-10 μ m fraction for a deep sea clay sample (85% <2 μ m). The amount of material outside this spectrum is 60% of the total sample mass (i.e. 8% >10 μ m & 52% <0.25 μ m).

The grain size distributions reveal that both the mode of the grain sizes between 0.25 μ m and 10 μ m (Fig. 29 to Fig. 32) and the median grain size (Table 18) shift towards smaller grain diameters with increasing clay fraction. This shift is accompanied by an increase in the amount of material (weight percent) within the 0.25 μ m to 10 μ m size window for samples with clay fractions of up to 70-75% (Fig. 31). For the very fine-grained samples (>50% <0.25 μ m, Table 18) the median of the grain sizes passed the 0.25 μ m to 10 μ m interval towards smaller diameters, resulting in a general decrease in sample material within the 0.25 μ m to 10 μ m size fraction.

3.1.1 Fossil-poor versus fossil-rich material

The sample set was divided into two major categories. The first is comprised of samples which do not contain significant amounts of fossil material. The second group contains the sample material where DSDP/ODP smear slide analyses identified larger amounts (>10%) of micro- and nanofossils or where X-ray diffraction analysis revealed the abundance of opal-A/CT (i.e. siliceous fossil material). Scanning electron microscopy was also used to examine the constituents of the samples.

The median grain sizes of the first category (fossil-poor samples) can be subdivided into three groups. The first group is mainly comprised of samples from wells 26/250 and 26/257, drilled into deep sea basin sequences which

show median grain diameters of $<0.45\mu\text{m}$ ($\Phi > 11.1$; Table 18). The majority of samples ($>80\%$) belongs to the second group, yielding median grain sizes between 0.6 to $3.2\mu\text{m}$ (~ 8.3 to 10.7Φ). The last and smallest group consists of 5 silty to sandy sediments, the latter reflected in Φ -values smaller than 7.8 ($>4.4\mu\text{m}$).

Many of the fine and very fine-grained deep water samples show the typical grain size distributions for eolian sediment input, where the size mode is just coarser than $2\mu\text{m}$ (9Φ) with very little material coarser than $16\mu\text{m}$ (6Φ ; Rea and Hovan 1995, Joseph et al. 1998).

A comparison of clay fraction and median grain size of the fossil-poor samples (Fig. 33) illustrates that both parameters are in very good agreement ($R^2 = 0.91$). It also shows that both clay fraction and median grain size characterize lithology in a similar manner.

The granulometric features of the fossil-rich samples in general resemble those of the fossil-poor material (Fig. 34 to Fig. 36; Table 19). However, median grain size and clay fraction are in less good agreement ($R^2 = 0.86$; Fig. 33) than they are for the fossil-poor samples.

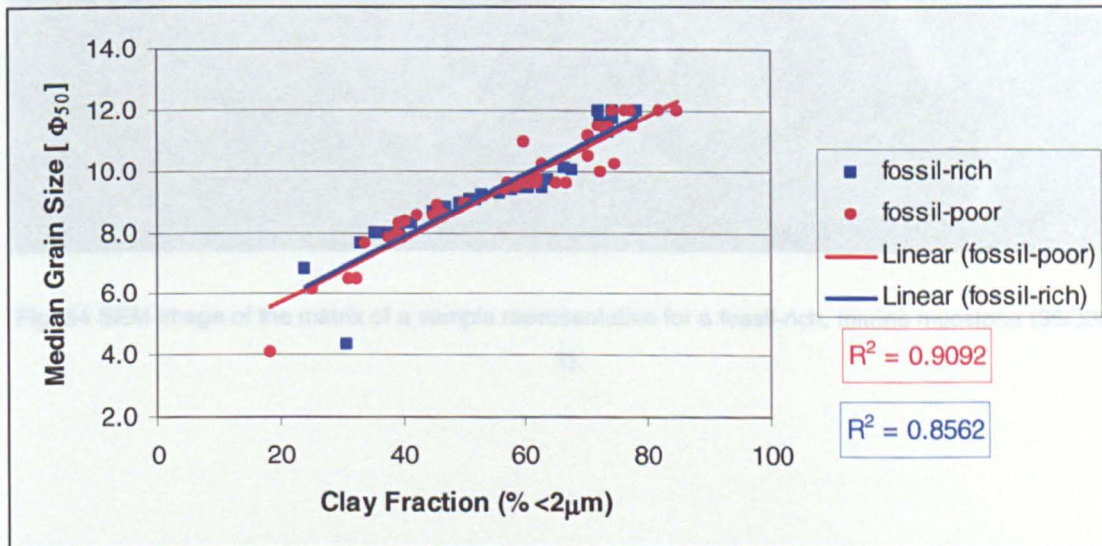


Fig. 33 A comparison of clay fraction and median grain size. Both fossil-rich and fossil-poor samples reveal a good agreement between the two parameters. However, the R^2 value for the fossil-rich material is lower than that of the fossil-poor samples.

In order to obtain some information about the general sorting of the smaller than 10 μm size fraction, the silt/clay ratio of this fraction was determined by dividing the mass percentage of the 2 μm to 10 μm fraction by the clay fraction ($\% \leq 2\mu\text{m}$). The results show that on average fossil-rich samples (Fig. 34) contain slightly more silt-sized grains relative to the clay fraction than fossil-poor samples. The determined silt/clay ratio for the former is 0.58 in contrast to 0.47 for the latter.

In comparison with fossil-poor samples of the same clay fraction, fossil-rich samples usually show higher porosities. This observation might partly be explained by the observed difference in silt/clay ratio and the different shape and rigidity of the fossil material (Fig. 34).

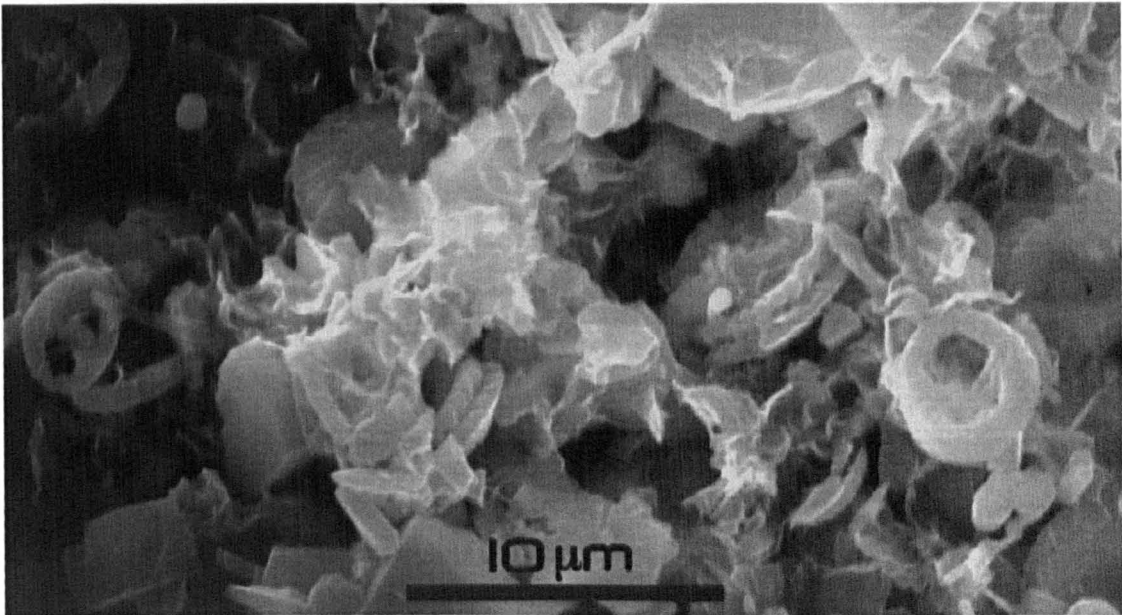


Fig. 34 SEM-image of the matrix of a sample representative for a fossil-rich, marine mudstone (36/330-1).

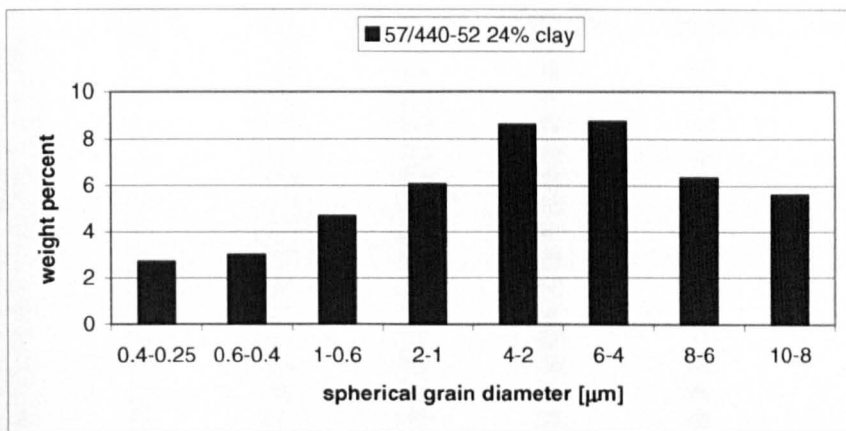


Fig. 35 Histogram of the size distribution in the 0.25 μm -10 μm fraction for a fossil-rich silty sample (54% <2 μm). The amount of material outside this spectrum is 55% of the total sample mass (i.e. 47% >10 μm & 8% <0.25 μm).

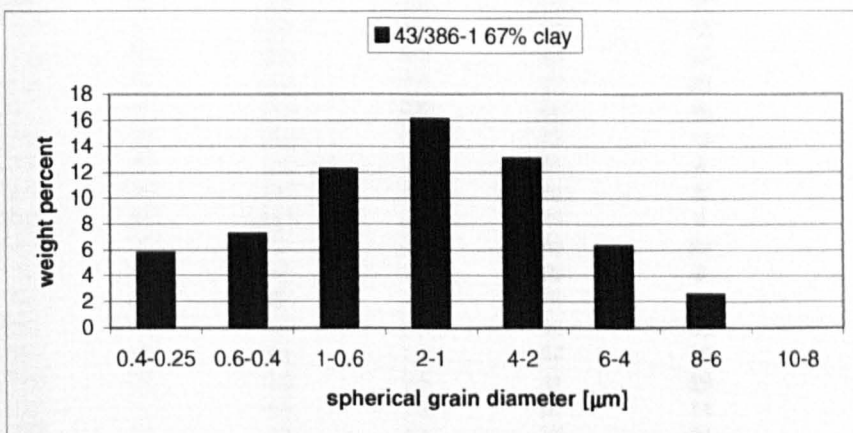


Fig. 36 Histogram of the size distribution in the 0.25 μm -10 μm fraction for a fossil-rich clay sample (67% <2 μm). The amount of material outside this spectrum is 37% of the total sample mass (i.e. 10% >10 μm & 27% <0.25 μm).

Well	Sample	Φ_{50}	Φ_{50} in μm	<2 μm [%]	>10 μm [%]	<0.25 μm [%]
26/250	4	11.5	0.4	72	9	45
26/250	6	11.5	0.4	72	8	46
26/250	9	>12.0	<0.3	77	8	51
26/250	11	>12.0	<0.3	74	11	51
26/257	1	11.1	0.5	70	15	41
26/257	3	>12.0	<0.3	76	8	57
26/257	5	11.3	0.4	73	8	44
26/257	9	>12.0	<0.3	82	8	59
36/330	6	8.0	4.0	39	34	19
36/330	8	9.6	1.3	62	11	23
36/330	9	9.5	1.4	59	12	15
36/330	10	9.7	1.2	62	11	16
36/330	11	9.0	2.0	50	21	12
36/330	13	7.8	4.4	40	39	15
36/330	14	6.2	14.0	25	60	14
43/386	4	8.9	2.1	46	11	19
43/386	11	9.6	1.3	59	9	30
43/386	36	11.5	0.4	74	11	45
43/386	42	9.6	1.3	60	8	23
43/386	50	>12.0	<0.3	85	8	52
43/386	54	9.6	1.3	67	8	25
43/386	55	10.5	0.7	71	10	26
43/386	59	10.2	0.8	75	8	24
43/386	65	10.0	1.0	73	8	25
116/719	11	8.3	3.2	40	16	16
116/719	14	8.5	2.7	42	12	16
116/719	16	8.5	2.7	45	20	21
116/719	17	11.0	0.5	60	16	44
116/719	22	10.2	0.8	63	13	28
116/719	28	9.6	1.3	61	8	32
116/719	33	9.6	1.3	60	8	24
116/719	38	11.5	0.4	78	8	44
127/794	11	8.4	3.0	40	22	12
127/794	17	9.6	1.3	65	8	14
127/794	20	9.4	1.5	57	12	13
150/906	14	9.0	2.0	51	30	22
150/906	31	9.6	1.3	57	15	21
150/906	33	8.6	2.5	47	29	18
174/1072	7	9.6	1.3	61	11	23
174/1072	11	7.8	4.4	38	34	17
174/1072	17	6.5	11.0	33	51	15
174/1072	25	6.5	11.0	31	52	17
174/1072	37	7.6	5.0	34	40	13
174/1072	46	<4.1	60.0	18	70	8

Table 18 Results of the grain size analysis of the samples selected for the compaction curves, i.e. samples which are poor in nannofossils and yield good quality porosity data. Φ_{50} - median grain size where $\Phi = -\log_2(\text{grain size in mm})$.

Well	Sample	Φ_{50}	Φ_{50} in μm	$<2\mu\text{m}$ [%]	$>10\mu\text{m}$ [%]	$<0.25\mu\text{m}$ [%]
26/250*	7	11.7	0.3	74	8	48
26/250*	8	11.3	0.4	74	9	41
26/250*	10	>12.0	0.3	78	8	56
26/250*	13	>12.0	0.3	74	11	54
26/250*	14	12.0	0.3	72	11	50
26/250*	17	11.6	0.3	73	11	46
36/330	1	9.0	1.9	51	19	15
36/330	2	9.0	1.9	52	10	15
43/386	1	10.1	0.9	68	10	26
43/386	14	9.7	1.2	64	8	27
43/386	26	8.3	3.2	41	32	14
43/386	28	10.1	0.9	67	8	33
43/386	32	<4.3	50.0	31	63	15
57/440b	8	8.0	4.0	37	32	10
57/440b	13	8.0	4.0	40	32	13
57/440b	24	7.6	5.0	33	33	8
57/440b	28	8.0	4.0	37	30	10
57/440b	39	8.7	2.4	45	18	10
57/440b	52	6.8	9.0	24	47	8
57/440b	60	8.0	4.0	35	33	10
57/440b	65	8.8	2.2	47	20	10
116/719ab	48	9.2	1.7	53	8	26
127/794a	1	9.0	2.0	50	19	17
127/794a	91	8.8	2.3	46	26	18
127/794a	95	9.0	2.0	49	24	16
150/906a	51	8.0	4.0	39	37	13
175/1084a	12	9.0	2.0	50	11	11
175/1084a	17	9.4	1.5	58	12	10
175/1084a	24	8.8	2.2	47	11	11
175/1084a	29	9.5	1.4	59	9	16
175/1084a	34	9.5	1.4	60	9	16
175/1084a	39	9.3	1.6	56	8	15
175/1084a	43	9.5	1.4	61	10	17
175/1084a	49	9.5	1.4	63	8	14

Table 19 Results of the grain size analysis of the samples with low quality porosity data (*) and high contents of nannofossils (mainly diatoms). Φ_{50} - median grain size where $\Phi = -\log_2(\text{grain size in mm})$.

3.1.2 Comparison with grain size data from DSDP/ODP

A comparison of the clay fractions obtained from this study with those published by ODP revealed the fundamental difficulties of using smear slide data. During smear slide analysis, a small portion of sediment is distributed on a glass slide for the microscopical evaluation of mineral and fossil composition. Results are usually recorded as numerical abundances by a member of the shipboard scientific party and are obviously biased due to the change of the analytical personnel.

A further problem arises from the use of different scales. Where ODP uses the Wentworth Scale (clay $\leq 4\mu\text{m}$) this study defines clay as being smaller than $2\mu\text{m}$. As a solution in this study, an empirical relationship was established where:

$$\leq 2\mu\text{m} = 0.48 + 0.82 * \leq 4\mu\text{m}.$$

After this scale conversion, the smear slide analysis of samples poor in fossils delivers clay fractions which deviate on average by about 14 %_{rel} from those determined by the Sedigraph method (Fig. 37).

A comparison of the clay fractions for fossil-rich sample material reveals remarkably higher deviations (Fig. 37). The average difference of these two values is 43%_{rel}.

These observations illustrate that clay fraction values based on a semi-quantitative smear slide analysis should not be used in any compaction study.

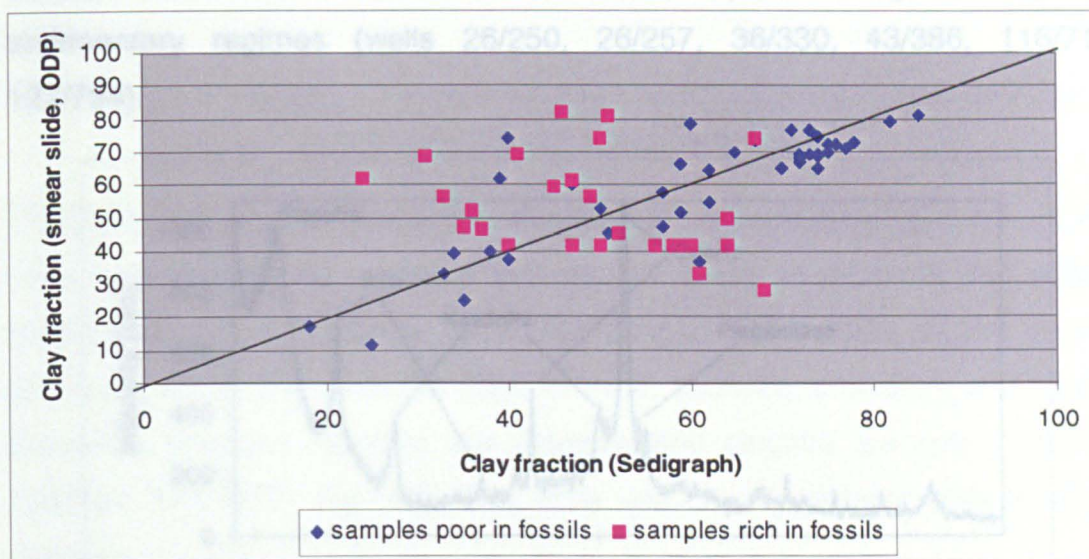


Fig. 37 A comparison of the clay fractions determined by smear slide analysis (ODP) and by Sedigraph measurement.

3.2 Grain density

Measured grain densities range from 2.1 g/cm³ in opal- and C_{org}-rich samples (55.2 % opal in 175/1084a-39, Lange et al. 1999) to about 2.9 g/cm³ in smectite-rich material (43/386-11; Table 20). The high grain densities in the smectite-rich samples are mainly caused by the loss of interlayer water due to heating of the sample material to 105° C prior to the density measurement (Colton-Bradley, 1987). The median of all samples (including the opal-rich samples), lies at about 2.61 g/cm³, where the median of the samples without a significant content of opal lies at about 2.71 g/cm³. The standard deviation

of the measurements was calculated as $\pm 0.02 \text{ g/ cm}^3$ using a quartz standard with a determined grain density of $2.65 \pm 0.02 \text{ g/ cm}^3$.

3.3 Bulk mineralogy

X-ray diffraction analysis allows a subdivision of the sample set into three groups of similar mineralogical composition.

The first group consists of samples which contain, besides quartz and illite, high amounts of smectite (Fig. 38 & Table 20). Common are kaolinite and calcite, zeolites are rare. Most of these samples belong to deep sea sedimentary regimes (wells 26/250, 26/257, 36/330, 43/386, 116/719, 127/794).

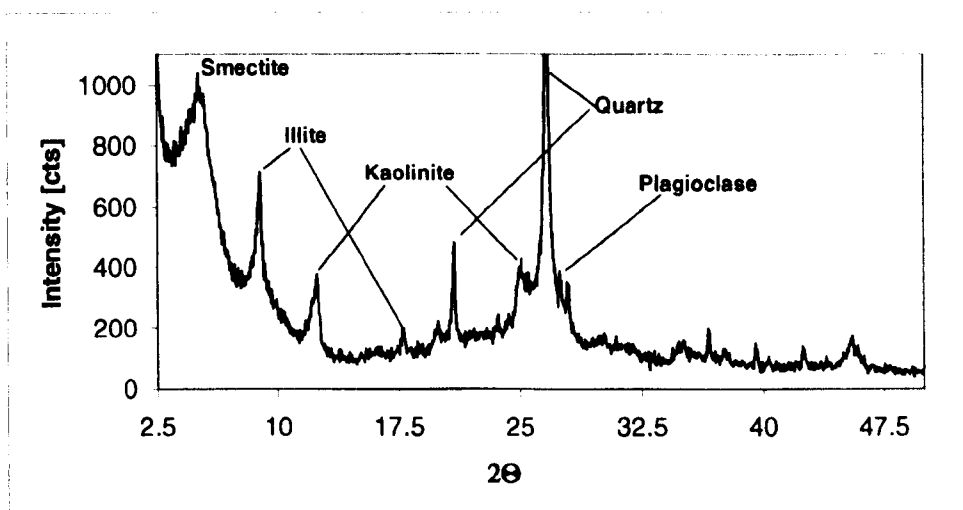


Fig. 38 X-ray diffractogram of a sample (25/250-11, glycolated) representative for a group one (smectite-rich) composition.

Samples of the second group contain predominantly quartz, mica/illite, calcite, and opal-A/CT (wells 36/330, 43/386, 57/440, 127/794 & 175/1084; Fig. 39). The latter two minerals originate from high abundances of micro- and nanofossils (diatoms, radiolaria etc.; Schieber et al., 2000) which in case of well 175/1084 (Fig. 34) originate from upwelling conditions. Moderate amounts of feldspar and smectite are common.

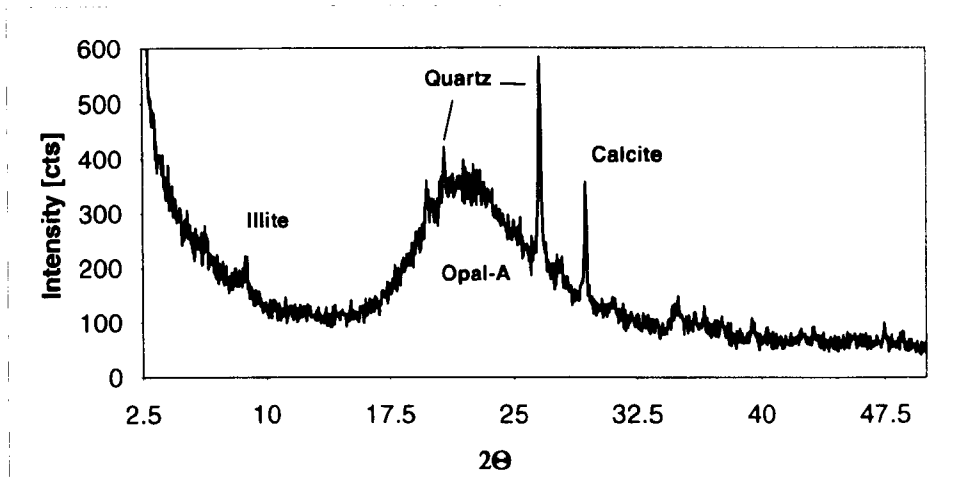


Fig. 39 X-ray diffractogram of a sample (175/1084-39) representative for a group two (opal-rich) composition. The opal-A content is striking.

The third and largest category of samples is characterised by a mix of the most common detrital minerals that can be found in proximal and deltaic environments (e.g. Windom, 1976; Füchtbauer, 1988; Aplin, 2000): quartz, feldspars, mica, clay minerals (illite, chlorite, kaolinite, smectite), and calcite dominate, whereas minerals like dolomite and gibbsite are rare (116/719, 150/906, 174/1072; Fig. 40). The latter are usually present only in small amounts.

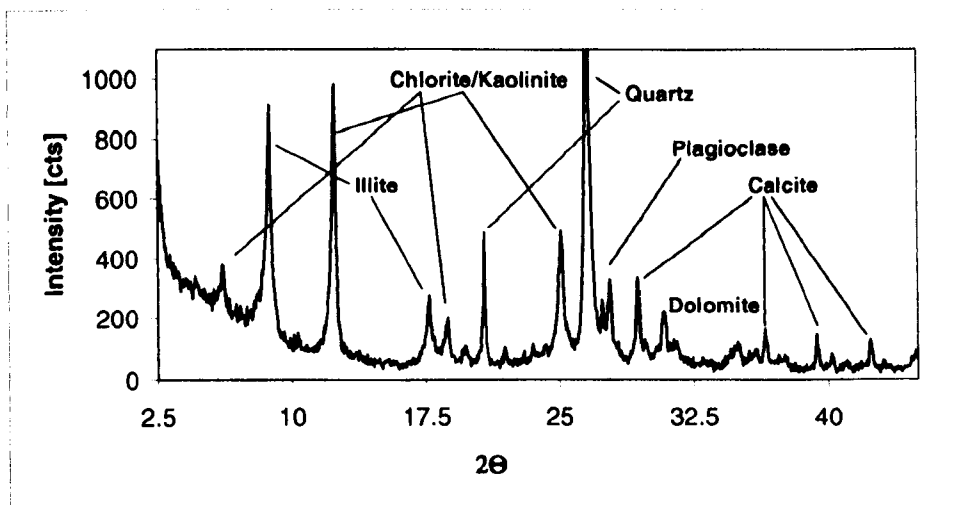


Fig. 40 X-ray diffractogram of a sample (174/1072-27) typical for a group three (detrital) composition.

Well	Sample	Qz	Fp	Mica	Illite	Kaolinite	Smectite	Chlorite	Zeolite	Calcite	var.	ρ	TOC	
26/250	4-6	xx		o	x	xx	x					2.59	0.53	
	6-3	xx			xx	xx	x					2.67	0.28	
	7-4	xx			x	xx	x			x		2.64	0.34	
	8-4	xx			x	xx	x			xx		2.67	0.28	
	9-3	xx	x	o	xx	xx	xx					2.61	0.39	
	10-2	xx	o		xx	xx	x					2.64	0.10	
	11-2	xx	o		xx	x	xx					2.63	0.10	
	13-4	xx	o		xx	x	xx					2.67	0.05	
	14-2	xx	x		xx	x	xx					2.64	0.04	
	17-2	xx	x		xx	x	xx					2.68	0.01	
	26/257	1	xx	xx	x	x	o	x		xx			2.53	0.65
		3	xx		o	x	xx	x					2.63	0.55
		5	xx	x		o	x	x		xx	x		2.51	0.61
	9	x						xx					2.60	0.49
1-4		x	x		o		o		x	xx		2.67	0.85	
36/330	2-2	x	x	o	o		o		xx	xx		2.75	0.97	
	6-4	xx	o	x	xx	x	x			xx		2.65	3.42	
	8-3	xx	o	x	xx	o	xx					2.66	3.17	
	9-2	xx		x	xx	o	x					2.69	1.99	
	10-2	xx	o	x	x		xx			o		2.69	1.83	
	11-2	xx		o	xx	xx				o		2.67	2.20	
	13-1	xx	xx	x	xx	xx				o		2.71	1.39	
	14-2	xx	xx	o	x	xx						2.72	0.79	
	43/386	1	xx	o	x	xx	xx	xx	o		xx		2.81	0.96
		4	xx	o	o	x	x	o			xx		2.80	0.79
11		o	o		o	o	xx			xx		2.95	0.67	
14		x		o	o	o	xx			xx		2.39	1.05	
26		x	??	?	o				xx	xx	opal/ct	2.47	0.95	
28		xx	??		x			x		x	opal/ct	2.53	0.90	
32		xx	??	?	o			xx		xx	opal/ct	2.59	0.93	
36		xx			xx	xx	xx			o		2.82	0.68	
42		xx		?			xx					2.76	0.34	
50		xx			x	x	xx					2.76	0.80	
54		xx			o	x						2.79	0.86	
55		xx	o	o	x	o	x			xx		2.76	2.85	
59		xx		x	o	o				x		2.74	1.34	
65		xx		x	o	x						2.83	0.69	
57/440	8-2	xx	xx		o	o	o			o	opal/a	2.45	1.18	
	13-3	xx	xx	x	xx	x	x			?	opal/a	2.52	1.14	
	24-1	xx	xx		x	o	o			x	opal/a	2.39	1.22	
	28-3	xx	xx		o	o	o				opal/a	2.38	0.93	
	39-2	xx	xx		o	o	o			o	opal/a	2.24	1.58	
	52-1	xx	x		o	o				o	opal/a	2.40	0.89	
	60-2	xx	xx	o	xx	x	x			o	opal/a	2.47	1.04	
	65-1	xx	xx	o	x	x					opal/a	2.36	0.99	
	116/719	11	xx	x	o	xx			xx				2.81	1.14
		14	xx	x		xx			xx				2.82	1.16
16		xx	x		xx			xx				2.82	1.15	
17		xx	x	o	x	x	x	o				2.75	1.84	
22		xx	o	o	x	x	x	o				2.79	1.89	
28		xx	x	o	xx	x	x	xx		o		2.77	1.78	
33		xx	x	o	xx	x	o	x		o		2.80	1.27	
38		xx	o	o	x	x	xx					2.73	0.78	
48		xx	x	o	xx				xx		o	2.80	0.95	
127/794		1H-1	xx	xx	xx	x	x	x	xx				2.67	0.37
	9H-5	xx	xx		x	x	o				opal/ct	2.33	0.64	
	9R-1	xx	x		x	x					opal/ct	2.38	0.36	
	11R-1	xx			o		x					2.57	0.61	
	17R-1	xx			x	o	x					2.58	1.30	
	20R-3	xx	o		x	x	x			x		2.59	1.05	
	150/906	14X-1	xx	o	xx	x	xx				xx		2.69	1.76
31X-1		xx	o	xx	x	xx		?				2.68	2.00	
33X-1		xx	o	xx	x	xx		?				2.63	1.92	
41X-3		xx		xx	x	xx						2.81	0.84	
51X-3		xx	x		o	o	o			xx		2.68	2.70	
59X-1		xx				o				xx		2.54	3.72	
174/1072		7R-1	xx	x	xx	x	x		xx		xx	Dolomite	2.78	0.42
	11R-1	xx	xx	x	x	x		xx		xx	Dolomite	2.73	0.29	
	17R-1	xx	x	xx	x	xx		o				2.74	0.34	
	25R-3	xx	o	xx	x	xx		x				2.75	0.46	
	37R-1	xx	xx	xx	x	xx		o			Gibbsite	2.69	0.60	
	46R-4	xx			x	x					o Gibbs.	2.69	0.46	
175/1084	12	xx	x	x	o					xx		2.35	7.99	
	17	x			o					xx		2.33	7.13	
	24	xx			o					xx	opal/a	2.50	3.12	
	29	xx	x	x	x	o				x	opal/a	2.29	8.42	
	34	xx	o	o	o					xx	opal/a	2.45	2.40	
	39	xx			o		o			xx	opal/a	2.07	3.73	
	43	xx	o	o	o	o					opal/a	2.10	6.49	
	49	x	x		o					xx	opal/a	2.28	2.91	

Table 20 Mineralogical composition obtained from X-ray diffraction analysis. Qz=quartz, Fp=feldspar, ρ =grain density (g/cm^3), TOC=total organic carbon (wt%); xx=abundant, x=common, o=rare.

3.4 Total organic carbon (TOC)

The results of the TOC analyses (Table 20) reflect the various sedimentological and palaeontological environments that were sampled. In the extreme case of upwelling conditions (175/1084) values of up to 8.4 weight percent of organic carbon were reached (Wefer et al. 1998 report values of up to 18.6 wt% from this well). However, samples of the deep sea basins (e.g. 26/250) contain only about 0.1 wt% TOC and the median of the complete sample set is 0.95 wt% TOC.

3.5 Porosimetry

The physical condition of 23 samples restricted the analysis by mercury intrusion porosimetry (MIP) to 56 samples of the total set of 79. The former were either too soft or too disintegrated to undergo the sample preparation process (**2 Samples and Methods**). In most cases only a few samples of each well were excluded, with the exception of well 175/1084, which had to be excluded completely.

The total porosities measured by ODP range in the examined sample set from 30% to 54%, the mode pore throat diameters span from 5nm up to 3000nm. The comparison of the observed total porosities with the porosities reported by DSDP and ODP revealed a significant feature of the analyzed material: most of the values determined by porosimetry are up to 15% lower than the initial on board measurements (Fig. 41 & Table 22). After consideration of various parameters like e.g. water content and time since sampling it is obvious that drying and shrinkage of the core material during storage must have led to a general decrease in pore space. In chapter **2 Samples and Methods** the effect of air drying on the pore space of soft, glacial clays was studied and confirmed these observations. There, samples lost up to 17% of their total porosity due to the several week long exposure to air.

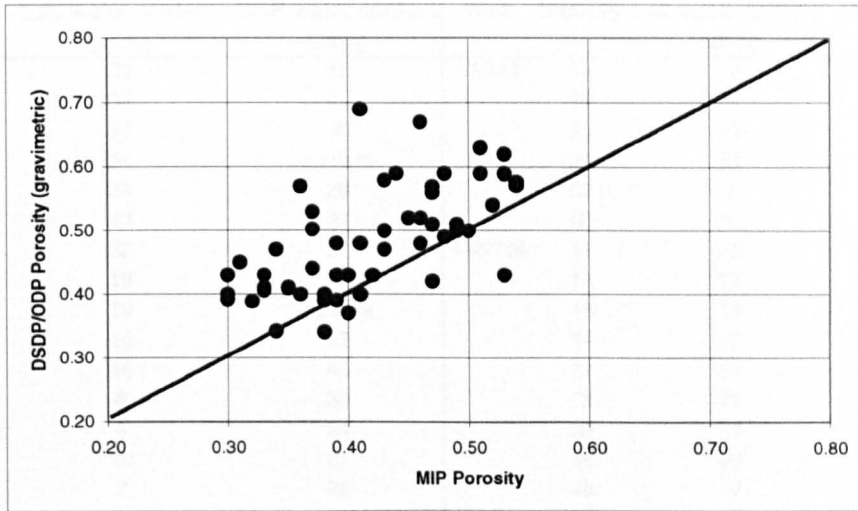


Fig. 41 Comparison of the porosities determined by DSDP/ODP directly after drilling and by mercury intrusion porosimetry (MIP) in this study.

The water contents for all samples analyzed by mercury intrusion porosimetry were measured during the previously described Freon™ freeze drying procedure. A comparison of the measured content with the data provided by ODP in Fig. 42 reveals the degree of drying during sample storage. The results are listed by well number (Fig. 42 & Table 21) and illustrate an increased water loss with increased storage time.

The measured water content of one sample (127/794-9_1) exceeds the values determined by ODP (Fig. 42). A comparison of the depths of the samples used in this case (7cm) suggests slight differences in the examined material. However, the sample also contains a significant amount of diatoms and was thus excluded from the subsequent compaction analysis.

Well	Sample	Lab water content [wt%]	ODP water content [wt%]	Well	Sample	Lab water content [wt%]	ODP water content [wt%]	
26/250	4	33	42	57/440	13	30	37	
	6	33	41		24	20	35	
	7	34	35		28	23	38	
	8	34	no data		39	25	38	
	9	24	28		52	7	no data	
	10	23	27		60	11	no data	
	11	22	27		116/719	11	22	28
	13	19	22			14	22	32
	14	19	no data			16	18	26
	17	16	22			17	20	34
36/330	1	16	45		22	21	30	
	2	8	30		28	25	29	
	6	6	24		33	15	27	
	8	10	27		38	28	34	
	9	7	22		48	17	24	
	10	8	25	127/794	9_1	32	22	
	11	6	21		11	26	33	
	13	4	21		20	24	27	
43/386	14	3	16	150/906	14	27	30	
	26	16	28		31	28	35	
	28	9	28		33	26	30	
	32	16	26		51	21	25	
	36	11	21	174/1072	7	25	26	
	42	6	24		11	18	22	
	50	7	19		17	17	19	
	54	11	20		25	16	20	
	55	12	20		37	15	18	
	59	9	19		46	17	18	
65	7	19						

Table 21 Water contents measured in this study (Lab) and by ODP. [wt%] = weight percent.

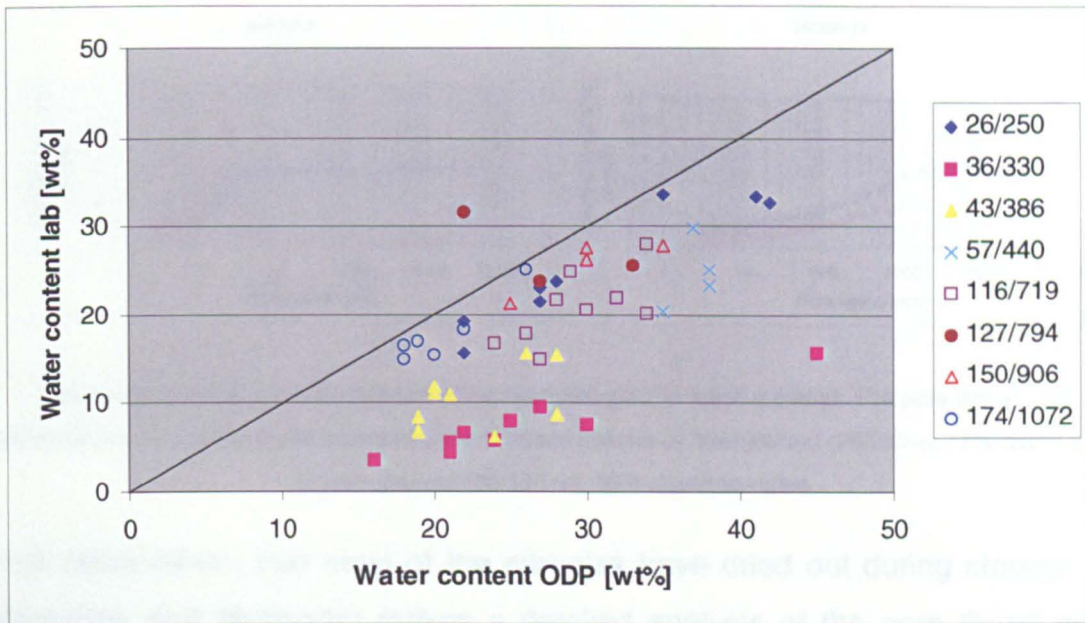


Fig. 42 Comparison of the water contents measured in this study (Lab) and shortly after drilling by ODP.

The pore throat size distribution curves in this study can be subdivided into two groups: unimodal and bimodal distributions (Fig. 43 & Fig. 44). The latter are characteristic for samples rich in micro- and nanofossils. They either show well defined “M”-shaped distributions or broad, shouldered peaks (Fig. 43). Samples yielding unimodal pore throat sizes show broad distributions of lower cumulative porosity (blue dots, Fig. 44) for coarse-grained material and narrow peaks of higher cumulative porosity for clay-rich samples. A characteristic flattening slope towards the small pore throat sizes reveals the relatively poor sorting of the coarser samples.

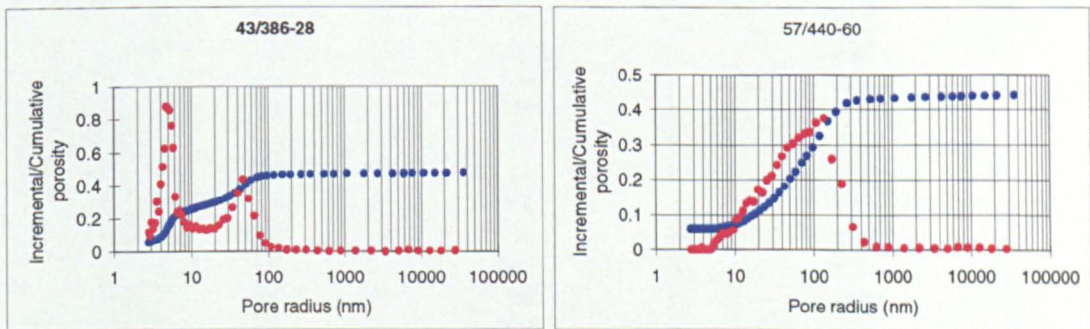


Fig. 43 The bimodal (left image) or "shouldered" (right image) pore throat size distributions of fossil-rich samples. The red dots mark the pore throat sizes, the blue dots the cumulative porosity. Clay fractions: 43/386-28=67%, 57/440-60=35%.

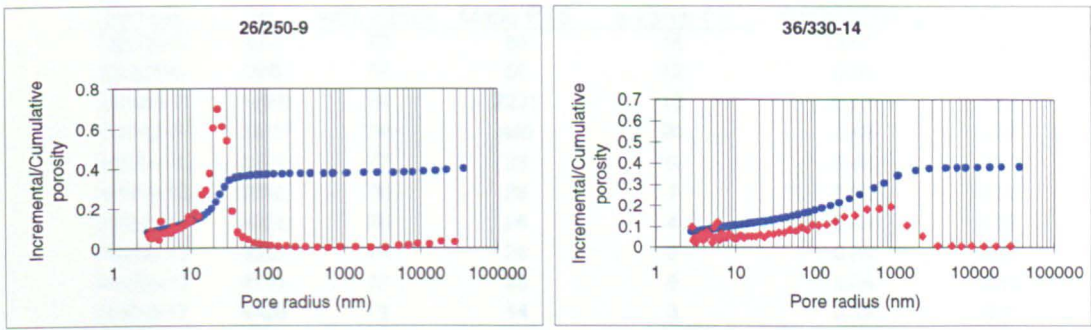


Fig. 44 Pore throat size distributions of two samples poor in fossil material. The pore throat size distributions (red dots) reveal exemplarily the different spectra of fine-grained (26/250-9, 77% <2µm) and coarse-grained (36/330-14, 39% <2µm) samples.

The observation, that most of the samples have dried out during storage (**2 Samples and Methods**) makes a detailed analysis of the pore throat size distributions very difficult. The different mineralogical compositions, varying grain sizes as well as initial porosities might have affected the changes in pore space to different degrees. Therefore, the comparison of sample properties obtained from MIP can only reflect general trends of the data.

By correlating samples from similar stress regimes but with different particle size distributions, trends towards smaller pore throat sizes with increasing clay fraction can be observed (Table 22). In addition, a general reduction in pore throat sizes with increasing effective stress is evident. Furthermore, a significant decrease in pores with very small throats (<3nm) occurs at rising vertical effective stresses in all groups of similar particle size.

Sample	Vertical effective stress (kPa)	Porosity (%)	PTS (nm)	Porosity (%)	PTS (nm)	Porosity (%)	PTS (nm)
26/250-9	100	81	01	0	0.00	0.48	0.00
26/250-9	2011	66	01	0	0.00	0.43	0.00
26/250-9	2632	79	20	0	0.00	0.43	0.00
26/250-9	3746	93	75	22	0.47	0.43	0.00
26/250-9	1332	40	11.8-46	0	0.43	0.43	0.00
26/250-9	1204	40	136	2	0.58	0.49	0.00
26/250-9	2366	37	135	4	0.51	0.47	0.00
26/250-9	181	61	78	6	0.50	0.48	0.00
26/250-9	2150	37	91	17	0.30	0.5	0.00
26/250-9	1048	47	110	7	0.51	0.49	0.00
26/250-9	2807	35	78	7	0.43	0.43	0.00
26/250-9	567	61	70	0	0.49	0.49	0.00
26/250-9	696	38	136	0	0.48	0.35	0.00
26/250-9	608	33	136	0	0.30	0.38	0.00
26/250-9	1420	31	136	0	0.41	0.38	0.00
26/250-9	2671	19	1412	0	0.27	0.4	0.00

Table 22: Preliminary data obtained from MIP in comparison with data provided by DSDP/GDF at = vertical effective stress, ϕ = porosity, PTS = pore throat size, (*) pore space not invaded by mercury, i.e. in pores with throats <3nm

Sample	σ'	wt% <2mm	Mode PTS	ϕ <3nm (*)	DSDP/ODP ϕ	MIP ϕ
26/250-4	572	72	80	15	0.57	0.47
26/250-6	986	72	56	12	0.59	0.53
26/250-7	1286	74	2231	10	0.57	0.54
26/250-8	1813	74	890	20	0.58	0.54
26/250-9	2220	77	23	9	0.43	0.39
26/250-10	2612	78	26	7	0.50	0.37
26/250-11	3035	75	26	4	0.41	0.33
26/250-13	3931	74	26	3	0.39	0.32
26/250-14	4141	72	26	9	0.34	0.34
26/250-17	4426	73	14	3	0.39	0.3
36/330-1	781	51	138	5	0.69	0.41
36/330-2	1077	52	316	10	0.54	0.52
36/330-6	2384	39	41	7	0.45	0.31
36/330-8	2689	62	56	7	0.44	0.37
36/330-9	2906	59	67	4	0.43	0.33
36/330-10	3234	62	67	10	0.47	0.34
36/330-11	3507	50	67	7	0.40	0.3
36/330-13	4200	40	67	5	0.41	0.33
36/330-14	4511	25	893	9	0.34	0.38
43/386-26	3110	41	5	5	0.48	0.46
43/386-28	3300	67	6 & 47	7	0.42	0.47
43/386-32	3780	31	6 & 26	4	0.48	0.41
43/386-36	4554	74	26	5	0.43	0.3
43/386-42	5344	60	13 & 41	6	0.43	0.4
43/386-50	6173	85	20	7	0.40	0.36
43/386-54	6606	67	35	6	0.40	0.41
43/386-55	6687	71	23	6	0.44	0.37
43/386-59	7019	75	48	5	0.39	0.39
43/386-65	7648	73	26	7	0.40	0.38
57/440-13	1443	40	233	9	0.63	0.51
57/440-24	2083	33	233	17	0.62	0.53
57/440-28	2363	37	233	14	0.59	0.51
57/440-39	2918	45	233	22	0.59	0.53
57/440-52	3723	24	315	9	0.67	0.46
57/440-60	4210	35	137	6	0.59	0.44
116/719-11	660	40	176	16	0.52	0.46
116/719-14	960	42	176	7	0.56	0.47
116/719-16	1112	45	91	8	0.48	0.39
116/719-17	1202	60	30	7	0.57	0.36
116/719-22	1573	63	35	7	0.53	0.37
116/719-28	2002	61	91	9	0.52	0.45
116/719-33	2411	60	91	6	0.50	0.43
116/719-38	2822	78	35	6	0.58	0.43
116/719-48	3746	53	78	23	0.47	0.43
127/794-91	1532	46	13 & 48	9	0.43	0.53
127/794-11	1664	40	138	2	0.59	0.48
127/794-20	2396	57	138	6	0.51	0.47
150/906-14	981	51	78	6	0.50	0.49
150/906-31	2180	57	91	17	0.50	0.5
150/906-33	2348	47	110	7	0.51	0.49
150/906-51	3807	39	78	7	0.43	0.42
174/1072-7	507	61	78	6	0.49	0.48
174/1072-11	690	38	138	6	0.48	0.39
174/1072-17	996	33	138	6	0.39	0.38
174/1072-25	1452	31	138	6	0.41	0.35
174/1072-46	2531	18	1412	8	0.37	0.4

Table 22 Porosimetry data obtained from MIP in comparison with data provided by DSDP/ODP. σ' = vertical effective stress, ϕ = porosity, PTS = pore throat size, (*) pore space not intruded by mercury, i.e. in pores with throats <3 μ m.

4 Discussion

4.1 Compaction trends

Understanding the evolution of porosity and permeability, thus, the compaction behaviour of clay-rich sedimentary sequences, underpins the prediction of fluid flow, seal formation and overpressure generation in modern basin studies. Earlier work in soil mechanics (Skempton 1970, Burland 1990) revealed that the decrease of porosity in clays and muds with increasing vertical effective stress is mainly controlled by the Atterberg Liquid Limit, a lithological parameter directly proportional to the clay fraction. Further investigations by Aplin et al. (1995); Dewhurst et al. (1998, 1999b) and Yang and Aplin (1998 & submitted) suggested, that the compaction behaviour of mudstones can be reasonably well described if the effective stress and the clay fraction can be estimated.

Fig. 45 displays the relationship between vertical effective stress (calculated from DSDP/ODP bulk density) and DSDP/ODP porosity of all analyzed samples, divided according to their clay fractions. Although samples of the 50-64% and >65% clay fraction groups plot into relatively well defined zones, the porosity/effective stress relationships are not obviously related to clay fraction. Many of the samples show much higher porosities at given effective stresses than one would expect from previous investigations (e.g. Skempton, 1970; Burland, 1990; Aplin et al. 1995; Giles et al. 1998; Yang & Aplin, 1998).

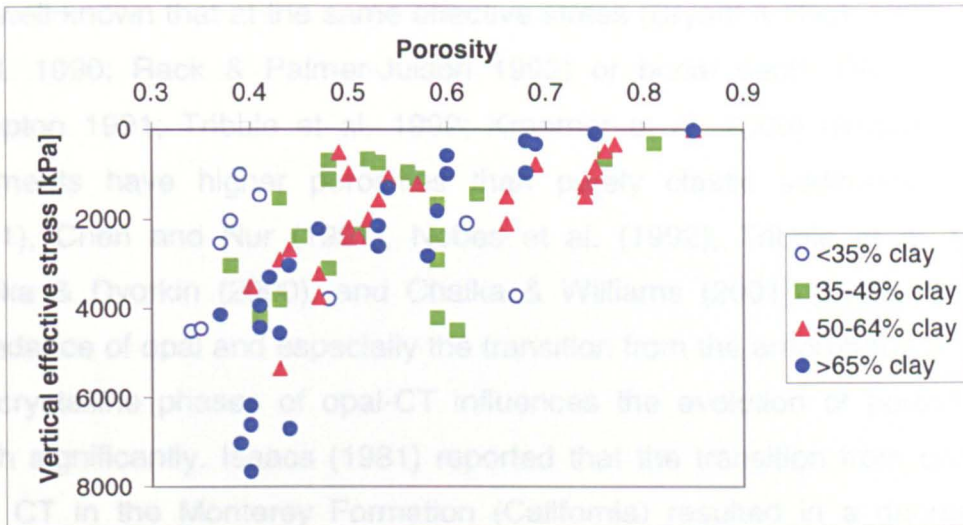


Fig. 45 The relationship between clay fraction, porosity (from DSDP/ODP) and vertical effective stress of the complete sample set.

The sample set can be subdivided into two main groups: 1. samples that contain only small amounts of fossil or fossil-related material (opal) or 2. samples that are rich ($\gg 15\%$) in micro- and nanofossils. Since previous work (e.g. Meade, 1963; Bryant & Rack 1990) revealed a positive correlation between fossil material (diatoms) and porosity the compaction analysis was divided into two parts. The first part examines the compaction of fossil-rich (opal-rich) samples, the second concentrates on the fossil-poor material.

4.1.1 Fossil-rich samples

Data from the relevant DSDP/ODP reports (Barker et al. 1974, Tucholke et al. 1975, Huene et al. 1977, Cochran et al. 1988, Tamaki et al. 1990, Mountain et al. 1994, Wefer et al. 1998) show that many of the samples contain high amounts of micro- and nanofossils. X-ray diffraction analyses (Fig. 34) confirmed this information in many cases, revealing high abundances of opal-A, opal-CT and calcite (Table 20). Particularly rich in opal are the samples from well 175/1084 (Benguela Current, SW Africa) which show extremely high porosities of more than 70% until depths of 450mbsf. Lange et al. (1999) showed that some of the sampled sequences in this well contain up to 55% opal, a common signature of sediments bearing silicious nanofossils like diatoms or radiolaria (Conger 1942; Kuenen 1950; Sears 1984).

It is well known that at the same effective stress (Bryant & Rack 1990; Bryant et al. 1990; Rack & Palmer-Julson 1992) or burial depth (Meade, 1963; Compton 1991; Tribble et al. 1992; Kraemer et al. 2000) diatom/opal-rich sediments have higher porosities than purely clastic sediments. Isaacs (1981), Chen and Nur (1991), Nobes et al. (1992), Tribble et al. (1992), Chaika & Dvorkin (2000), and Chaika & Williams (2001) showed that the abundance of opal and especially the transition from the amorphous opal-A to the crystalline phases of opal-CT influences the evolution of porosity with depth significantly. Isaacs (1981) reported that the transition from opal-A to opal CT in the Monterey Formation (California) resulted in a decrease of diatom porosity from 70% to 27%. Typical burial depths for the opal-A/CT conversion are 500m to 800m (Tribble et al., 1992). The reaction temperature for this reaction varies with time (Tribble et al. (1992) and references therein) and can be as low as about 10°C (for sediment older than 40Ma).

Kraemer et al. (2000) showed that both large pores (5-50 μ m) between the diatom skeletons and small pores (2 μ m) within the diatoms result in the observed elevated porosities of diatom-rich sediments. A comparison with SEM photomicrographs (Bryant et al. 1990; Lange et al. 1999) reveals that many pores are actually an order of magnitude smaller.

The examination of the fossil-rich material by mercury intrusion porosimetry in this study could also not confirm the dimensions quoted by Kraemer et al. (2000). Most of the analyzed samples either show remarkably broad pore throat size distributions (PTSD) in the range of 100-500nm (**3 Results**; see also Appendix) or bimodal PTSDs, with mode pore throat sizes between 3nm and 50nm. Both smaller amounts of intact diatoms and higher amounts of fine-grained clay and fossil-debris might explain this discrepancy. Additional, more detailed studies of the pore size distribution in fossil-rich sediments are necessary to constrain this data.

A further consequence of the elevated porosities in fossil-rich samples are unusual stress/burial depth relationships (Fig. 46 & Fig. 47). Due to the high porosities, fossil-rich sequences require much greater thicknesses to

generate a given overburden stress (sub sea floor), compared to non-fossiliferous sediments (Hamilton, 1976).

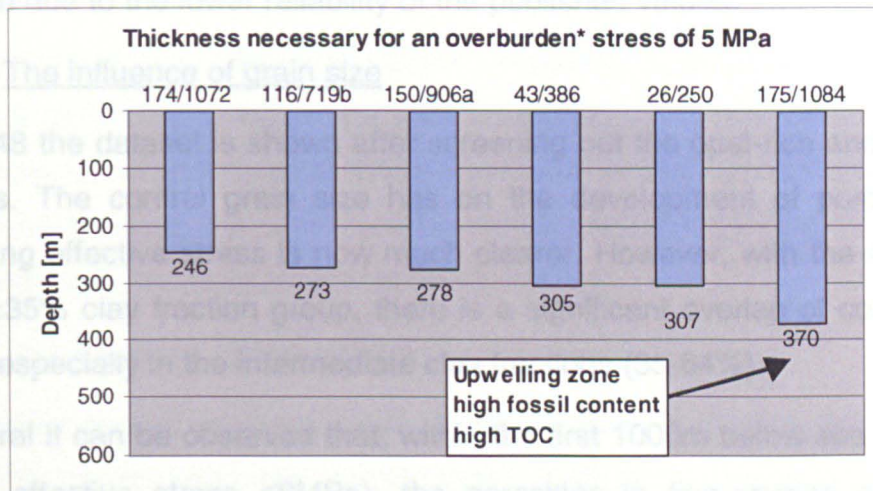


Fig. 46 The sediment thickness at which an overburden* stress of 5Mpa occurs for these DSDP/ODP sections. (*) Overburden sub sea floor.

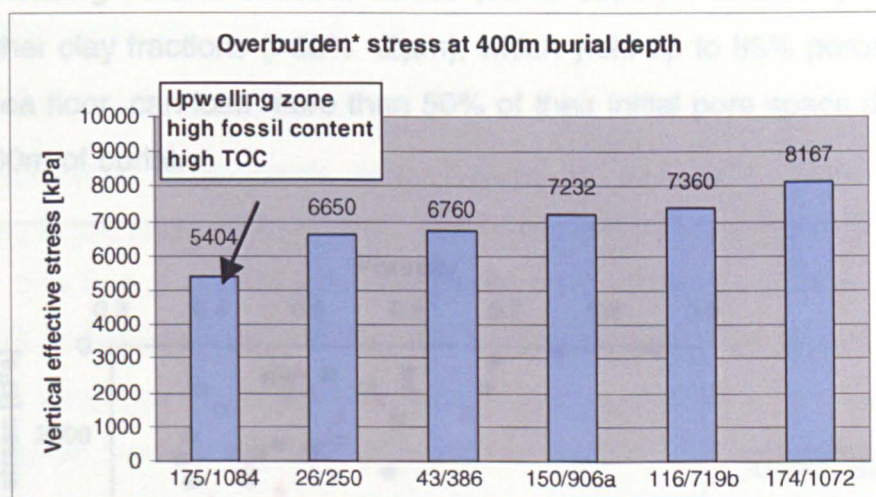


Fig. 47 Calculated overburden* stress at 400mbsf. Note the low stress for the fossil-rich well (175/1084). (*) Overburden sub sea floor.

As a further consequence, the lithostatic gradients of 0.0135-0.0204MPa/m (0.6-0.9 psi/ft) can be significantly smaller than those typically observed in petroleum basins (0.0225-0.0231MPa/m or ~1psi/ft; Luo et al., 1994).

4.1.2 Fossil-poor samples

One of the aims was to investigate the influence of grain size on compaction trends. Fossil-rich samples were therefore excluded from further

interpretations of the compaction trends. Samples where the porosities had been determined using the GRAPE tool (Boyce 1976, 1984) were also excluded due to the lower reliability of the published values.

4.1.2.1 The influence of grain size

In Fig. 48 the dataset is shown after screening out the opal-rich and GRAPE samples. The control grain size has on the development of porosity with increasing effective stress is now much clearer. However, with the exception of the <35% clay fraction group, there is a significant overlap of compaction trends, especially in the intermediate clay fractions (35-64%).

In general it can be observed that, within the first 1000m below sea floor (i.e. vertical effective stress $\leq 8\text{MPa}$), the porosities in fine-grained sediments decrease with decreasing clay fraction at a given effective stress. Furthermore, sediments of all grain sizes lose their porosity systematically with increasing vertical effective stress (burial depth). Particularly lithologies with higher clay fractions (>65% <2 μm), which yield up to 85% porosity close to the sea floor, can lose more than 50% of their initial pore space during the first 1000m of burial.

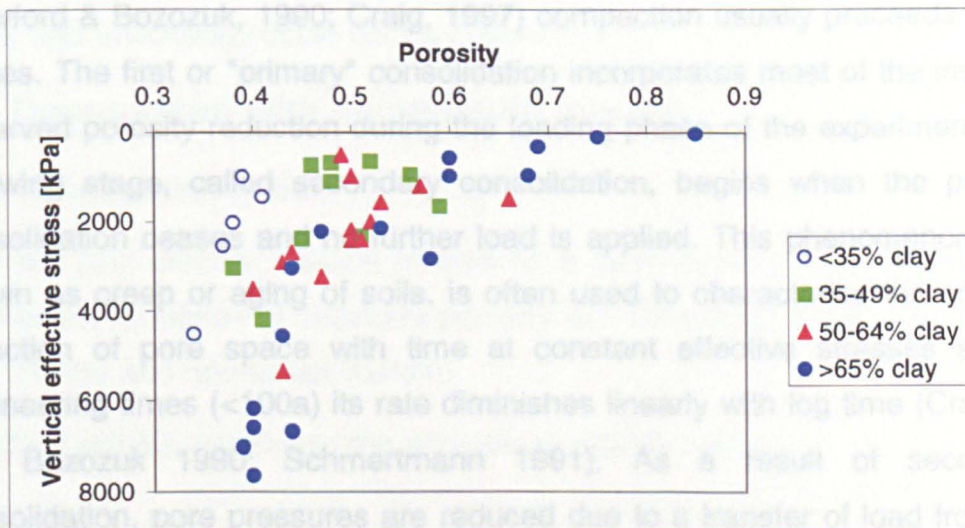


Fig. 48 The relationship between clay fraction, porosity (from DSDP/ODP) and vertical effective stress of the screened sample set. Fossil-rich and GRAPE samples have been excluded.

The poor separation of porosity-effective stress trends of samples with intermediate clay fractions (Fig. 48) might be due to various reasons. On the

one hand, the lack of information about the total distribution of grain sizes (**2 Samples and Methods**) makes an assumption about the degree of sorting impossible. It is well known from literature (Pettijohn 1975) that sorting has a significant influence on the pore volume of granular aggregates. On the other hand, the internal lamination and thus heterogeneity of the sample material might have led to uncertainties in the correlation of clay fraction and porosity. Differences between the core material used by DSDP/ODP and in this study could also have contributed to these uncertainties.

4.1.2.2 The influence of temperature

All sampled sequences have never reached higher formation temperatures than 40°C, hence diagenetic reactions should not have substantially changed the siliciclastic sediment matrix. Significant alterations have been reported to occur at low temperatures in opal-rich sediments (Chen and Nur 1991; Nobes et al. 1992; Tribble et al. 1992), but these sediments were excluded from this compaction analysis.

4.1.2.3 The influence of time

In consolidation experiments (e.g. Kabbaj et al., 1988; Burland, 1990; Crawford & Bozozuk, 1990; Craig, 1997) compaction usually proceeds in two stages. The first or "primary" consolidation incorporates most of the instantly observed porosity reduction during the loading phase of the experiment. The following stage, called secondary consolidation, begins when the primary consolidation ceases and no further load is applied. This phenomenon, also known as creep or aging of soils, is often used to characterise the ongoing reduction of pore space with time at constant effective stresses and in engineering times (<100a) its rate diminishes linearly with log time (Crawford and Bozozuk 1990; Schmertmann 1991). As a result of secondary consolidation, pore pressures are reduced due to a transfer of load from the pore fluid to the sediment skeleton and pores, mainly in the size range of 100-1000nm (Griffiths & Joshi 1990), are reduced in volume.

The important question is, if there is any evidence for a relationship between age and porosity in the examined sample set. For a thorough analysis of any time effect the following prerequisites have to be fulfilled: 1. the samples

need to be of similar lithology (clay fraction), 2. they must have experienced the same maximum vertical effective stress, and 3. their age can be sufficiently well estimated. The sample set used in this study is too small and diverse to either underpin or rule out any influence of time on compaction during geological time spans. However, the typical aging effect (secondary consolidation) in soils with asymptotical trends of pore space reduction with time (Schmertmann 1991; Crawford and Bozozuk 1990), suggests that the major changes in porosity occur within the first tens or hundreds of years of burial and would be completed for all samples at the time of sampling.

4.1.2.4 The influence of mineralogy

The origin of the sample material is highly variable. Consequently, the possible influence of different mineralogical compositions on the compaction trends needs to be addressed. If changes of the mineralogy due to diagenetic processes can be neglected, the mineralogical composition should only be an indicator for hydrodynamic processes, i.e. grain size related. In this case, the energy level of the depositional environment (Hjulstrøm 1955) as well as the provenance area (Aplin, 2000) can determine the amount and type of clay fraction present. In this study, systematic relations between porosity/effective stress and mineralogy could not be observed.

4.2 Comparison with compaction models

4.2.1 Compaction trends

Over the past century, various models have been developed to describe the mechanical reduction of sediment porosity with increasing burial depth (Giles et al. (1998) and references therein).

In 1921 Terzhagi introduced the principle of effective stress:

$$(1) \quad \sigma' = \sigma - u$$

where the effective stress (σ') is defined as the difference between total stress (σ) and pore fluid pressure (u).

Since then, several empirical laws were used to describe one dimensional mechanical compaction. For example, Athy's law (Athy, 1930) states that porosity decreases exponentially with increasing effective stress.

Skempton (1970), Smith (1971), Burland (1990), Audet & McConnel (1992) and Aplin et al. (1995) use a different approach which was developed in soil mechanics:

$$(2) \quad e = e_{100} - \beta \ln\left(\frac{\sigma'}{100}\right)$$

where the void ratio (e) is defined as the ratio of the pore volume and solid volume; e_{100} and β are the void ratio at 100kPa and the compaction coefficient, respectively.

The relationship described by equation (2) is well established in soil mechanics from both in situ observation and laboratory experiments (Skempton, 1970; Burland, 1990). However, the use of this equation in petroleum basins was problematic since the aforementioned studies mainly covered stress ranges of less than 10MPa.

In soil mechanics studies (Skempton, 1970; Burland, 1990; Aplin et al., 1995) it is suggested that the compression coefficients (β) are strongly related to lithology. In most of these studies (e.g. Skempton, 1970; Burland, 1990; Craig, 1997) the lithology of fine-grained sediments is quantitatively characterised using the Atterberg Liquid Limit (ALL). Since this parameter is not suitable for samples from oil wells (too much sample material needed), Aplin et al. (1995) and Yang & Aplin (1998; submitted) generated a compaction model for clay rich sediments using grain size (clay fraction) as lithological descriptor.

Yang & Aplin (submitted) managed to correlate ALL and clay fraction (Skempton Model) by reevaluating data that were available in soil mechanics literature (Skempton, 1970; Burland, 1990). They used these data together with laboratory and wireline data from 22 petroleum wells from the North Sea and Gulf of Mexico to calibrate a compaction model for fine-grained sediments in petroleum basins. In order to be able to use wireline data Yang

& Aplin (submitted) also used calibrated Artificial Neural Networks (ANN) to extract clay fraction data from geophysical well logs. Of their data set of 3847 data points, 168 points were derived from core and cutting samples and 3579 points from wireline logs.

They established the following relationships between clay fraction (*clay*), e_{100} and the compression coefficient (β):

Skempton Model:

$$(3) \quad e_{100} = 0.3024 + 1.6867clay + 1.9505clay^2$$

$$(4) \quad \beta = 0.0407 + 0.2479clay + 0.3684clay^2$$

Yang & Aplin (submitted) Model:

$$(5) \quad e_{100} = 0.71 + 0.563clay + 2.308clay^2$$

$$(6) \quad \beta = 0.0712 + 0.0953clay + 0.391clay^2$$

Although Yang & Aplin's (submitted) model included effective stresses between 0.8MPa and 38MPa corresponding to burial depth of 100m to 3500m, the data coverage for the interval between 100mbsf and 1000mbsf was poor. Since most fine-grained sediments lose up to 50% of their initial porosity within this interval (Fig. 1), this study aimed at using the examined DSD/ODP sample set to verify the provided mudstone compaction models.

Examples for compaction curves derived from both models are displayed in Fig. 49. At very low effective stresses (<1kPa) the porosity predictions for three exemplified lithologies are similar for both models. However, as soon as the vertical effective stress exceeds 1kPa the differences between both model become obvious. In general, the Skempton model delivers higher porosities than the Yang & Aplin model.

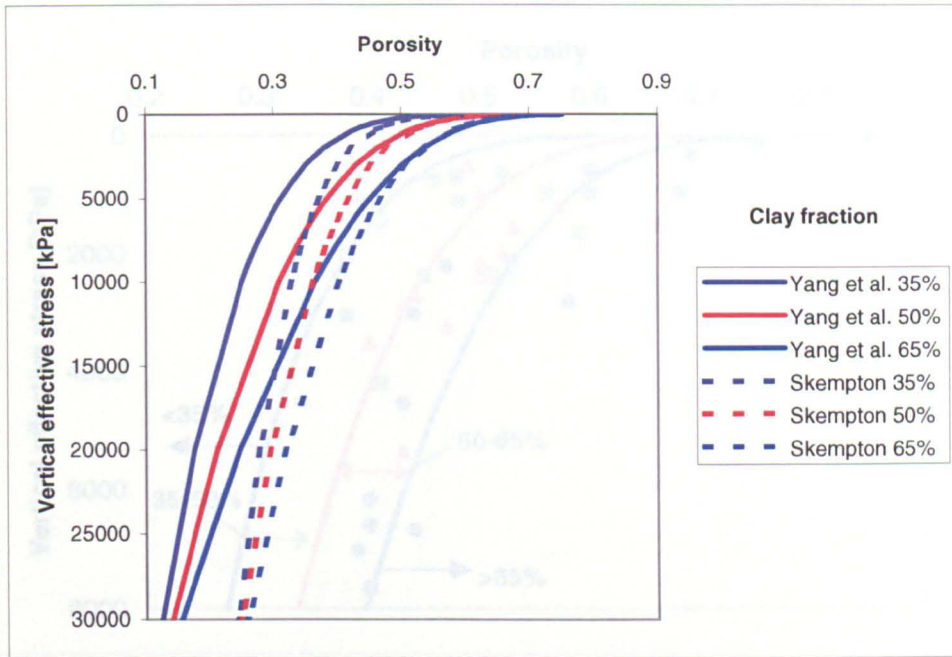


Fig. 49 Comparison of the two compaction models for clay-rich siliciclastic sediments. Curves derived from Yang & Aplin (submitted) and Skempton (1970).

As can be seen in Fig. 50 and Fig. 51, the values for the fossil-poor samples fit reasonably well into the predicted trends, although for 6 samples (12.5%) the measured porosities deviate 10% or more from the predictions (

Table 23). A direct comparison reveals that the average difference between the measured and predicted porosities is 4% for the total sample set (no fossils, no GRAPE data). The average differences for the chosen clay fraction ranges are slightly different, with 5% for the <35% and 35-49% clay fraction, 3% for the 50-64% clay fraction and 4% for the >65% clay fraction.

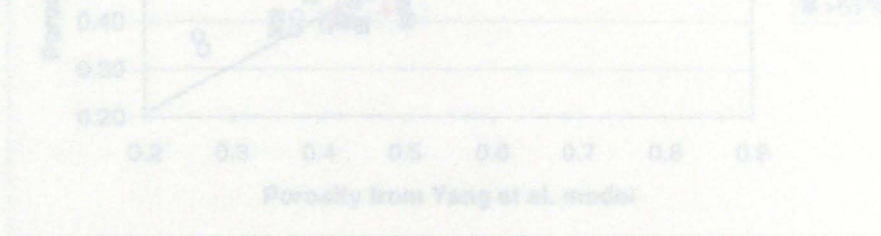


Fig. 51 Comparison of the absolute values for porosities measured by DQIP/DQP and previous in Yang & Aplin's (submitted) model. The average absolute deviations are ± 5% for the <35% and 35-49% clay fraction, ± 3% for the 50-64% clay fraction, ± 4% for the >65% clay fraction, and ± 4% for the total dataset.

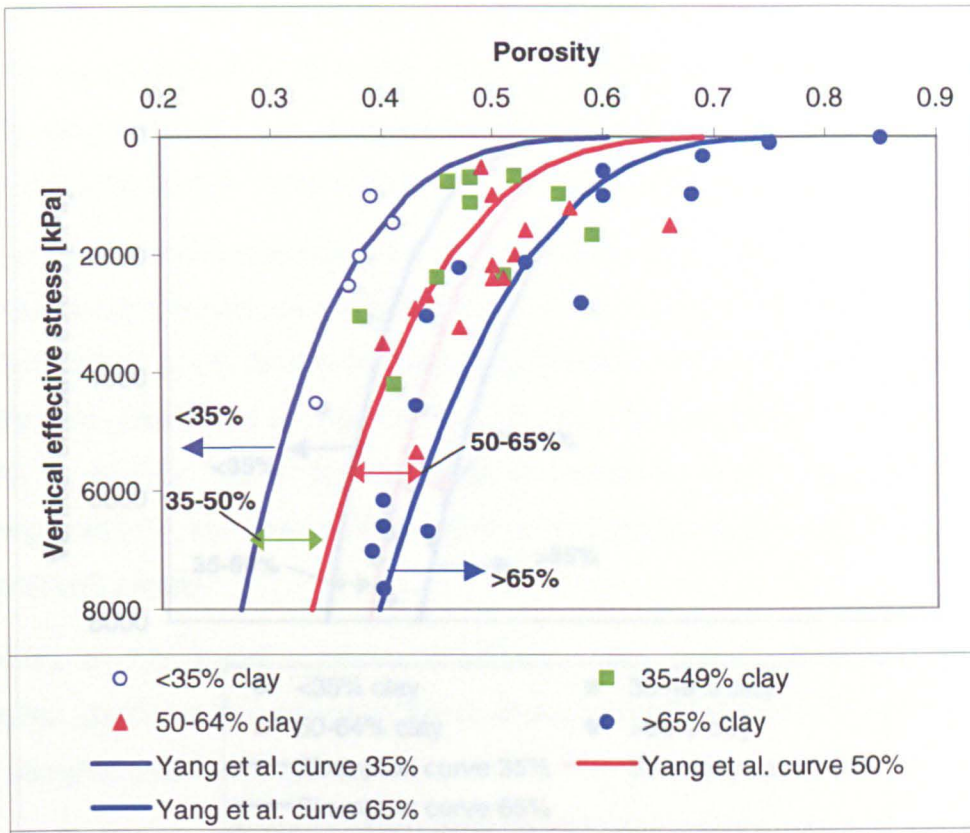


Fig. 50 Porosity-effective stress data for the fossil-poor samples of this study, compared with predictions of the Yang & Aplin (submitted) model.

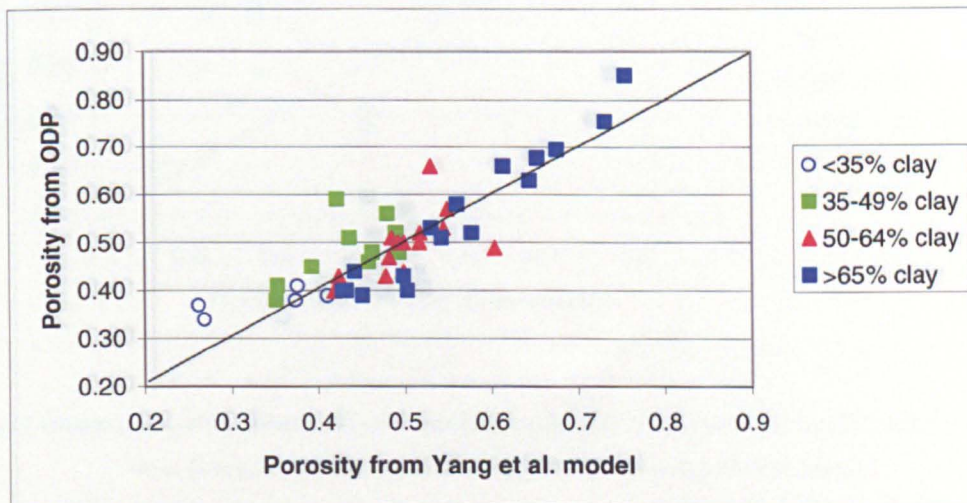


Fig. 51 Comparison of the absolute values for porosities measured by DSDP/ODP and predicted by Yang & Aplin's (submitted) model. The average absolute deviations are $\pm 5\%$ for the $<35\%$ and $35-49\%$ clay fraction, $\pm 3\%$ for the $50-64\%$ clay fraction, $\pm 4\%$ for the $>65\%$ clay fraction, and $\pm 4\%$ for the total dataset.

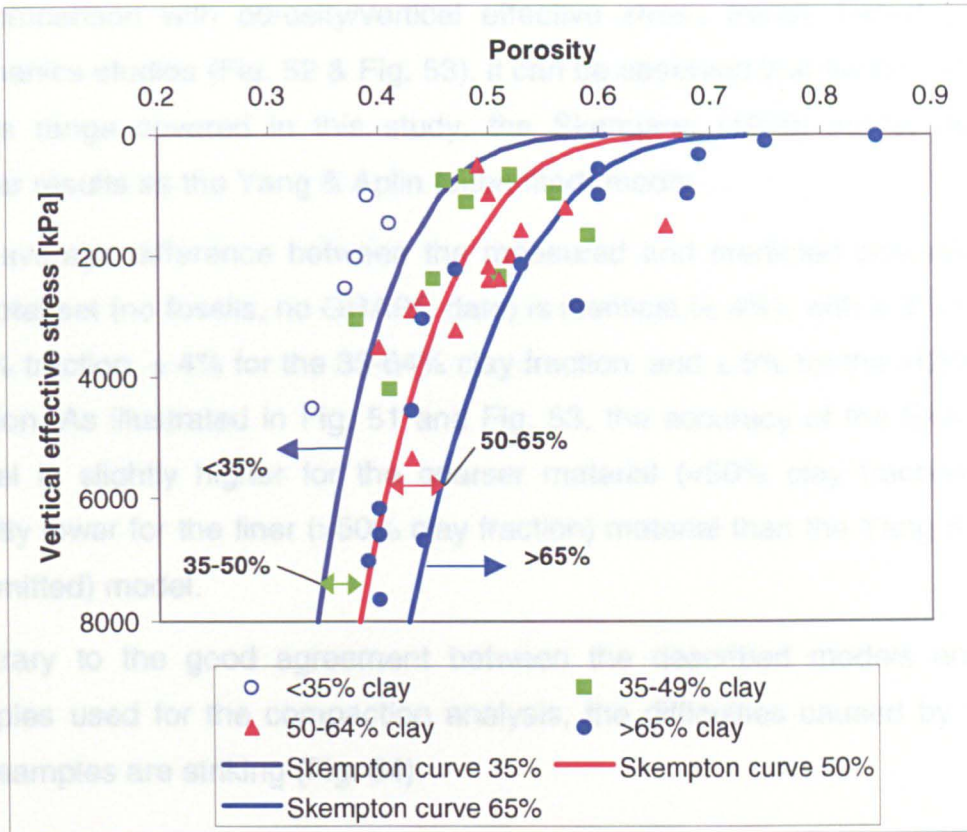


Fig. 52 Porosity-effective stress data for the fossil-poor samples of this study, compared with predictions of the Skempton (1970) model.

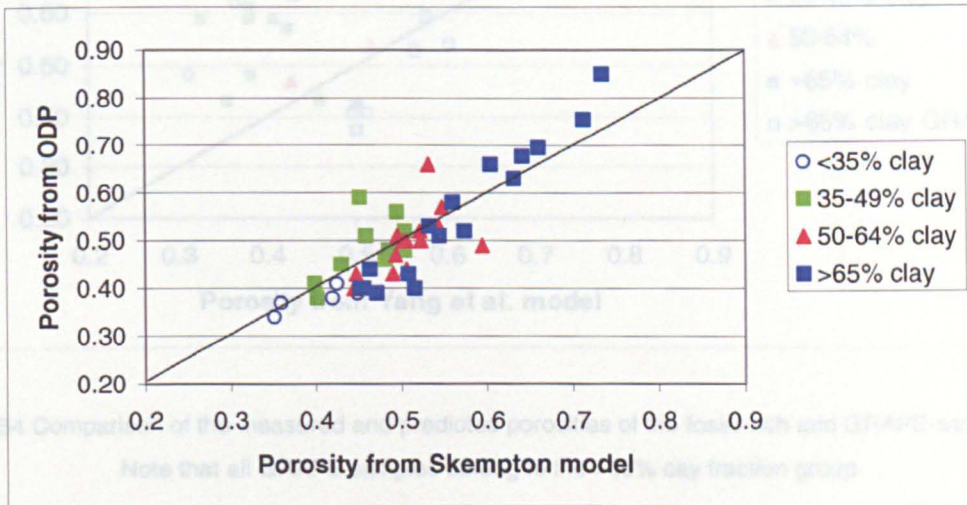


Fig. 53 Comparison of the absolute values for porosities measured by DSDP/ODP and predicted by Skempton's (1970) model. The average absolute deviations are $\pm 3\%$ for the $<35\%$ clay fraction, $\pm 4\%$ for the 35-49% and 50-64% clay fraction, $\pm 5\%$ for the $>65\%$ clay fraction, and $\pm 4\%$ for the total dataset.

In comparison with porosity/vertical effective stress trends based on soil mechanics studies (Fig. 52 & Fig. 53), it can be observed that for the effective stress range covered in this study, the Skempton (1970) model delivers similar results as the Yang & Aplin (submitted) model.

The average difference between the measured and predicted porosities for the total set (no fossils, no GRAPE data) is identical ($\pm 4\%$), with $\pm 3\%$ for the $<35\%$ fraction, $\pm 4\%$ for the 35-64% clay fraction, and $\pm 5\%$ for the $>65\%$ clay fraction. As illustrated in Fig. 51 and Fig. 53, the accuracy of the Skempton model is slightly higher for the coarser material ($<50\%$ clay fraction) and slightly lower for the finer ($>50\%$ clay fraction) material than the Yang & Aplin (submitted) model.

Contrary to the good agreement between the described models and the samples used for the compaction analysis, the difficulties caused by fossil-rich samples are striking (Fig. 54).

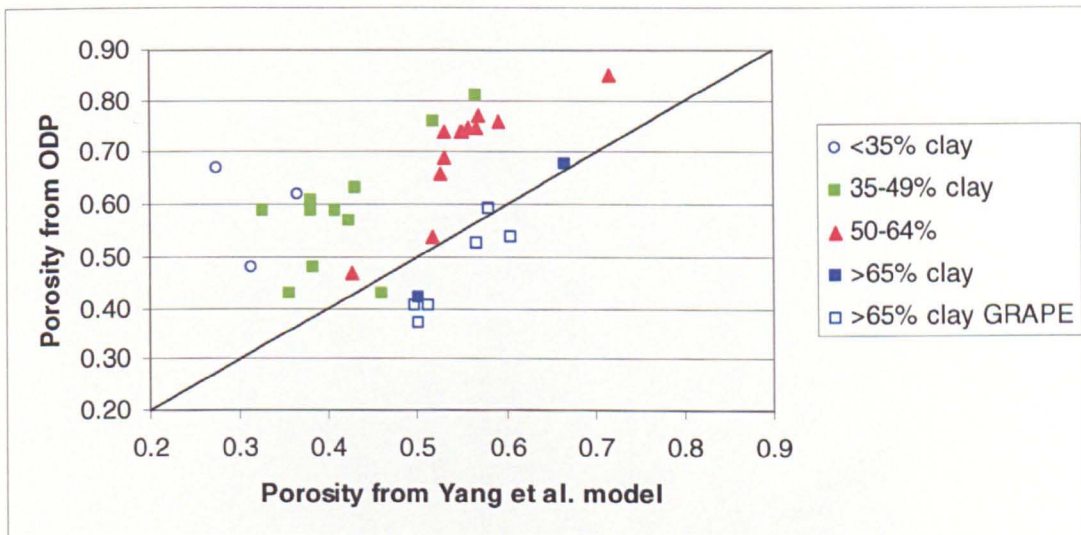


Fig. 54 Comparison of the measured and predicted porosities of the fossil-rich and GRAPE-samples.

Note that all GRAPE samples belong to the $>65\%$ clay fraction group.

For almost all samples with less than 65% clay fraction the measured porosities are much higher than the predictions by the Yang & Aplin (submitted) model (

Table 23). The Skempton (1970) model produces similar results. The samples whose porosities were determined by applying the GRAPE method

belong completely to the >65% clay fraction group and are more or less free of fossiliferous material. The porosity predictions for this group come close to or exceed the measured values (Fig. 54). However, since the general reliability of the GRAPE data is hard to predict (**2 Samples and Methods**) it should only be used if calibration data are available.

In general these results show how important a thorough characterization of fine-grained lithologies in shallow sedimentary sequences is for a successful compaction analysis.

Leg	Site	Core	σ'	mbsf	clay	ϕ ODP	ϕ Model	ϕ SK	ϕ PSM
26	250	4-6	572	119.38	0.72	0.63	0.57	0.63	0.47
26	250	6-3	986	189.6	0.72	0.66	0.57	0.60	0.53
26	250	7-4	1286	238.65	0.74	0.54	0.57	0.60	0.54
26	250	8-4	1813	295.65	0.74	0.59	0.57	0.58	0.54
26	250	9-3	2220	351.22	0.77	0.52	0.58	0.57	0.39
26	250	10-2	2612	407.3	0.78	0.53	0.58	0.57	0.37
26	250	11-2	3035	464.97	0.75	0.51	0.57	0.54	0.33
26	250	13-4	3931	571.67	0.74	0.41	0.57	0.52	0.32
26	250	14-2	4141	806.7	0.72	0.37	0.57	0.51	0.34
26	250	17-2	4426	645.71	0.73	0.41	0.57	0.51	0.3
26	257	1-5	20	7.2	0.7	0.85	0.56	0.73	n/a
26	257	3-2	97	49.2	0.76	0.75	0.58	0.71	n/a
26	257	5-2	322	124.04	0.73	0.69	0.57	0.66	n/a
26	257	9-2	958	248.7	0.82	0.68	0.59	0.64	n/a
36	330	1-4	781	134.71	0.51	0.69	0.48	0.53	0.41
36	330	2-2	1077	177.41	0.52	0.54	0.48	0.52	0.52
36	330	6-4	2384	314.55	0.39	0.45	0.44	0.43	0.31
36	330	8-3	2689	350.37	0.62	0.44	0.51	0.51	0.37
36	330	9-2	2906	377.75	0.59	0.43	0.50	0.49	0.33
36	330	10-2	3234	405.95	0.62	0.47	0.51	0.49	0.34
36	330	11-2	3507	434.8	0.5	0.40	0.48	0.44	0.3
36	330	13-1	4200	490.83	0.4	0.41	0.45	0.40	0.33
36	330	14-2	4511	519.88	0.25	0.34	0.38	0.35	0.38
43	386	1-6	246	59.28	0.68	0.68	0.51	0.65	n/a
43	386	4-4	750	151.97	0.38	0.46	0.43	0.48	n/a
43	386	11-2	1493	252.94	0.59	0.66	0.49	0.53	n/a
43	386	14-5	2097	335.82	0.64	0.66	0.50	0.53	n/a
43	386	26-2	3110	480.81	0.41	0.48	0.44	0.42	0.46
43	386	28-3	3300	502	0.67	0.42	0.51	0.51	0.47
43	386	32-5	3780	562.96	0.31	0.48	0.40	0.38	0.41
43	386	36-4	4554	646.8	0.74	0.43	0.53	0.51	0.3
43	386	42-4	5344	731.8	0.6	0.43	0.49	0.45	0.4
43	386	50-4	6173	818.22	0.85	0.40	0.55	0.52	0.36
43	386	54-6	6606	858.82	0.67	0.40	0.51	0.45	0.41
43	386	55-4	6687	865.05	0.71	0.44	0.52	0.46	0.37
43	386	59-3	7019	900.59	0.75	0.39	0.53	0.47	0.39
43	386	65-2	7648	957.37	0.73	0.40	0.52	0.46	0.38
57	440	8-2	1091	208.2	0.36	0.57	0.40	0.46	n/a
57	440	13-3	1443	257.23	0.4	0.63	0.41	0.46	0.51
57	440	24-1	2083	358.74	0.33	0.62	0.39	0.41	0.53
57	440	28-3	2363	399.7	0.37	0.59	0.40	0.42	0.51
57	440	39-2	2918	502.72	0.45	0.59	0.43	0.44	0.53
57	440	52-1	3723	624.7	0.24	0.67	0.35	0.36	0.46
57	440	60-2	4210	702.2	0.35	0.59	0.39	0.38	0.44
57	440	65-1	4497	748.24	0.47	0.61	0.43	0.42	n/a
116	719	11X-1	660	90.58	0.42	0.52	0.35	0.50	0.46
116	719	14X-2	960	120.12	0.44	0.56	0.35	0.49	0.47
116	719	16X-1	1112	138.26	0.48	0.48	0.36	0.50	0.39
116	719	17X-3	1202	150.87	0.6	0.57	0.38	0.55	0.36
116	719	22X-4	1573	200	0.63	0.53	0.38	0.54	0.37
116	719	28X-1	2002	251.55	0.61	0.52	0.38	0.52	0.45
116	719	33X-2	2411	300.75	0.6	0.50	0.38	0.51	0.43
116	719	38X-3	2822	350.3	0.78	0.58	0.40	0.56	0.43
116	719	48X-6	3746	448.95	0.53	0.47	0.37	0.45	0.43
127	794	1H-1	3	1.02	0.5	0.85	0.35	0.70	n/a
127	794	9H-5	317	80.28	0.49	0.81	0.35	0.56	n/a
127	794	9R-1	1532	376.07	0.46	0.43	0.35	0.48	0.53
127	794	11R-1	1664	395.75	0.4	0.59	0.34	0.45	0.48
127	794	17R-1	2137	453.6	0.65	0.53	0.37	0.53	n/a
127	794	20R-3	2396	485.35	0.57	0.51	0.36	0.49	0.47
150	906	14X-1	981	121.31	0.51	0.50	0.33	0.52	0.49
150	906	31X-1	2180	285.6	0.57	0.50	0.34	0.50	0.5
150	906	33X-1	2348	305.05	0.47	0.51	0.33	0.46	0.49
150	906	41X-3	3052	384.53	0.35	0.38	0.31	0.40	n/a
150	906	51X-3	3807	481.1	0.39	0.43	0.32	0.40	0.42
174	1072	7R-1	507	51.35	0.61	0.49	0.32	0.59	0.48
174	1072	11R-1	690	71.08	0.38	0.48	0.30	0.48	0.39
174	1072	17R-1	996	100.21	0.33	0.39	0.29	0.45	0.38
174	1072	25R-3	1452	145.16	0.31	0.41	0.28	0.42	0.35
174	1072	37R-1	2026	198.34	0.34	0.38	0.29	0.42	n/a
174	1072	46R-4	2531	249.68	0.18	0.37	0.25	0.36	0.4
175	1084	12H-5	336	103	0.5	0.77	0.31	0.57	n/a
175	1084	17H-1	476	145.8	0.58	0.76	0.32	0.59	n/a
175	1084	24X-1	659	201	0.47	0.76	0.31	0.52	n/a
175	1084	29X-1	837	250.1	0.59	0.75	0.32	0.56	n/a
175	1084	34X-3	1024	300.1	0.6	0.75	0.32	0.56	n/a
175	1084	39X-3	1173	349.5	0.56	0.74	0.32	0.53	n/a
175	1084	43X-4	1274	389.4	0.61	0.74	0.32	0.55	n/a
175	1084	49X-6	1496	449.3	0.64	0.74	0.32	0.55	n/a

Table 23 The measured and modeled porosities and permeabilities of the complete sample set. σ' = vertical effective stress; ϕ SK = porosity predicted by Skempton model; ϕ Model = porosity predicted by Yang & Aplin model; ϕ PSM = porosity measured by mercury intrusion porosimetry; clay = clay fraction (mass <2 μ m spherical diameter). ***Bolt italic font*** = *GRAPE-data*, Times font = fossil-rich samples; ϕ ODP = porosity measured gravimetrically by ODP in lab; n/a = samples not suitable for mercury intrusion porosimetry.

4.3 Case studies

4.3.1 Compaction trends of the shallow Norwegian North Sea sequences

4.3.1.1 Background

The Middle Miocene to Recent sedimentary sequence (Nordland Formation) of the Norwegian North Sea and Mid-Norway area (Fig. 55) is known for being dominated by thick (up to 1000m) marine and glacial clay rich lithologies (e.g. Jordt et al. 1995; Gradstein & Backström, 1996; Gregersen, 1998). These range from soft clays and muds to silty and micaceous claystones and were deposited at rates between tens of meters per Ma in the Miocene of the South Viking Graben (Galloway et al. 1993) and hundreds of meters per Ma in the Pliocene in the Haltenbanken area (Gradstein & Backström, 1996). The thickness of the Nordland Formation increases from ~600m in the South Viking Graben to approx. 1500m along the Mid-Norway margin.

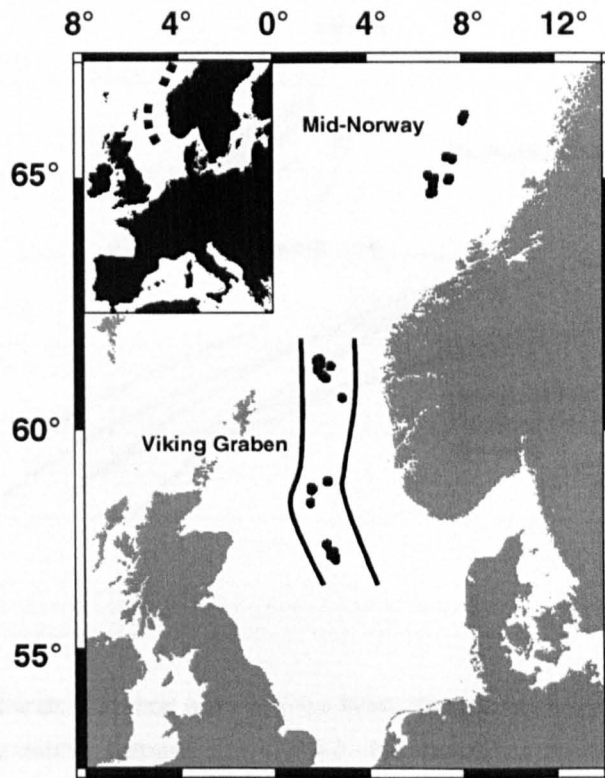


Fig. 55 Map of the study area. All wells were drilled in the Norwegian sector of the North Sea.

The analysis of the density log-derived compaction trends of the Nordland Formation in the North Viking Graben (Norwegian quadrants 30, 33 & 34) and Mid-Norway area (quadrants 6406, 6407, 6506, 6507 & 6608) revealed porosity-depth relationships which are very untypical for shallow fine-grained sequences (Fig. 56). In comparison with other shallow clay-dominated formations (e.g. Giles et al., 1998) the observed porosities are not only very low, they also decrease linearly, which is uncommon at these shallow depths. The lower boundary of this shallow "low porosity"-section is marked in most of the examined wells by a prominent porosity reversal between the Nordland and underlying Hordaland Formation (Fig. 56).

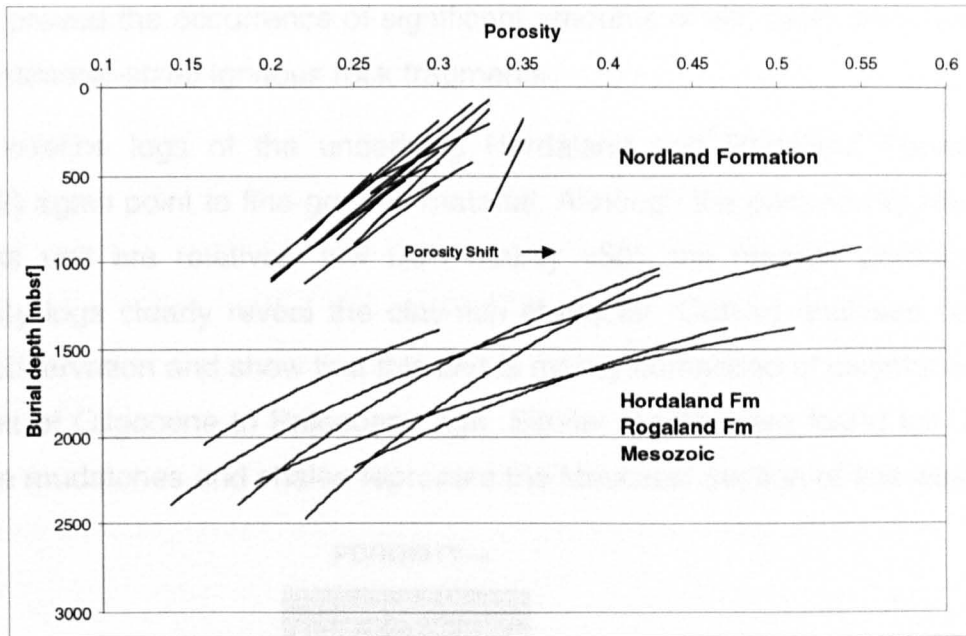


Fig. 56 Compaction trends of several wells from the North Viking Graben and Mid-Norway area. Note the prominent porosity reversal between 700mbsf and 1100mbsf, which divides the Nordland Formation from the underlying Tertiary and Mesozoic sequences.

In order to provide a representative analysis of the observed porosity-depth trends the following chapter will contain a detailed compaction study of a well from the Mid-Norway area.

4.3.1.2 Compaction analysis of a well from offshore Mid-Norway

The lithological characterisation of the present well was based on the analysis of both geophysical well logs (Fig. 62) and cutting samples. A simplified lithological profile is displayed in Fig. 57.

The top (Unit1) of the 2200m thick sequence is represented by the Mid-Miocene to Recent Nordland Formation and dominated by muds, silts and sands with frequently occurring igneous rock fragments (Fig. 58). This classification is the result of the combined use of wireline logs and cutting samples and would significantly differ if the latter material were not available. The wireline logs (Fig. 62) clearly point to clay-rich sediments and reveal no striking evidence for the presence of coarser material. Both the neutron/density log and the gamma ray log show levels typical (Rider, 1996) for a mud dominated interval. The analysis of the cutting material on the other

hand proved the occurrence of significant amounts of silt, sand and millimeter to centimeter-sized igneous rock fragments.

The wireline logs of the underlying Hordaland and Rogaland Formations (Unit2) again point to fine-grained material. Although the gamma ray readings of this unit are relatively low (API mainly <50), the neutron porosity and density logs clearly reveal the clay-rich character. Cutting analyses confirm this observation and show that this unit is mainly comprised of claystones and shales of Oligocene to Paleocene age. Similar results were found for Unit 3, where mudstones and shales represent the Mesozoic section of this well.

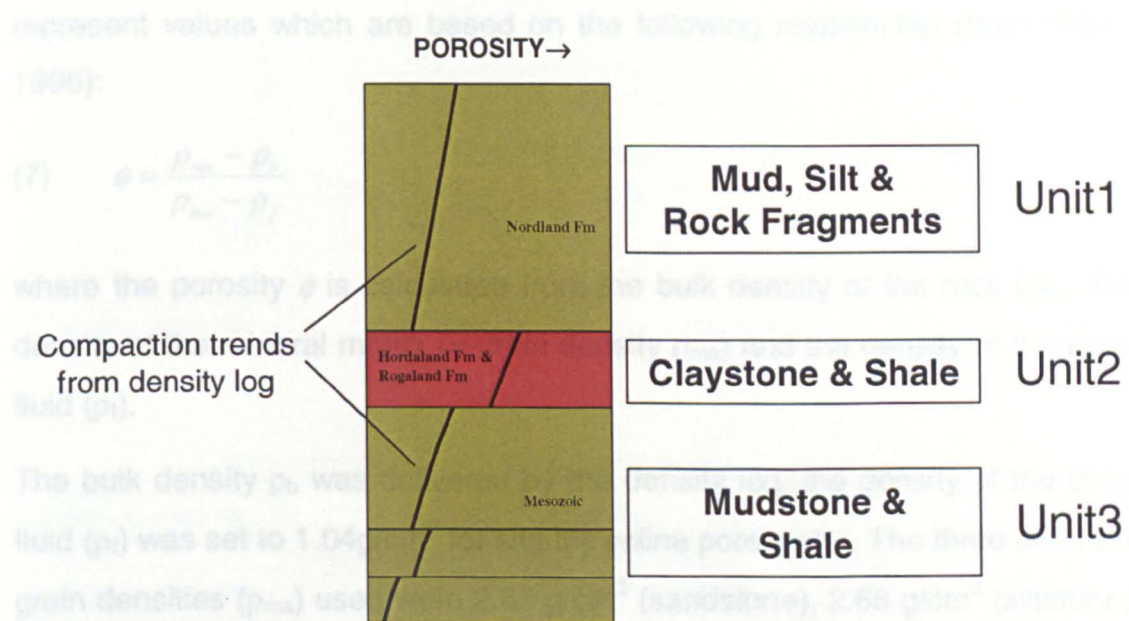


Fig. 57 Simplified lithological profile based on wireline logs and cutting samples. The compaction trends are based on the analysis of the density log.

The occurrence of igneous rock fragments in cuttings from the Nordland Formation points to a significant glacial influence during the deposition of Unit1 (Füchtbauer, 1988; Munro-Stasiuk, 2000). This observation agrees with previous studies (Rokoengen & Rønningsland, 1983; Hollander, 1984; Riis & Fjeldskaar, 1992; Høltedahl, 1993; Henriksen & Vorren, 1996; Gregersen, 1997) where glacial sediments were reported to comprise significant amounts of the first few hundred meters ($\leq 500\text{m}$) of the Nordland Formation. In contrast, in the examined Mid-Norway well the glacial influence seems to extend much deeper until a depth of at least 650m (Fig. 58).

For the present compaction study this information is of great importance, since the compressibility of glacial sediments (boulder clay & till) is different from that of purely marine clays and muds (Hossain, 1996; Clarke et al., 1998; Lind, 1999; Tulaczyk et al. 2001). The characteristic poor sorting and wide range of grain sizes in glacial tills results in porosities and permeabilities which are often significantly different from those of marine clay-rich sediments (Boulton & Dobbie, 1993; Neuzil, 1994; Blum, 1996; Gerber & Howard, 2000).

The porosities used in this study were solely derived from the density log and represent values which are based on the following relationship (from Rider, 1996):

$$(7) \quad \phi = \frac{\rho_{ma} - \rho_b}{\rho_{ma} - \rho_f}$$

where the porosity ϕ is calculated from the bulk density of the rock (ρ_b), the density of the mineral matrix (= grain density ρ_{ma}) and the density of the pore fluid (ρ_f).

The bulk density ρ_b was delivered by the density log, the density of the pore fluid (ρ_f) was set to 1.04g/cm³ for slightly saline pore water. The three different grain densities (ρ_{ma}) used were 2.65 g/cm³ (sandstone), 2.68 g/cm³ (siltstone) and 2.71 g/cm³ (mudstone). The classification of the different lithologies (for the assessment of porosity) was based on the gamma ray log, where 20API was set as the boundary between sand and silt and 65API as the boundary between silt and mudstone.

Although this classification is a practicable way of allocating grain densities to the drilled sections, it is also cause for significant uncertainty. Since the cutting samples from Unit1 revealed that there can be a significant difference between the log-derived and actual lithology, these uncertainties have to be considered for a wireline log-based compaction analysis.

Fig. 58 shows the porosity profile derived from the density log by applying equation (7). The previous subdivision of the well into 3 lithological units (Fig. 57) is clearly reflected by changes in porosity. The most obvious separation

exists between Unit1 (Nordland Fm.) and Unit2 (Hordaland/Rogaland Fm.). Here, porosity shifts by approximately 30% from about 20% at the bottom of Unit1 to about 50% at the top of Unit2. The next significant change of porosity can be observed between Unit2 and Unit3 at the top of the Mesozoic. In this case, porosity shifts from just over 40% at the bottom of Unit2 down to about 30% at the top of Unit3. Two further shifts of similar amplitude occur within the Mesozoic beyond 1750mbsf.

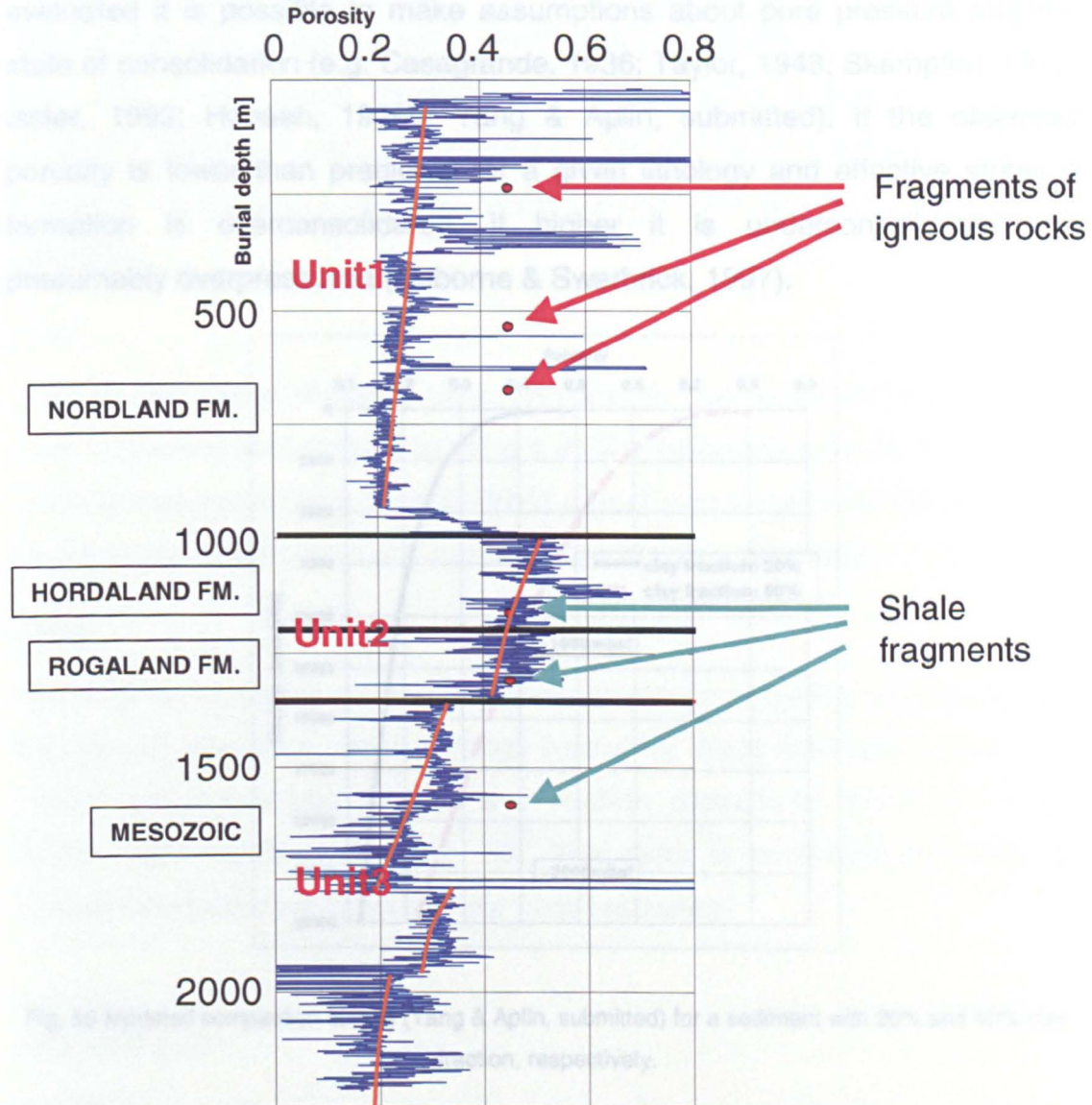


Fig. 58 Porosity/depth plot for a Mid-Norway well. Porosities were calculated from the density log, assuming grain densities of 2.71g/cm^3 for $\text{API}>65$, 2.68g/cm^3 for $\text{API} 20-65$, 2.65g/cm^3 for $\text{API}<20$ and a pore fluid density of 1.04g/cm^3 . The red dots mark positions where cuttings have been analyzed.

Since the observed shifts coincide with changes in lithology, the use of different compaction curves for each unit and subunit seems to be appropriate. A comparison with compaction curves based on Yang & Aplin's (submitted) model (Fig. 59) shows that the observed porosities fall well into the range predicted for fine-grained lithologies.

For every compaction analysis it is crucial to have information about lithology, porosity and effective stress. If these parameters can be sufficiently well evaluated it is possible to make assumptions about pore pressure and the state of consolidation (e.g. Casagrande, 1936; Taylor, 1948; Skempton, 1970; Issler, 1992; Hansen, 1996b; Yang & Aplin, submitted). If the observed porosity is lower than predicted for a given lithology and effective stress a formation is overconsolidated, if higher it is underconsolidated and presumably overpressured (Osborne & Swarbrick, 1997).

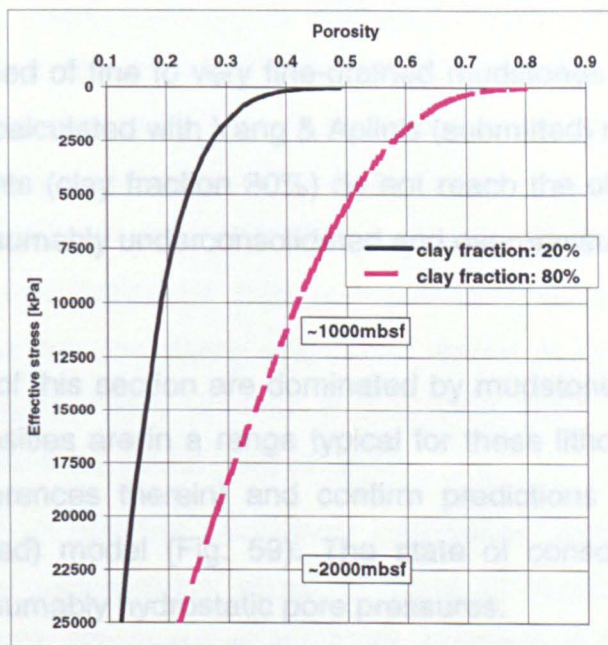


Fig. 59 Modeled compaction curves (Yang & Aplin, submitted) for a sediment with 20% and 80% clay fraction, respectively.

Since high quality sample material (core) is not available in the present study, information about the exact clay fraction could not be obtained. Thus, Yang & Aplin's (submitted) model, which is based on clay fraction as descriptor of lithology, can not be applied to infer the state of consolidation.

By using the available wireline-logs and cutting samples to characterize the lithology of the present well the following assumptions about porosity and the state of consolidation can be made:

SCENARIO A

Unit1

The sediment is dominated by relatively coarse-grained material of presumably glaciomarine origin. The observed porosities are typical for this type of sediment (Tulaczyk et al., 2001) which often has clay fractions of less than 20% (Lind, 1999). Predictions based on Yang & Aplin's (submitted) model for sediments with clay fractions of about 20% (Fig. 59) agree with this scenario and point to a state of normal consolidation with hydraulic pore fluid pressures.

Unit2

Unit2 is comprised of fine to very fine-grained mudstones and shales. Since even porosities calculated with Yang & Aplin's (submitted) model for very fine-grained sediments (clay fraction 80%) do not reach the observed levels, the formation is presumably underconsolidated and overpressured.

Unit3

The sediments of this section are dominated by mudstones and shales. The log-derived porosities are in a range typical for these lithologies (Giles et al. (1998) and references therein) and confirm predictions made by Yang & Aplin's (submitted) model (Fig. 59). The state of consolidation should be normal with presumably hydrostatic pore pressures.

SCENARIO B

Unit1

Unit1 is mainly comprised of fine-grained sediments with a regular occurrence of coarser, glacial-derived material. The observed porosities are generally too low for this type of sediment and burial depth (Giles et al., 1998) and point to a significant degree of overconsolidation.

Unit2

Similar to scenario A.

Unit3

Similar to scenario A.

If scenario A is correct the huge shift of porosity between Unit1 and Unit2 could be explained by a radical change of sedimentary environment. The fine-grained sediments of the Hordaland and Rogaland Formations (Unit2) have been deposited at relatively low accumulation rates of often much less than 80m/Ma (Galloway et al., 1993; Wensaas et al., 1994). The subsequent deposition of the coarser Nordland Formation (Unit1) marked in many areas a shift towards higher sedimentation rates of up to 140m/Ma (Hollander, 1984; Wensaas et al., 1994; Kvilhaug & Roaldset, 1998). This combination of increased sediment accumulation and change of lithology can explain both the underconsolidated state of Unit2 and the normal consolidated state of Unit1. Since marine shales like Unit2 usually have much lower permeabilities than glacial tills like Unit1 (Neuzil, 1994; Lind, 1999; Gerber & Howard, 2000) a rapid load of about 1000m of Unit1 on top of Unit2 would have two effects: 1. it would hinder the dewatering and consolidation of Unit2 ('disequilibrium compaction'; Magara, 1978; Osborne & Swarbrick, 1997; Grauls, 1999), but 2. it would also allow the dewatering of Unit1.

Due to the lack of detailed lithological information about Unit3 it is very difficult to make assumptions about its state of consolidation. Both low sedimentation rates (Wensaas et al., 1994; Kvilhaug & Roaldset, 1998) as well as observed porosities do not point to significant degrees of underconsolidation or overpressure. However, as described by Hermanrud et al. (1998) it is possible that fluid overpressuring post-dating shale compaction resulted in higher than normal pore pressures.

If scenario B is be correct, Unit1 is overconsolidated whereas Unit2 and Unit3 have the same states as in scenario A.

In order to explain a possible state of overconsolidation in Unit1, several geological models can be used:

Firstly, the sequence could have been uplifted (Fig. 60). In this case, erosion of an overlying section would have led to porosities, which represent much higher effective stresses than observed today. Difficulties with this model are, that the underlying Units 2 and 3 do not show any evidence for higher effective stresses in the past. The recently observed porosities should be much lower than today if a significant additional load of sediment had been in place. Furthermore, Hansen (1996b) showed that the Mid-Norway well is located in an area where no major uplift or erosion occurred during the last few million years.

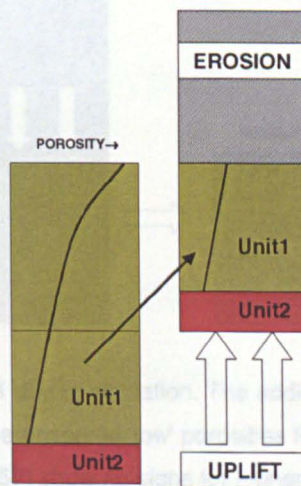


Fig. 60 Overconsolidation of Unit1 due to uplift and erosion. Recently observed porosities (black compaction curve) correspond to effective stresses that were much higher in the past. Difficulties with this model are that the underlying Units 2 & 3 (Fig. 57) do not show signs for higher effective stresses in the past.

Secondly, the cause of overconsolidation could be connected to a series of glaciations which happened in the described area during the Pliocene/Pleistocene (e.g. Henriksen & Vorren, 1996; Mangerud et al., 1996; Carr, 1999; Lambeck et al., 2000). In this model, the presence of glaciers could have resulted in an increase of effective stress (Fig. 61). Then, after deglaciation the effective stress would have returned to lower levels, hence the observed overconsolidation. There are three main difficulties with this model. Firstly, The glacier must have had direct contact to the sediment surface, since any water in between would have transferred the ice load to the

pore fluid and not to the grain matrix (i.e. increase in hydraulic pressure and not effective stress; Boulton & Dobbie, 1993). Since Henriksen & Vorren (1996) showed that the examined area was mostly ice-free and one of the sediment depocenters (i.e. submerged) it is highly unlikely that these glaciations generated the effective stress necessary for a significant degree of overconsolidation. Secondly, even if there would have been the necessary extent of glacial cover it would have been difficult to expell the pore water of Unit1 sideways or through the underlying, less permeable sediments. Finally, higher effective stresses in the past are very unlikely, because Units 2 and 3 do not show any evidence of overconsolidation.

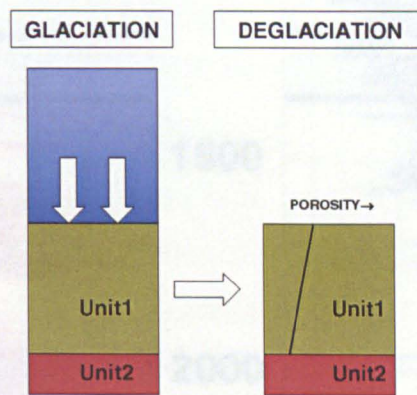


Fig. 61 Overconsolidation of Unit1 due to glaciation. The additional ice load increased the effective stress in the past and resulted in the observed 'low' porosities for Unit1. Difficulties with this model are 1. the underlying Units 2 & 3 (Fig. 57) show no signs for higher effective stresses in the past; 2. since Unit2 should be of much lower permeability than Unit1 there is no obvious pathway to expell the excess pore water of Unit1 during compaction.

4.3.1.5 Deglaciation and Overconsolidation

Two basic scenarios were presented to explain the compaction history of the Mid-Norway well.

Scenario B is based on the assumption that Unit 1 consists of fine-grained material and that the log-derived porosity curve is a result of overconsolidation. The theory that other glaciations or glacial cover have resulted in higher effective stresses in the past is very unlikely since Units 2 and 3 show no evidence of overconsolidation. On the contrary, the porosity of Unit 2 are higher than the log-derived porosity, which is a sign of underconsolidation.

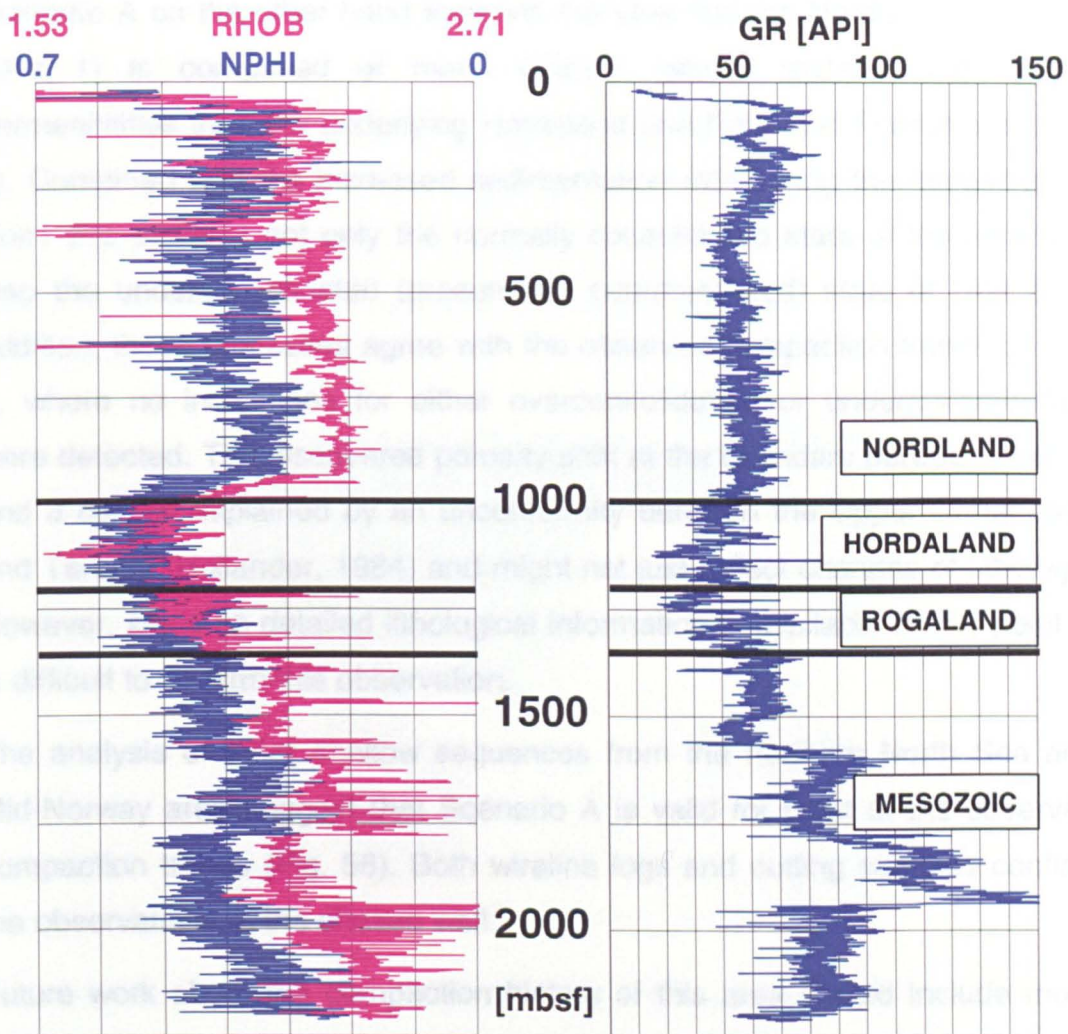


Fig. 62 Neutron/density and gamma ray logs of the examined Mid-Norway well. RHOB: bulk density; NPHI: neutron porosity; GR: gamma ray.

4.3.1.3 Discussion and conclusions

Two basic scenarios were presented to explain the compaction trends of the Mid-Norway well.

Scenario B is based on the assumption that Unit1 consists of fine-grained material and that the log-derived porosities point to a state of overconsolidation. The theory that either uplift/erosion or glaciation could have resulted in higher effective stresses in the past is very unlikely since Units 2 and 3 show no evidence of overconsolidation. On the contrary, the porosities of Unit 2 are rather too large than two small and thus indicate a state of underconsolidation. (Fig. 64) which mainly comprised silts and clays

Scenario A on the other hand supports the idea that the Nordland Formation (Unit 1) is comprised of much coarser, glacial material with higher permeabilities than the underlying Hordaland and Rogaland Formations (Unit 2). Combined with the increased sedimentation rate during the deposition of Unit 1 this explains not only the normally consolidated state of the latter but also the underconsolidated (presumably overpressured) state of Unit 2. In addition, these processes agree with the observed compaction trends of Unit 3, where no indications for either overconsolidation or underconsolidation were detected. The discovered porosity shift at the boundary between Units 2 and 3 can be explained by an unconformity between the Upper Cretaceous and Tertiary (Hollander, 1984) and might not just reflect changes of lithology. However, since no detailed lithological information is available at this point it is difficult to confirm this observation.

The analysis of other shallow sequences from the northern North Sea and Mid-Norway area suggest that Scenario A is valid for most of the observed compaction trends (Fig. 56). Both wireline logs and cutting samples confirm the observations of the chosen well.

Future work about the compaction history of this area should include more high quality sample material to allow a better characterization of the examined lithology. Pore pressure data should also help to explain the sudden shifts of porosity between the different lithological units.

4.3.2 The New Jersey shelf and continental slope

4.3.2.1 Background

Dugan & Flemings (2000a/b) examined the compaction history of a sedimentary sequence drilled in 1998 by the Ocean Drilling Program on the New Jersey continental slope (Fig. 63). Their analysis of porosity data at this site (174/1073) implied the occurrence of highly overpressured pore fluids, which they suggested led to the slope failures previously identified in the region (Fig. 66; MacDonald et al., 1990).

Well 174A/1073, drilled at a water depth of 639m, is represented by a 663m thick sedimentary sequence (Fig. 64) which mainly comprised silts and clays

with few sandy interlayers. The deeper sections (>560mbsf) are dominated by siliceous and calcareous fossil material (Table 24).

The well can be subdivided into three lithostratigraphic units. Unit I is of Pleistocene-Holocene age and extends from sea floor down to 519.8mbsf. Unit II covers depths from 519.8mbsf to 654.1mbsf and is Oligocene to Pliocene in age. Unit III extends from 654.1mbsf to 663.6mbsf and is of Eocene age.

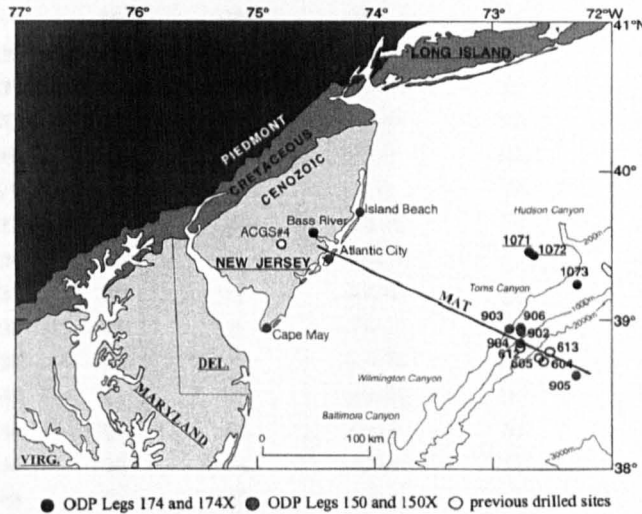


Fig. 63 Location of site 1073 at the New Jersey continental Slope (Vanderaveroet 2000).

Sedimentation rates of less than 100m/Ma for the Pliocene and Miocene and a maximum of about 1100m/Ma for the Pleistocene are based on biostratigraphic data (Dugan & Flemings, 2000b).

Depth [mbsf]	Qz & Fp	Clay	Total Fossils	Depth [mbsf]	Qz & Fp	Clay	Total Fossils
0.1	34	23	34	338.2	37	34	17
1.2	32	39	17	347.6	31	44	9
7.8	34	37	13	357.3	32	47	7
17.2	32	38	15	366.5	35	41	10
26.53	30	38	14	375.9	35	44	7
33.13	40	23	19	385.13	37	35	16
35.33	42	18	21	394.8	38	37	10
40.36	40	26	16	403.6	37	43	5
47.51	37	38	11	412.74	37	42	8
59.3	40	22	19	422.69	34	26	30
62.9	41	20	20	428.15	37	11	39
64.3	35	36	15	433.2	36	23	29
74.1	35	36	11	444.43	36	39	11
75.8	32	50	6	452.96	35	44	7
79.91	28	34	22	461.51	35	41	9
80.4	21	60	7	472	36	48	6
83.4	27	50	8	480.78	27	48	13
87.9	26	55	6	489.7	27	54	8
93.3	31	47	10	497.9	30	45	10
101.7	36	48	6	518.3	22	39	25
112.2	33	48	5	519.76	21	23	37
114.3	38	43	9	519.99	23	35	25
118.8	44	29	14	523.4	20	35	31
122.4	38	36	14	526	20	42	28
139.9	43	33	10	535.3	15	43	35
147.6	26	26	39	542.1	25	35	28
159.1	33	35	18	551.04	15	37	14
168.6	31	31	20	552.22	16	25	25
178.1	31	30	23	553.62	16	44	29
185.6	31	32	23	563.9	17	33	37
190.3	27	5	50	573.35	16	19	46
198.27	30	30	28	582.6	16	25	43
201.3	35	6	44	583.92	13	12	56
213.86	39	33	13	593.52	13	17	52
218	37	36	16	598.36	17	10	48
228.2	31	48	7	600.15	13	19	54
236.2	30	42	14	606.14	12	14	46
245.8	31	44	13	610.92	13	16	52
256.8	20	55	7	616.45	11	26	51
266.3	32	48	8	619.05	13	10	58
273.2	21	56	11	625.04	15	13	48
282.4	26	44	19	628.62	14	9	54
292	32	43	14	632.9	36	9	44
301.4	25	52	17	641.1	13	21	49
310.7	20	44	26	647.02	11	23	51
319.6	31	49	10	657.7	3	18	69
328.37	31	50	9				

Table 24 Main mineralic constituents of well 174/1073 (Austin et al., 1998). Percentages are derived from smear slide analysis.

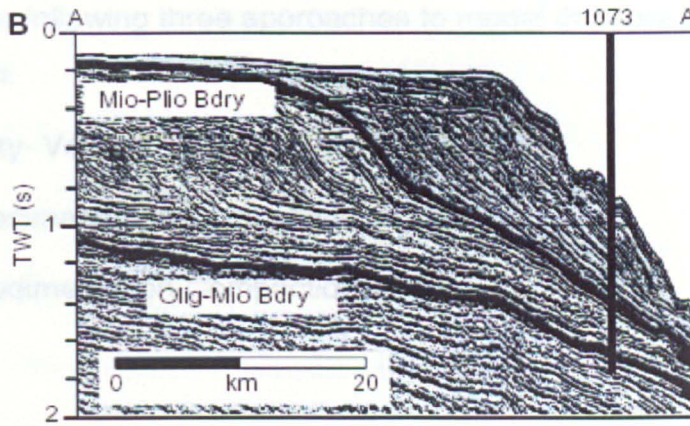


Fig. 64 Seismic section at site 1073 (Dugan & Flemings 2000a).

4.3.2.2 Conclusions of the compaction study of Dugan & Flemings (2000a/b)

Based on porosities derived from core data, Dugan & Flemings (2000a/b) subdivided site 1073 into three zones (Fig. 65 & Fig. 66): a shallow zone (0-100mbsf) of decreasing porosity, a thick intermediate section (100-550mbsf) of constant porosity, and a deep zone (550-660mbsf) of increased porosity.

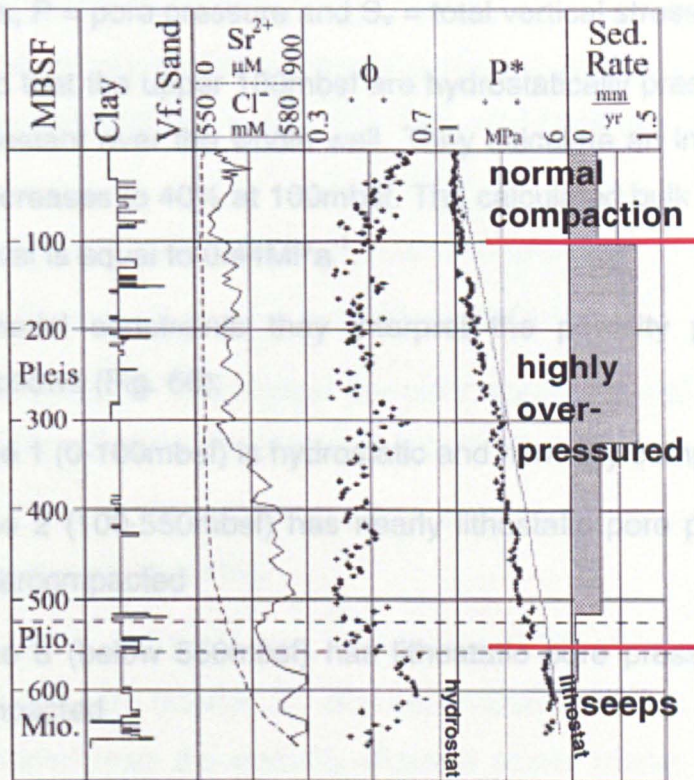


Fig. 65 Well section for Site 1073 (from Dugan & Flemings 2000b). φ = porosity, P* = fluid pressures predicted from porosity.

They used the following three approaches to model the pore pressures for the drilled section:

1. Porosity- Vertical Effective Stress Model
2. 1-D Sedimentation-Compaction Model
3. 2-D Sedimentation-Compaction Model

Model 1:

Based on the assumption that compaction is governed by vertical effective stress they used two relationships to constrain a compaction model and to infer pore pressure:

$$(8) \quad \phi = \phi_0 e^{-\beta \sigma_v}$$

$$(9) \quad P = S_v - 1/\beta [\ln (\phi_0/\phi)]$$

where; ϕ = porosity, ϕ_0 = initial porosity, β = compressibility, σ_v = vertical effective stress, P = pore pressure and S_v = total vertical stress.

They assumed that the upper 100mbsf are hydrostatically pressured and that lithology is constant over the whole well. They calculate an initial porosity of 61% which decreases to 40% at 100mbsf. The calculated bulk compressibility β for this interval is equal to 0.44MPa^{-1} .

From their model constraints they interpret the porosity profile for well 174/1073 as follows (Fig. 66):

1. Zone 1 (0-100mbsf) is hydrostatic and normally compacted
2. Zone 2 (100-550mbsf) has nearly lithostatic pore pressure and is undercompacted
3. Zone 3 (below 550mbsf) has lithostatic pore pressure and is not compacted

Model 2

Here Dugan and Flemings (2000a/b) use sedimentation rate and permeability in a one-dimensional model to simulate the pore pressure evolution during

sediment accumulation at site 1073. They assume a constant sedimentation rate of 950m/Ma for the duration of the Plio-Pleistocene, a constant vertical permeability of $K_v = 10^{-18}m^2$ for the Plio-Pleistocene and a constant vertical permeability of $K_v = 10^{-16}m^2$ for the Miocene strata. In their model the Miocene sediments are hydrostatically pressured prior to the sedimentation of the Plio-Pleistocene strata.

The results of this pressure model are as follows (Fig. 66):

1. Pore pressure is near lithostatic until 50mbsf
2. Below 50mbsf overpressures reach values of about 75% of those predicted by Model 1

Model 3

This approach uses a two-dimensional sedimentation-compaction model to evaluate the contribution of lateral fluid flow to the regional pressure field (Fig. 66). Here the model incorporates a spatially varying sedimentation rate (100-2000m/Ma) and an anisotropic permeability field (vertical permeability = $10^{-18}m^2$, horizontal permeability = $10^{-17}m^2$). The sedimentation rate is constant over time.

From this two-dimensional model they obtain the following results (Fig. 66):

1. Pore pressure is nearly lithostatic until 200mbsf
2. From 250mbsf to 500mbsf the pore pressures match those of the porosity-effective stress model (nearly lithostatic)
3. For Zone 3 the model predicts high overpressure (68% of the porosity-based model)

Model 3 was introduced by Dugan & Flemings (2000a/b) because the one-dimensional approach (Model 2) did not manage to produce the pore pressures obtained from the porosity-effective stress model (Model 1). The additional pore pressures generated by lateral fluid flow resulted in similar pressures as in Model 1 for the intermediate section (250-500mbsf) but still

failed to explain both the hydrostatic shallow section (<100mbsf) or the lithostatic bottom section (>550mbsf).

Dugan & Flemings (2000a) quote two main reasons why they probably did not manage to achieve a complete match between the sedimentation-compaction models and the porosity-effective stress model. Firstly, they debate whether due to the higher porosities at these depths, the permeabilities in the shallow section are in fact significantly higher than the assumed value of 10^{-18}m^2 . Secondly, they consider that the porosity-effective stress behaviour inferred from the shallow, hydrostatic section might not be accurate to describe the compressibility of the deeper sections. The latter point basically means that their assumption that lithology is constant does not apply for the whole section of well 174/1073.

In the following chapter the results of Dugan & Flemings' (2000a/b) model will be compared to predictions based on Yang & Aplin's (submitted) approach, which incorporates changing lithologies into a porosity-effective stress model.

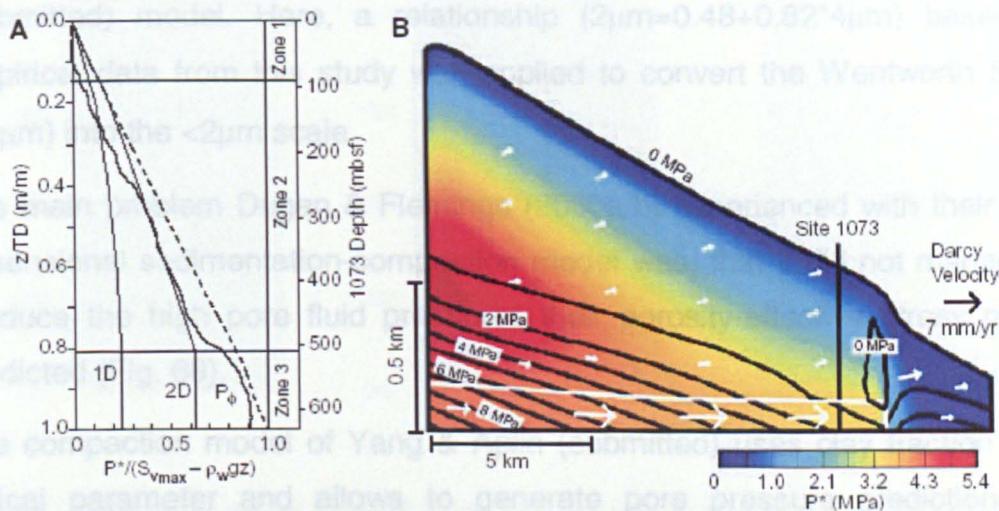


Fig. 3. (A) Normalized plot of overpressures for Site 1073. $T D$ is the total sediment thickness at Site 1073 and z is the distance below the sea floor. The dashed line is the reduced lithostat. Solid lines are one-dimensional model (1D), two-dimensional model (2D), and porosity-predicted (P_{ϕ}) pressures at Site 1073. Porosity zones and measured depth for Site 1073 are labeled for reference (Fig. 2). (B) Simulated 2D vertical effective stress (contour interval = 1 MPa), overpressure (color contours), and flow fields for the New Jersey slope after 1 million years of simulation. The left edge (upper slope) is a no-flow boundary, and the right edge (lower slope) is a constant-pressure boundary ($P^* = 0$). The model geometry is constrained from regional seismic data (Fig. 1B). The white surface is the Miocene-Pliocene boundary. Vertical effective stress is less than 1 MPa for much of the section and is < 0 MPa above the toe of the Miocene bed. The low vertical effective stress indicates that the lower slope is at near-failure conditions.

Model A (Fig. 66) sets the clay fraction to a constant 30%, which represents a

Fig. 66 Sketch from Dugan & Flemings' (2000a) publication. It shows the results of the different pore pressure models and explain the consequences of the lateral fluid flow model (Model 3).

4.3.2.3 Re-examination of the compaction history at Site 1073

Based on the core data provided by ODP (Austin et al. 1998), several compaction models can be used to explain the observed porosity/depth profile (Fig. 65).

In Fig. 67 the three most relevant core parameters for the compaction study are displayed. Former investigations revealed that the clay content can be used to characterize changes in lithology which significantly influence the compaction behaviour of siliciclastic sediments (Aplin et al., 1995; Dewhurst et al, 1998, 1999b; Yang & Aplin, 1998 & submitted). In addition, the presence of high fossil contents was proven to be an important factor in porosity prediction (Meade, 1963; Bryant and Rack 1990; Bryant et al. 1990; Compton 1991; Rack and Palmer-Julson 1992; Tribble et al. 1992; Kraemer et al. 2000).

For this study the $<4\mu\text{m}$ clay fraction provided by Austin et al. (1998) in Table 24 was used to calculate the $<2\mu\text{m}$ clay fraction needed for Yang & Aplin's (submitted) model. Here, a relationship ($2\mu\text{m}=0.48+0.82*4\mu\text{m}$) based on empirical data from this study was applied to convert the Wentworth Scale ($<4\mu\text{m}$) into the $<2\mu\text{m}$ scale.

The main problem Dugan & Flemings (2000a/b) experienced with their one-dimensional sedimentation-compaction model was, that it did not manage to produce the high pore fluid pressures their porosity-effective stress model predicted (Fig. 66).

The compaction model of Yang & Aplin (submitted) uses clay fraction as a critical parameter and allows to generate pore pressure predictions for different types of siliciclastic lithologies. Based on Dugan & Flemings (2000a/b) premise of a constant lithology three different pore pressure models have been generated applying the compaction model of Yang & Aplin (submitted) to sediments with 30%, 40% and 50% clay fraction (Fig. 69 & Fig. 70).

Model A (Fig. 69) sets the clay fraction to a constant 30%, which represents a silty sediment. The modeled porosities for this clay fraction are much lower

than the porosities measured by ODP (Fig. 68). As a result of this porosity difference the sediment seems to be completely uncompacted and thus highly overpressured. In fact, Model A produces lithostatic pore fluid pressures over most of the interval.

In comparison with Dugan & Flemings' porosity-effective stress model (Model1) the predicted pore pressures are higher, especially in the shallow (Zone 1, <800kPa) section (Fig. 69). The obtained pore pressures for the deep section (Zone 3, >4600kPa) are very similar.

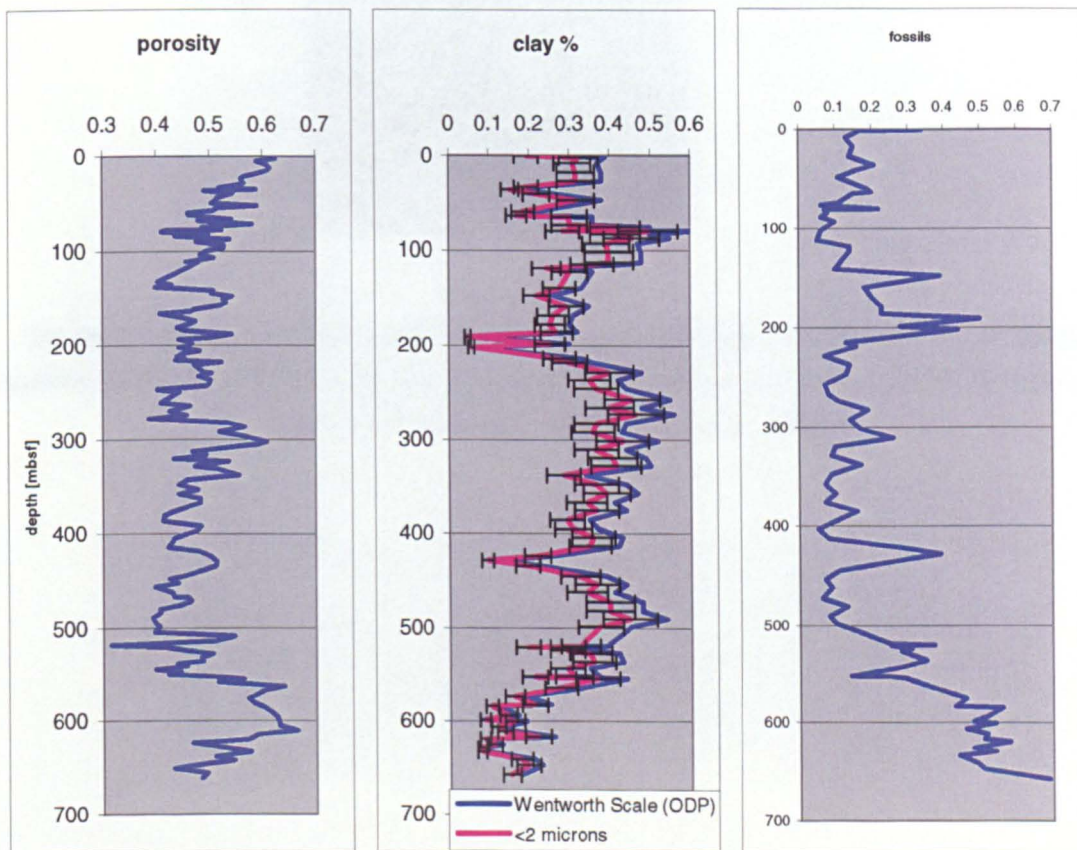


Fig. 67 Porosity, clay content and fossil content based on data from Austin et al. (1998). The $2\mu\text{m}$ fraction was derived from the $4\mu\text{m}$ (Wentworth Scale) data (Austin et al., 1998) using a relation based on empirical data, where $2\mu\text{m}=0.48+0.82*4\mu\text{m}$. The error bars reflect an uncertainty of the ODP values of $\pm 15\%_{\text{rel}}$ which was established by laboratory experiments.

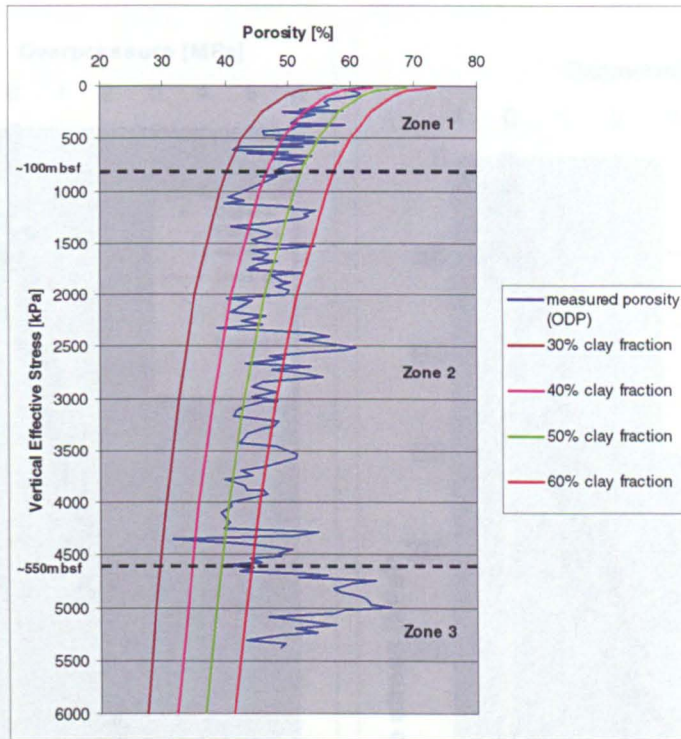


Fig. 68 A comparison of the porosities measured by ODP and those resulting from Yang & Aplin's (submitted) model for different clay fractions. Zones 1-3 from Dugan & Flemings (2000b). Stresses are calculated from bulk densities (Austin et al., 1998).

Fig. 69 (LHS) Pore fluid pressure based on the porosity/pressure model of Dugan & Flemings (2000b) (RHS) Comparison of the Dugan & Flemings model and pore pressures predicted for a constant clay fraction of 20% (Model A). (*) - Reduced lithostatic stress (total vertical stress-hydrostatic stress) for Dugan & Flemings' pore pressures.

Model B (Fig. 70) sets the clay fraction to a constant 40%. This is compatible to a silty mud, and matches the general lithological description for the examined sedimentary sequence (Austin et al., 1998). In this case, the pore fluid pressures generated by the model are very similar to those predicted by Dugan & Flemings (Fig. 70). However, Model B like Model A does not

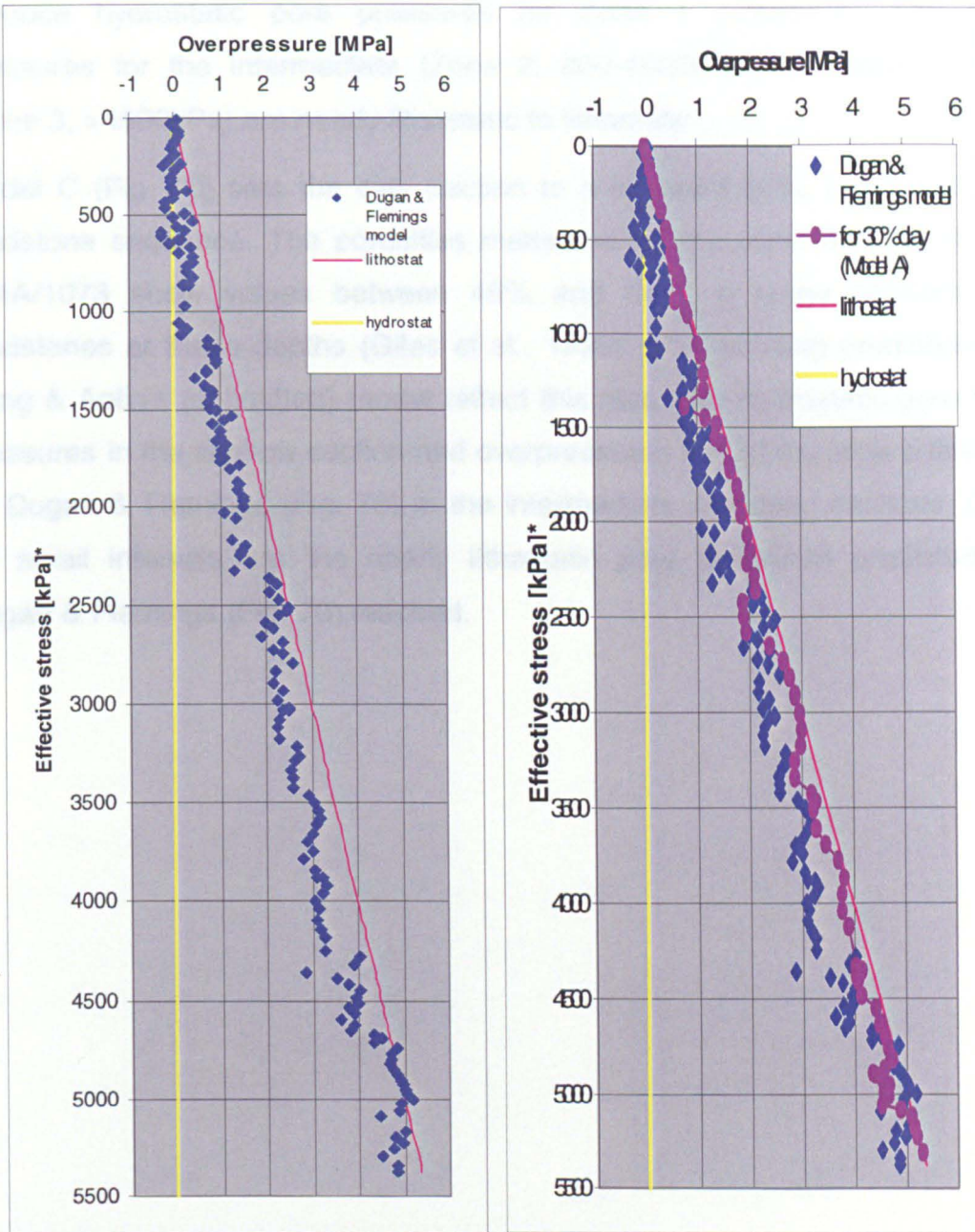


Fig. 69 (LHS) Pore fluid pressure based on the porosity/pressure model of Dugan & Flemings (2000b). (RHS) Comparison of the Dugan & Flemings model and pore pressures predicted for a constant clay fraction of 30% (Model A). (*) - Reduced lithostatic stress (total vertical stress-hydrostatic stress) for Dugan & Flemings' pore pressures.

Model B (Fig. 70) sets the clay fraction to a constant 40%. This is compatible to a silty mud, and matches the general lithological description for the examined sedimentary sequence (Austin et al., 1998). In this case, the pore fluid pressures generated by the model are very similar to those predicted by Dugan & Flemings (Fig. 70). However, Model B like Model A does not

produce hydrostatic pore pressures for Zone 1 (<800kPa). The fluid pressures for the intermediate (Zone 2, 800-4600kPa) and deep section (Zone 3, >4600kPa) are nearly lithostatic to lithostatic.

Model C (Fig. 70) sets the clay fraction to a constant 50%, representing a mudstone sequence. The porosities measured on the core material of well 174A/1073 show values between 45% and 60%, a range common for mudstones at these depths (Giles et al., 1998). The resulting predictions of Yang & Aplin's (submitted) model reflect this fact, with hydrostatic pore fluid pressures in the shallow section and overpressures half of the level predicted by Dugan & Flemings (Fig. 70) in the intermediate and deep sections. Only for small intervals are the nearly lithostatic pore pressures predicted by Dugan & Flemings (Fig. 70) reached.

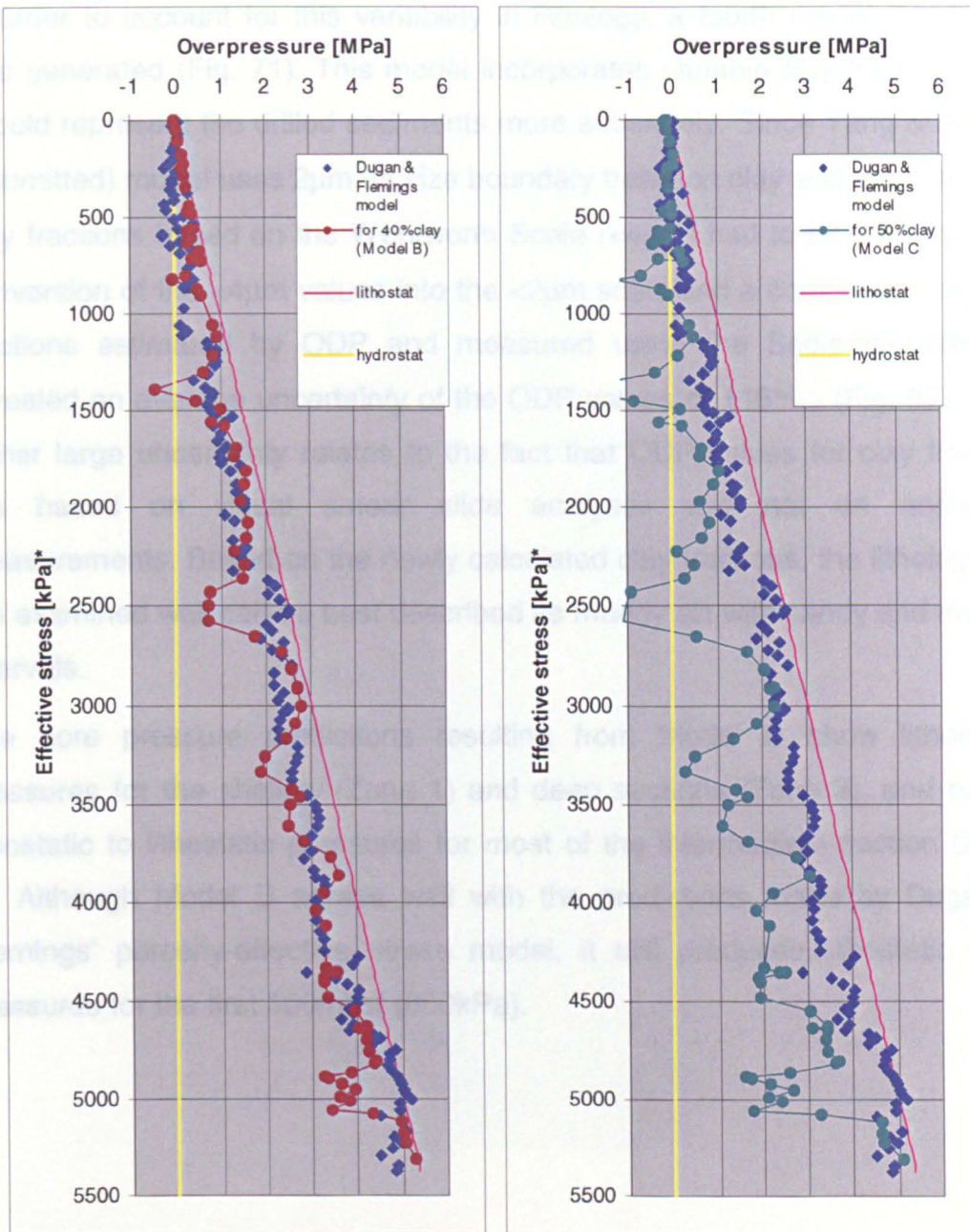


Fig. 70 Comparison of Dugan & Flemings' model with Model B (clay fraction of 40%, LHS) and Model C (50% clay fraction, RHS). (*) - Reduced lithostatic stress (total vertical stress-hydrostatic stress) for Dugan & Flemings' pore pressures.

The mineralic composition of well 174A/1073 (Table 24) reveals that Dugan & Flemings' (2000a/b) assumption of a constant lithology is very difficult to maintain, especially if taking into account the sensitivity of normal compaction curves to changes in clay fraction (this study, Aplin et al., 1995; Yang & Aplin, 1998 & submitted; Dewhurst et al., 1999b).

In order to account for this variability in lithology, a fourth model (Model D) was generated (Fig. 71). This model incorporates variable clay fractions and should represent the drilled sediments more accurately. Since Yang & Aplin's (submitted) model uses $2\mu\text{m}$ as size boundary between clay and silt, the ODP clay fractions based on the Wentworth Scale ($<4\mu\text{m}$) had to be converted. A conversion of the $<4\mu\text{m}$ values into the $<2\mu\text{m}$ scale and a comparison of clay fractions estimated by ODP and measured using the Sedigraph method revealed an average uncertainty of the ODP values of $\pm 15\%_{\text{rel}}$ (Fig. 67). This rather large uncertainty relates to the fact that ODP values for clay fraction are based on visual smear slide analyses and not on analytical measurements. Based on the newly calculated clay fractions, the lithology for the examined well can be best described as muddy silt with sandy and muddy intervals.

The pore pressure predictions resulting from Model D show lithostatic pressures for the shallow (Zone 1) and deep sections (Zone 3), and nearly lithostatic to lithostatic pressures for most of the intermediate section (Zone 2). Although Model D agrees well with the predictions made by Dugan & Flemings' porosity-effective stress model, it still produces lithostatic pore pressures for the first 100mbsf (800kPa).

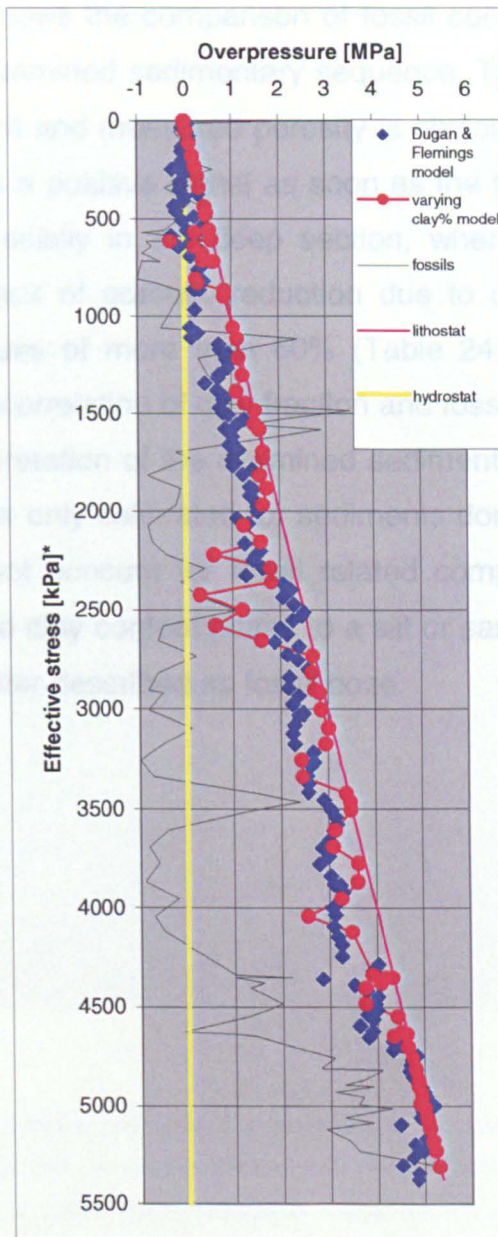


Fig. 71 (LHS) Model 4: Comparison of the Dugan & Flemings' model and pore pressures predicted by the Yang & Aplin (submitted) model for variable clay fractions. The fossil content ($\times 10^{-1}$) is set to 0 at 15%, the boundary where an influence on porosity becomes significant (Bryant & Rack, 1990). (*) - Reduced lithostatic stress (total vertical stress-hydrostatic stress) for Dugan & Flemings' pore pressures.

A critical flaw of all the models used to understand pore pressure is the neglect of a possible influence of the fossil content on the measured porosities. Here, as in other studies (e.g. Bryant & Rack, 1990; Tribble et al. 1992; Kraemer et al. 2000) it is clear that the abundance of nanno- and microfossils has a very significant impact on porosity in shallow marine

sediments. Fig. 72 shows the comparison of fossil content with porosity and clay fraction in the examined sedimentary sequence. The positive correlation between fossil content and measured porosity is obvious. In most cases, the porosity curve shows a positive signal as soon as the fossil content exceeds values of 15%. Especially in the deep section, where Dugan & Flemings (2000a/b) report a lack of porosity reduction due to compaction, the fossil content reaches values of more than 60% (Table 24). In addition, Fig. 72 reveals the negative correlation of clay fraction and fossil content. This results in a further misinterpretation of the examined sediments. The model of Yang & Aplin (submitted) is only calibrated for sediments dominated by siliciclastic material and does not account for fossil related compaction features. This means that where the clay content points to a silt or sandy silt, the sediments would actually be better described as fossil ooze.

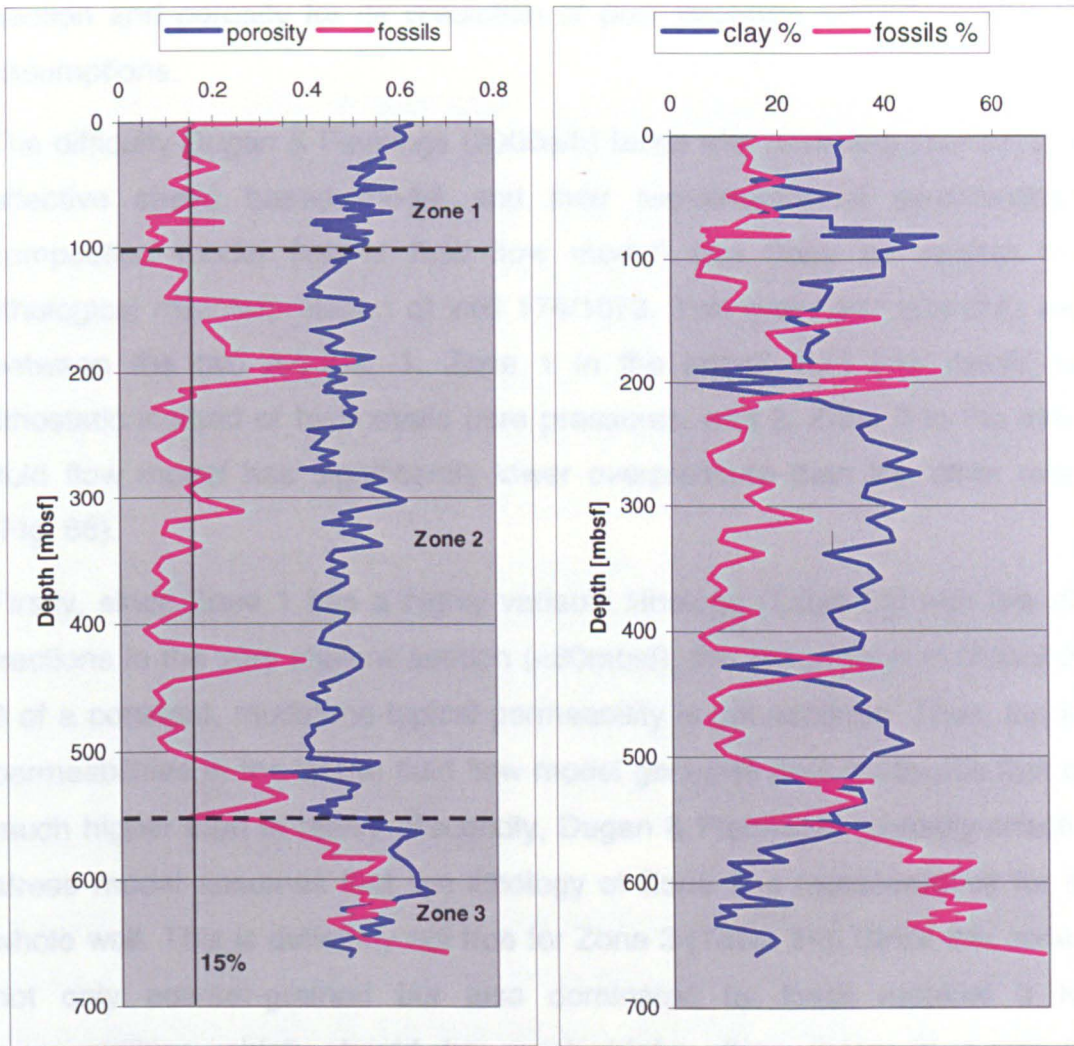


Fig. 72 (LHS) Correlation of porosity and fossil content measured on core material from site 174A/1073. The 15% line represents the value where the influence of fossil content on porosity becomes significant (Bryant & Rack, 1990). (RHS) correlation of fossil content and clay fraction.

4.3.2.4 Summary and Conclusions

In general, both Dugan & Flemings' (2000a/b) porosity-effective stress model and Yang & Aplin's (submitted) model for clay fractions between 30% and 40% predict near lithostatic to lithostatic pore pressures for most of well 174/1073. A major difference exists only for the pore fluid pressure predictions made by Yang & Aplin's (submitted) model for the shallow (<100mbsf) section. The reason for this difference is obvious, since Dugan & Flemings based their compaction model on the assumption that this interval is hydrostatically pressured. In contrast, Yang & Aplin's model only uses clay

fraction and porosity for its prediction of pore pressure without making any assumptions.

The difficulty Dugan & Flemings (2000a/b) faced with matching their porosity-effective stress based model and their two-dimensional sedimentation-compaction model (lateral fluid flow model) can likely be related to a lithological misinterpretation of well 174/1073. Two main discrepancies exist between the two models: 1. Zone 1 in the lateral fluid flow model has lithostatic instead of hydrostatic pore pressures, and 2. Zone 3 in the lateral fluid flow model has significantly lower overpressure than the other model (Fig. 66).

Firstly, since Zone 1 has a highly variable lithology (Table 24) with low clay fractions in the very shallow section (<60mbsf), the assumption in Model 2 & 3 of a constant, mudstone-typical permeability is not accurate. Thus, too low permeabilities in the lateral fluid flow model generate pore pressures that are much higher than in reality. Secondly, Dugan & Flemings's porosity-effective stress model assumes that the lithology of Zone 1 is representative for the whole well. This is definitely not true for Zone 3 (Table 24). Since this zone is not only coarser-grained but also dominated by fossil material it has permeabilities which should be much higher than those of a clay/silt dominated sediment (Bryant & Rack, 1990). As a consequence, Dugan & Flemings' compaction curve for Zone 1 does not represent the compaction behaviour of Zone 3 and presumably overestimates the pore pressure considerably.

Dugan & Fleming's (2000a/b) conclusion that the overpressures in Zone 3 and the lateral fluid flow regime could cause the cold seeps and slope failures observed by MacDonald et al., (1990) is still justified. Although the pore pressures predicted by their two-dimensional sedimentation-compaction model might be slightly higher than in reality, the proposed fossil content-related enhancement of permeability might lead to even higher down-slope flow rates of pore fluids (Fig. 66). These would then result in a similar way as the lithostatic pore pressures predicted by their porosity-effective stress model.

5 Conclusions

In general, the data of this study support previous compaction models (Skempton, 1970; Burland, 1990; Yang & Aplin, submitted) and the observation that grain size seems to be the single most important control on the mechanical compaction of fine-grained, siliciclastic sediments. Both mineralogy and geological age do not seem to affect the development of porosity with increasing effective stress. In this study, the effect of particle sorting could not be analysed but should be subject to future investigations.

The previously observed positive correlation between nannofossil content and porosity (e.g. Bryant & Rack, 1990; Kraemer, 2000) could be confirmed. This will help to understand porosity-effective stress trends with unexpectedly high porosities in shallow buried, clay-rich sediments. Furthermore, pore throat size distributions distinctly different to samples poor in fossil material also point to significant differences in physical properties like porosity and permeability of fossil-rich sediments.

The strong influence of grain size and fossil-content on the porosity-effective stress relationship of fine-grained sediments had important implications for the compaction study of the Mid-Norway and New Jersey case studies. It became clear that good quality grain size information and the consideration of the fossil content underpin a thorough compaction study of shallow buried formations.

Laboratory experiments conducted in this study confirmed, that air and oven drying significantly alters the pore volume-related physical properties of soft, clay-rich sediments. It is therefore very important to ensure that samples of shallow buried, clay-rich siliciclastics are preserved wet if porosity and pore size distribution data are to be meaningful.

Part B

6 Samples and Methods

Although extensive work has been done to examine the fabric of argillaceous rocks (references see next chapter) little is known about the effects of clay fabric development on sediment compaction (i.e. the reduction of porosity with increasing effective stress). Since previous studies focused mainly on the qualitative description of clay mineral fabric, a systematic, quantitative approach to describe the fabric development during sediment compaction remains to be established.

The objective of this study is

- to quantify the clay mineral fabric of phyllosilicate-rich rocks from various sedimentary basins around the world using the High Resolution X-ray Texture Goniometry approach (Van der Pluijm et al. 1994; Ho et al., 1999)
- to determine the physical properties (e.g. porosity, pore size distribution, grain size) of these sediments and to relate them to the fabric
- to determine the diagenetic grade (for clay minerals) of the samples and to establish whether systematic relationships exist between fabric, compaction and diagenesis

6.1 High Resolution X-ray Texture Goniometry: Background

The orientation of clay minerals in sediments and sedimentary rocks has been at the centre of research in various fields of geoscience. One application is the use of phyllosilicate orientation in sedimentary and metamorphic rocks as an indicator for cleavage development and tectonic strain in structural geology (Turner and Weiss, 1963; Oertel, 1970, 1983; Oertel et al., 1989; Lee et al., 1985, 1986; van der Pluijm & Kaars-Sijpensteijn, 1984; van der Pluijm et al., 1998; Holeywell & Tullis, 1975; Ramsey and Huber, 1983; Ho et al., 1995, 1996, 2001; Jacob et al., 2000). Another is the application of the same principles to the investigation of the mineralogical changes during diagenesis and low-grade metamorphism (Ahn & Peacor, 1986; Freed & Peacor, 1989, Merriman et al., 1990; Li et al., 1994).

The third group of studies has utilized the degree of clay mineral orientation for the analysis of sediment compaction, i.e. the development of physical properties with increasing effective stress (Meade, 1963, 1966; Bowles et al., 1969; Oertel & Curtis, 1972; Curtis et al. 1980; Sintubin, 1994; Ho et al., 1999; Jacob et al., 2000).

These investigations share the common premise that at deposition most clay minerals are randomly oriented (O'Brien, 1970; O'Brien & Slatt, 1990). Any measurable preferred orientation (or change in preferred orientation in the case of cleavage development) must therefore be caused subsequently by either compactional (overburden) or tectonic stress (e.g. Holeywell & Tullis, 1975; van der Pluijm & Kaars-Sijpensteijn, 1984). At later stages, during the transformation of mudstones into shales and slates, increasing temperatures and stresses induce mineralogical processes, which also lead to extended levels of preferred orientation (Ramsey and Huber, 1983; Ho et al., 1995, 1996, 1999, 2001; van der Pluijm et al. 1998; Jacob et al., 2000).

Over the last 40 years various methods have been developed to determine the degree of clay particle alignment. Meade (1961) described a way to use ratios of X-ray diffraction peak intensities to obtain information about clay mineral orientation. For this method, sections of three orthogonal cuts (parallel to bedding and orthogonal to bedding) of a sample had to be prepared very carefully. In 1969 Baker et al. used an X-ray goniometer in transmission mode to examine the preferred orientation in clay-rich sediments. This technique was later applied and improved by Oertel (1970, 1983), Wood et al. (1976), O'Brien et al. (1987) and Sintubin (1994). One limitation of this method was that only large (tens of mm²) sample areas could be analysed. Van der Pluijm et al. (1994) tried to overcome this problem by developing High Resolution X-ray Texture Goniometry (HRXTG). This method "is able to record variations in the strain state of deformed (compacted) rocks over small, mm-scale distances" (van der Pluijm et al., 1994). Since then, several publications have demonstrated the capabilities of the new methodology (Ho et al., 1995, 1996, 1999; van der Pluijm et al. 1998, Jacob et al. 2000).

6.2 Sample set

Ho et al.'s (1999) key study about the use of High Resolution X-ray Texture Goniometry to quantify changes in the fabric of mudstones during diagenesis concentrated on a single well in onshore Gulf of Mexico. For the verification of the general applicability of the HRXTG method for compaction studies more samples from different locations were needed. In order to represent a wide range of effective stresses (burial depths), depositional environments and lithologies (grain sizes) samples from various sedimentary systems around the world were chosen for analysis. These include deep sea samples from the Central Bermuda Rise (DSDP well 43/386) and cutting and core samples from the North Sea, Mid-Norway, Caspian Sea, deep water Gulf of Mexico and Bay of Bengal (Table 25).

6.2.1 Well 43/386 Central Bermuda Rise

12 samples from the Central Bermuda Rise were chosen for the analysis by HRXTG. Sample details are listed in Table 25. For more information on this sample set see chapter 2 **Sample locations**.

6.2.2 North Viking Graben (North Sea): NVG

Samples from several wells were chosen to represent mudstones from various depths of the Viking Graben (Fig. 55). The sampled depths range from 2047mbsf to 4435mbsf (Table 25). All of the 8 samples were taken from conventional, unpreserved core material. Most of the samples are from mid Jurassic formations within the deltaic Brent Group or from the underlying marine Drake or Dunlin Formation.

6.2.3 Central Viking Graben: CVG

4 core samples of a red marine mudstone sequence from the Central Viking Graben were analyzed in this study. The samples are from three wells, covering depths between 1565mbsf 1848mbsf (Table 25). The water depths at the drilling sites were about 125m.

6.2.4 Mid-Norway area: MN

A set of 5 cutting samples was chosen from marine Tertiary and Cretaceous formations in one well from the Mid-Norway area (Fig. 55, Table 25). The water depth at the well location was about 330m. The sample depths ranges from 812mbsf to 2499mbsf.

6.2.5 Bay of Bengal: BB

The sampled well is located in the Bay of Bengal (South East Asia) in a water depth of about 15m. Five mudstone cuttings samples were taken from burial depths between 1270m and 3495m (Table 25). The well was drilled into a succession of Tertiary deltaic sediments.

6.2.6 Caspian Sea: CS

Four samples were taken from a well located in the southern Caspian Sea. The examined core material comes from a deeply buried (4863mbsf to 5383mbsf, Table 25), lacustrine sedimentary section from a well drilled in a water depth of about 350m.

6.2.7 Deep water Gulf of Mexico: Panis, Ikon, Diva

A total of 50 samples from three wells in the deep water Gulf of Mexico were examined in this study. A first screening of these samples revealed that only about 30 were of a quality suitable for HRXTG measurements. The excluded samples mainly comprise cutting samples which were either severely damaged by the drilling process or too soft for the sample preparation necessary for HRXTG.

The water depths at the three well locations range from 1730 to 2030 meters, the sampled sections cover 895mbsf to 6041mbsf (Table 25). The sample set was comprised of 14 dry cuttings (Panis), 22 wet (canned) cuttings (Ikon & Diva), 5 side wall cores (Ikon & Diva) and 9 conventional core samples (Ikon & Diva). All samples are of Tertiary age.

Ikon and Diva are within a few kilometers of each other and are therefore often combined to represent a single virtual well.

Well	Burial depth [mbsf]	Sample type	Well	Burial depth [mbsf]	Sample type
lkon	2529	cutting	Panis	895	cutting
lkon	2685	cutting	Panis	1444	cutting
lkon	2840	cutting	Panis	2175	cutting
lkon	2986	cutting	Panis	2541	cutting
lkon	3142	cutting	Panis	2724	cutting
lkon	3297	cutting	Panis	2907	cutting
lkon	3453	cutting	Panis	3090	cutting
lkon	3599	cutting	Panis	3263	cutting
lkon	3745	cutting	Panis	1633	cutting
lkon	3901	cutting	Panis	1816	cutting
lkon	4126	cutting	Panis	1999	cutting
lkon	4128	core	Panis	3370	cutting
lkon	4321	swc	Panis	3553	cutting
lkon	4418	core	Panis	3644	cutting
lkon	4660	cutting	NVG	1908	core
lkon	5133	core	NVG	2311	core
lkon	5282	cutting	NVG	2671	core
lkon	5420	swc	NVG	2687	core
lkon	5739	cutting	NVG	3410	core
lkon	5884	swc	NVG	3700	core
lkon	6041	cutting	NVG	4000	core
Diva	1515	cutting	NVG	4331	core
Diva	2392	cutting	CVG	1565	core
Diva	3481	cutting	CVG	1711	core
Diva	3746	cutting	CVG	1754	core
Diva	4477	cutting	CVG	1848	core
Diva	4849	cutting	MN	812	cutting
Diva	4855	swc	MN	1362	cutting
Diva	4945	core	MN	1487	cutting
Diva	5001	core	MN	2301	cutting
Diva	5428	cutting	MN	2499	cutting
Diva	5435	swc	43/386	153	core
Diva	5511	core	43/386	254	core
Diva	5516	core	43/386	336	core
Diva	5518	core	43/386	482	core
Diva	5647	core	43/386	505	core
Diva	5649	core	43/386	563	core
BB	1270	cutting	43/386	647	core
BB	2030	cutting	43/386	820	core
BB	2310	cutting	43/386	859	core
BB	3305	cutting	43/386	867	core
BB	3495	cutting	43/386	959	core

Table 25 The sample set chosen for HRXTG measurements (swc = side wall core).

6.3 High Resolution X-ray Texture Goniometry

X-ray texture goniometry is commonly used to determine the average crystallographic orientation of a large number of minerals grains over a sample area of tens of mm² (Oertel, 1983; Wenk, 1985; van der Pluijm et al., 1994). The output of these measurements is usually displayed in pole figure

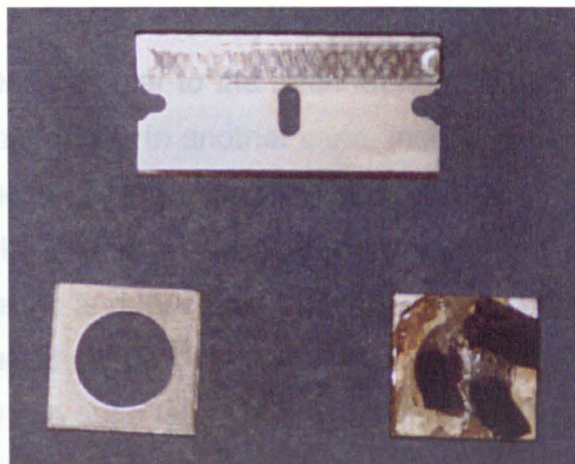
diagrams (Fig. 78). A pole figure is a stereogram showing the distribution of crystallographic orientations (lattice planes hkl), usually in the form of poles to crystallographic planes. For a statistical analysis the distributions are plotted on an equal-area diagram.

For High Resolution X-ray Texture Goniometry van der Pluijm et al. (1994) constructed an X-ray pole figure device for the Enraf-Nonius CAD4 automated single-crystal diffractometer (Fig. 75), equipped with an Mo source, which allows measurements of crystallographic orientations in transmission mode. A description of the technical details can be found in van der Pluijm et al. (1994). Compared to the older method, the advantages of this method are the use of thicker sections (200-400 μm) and small sample areas (< 1mm²).

6.3.1 Sample preparation

The first step is to prepare a thin section perpendicular to the main fabric direction of the sample material (Fig. 77). If it is not possible to determine a fabric direction with macro- or microscopic means (lens, binocular microscope) a cut perpendicular to the bedding plane should be used. The thin section should be between 200 μm and 400 μm thick (van der Pluijm et al., 1994). The grinding powder used for the preparation of the thin sections should be of 400 grit or finer.

The rock slabs are then detached from the glass slides and glued to an aluminium sample holder (Fig. 73) with super glue. Both sample surfaces should be free of any sticky wax left over from the thin section preparation. Any wax can be carefully removed with acetone prior to attachment to the sample holders.



sample holder

sample attached to holder

Fig. 73 Aluminium sample holder before and after attachment of the rock slab.

6.3.2 Measurements

The HRXTG analysis is a two step process. First, the samples are scanned over the range of 0.5-6.0 2θ Mo (1-13 2θ Cu). This is to validate the clay mineral phases present and to determine the exact diffraction angles for data collection (" 2θ -scan" in Ho et al., 1999; see Fig. 74). It is very helpful to use standard powder diffraction prior to these measurements to get an idea of the bulk mineralogy of the examined sample material.

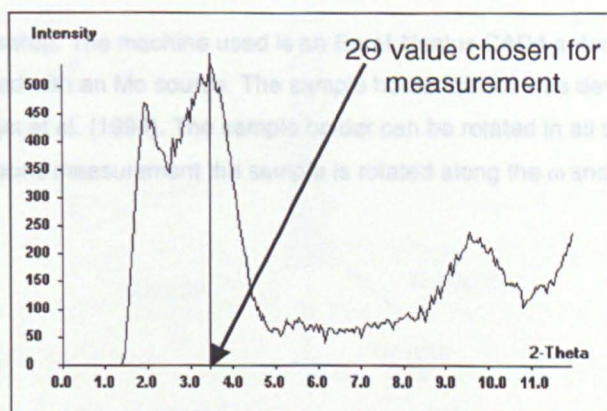


Fig. 74 Diffractogram resulting from a 2θ scan using a Mo source (2θ Cu $K\alpha = 2.1788 * 2\theta$ Mo - 0.0236).

The 2θ -scan gives a very good indication of whether the sample slab is aligned perpendicular to the predominant clay mineral fabric. Three explanations are possible if the 2θ diffractograms (Fig. 74) do not show

distinct peaks for any of the clay minerals present. In one case, the sample is not aligned perpendicular to the main fabric direction and therefore has to be cut at a different angle. In another case, insufficient numbers of clay minerals in the analyzed area of the sample fail to produce a signal strong enough to be detected. In a third scenario, the sample does not have a predominant clay mineral fabric and thus should not be analyzed by HRXTG any further. In order to validate the third case, the sample should be cut perpendicular to the first section to rule out a fabric in any other possible direction.

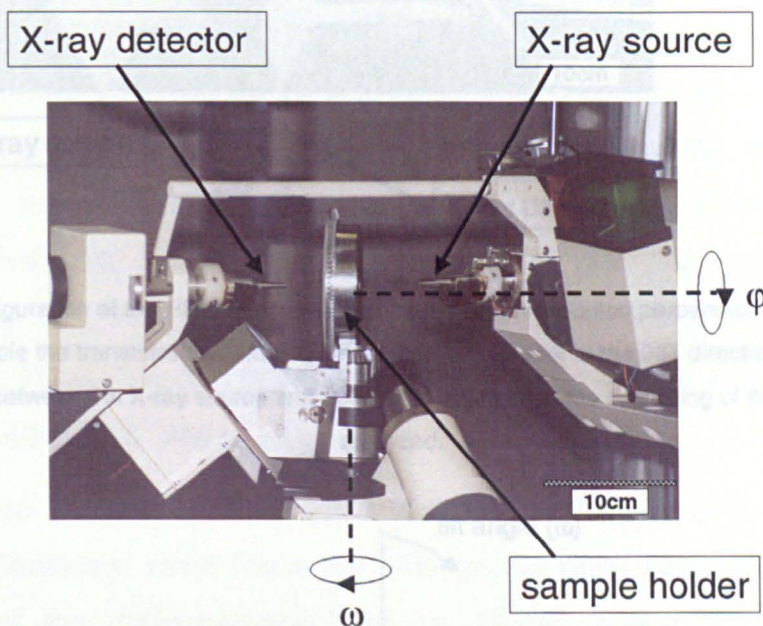


Fig. 75 HRXTG setup. The machine used is an Enraf-Nonius CAD4 automated single-crystal diffractometer equipped with an Mo source. The sample holder device was developed and described in detail by van der Pluijm et al. (1994). The sample holder can be rotated in all three dimensions. During the fabric measurement the sample is rotated along the ω and ϕ axes.

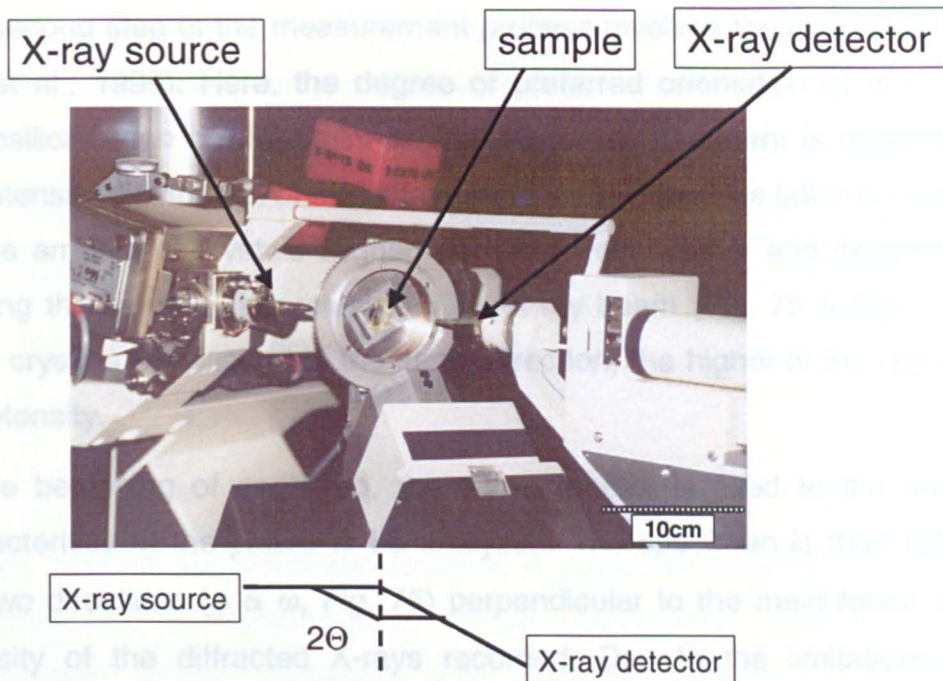


Fig. 76 Configuration of the HRXTG setup. The sample slab is mounted perpendicular to the X-ray source to enable the transmission diffraction measurement parallel to the 001 direction (Fig. 77). The angle (2θ) between the X-ray source and detector is adjusted to the d-spacing of the phase to be analyzed.

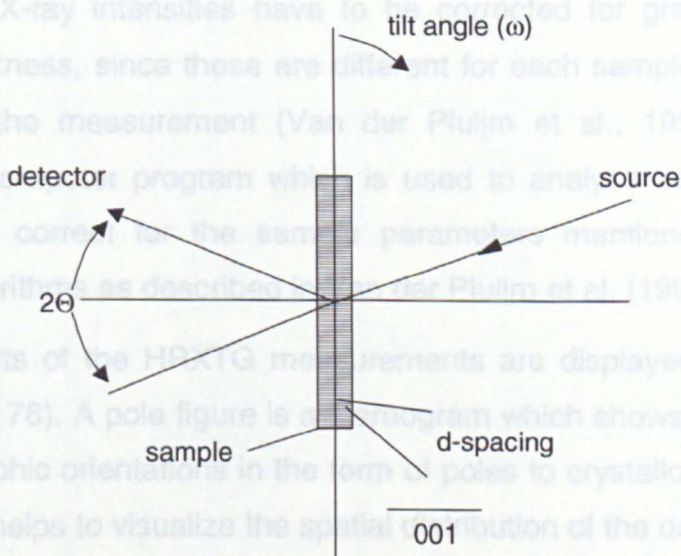


Fig. 77 Geometry of the X-ray transmission diffraction setup. The sample is cut perpendicular to the 001 direction (i.e. fabric) of the analyzed phyllosilicates. The generated X-rays (source) pass through the sample and are diffracted at the 001 crystal planes of the examined phase. The more crystals are aligned in the same direction, the higher is the intensity of the diffracted X-ray beams that reach the detector.

The second step of the measurement process involves the "pole-figure scan" (Ho et al., 1999). Here, the degree of preferred orientation of any present phyllosilicate can be determined. The degree of alignment is obtained from the intensity distribution of the diffracted X-ray beams. The latter is dependent on the amount of crystals aligned parallel to each other and determined by rotating the sample slab relative to the X-ray beam (Fig. 75 & Fig. 77). The more crystals are aligned in the same direction, the higher is the resulting X-ray intensity.

At the beginning of each run, the diffractometer is fixed to the d-spacing characteristic of the phase to be analyzed. The specimen is then rotated in the two directions (φ & ω , Fig. 75) perpendicular to the main fabric and the intensity of the diffracted X-rays recorded. Due to the limitations of the apparatus (van der Pluijm et al., 1994) the samples can only be rotated between 0° and 40° . This leads to the blank areas in the resulting pole figures (Fig. 78). Diffraction intensity data is collected every 2.5° ($0-360^\circ$) for angles of $0-40^\circ$ (in 5 steps).

The obtained X-ray intensities have to be corrected for grain density and specimen thickness, since these are different for each sample and influence the result of the measurement (Van der Pluijm et al., 1994). Ho (1996) developed a computer program which is used to analyse the HRXTG data and allows to correct for the sample parameters mentioned above. The correction algorithms as described in Van der Pluijm et al. (1994).

The final results of the HRXTG measurements are displayed in pole figure diagrams (Fig. 78). A pole figure is a stereogram which shows the distribution of crystallographic orientations in the form of poles to crystallographic planes. In this case it helps to visualize the spatial distribution of the determined X-ray intensities, i.e. it displays contour lines representing the distribution of phyllosilicate 001 orientations. The degree of particle alignment is expressed as maximum pole density in multiples of a random distribution [m.r.d.] where higher values reflect higher degrees of alignment (Fig. 78).

Investigations by Ho et al. (1995, 1996, 1999, 2001) and Jacob et al. (2000) as well as measurements from this study revealed that typical maximum pole densities for sedimentary rocks are:

<1.8 m.r.d. no/very weak fabric

2-3 m.r.d. weak fabric

3-4 m.r.d. moderate fabric

4-5 m.r.d. strong fabric

>5 m.r.d. very strong fabric.

Studies by Ho et al. (1996) and Jacob et al. (2000) also showed, that incipient metamorphism at temperatures above 180°C can lead to cleavage development where maximum pole densities exceed 12-16m.r.d. An extremely strong fabric has been determined by John Solum (pers. com.) for a biotite single crystal, yielding a value of 45 m.r.d. (pole figure g in Fig. 78).

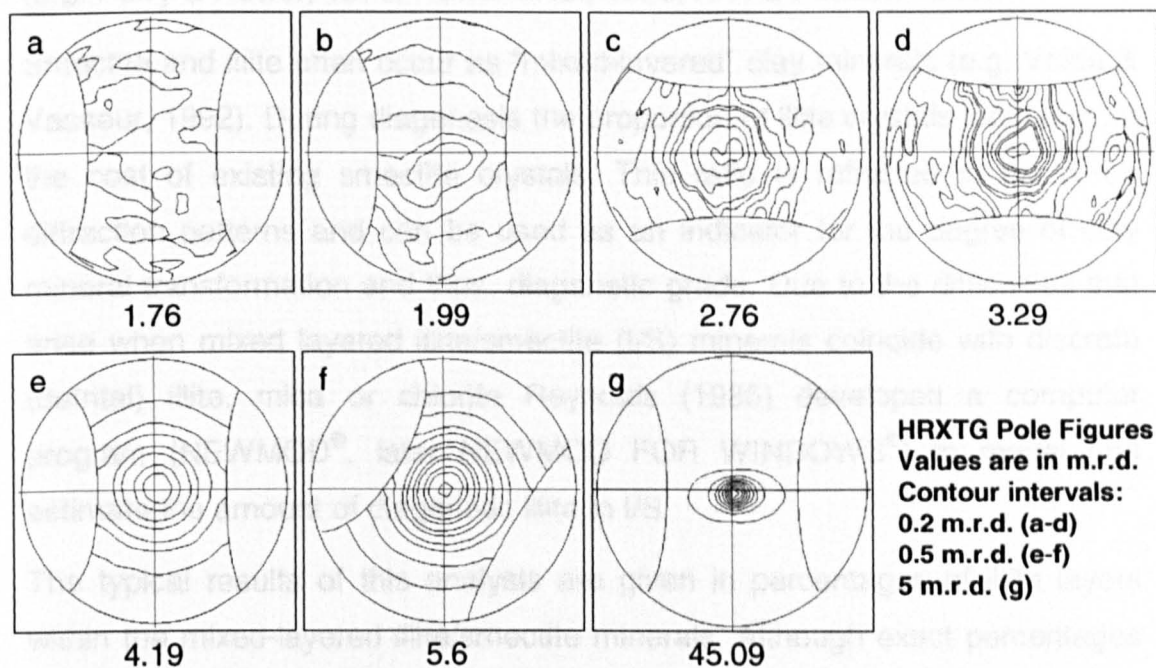


Fig. 78 HRXTG pole figures for different degrees of phyllosilicate alignment. Samples a-f represent clay-rich lithologies sampled in this study. Pole figure g was obtained by John Solum (pers. com.) at the University of Michigan during the fabric analysis of a biotite single crystal.

6.4 Mineralogy

The bulk mineralogy of all samples was determined by X-ray diffraction (**2 Samples and Methods**). In addition to the whole rock measurements the <2 μm fractions of most samples were separated and analyzed by XRD. Here, both air-dried and glycolated samples were examined. In order to generate oriented clay mineral aggregates the specimens were prepared applying a procedure similar to the "Millipore[®] Filter Transfer Method" described by Moore & Reynolds (1997).

6.5 Clay mineral diagenesis

Based on the method described by Moore & Reynolds (1997) results of the X-ray diffraction analysis of the glycolated <2 μm fractions were used to obtain information about the diagenetic grade of the samples. The method takes advantage of the crystallographic changes that accompany the conversion of smectite into illite with increasing diagenetic maturity of clay rich sediments (e.g. Perry & Hower, 1970; Hower et al., 1976; Ahn & Peacor, 1986).

Smectite and illite often occur as "mixed-layered" clay minerals (e.g. Velde & Vasseur, 1992). During diagenesis the proportion of illite crystals increases at the cost of existing smectite crystals. This ratio is reflected in the X-ray diffraction patterns and can be used as an indicator for the degree of clay mineral transformation and thus, diagenetic grade. Due to the difficulties that arise when mixed layered illite/smectite (I/S) minerals coincide with discrete (detrital) illite, mica or chlorite Reynolds (1985) developed a computer program (NEWMOD[®], later NEWMOD FOR WINDOWS[®]) to model and estimate the amount of diagenetic illite in I/S.

The typical results of this analysis are given in percentages of illite layers within the mixed-layered illite/smectite minerals. Although exact percentages of illite and smectite can be determined by Transmission Electron Microscopy (e.g. Ahn & Peacor, 1986; Freed & Peacor, 1989; Masuda et al., 2001), XRD methods only yield ranges (10%, 30-40% etc.). Furthermore, a value for the *Reichweite* (Jadgozinski, 1949; Moore & Reynolds, 1997) will be given. The *Reichweite* describes the degree of ordering within a mixed-layered

illite/smectite crystal, i.e. *R0* stands for randomly mixed illite and smectite, *R1* for at least 50% illite in I/S and *R3* for 90-100% illite in I/S.

All values for illite in I/S listed in this study were derived using the XRD method.

6.6 Physical properties and total organic carbon content

Grain size, porosity (by mercury intrusion porosimetry), grain density and total organic carbon content were determined using the methods described in chapter 2 **Samples and Methods**.

7 Results

7.1 Grain size distribution/Clay fraction

The clay fractions displayed in Table 26 illustrate the sedimentological and lithological diversity of the chosen sample set.

The coarsest material belongs to the North Viking Graben sample set with clay fractions ranging from 13% to 41% and about 1-34% $>63\mu\text{m}$. These sediments can be best described as fine sandstones and siltstones. Samples from the Bay of Bengal range in clay fraction between 26% and 35%, thus representing silt dominated lithologies.

Fine silt/siltstone and mud/mudstone comprise most of the sediments from the Gulf of Mexico and Caspian Sea. In the former province, samples from Ikon and Diva (Median = 39% $<2\mu\text{m}$) contain slightly lower clay fractions than those from Panis (Median = 43% $<2\mu\text{m}$). The four Caspian Sea samples cover clay fraction from 26% to 53%.

Samples from the Mid-Norway well are dominated by mudstones (51% to 59% $<2\mu\text{m}$). An additional siltstone (33% $<2\mu\text{m}$) and claystone sample (67% $<2\mu\text{m}$) complete this sample set.

Red shales from the Central Viking Graben and deep sea clays from the Central Bermuda Rise represent the fine-grained end of the data set. The measured clay fractions range from 58% to 85% $<2\mu\text{m}$ (Median = 74% $<2\mu\text{m}$) and 31% to 85% $<2\mu\text{m}$ (Median = 67% $<2\mu\text{m}$), respectively.

Well	Depth [mbsf]	Temp.[°C]	Clay fraction	Well	Depth [mbsf]	Temp.[°C]	Clay fraction
Panis	1444	33	45	Ikon	5420	111	44
Panis	1633	37	40	Ikon	5739	115	30
Panis	1816	40	39	Ikon	5884	116	40
Panis	2299	51	44	Ikon	6041	118	40
Panis	2541	56	47	Central Viking G.	1565	73	85
Panis	2907	64	43	Central Viking G.	1711	79	58
Panis	3090	67	41	Central Viking G.	1754	81	82
Panis	3263	71	39	Central Viking G.	1848	85	65
Panis	3553	77	43	North Viking G.	1908	76	13
Diva	1515	33	46	North Viking G.	2311	90	22
Diva	2392	60	46	North Viking G.	2671	103	31
Diva	3481	88	40	North Viking G.	2687	104	38
Diva	4477	110	39	North Viking G.	3410	130	21
Diva	4849	117	35	North Viking G.	3700	140	19
Diva	4855	117	36	North Viking G.	4000	151	20
Diva	5001	120	49	North Viking G.	4331	163	41
Diva	5428	127	36	Mid-Norway	812	32	33
Diva	5435	127	39	Mid-Norway	1362	52	67
Diva	5511	128	37	Mid-Norway	1487	57	58
Diva	5516	128	33	Mid-Norway	2301	86	51
Diva	5518	128	60	Mid-Norway	2499	93	59
Diva	5647	130	22	Bay of Bengal	1270	56	35
Diva	5649	130	38	Bay of Bengal	2030	83	30
Ikon	2529	54	39	Bay of Bengal	2310	93	28
Ikon	2685	58	45	Bay of Bengal	3305	136	26
Ikon	2840	62	19	Caspian Sea	4863	124	53
Ikon	2986	66	48	Caspian Sea	4887	124	43
Ikon	3142	69	42	Caspian Sea	5280	134	26
Ikon	3297	73	42	Caspian Sea	5383	137	40
Ikon	3453	76	48	43/386	153	5 [†]	38
Ikon	3599	79	39	43/386	254	7 [†]	59
Ikon	3746	82	33	43/386	336	9 [†]	64
Ikon	3901	85	39	43/386	505	12 [†]	67
Ikon	4126	90	42	43/386	563	13 [†]	31
Ikon	4128	90	46	43/386	647	15 [†]	74
Ikon	4321	93	52	43/386	820	18 [†]	85
Ikon	4418	95	39	43/386	859	19 [†]	67
Ikon	4660	99	39	43/386	867	19 [†]	71
Ikon	5133	107	56	43/386	959	21 [†]	73
Ikon	5282	109	39				

Table 26 Clay fractions for the samples examined by HRXTG. ([†]) Based on information from ODP Leg

172

7.2 Grain density

In this study the grain densities of the Gulf of Mexico samples had to be determined for grain size and porosimetry measurements. For most of the remaining samples the grain and pore throat size distributions were already known from previous investigations (Table 27).

The grain densities of the three Gulf of Mexico wells were measured applying the pycnometer method described in chapter 2 **Samples and Methods**. The results of the measurements are listed in Table 27.

Well	Depth [mbsf]	Type	Gs	Well	Depth [mbsf]	Type	Gs
Panis	901	cutting	2.59	Diva	5428	cutting	2.625
Panis	1444	cutting	2.6	Diva	5435	swc	2.783
Panis	1633	cutting	2.65	Diva	5511	core	2.764
Panis	1816	cutting	2.62	Diva	5516	core	2.764
Panis	1999	cutting	2.63	Diva	5518	core	2.773
Panis	2175	cutting	2.55	Diva	5647	core	2.726
Panis	2541	cutting	2.56	Diva	5649	core	2.753
Panis	2724	cutting	2.67	Diva	6906	cutting	2.466
Panis	2907	cutting	2.58	NVG	1908	core	2.74
Panis	3090	cutting	2.64	NVG	2311	core	2.78
Panis	3263	cutting	2.66	NVG	2671	core	2.75
Panis	3370	cutting	2.63	NVG	2687	core	2.75
Panis	3553	cutting	2.68	NVG	3410	core	2.72
Panis	3644	cutting	2.66	NVG	3700	core	2.74
Ikon	2529	cutting	2.779	NVG	4000	core	2.73
Ikon	2685	cutting	2.755	NVG	4331	core	2.82
Ikon	2840	cutting	2.632	BB	1270	cutting	-
Ikon	2986	cutting	2.651	BB	2030	cutting	-
Ikon	3142	cutting	2.678	BB	2310	cutting	-
Ikon	3297	cutting	2.733	BB	3305	cutting	-
Ikon	3453	cutting	2.674	BB	3495	cutting	-
Ikon	3599	cutting	2.517	CS	4863	core	2.79
Ikon	3746	cutting	2.628	CS	4887	core	2.81
Ikon	3901	cutting	2.61	CS	5280	core	2.76
Ikon	4126	cutting	2.598	CS	5383	core	2.82
Ikon	4128	core	2.807	CVG	1565	core	-
Ikon	4321	swc	2.666	CVG	1711	core	-
Ikon	4418	core	2.766	CVG	1754	core	-
Ikon	4660	cutting	2.744	CVG	1848	core	-
Ikon	5133	core	2.771	43/386	151.97	core	2.798
Ikon	5282	cutting	2.558	43/386	252.94	core	2.946
Ikon	5420	swc	2.78	43/386	335.82	core	2.394
Ikon	5739	cutting	2.525	43/386	480.81	core	2.465
Ikon	5884	swc	2.752	43/386	502	core	2.53
Ikon	6041	cutting	2.62	43/386	562.96	core	2.586
Diva	1515	cutting	2.738	43/386	646.8	core	2.82
Diva	2392	cutting	2.708	43/386	818.22	core	2.758
Diva	3481	cutting	2.639	43/386	858.82	core	2.793
Diva	4477	cutting	2.46	43/386	865.05	core	2.76
Diva	4849	cutting	2.738	43/386	900.59	core	2.74
Diva	4855	swc	2.792	43/386	957.37	core	2.828
Diva	5001	core	2.788				

Table 27 Grain density data of the samples examined by HRXTG. Gs – grain density [g/cm^3]; swc – side wall core.

The density values range from 2.55g/cm^3 to 2.68g/cm^3 for Panis and from 2.46 g/cm^3 to 2.81 g/cm^3 for Ikon and Diva. The average grain densities are $2.62\pm 0.02\text{g/cm}^3$ and $2.69\pm 0.02\text{g/cm}^3$, respectively.

The extremely low grain densities ($<2.6\text{g/cm}^3$) of some of the Panis, Ikon and Diva samples are related to very high contents of organic carbon in the cuttings material (Table 34). This organic carbon originated from additives to the drilling mud and can be regarded as sample contamination.

7.3 Bulk mineralogy

The bulk mineralogies of the majority of the samples were determined by X-ray powder diffraction analysis. Due to a lack of sample material no powder XRD data could be collected for the Bay of Bengal samples. Instead, the results listed in Table 28 were obtained from the 2θ whole rock scans derived during HRXTG (**6 Samples and Methods**).

7.3.1 North Viking Graben

The North Viking Graben sample set is dominated by minerals typical for silt-rich siliciclastics. The major phases are quartz, kaolinite and illite/mica with smaller amounts of chlorite and feldspar (Table 28). Smectite is rare in relation to the other minerals.

Well	Depth [mbsf]	Sm	Cl	I/M	K	Qz	KFp	Plg	Cc	other
NVG	1908	o		xx	x	xx				
NVG	2311		x	xx	xx	xx				
NVG	2671		o	xx	xx	xx	o	o		
NVG	2687		o	xx	xx	xx	x	xx		
NVG	3410			xx	xx	xx	o	o		
NVG	3700		o	xx	xx	xx				
NVG	4000	o	o	xx	xx	xx				
NVG	4331			o	x	xx				
CVG	1565	xx		o	x	xx				
CVG	1711	xx		o	x	xx				
CVG	1754	xx			o	xx				
CVG	1848	x		o	x	xx				
MN	812			x	x	xx	x	x	xx	
MN	1362	x		x	xx	xx				
MN	1487			o	o	xx				
MN	2301		x	x	x	xx		x		
MN	2499	o	x	x	xx	xx		o		
BB*	1270			x	xx	xx				
BB*	2030			xx	xx	xx				
BB*	2310		x	xx	xx	xx				
BB*	3305			x	xx	xx				
BB*	3495		x	x	xx	xx				
CS	4863	o	xx	xx	x	xx		x	x	
CS	4887	o	o	xx	xx	xx		x	x	
CS	5280	o	o	xx	xx	xx		xx	x	
CS	5383	o	o	x	x	xx		x	x	
43/386	153	o		x	x	xx	o	o	xx	
43/386	254	xx		o	o	o	o	o	xx	
43/386	336	xx		o	o	x			xx	
43/386	505	x		x		xx			x	Zeo, Op
43/386	563	xx		o		xx			xx	Op
43/386	647	xx		xx	xx	xx			o	
43/386	820	xx		x	x	xx				
43/386	859			o	x	xx				
43/386	867	x		x	o	xx			xx	
43/386	959			x	x	xx				

Table 28 The main mineral constituents of the Viking Graben (NVG, CVG), Mid-Norway (MN), Caspian Sea (CS), Bay of Bengal (BB) and Bermuda Rise (43/386) samples. The data was obtained from whole rock powder XRD analyses and HRXTG (*). xx = abundant; x = common; o = rare; Sm = smectite; Cl = chlorite; I/M = illite/mica; K = kaolinite; Qz = quartz; KFp = K-Feldspar; Plg = plagioclase; Cc = calcite; Zeo = zeolite; Op = opal-a/ct.

7.3.2 Central Viking Graben

The higher clay fractions (Table 26) of the samples from the Central Viking Graben are reflected in their mineralogy. Smectite is an important component, besides quartz, kaolinite and illite/mica (Table 28).

7.3.3 Mid-Norway

The main constituents of the five samples from this well are very similar to those of the North Viking Graben. Quartz, kaolinite and illite/mica prevail, whereas chlorite and feldspar are common (Table 28). Calcite and smectite are comparatively rare.

7.3.4 Bay of Bengal

A detailed mineralogical analysis of the Bay of Bengal well was prohibited by a lack of sufficient sample material. Nevertheless, the transmission x-ray diffraction analysis (2 θ -scan) performed during the HRXTG measurements delivered a rough estimate of the main phases present (Table 28). These are for all samples quartz, kaolinite and illite/mica, with an occasional occurrence of chlorite.

7.3.5 Caspian Sea

The deeply buried silt and mudstones from the Caspian Sea show a distinctly different composition to those of the North Sea and Bay of Bengal (Table 28). Firstly, all four samples contain significant amounts of calcite and plagioclase, in addition to quartz. Furthermore, with illite/mica, kaolinite, chlorite and smectite all major clay minerals are common.

7.3.6 Central Bermuda Rise

The bulk mineralogy of the deep sea sequences sampled at the Central Bermuda Rise is different in several ways to that of the other regions studied here. In contrast to the dominance of quartz, illite/mica and kaolinite, there are higher abundances of minerals like calcite, opal-a and zeolites. The prevailing clay mineral is smectite, and feldspars occur in trace amounts in the shallowest samples.

Well	Depth*	Sm	I/M	K	Qz	KFp	Plg	Ba	Cc	Do	other
Panis	901	xx	x	x	xx	x	x		xx		P
Panis	1444	xx	x	x	xx	o	xx		xx	xx	
Panis	1633	xx	x	xx	xx	o	xx	x	xx		P, Ap
Panis	1816	xx	xx	xx	xx	x	xx	o			P
Panis	1999		o	o	xx	x	xx	x			Ah,P
Panis	2175	xx	x	o	xx	o	o		xx	x	
Panis	2541	xx	x	x	xx	o	o	x	x		
Panis	2724	o	x	x	xx	o	xx	xx	x		G
Panis	2907		xx		xx				x		Ap, Op
Panis	3090	x	x	x	xx	o	o	o	xx		P
Panis	3263	xx	xx	xx	xx	x	o	xx	x		
Panis	3370		xx	xx	xx	o	o	o	xx		
Panis	3553		xx	xx	xx	x	x	x			Ap, P
Panis	3644		o	o	xx	o	o	o			

Table 29 The main mineral constituents of Panis. The data was obtained from whole rock powder XRD analyses. xx = abundant; x = common; o = rare; Sm = smectite; I/M = illite/mica; K = kaolinite; Qz = quartz; KFp = K-Feldspar; Plg = plagioclase; Ba = barite; Cc = calcite; Ap = apatite; Do = dolomite; Ah = anhydrite; G = goethite; P = pyrite; Op = opal-a/ct; (*) in [mbsf].

7.3.7 Gulf of Mexico: Panis

The mineral composition of the cutting samples from the Panis well in the Gulf of Mexico shows noticeable differences to those of the wells described above. Although quartz, illite/mica, kaolinite and smectite are the dominant phases, calcite, K-feldspar and plagioclase are very common and minerals like dolomite, apatite and pyrite are also frequently present (Table 29). The abundance of barite in several samples illustrates the degree of contamination caused by additives to the drilling mud.

7.3.8 Gulf of Mexico: Ikon & Diva

The XRD results for Ikon and Diva are very similar to those of the Panis well (Table 30). However, minerals like calcite, siderite and goethite are more common throughout the sample set. Widely occurring gypsum reveals the presence of evaporites in the drilled formations.

Well	Depth*	Sm	Cl	I/M	K	Qz	KFp	Plg	Ba	Cc	Ap	Do	G	Si	other
Ikon	2529	XX		XX	XX	XX	X			X	O		X	X	
Ikon	2685			X	O	XX	O	O		O	O	XXX	O	O	Ah
Ikon	2840			X	X	XX	X	X		XX	X	X	XX	X	H
Ikon	2986			XX	XX	XX	XX	X		O			O	O	
Ikon	3142			XX	XX	XX	X	XX		XX	O		XX	X	
Ikon	3297	XX		XX	X	XX	X	XX		X	O	O	X	X	
Ikon	3453	XX		XX	XX	XX	XX	X		XX	O	X	XX	X	
Ikon	3599			XX	XX	XX	X	X		XX	O		O	X	
Ikon	3745			X	X	XX	XX	XX		X	O		XX	X	H
Ikon	3901	XX		XX	XX	XX		XX	XX	X	O		XX	XX	
Ikon	4126			XX	XX	XX		O		X	O		XX	X	
Ikon	4128			XX	XX	XX		X		X	O		X		
Ikon	4321			XX	XX	XX	X	X		O	O		X	O	
Ikon	4418			XX	X	XX	XX	X		XX	X		XX		
Ikon	4660			XX	XX	XX			XX	XX	X		X	X	Zeo
Ikon	5133			XX	XX	XX	O	X		O	O		X	X	H
Ikon	5282			X	X	XX	O	X	X	X		XXX	X	X	P, Ah
Ikon	5420			XX	X	XX	X	X		X	O		XX	X	P, H
Ikon	5739			XX	XX	XX	X	X	XX	O	O		XX	X	
Ikon	6041			X	XX	XX		O	X	XX	X		X		
Diva	1515			XX	X	XX	X	X	O	O	O		X	O	
Diva	2392			XX	XX	XX	X	X		XX	O	O	X	X	P, H, Op
Diva	3481			XX	XX	XX	X	X		X			O	O	Op
Diva	3746			XX	XX	XX	X	XX	X	X	O		X		Op
Diva	4477			XX	XX	XX	O	O	XX	X	O		XX		P
Diva	4849			XX	XX	XX	O	X		X	O		X	X	
Diva	4855			XX	X	XX	X	XX		X	O		XX	X	P, H
Diva	5001			XX	XX	XX	XX	XX		X	O		X	X	
Diva	5428			XX	XX	XX	X	X	X	XX	O		X		
Diva	5435			X	XX	XX				XX			X	X	Op, H
Diva	5511			XX	X	XX	X	XX		X	O		XX	X	
Diva	5516			XX	XX	XX	X	X		X	O		XX	X	P, Str
Diva	5518			XX	X	XX	O	XX		X	O		XX	X	
Diva	5647			O	XX	XX	XX	XX	XX	X	O	O	XX	X	
Diva	5649a			O		XX	X	X		X	X		XX	X	
Diva	5649b			XX	XX	XX	XX	XX		X	X		XX	X	
Diva	6906			O	X	XX		XX		XXX			XX	X	

Table 30 The main mineral constituents of Ikon and Diva. The data was obtained from whole rock powder XRD analyses. XX = abundant; X = common; o = rare; Sm = smectite; Cl = chlorite; I/M = illite/mica; K = kaolinite; Qz = quartz; KFp = K-Feldspar; Plg = plagioclase; Ba = barite; Cc = calcite; Ap = apatite; Do = dolomite; Ah = anhydrite; H = hematite; G = goethite; P = pyrite; Si = siderite; Zeo = zeolite; Op = opal-a/ct; Str = strontianite (*) mbsf.

7.4 Clay mineralogy

7.4.1 North Sea, Mid-Norway, Caspian Sea & Bay of Bengal

Limited amounts of sample material restricted the detailed XRD analysis of the clay fraction to the samples listed in Table 31. Results of the analyses

show that in the case of the North Viking Graben (NVG) and Mid-Norway (MN) area the clay fraction of most samples is mainly comprised of detrital illite/mica, chlorite, kaolinite and quartz. Mixed layer illite/smectite is very rare in the silt dominated samples from the North Viking Graben and sparse in the slightly fine-grained samples from the Mid-Norway well.

Well	Depth [mbsf]	Temp. [°C]	Sm	I/M	K	Cl	Qz	other
NVG	1908	76		o	xx		o	
NVG	2311	90		o	xx		o	
NVG	3700	140	o	xx	xx		xx	
NVG	4000	151	o	xx	xx	o	xx	
NVG	4331	163		xx		xx	xx	
CVG	1711	79	xx	x	x	x	xx	
MN	812	32	x	x	x		x	x KFp, x CC
MN	2301	86		xx	xx	xx	xx	
MN	2499	93	o	x	xx	xx	xx	
BB	3495	136		xx		xx	xx	
CS	4863	124	o	xx	o	xx	xx	o CC
CS	5280	134	x	xx	x	x	xx	x CC

Table 31 Mineralogical compositions of the clay fraction (<2 μ m) of the North Sea, Mid-Norway, Caspian Sea and Bay of Bengal wells obtained from XRD analysis. XX = abundant; X = common; o = rare; Sm = smectite; Cl = chlorite; I/M = illite/mica; K = kaolinite; Qz = quartz; Cc = calcite; KFp = K-Feldspar.

One sample was chosen to represent the red claystones from the Central Viking Graben and revealed that the clay fraction is dominated by smectite, illite/mica and quartz.

The Bay of Bengal sample shows a similar composition to those from Mid-Norway and the North Viking Graben. Detrital illite/mica, chlorite and quartz prevail, whereas kaolinite and smectite are missing.

The clay fractions of both Caspian Sea samples are dominated by illite/mica and kaolinite with significant contents of quartz, chlorite, smectite and calcite.

7.4.2 Gulf of Mexico: Panis, Ikon & Diva

The mineralogical composition of the <2 μ m fraction of the three Gulf of Mexico wells are displayed in Table 32 & Table 33. In general, samples from both wells contain smectite, illite/mica, kaolinite and quartz as their main constituents. In contrast to Ikon and Diva, the cuttings samples from Panis also contain significant amounts of chlorite. All three wells show a sporadic occurrence of opal-A and calcite.

Well	Depth [mbsf]	Temp. [°C]	Sm	I/M	K	Cl	Qz	other
Panis	901	21	xx	xx	xx	xx	xx	
Panis	1444	33	xx	xx	xx	xx	xx	
Panis	1633	37	xx	xx	xx	o	xx	Op
Panis	1816	40	xx	xx	xx	xx	xx	Cc
Panis	1999	44	xx	xx	xx	xx	xx	
Panis	2175	48	xx	xx	xx	xx	xx	Cc
Panis	2541	56	xx	xx	xx	xx	xx	Cc
Panis	2724	60	xx	xx	xx		xx	Op
Panis	2907	64	xx	xx	xx	o	xx	
Panis	3090	67	xx	xx	xx	o	xx	
Panis	3263	71	xx	xx	xx	o	xx	Op
Panis	3370	73	xx	xx	xx	o	xx	
Panis	3553	77	xx	xx	xx	o	xx	
Panis	3644	79	xx	xx	xx	o	xx	

Table 32 The mineralogical composition of the Panis well clay fraction (<2 μ m) obtained from XRD analysis. XX = abundant; X = common; o = rare; Sm = smectite; Cl = chlorite; I/M = illite/mica; K = kaolinite; Qz = quartz; Cc = calcite; Op = opal-a.

Well	Depth [mbsf]	Temp. [°C]	Sm	I/M	K	Cl	Qz	other
Ikon	2529	54	xx	x	xx		xx	
Ikon	2685	58	xx	xx	xx		xx	
Ikon	2840	62	xx	xx	xx		xx	
Ikon	2986	66	xx	xx	xx		xx	
Ikon	3142	69	xx	xx	xx		xx	
Ikon	3297	73	xx	xx	xx		xx	
Ikon	3453	76	xx	xx	xx	o	xx	
Ikon	3599	79	xx	xx	xx		xx	
Ikon	3745	82	xx	xx	xx	o	xx	
Ikon	3901	85	xx	xx	xx	o	xx	
Ikon	4126	90	xx	xx	xx		xx	
Ikon	4128	90	xx	xx	xx		xx	
Ikon	4321	93	xx	xx	xx		xx	
Ikon	4418	95	xx	xx	xx		xx	
Ikon	4660	99	xx	xx	xx		xx	Cc
Ikon	5133	107	xx	xx	xx		xx	
Ikon	5282	109	xx	xx	xx		xx	
Ikon	5420	111	xx	xx	xx		xx	
Ikon	5739	115	xx	xx	xx		xx	
Ikon	6041	118	xx	xx	xx		xx	
Diva	1515	33	xx	xx	xx		xx	
Diva	2392	60	xx	xx	xx		xx	
Diva	3481	88	xx	xx	xx		xx	
Diva	3746	95	xx	xx	xx		xx	
Diva	4477	110	xx	xx	xx		xx	
Diva	4849	117	xx	xx	xx		xx	
Diva	4855	117	xx	xx	xx		xx	
Diva	5001	120	xx	xx	xx		xx	Cc, Op
Diva	5428	127	xx	xx	xx		xx	
Diva	5435	127	xx	xx	xx		xx	Op
Diva	5511	128	xx	xx	xx		xx	
Diva	5516	128	xx	xx	xx		xx	
Diva	5518	128	xx	xx	xx		xx	
Diva	5647	130	xx	xx	xx	o	xx	
Diva	5649b	130	xx	xx	xx	o	xx	
Diva	6906	145	xx	xx	xx	o	xx	

Table 33 The mineralogical composition of the Ikon and Diva clay fractions (<2µm) obtained from XRD analysis. XX = abundant; X = common; o = rare; Sm = smectite; Cl = chlorite; I/M = illite/mica; K = kaolinite; Qz = quartz; Cc = calcite; Op = opal-a.

7.5 Total organic carbon content (TOC)

The determination of the total organic carbon content (Table 34) revealed that most of the cutting samples were contaminated by organic additives to the drilling mud. Where possible (Panis), careful cleaning of the cuttings limited the contamination to relatively low levels. However, a comparison of the TOC levels typical of the cuttings (0.8-6%) and uncontaminated core samples (0.2-

0.5%) from Ikon and Diva indicated that the measured TOC values for Panis might still be too high by a factor of about 4.

The typical inorganic carbon contents on the other hand remain within a small range (0.2-1.8%) and do not reveal a bias towards any particular type of sample. A reason for the strong contamination of the cuttings from Ikon and Diva might be the way the samples are stored. The cuttings were taken immediately after drilling and put into metal cans together with the drilling mud. This permanent immersion in oil based drilling fluid could have led to the high levels (2.2% - 7.1%) of organic carbon measured in this study.

Well	Depth [mbsf]	Type	TOC [%]	TIC [%]	TC [%]
Panis	901	cutting	2.67	2.64	5.31
Panis	1444	cutting	0.76	1.61	2.37
Panis	1633	cutting	1.96	1.84	3.8
Panis	1816	cutting	1.60	2.78	4.38
Panis	1999	cutting	2.56	1.47	4.03
Panis	2175	cutting	2.36	1.51	3.87
Panis	2541	cutting	1.97	0.29	2.26
Panis	2724	cutting	2.20	0.57	2.77
Panis	2907	cutting	2.77	0.63	3.4
Panis	3090	cutting	1.38	0.73	2.11
Panis	3263	cutting	2.07	0.37	2.44
Panis	3370	cutting	1.98	0.83	2.81
Panis	3553	cutting	2.20	0.21	2.41
Panis	3644	cutting	1.95	0.60	2.55
Ikon	2529	cutting*	3.56	0.88	4.44
Ikon	2685	cutting*	3.02	0.57	3.59
Ikon	2840	cutting*	2.26	0.68	2.94
Ikon	2986	cutting*	3.27	0.24	3.51
Ikon	3142	cutting*	3.5	0	3.5
Ikon	3297	cutting*	3.03	0.13	3.16
Ikon	3453	cutting*	3.66	0.55	4.21
Ikon	3599	cutting*	7.07	1.45	8.52
Ikon	3745	cutting*	3.76	1.28	5.04
Ikon	3901	cutting*	4.47	0.96	5.43
Ikon	4126	cutting*	6.35	0.22	6.57
Ikon	4128	core	0.303	0.602	0.905
Ikon	4321	swc	2.28	0.33	2.61
Ikon	4418	core	0.996	0.284	1.28
Ikon	4660	cutting*	5.19	3.93	9.12
Ikon	5133	core	0.569	0.311	0.88
Ikon	5282	cutting*	5.02	0.21	5.23
Ikon	5420	swc	0.881	0.839	1.72
Ikon	5739	cutting*	6.03	0.68	6.71
Ikon	6041	cutting*	6.43	1.39	7.82
Diva	1515	cutting*	2.19	0.22	2.41
Diva	2392	cutting*	2.31	0.58	2.89
Diva	3481	cutting*	2.7	0.41	3.11
Diva	4477	cutting*	4.6	0	4.6
Diva	4849	cutting*	4.73	0.25	4.98
Diva	4855	swc	1.34	0.82	2.16
Diva	5001	core	0.524	0.536	1.06
Diva	5428	cutting*	5.11	1.11	6.22
Diva	5435	swc	0.567	1.173	1.74
Diva	5511	core	0.764	0.246	1.01
Diva	5516	core	0.465	0.45	0.915
Diva	5518	core	0.558	0.405	0.963
Diva	5647	core	0.183	1.767	1.95
Diva	5649a	core	0.289	0.084	0.373
Diva	5649b	core	0.587	0.171	0.758

Table 34 Total carbon (TC), organic carbon (TOC) and inorganic carbon (TIC) content of the Gulf of Mexico samples; * = canned (wet) cutting; a/b = silty/shaly.

7.6 Water content

Most of the examined samples in this study were comprised of dried out core chips and cuttings which made a determination of the total water content impossible. Only in case of two (Ikon & Diva) of the three Gulf of Mexico wells was the initial water content of many of the samples preserved. Although great care was taken to avoid the loss of pore water from the core material (wrapping in plastic and aluminium foil), only the water content of the canned cuttings was regarded as being close to the initial level (Table 35). This is of particular importance since experiments in this study (**2 Samples and Methods**) showed that air drying of soft, clay-rich material significantly alters their poroperm properties.

The determined water contents (weight %) for all Ikon and Diva samples are listed in Table 35. They range from as low as 2% in some of the cores and side wall cores to about 32% in the cuttings. As can be seen in Table 35, the water content of all cuttings is significantly higher than that of core material taken from adjacent sequences.

Well	Depth [mbsf]	Type	Water [wt%]	Water [vol%]
Diva	1515	cutting*	26	36
Diva	2392	cutting*	27	37
Diva	3481	cutting*	30	44
Diva	4660	cutting*	14	17
Diva	4855	swc	4	4
Diva	5001	core	5	6
Diva	5282	cutting*	20	25
Diva	5435	swc	3	3
Diva	5511	core	5	5
Diva	5516	core	4	4
Diva	5518	core	5	5
Diva	5647	core	2	2
Diva	5649	core	2	2
Diva	5739	cutting*	23	30
Ikon	2529	cutting*	24	31
Ikon	2685	cutting*	28	39
Ikon	2840	cutting*	17	20
Ikon	2986	cutting*	26	36
Ikon	3142	cutting*	20	26
Ikon	3297	cutting*	24	32
Ikon	3453	cutting*	28	39
Ikon	3599	cutting*	18	22
Ikon	3746	cutting*	18	22
Ikon	3901	cutting*	18	23
Ikon	4126	cutting*	19	23
Ikon	4128	core	6	7
Ikon	4321	dry swc	3	3
Ikon	4418	core	7	8
Ikon	4477	cutting*	32	47
Ikon	4849	cutting*	9	10
Ikon	5133	core	6	6
Ikon	5420	swc	3	3
Ikon	5428	cutting*	24	32
Ikon	5884	swc	2	2
Ikon	6041	cutting*	21	26
Ikon	6906	cutting*	12	14

Table 35 Water contents of the Gulf of Mexico well Ikon & Diva. swc = side wall core; * = canned cuttings; wt% = weight percent; vol% = volume percent.

7.7 Porosimetry

The total porosities and pore throat size distributions of most of the samples examined in this study were determined by mercury intrusion porosimetry (Table 36 & Table 37; see Appendix for figures). Results for the Central Bermuda Rise (43/386) were described in chapter 3 **Results** and it was concluded that drying during storage significantly altered the pore structure. Thus, only the total porosities determined gravimetrically by ODP were used for later analysis. A lack of useful sample material from the Mid-Norway well

prohibited any measurements from this site. The poor quality of the Ikon and Diva cuttings restricted the pore space analysis from these wells to core material.

Well/Sample	Depth [mbsf]	Type	MIP ϕ	w ϕ	Well/Sample	Depth [mbsf]	Type	MIP ϕ	w ϕ
Diva	1515	cutting*	0.5	0.52	Panis	901	cutting	0.19	-
Diva	2392	cutting*	0.38	0.53	Panis	1444	cutting	0.2	-
Ikon	2529	cutting*	0.36	0.49	Panis	1633	cutting	0.19	-
Ikon	2685	cutting*	0.52	0.55	Panis	1816	cutting	0.15	-
Ikon	2840	cutting*	0.43	0.38	Panis	1999	cutting	-	-
Ikon	2986	cutting*	0.57	0.51	Panis	2175	cutting	0.15	-
Ikon	3142	cutting*	0.41	0.44	Panis	2541	cutting	0.12	-
Ikon	3297	cutting*	0.47	0.49	Panis	2724	cutting	0.17	-
Ikon	3453	cutting*	0.52	0.54	Panis	2907	cutting	0.14	-
Diva	3481	cutting*	0.53	0.56	Panis	3090	cutting	0.18	-
Ikon	3599	cutting*	0.37	0.39	Panis	3263	cutting	0.15	-
Ikon	3746	cutting*	0.4	0.40	Panis	3370	cutting	0.16	-
Ikon	3901	cutting*	0.38	0.40	Panis	3553	cutting	0.21	-
Ikon	4126	cutting*	0.39	0.40	Panis	3644	cutting	0.19	-
Ikon	4128	core	0.22	0.19	43/386-4	151.97	core	-	0.46
Ikon	4321	swc	0.15	0.10	43/386-11	252.94	core	-	0.66
Ikon	4418	core	0.16	0.21	43/386-14	335.82	core	-	0.66
Diva	4477	cutting*	0.58	0.56	43/386-26	480.81	core	0.46	0.48
Ikon	4660	cutting*	0.33	0.35	43/386-28	502	core	0.47	0.42
Diva	4849	cutting*	0.21	0.25	43/386-32	562.96	core	0.41	0.48
Diva	4855	swc	0.17	0.14	43/386-36	646.8	core	0.3	0.43
Diva	5001	core	0.17	0.18	43/386-50	818.22	core	0.36	0.40
Ikon	5133	core	0.19	0.19	43/386-54	858.82	core	0.41	0.40
Ikon	5282	cutting*	0.47	0.42	43/386-55	865.05	core	0.37	0.44
Ikon	5420	swc	0.17	0.12	43/386-59	900.59	core	0.39	0.39
Diva	5428	cutting*	0.5	0.49	43/386-65	957.37	core	0.38	0.40
Diva	5435	swc	0.14	0.11	CS	4863	core	0.1	-
Diva	5511	core	0.13	0.15	CS	4887	core	0.11	-
Diva	5516	core	0.16	0.14	CS	5280	core	0.11	-
Diva	5518	core	0.15	0.16	CS	5383	core	0.11	-
Diva	5647	core	0.09	0.08	CVG	1565	core	0.24	-
Diva	5649	core	0.12	0.08	CVG	1711	core	0.28	-
Ikon	5739	cutting*	0.51	0.46	CVG	1754	core	0.25	-
Ikon	5884	swc	0.16	0.10	CVG	1848	core	0.2	-
Ikon	6041	cutting*	0.46	0.44	NVG	1908	core	0.27	-
Diva	6906	cutting*	0.27	0.29	NVG	2311	core	0.14	-
BB	1270	cutting	0.25	-	NVG	2671	core	0.12	-
BB	2030	cutting	0.2	-	NVG	2687	core	0.12	-
BB	2310	cutting	0.15	-	NVG	3410	core	0.06	-
BB	3305	cutting	0.15	-	NVG	3700	core	0.1	-
BB	3495	cutting	0.14	-	NVG	4000	core	0.06	-
					NVG	4331	core	0.11	-

Table 36 The porosities of the HRXTG sample set. MIP ϕ = total porosity from mercury intrusion porosimetry; w ϕ = total porosity from water content.

Well	Depth	Mode	Well	Depth	Mode
Panis	901	18	CVG	1565	8
Panis	1444	18	CVG	1711	7
Panis	1633	10	CVG	1754	10
Panis	1816	13	CVG	1848	5
Panis	1999	12	CS	4863	4
Panis	2175	10	CS	4887	4
Panis	2541	10	CS	5280	8 & 100
Panis	2724	8	CS	5383	5
Panis	2907	10	BB	1270	73
Panis	3090	10	BB	2030	52
Panis	3263	13	BB	2310	38
Panis	3370	12	BB	3305	-
Panis	3553	16	BB	3495	-
Panis	3644	20	NVG	1908	1474*
Diva	4855	9	NVG	2311	41*
Diva	5001	8	NVG	2671	4*
Diva	5435	8	NVG	2687	8*
Diva	5511	8	NVG	3410	3*
Diva	5516	10	NVG	3700	4*
Diva	5518	14	NVG	4000	5*
Diva	5647	7	NVG	4331	3*
Diva	5649	6			
Ikon	4321	9			
Ikon	4418	12			
Ikon	5133	12			
Ikon	5420	10			
Ikon	5884	6 & 26			

Table 37 Mode or mean (*) pore throat diameters [nm] of the sample set. Two values describe bimodal pore throat size distributions.

7.7.1 North Viking Graben

The core samples from the North Viking Graben range in total porosity between 6% and 27% (Table 36). The mean pore throat diameters span 1471nm, from 1474nm in the shallowest sample down to 3nm in the deepest sample (Table 37). The different magnitudes of these values reflect the diversity of the sampled lithologies: 13% clay fraction for the shallowest sample and 41% for the deepest sample.

7.7.2 Central Viking Graben

In contrast to the North Viking Graben the four samples from the Central Viking Graben show different features. Although the clay fractions (58-85%) and total porosities (20-28%, Table 36) vary significantly, the measured pore throat sizes are relatively similar. The absolute value for these mud- and claystones range from 5 to 10nm (Table 37).

7.7.3 Bay of Bengal

The porosities and mode pore throat sizes of the Bay of Bengal samples decrease with increasing depth from 25% at 1270mbsf to 14% at 3495mbsf and from 73nm to 38nm, respectively. Almost constant porosities between 15% and 14% were measured from 2310mbsf down to 3495mbsf (Table 36).

7.7.4 Caspian Sea

The relatively thin (520m) interval sampled from the Caspian Sea shows only insignificantly varying porosities between 10% and 11%. The observed mode pore throat sizes range between 4nm and 5nm for the sampled mudstones and between 8nm and 100nm for the examined siltstone sample.

7.7.5 Gulf of Mexico: Panis , Ikon & Diva

Several observations were made comparing the pore space analysis of Ikon and Diva core and cuttings samples:

- As displayed in Fig. 79 and Table 36 all cuttings yield higher porosities than any of the adjacent core samples. Although the lithologies and burial depths (effective stresses) are similar, both the mercury intrusion (MIP) and water content methods produced cuttings porosities which are often about twice as high as those of the core samples.
- The MIP results typical for the cuttings samples of Ikon and Diva are very different to those of the core samples. Fig. 80 illustrates, that mode pore throat sizes differ by 3 orders of magnitude between many of the cutting and core samples from Ikon and Diva.
- Elevated total organic carbon contents (Table 34) and resulting low grain densities revealed a high degree of contamination of the cuttings samples.
- Tool marks indicate an intensive mechanical deformation of the cuttings material during drilling.

Due to these fundamental differences all Ikon and Diva cuttings were regarded as low quality and thus excluded from any further pore space related analysis.

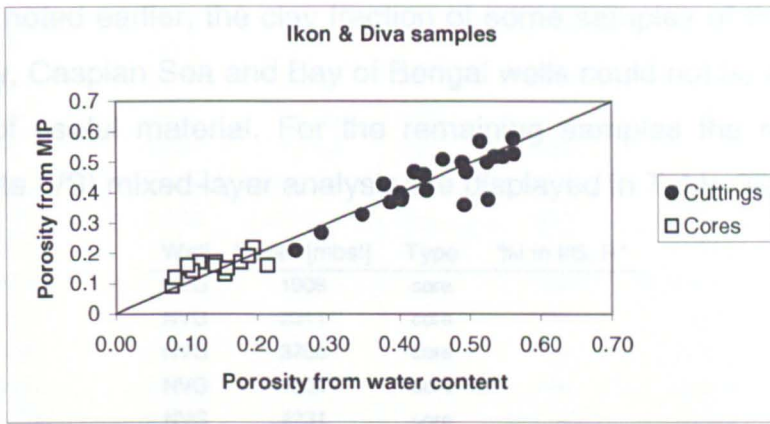


Fig. 79 Comparison of the porosities derived by mercury intrusion porosimetry (MIP) and sample drying (water content). Porosities of cuttings are significantly higher than those of the core samples.

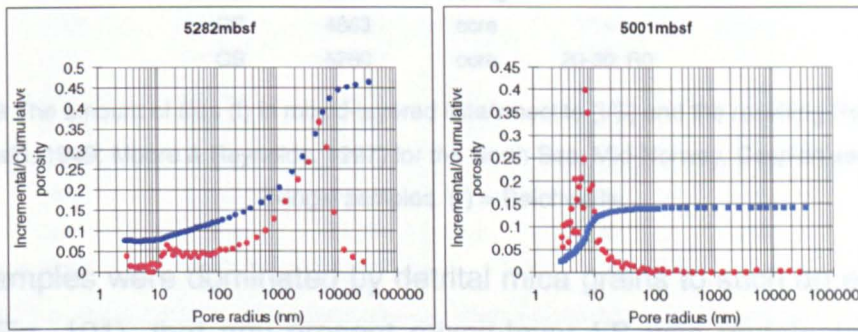


Fig. 80 Typical results of the mercury intrusion measurements for Diva and Ikon cutting (lhs) and core samples (rhs).

The absolute porosities for the Ikon and Diva core samples range from 9% at 5647mbsf to 22% at 4128mbsf (Table 36). The mode pore throat sizes range from 6nm to 26nm (Table 37).

The whole Panis sample set was comprised of nearly dried out cuttings, thus, no water content derived porosities were available for this well. The total porosities from MIP are displayed in Table 36 and range from 12% at 2541mbsf to 21% at 3553mbsf.

Since both MIP porosities and mode pore throat sizes in the range of 8nm to 20nm are in good agreement with those of the Ikon and Diva core material the Panis cuttings were regarded as good quality and thus useful samples.

7.8 Clay mineral diagenesis

7.8.1 North Sea, Mid-Norway, Caspian Sea & Bay of Bengal

As already noted earlier, the clay fraction of some samples of the North Sea, Mid-Norway, Caspian Sea and Bay of Bengal wells could not be analyzed due to a lack of useful material. For the remaining samples the results of the illite/smectite (I/S) mixed-layer analysis are displayed in Table 38.

Well	Depth [mbsf]	Type	%I in I/S, R*
NVG	1908	core	-
NVG	2311	core	-
NVG	3700	core	-
NVG	4000	core	-
NVG	4331	core	-
CVG	1711	core	30, R0
MN	812	cutting	10, R0
MN	2301	cutting	10, R0
MN	2499	cutting	-
BB	3495	cutting	-
CS	4863	core	-
CS	5280	core	20-30, R0

Table 38 The amount of illite (I) in mixed-layered illite/smectite (I/S) and the resulting Reichweite R (Jadgozinski, 1949; Moore & Reynolds, 1997) for the North Sea, Mid-Norway, Caspian sea and Bay of Bengal samples. (*) = Reichweite.

Many samples were dominated by detrital mica grains to such an extent (Fig. 100 & Fig. 101), that any present mixed-layer I/S was undetectable in the <2 μ m fraction. For the few North Sea samples where the amount of illite in I/S could be quantified the results reveal values of not more than 10% illite in I/S, representing a Reichweite (Jadgozinski, 1949; Moore & Reynolds, 1997) of R0. Samples of the Central Viking Graben and Caspian Sea reach illite percentages in I/S of up to 30% (R0).

7.8.2 Gulf of Mexico: Panis, Ikon & Diva

In all but 9 cases the analysis of the mixed-layered I/S minerals revealed early diagenetic grades for the Gulf of Mexico samples (Table 39). Illite in I/S in generally comprises 10% or less, with a resulting Reichweite of R0. All samples from Panis belong to this group. Only the deeper samples of Ikon and Diva reach grades where the amount of illite increases to 30-50% and 40-80%, respectively (Fig. 81).

In contrast to the pore space analysis the mineralogical observations for the Ikon and Diva cuttings agree very well with those for the core material, and thus were not excluded from this study.

Well	Depth [mbsf]	Type	%I in I/S, R**	Well	Depth [mbsf]	Type	%I in I/S, R**
Panis	901	cutting	±10, R0	Ikon	4128	core	±10, R0
Panis	1444	cutting	±10, R0	Ikon	4321	swc	±10, R0
Panis	1633	cutting	±10, R0	Ikon	4418	core	±10, R0
Panis	1816	cutting	±10, R0	Ikon	4660	cutting*	30, R0
Panis	1999	cutting	±10, R0	Ikon	5133	core	10-20, R0
Panis	2175	cutting	±10, R0	Ikon	5282	cutting*	±10, R0
Panis	2541	cutting	±10, R0	Ikon	5420	swc	±10, R0
Panis	2724	cutting	±10, R0	Ikon	5739	cutting*	10-20, R0
Panis	2907	cutting	±10, R0	Ikon	5884	swc	30, R0
Panis	3090	cutting	±10, R0	Ikon	6041	cutting*	50, R0
Panis	3263	cutting	±10, R0	Diva	1515	cutting*	±10, R0
Panis	3370	cutting	±10, R0	Diva	2392	cutting*	±10, R0
Panis	3553	cutting	±10, R0	Diva	3481	cutting*	±10, R0
Panis	3644	cutting	±10, R0	Diva	4477	cutting*	±10, R0
Ikon	2529	cutting*	±10, R0	Diva	4849	cutting*	±10, R0
Ikon	2685	cutting*	±10, R0	Diva	4855	swc	±10, R0
Ikon	2840	cutting*	±10, R0	Diva	5001	core	±10, R0
Ikon	2986	cutting*	±10, R0	Diva	5428	cutting*	±10, R0
Ikon	3142	cutting*	±10, R0	Diva	5435	swc	±10, R0
Ikon	3297	cutting*	±10, R0	Diva	5511	core	40, R0
Ikon	3453	cutting*	±10, R0	Diva	5516	core	40, R0
Ikon	3599	cutting*	±10, R0	Diva	5518	core	10, 40-50, R0
Ikon	3745	cutting*	±10, R0	Diva	5647	core	70, R1
Ikon	3901	cutting*	±10, R0	Diva	5649	core	80, R1
Ikon	4126	cutting*	±10, R0				

Table 39 The amount of illite (I) in mixed-layered illite/smectite (I/S) and the resulting Reichweite R (Jadgozinski, 1949; Moore & Reynolds, 1997). (*) = wet cuttings; (**) = Reichweite.

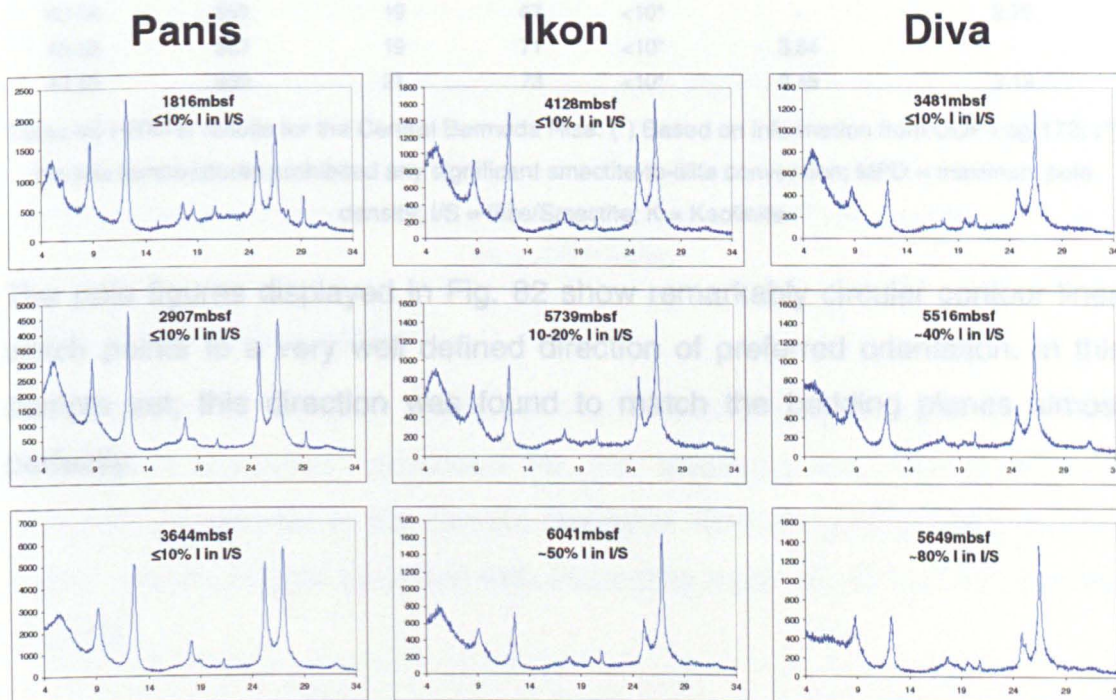


Fig. 81 XRD traces of the clay fraction of representative samples from Panis, Ikon and Diva. Values for illite in I/S were determined using NEWMOD© (Reynolds, 1985).

7.9 HRXTG

7.9.1 Central Bermuda Rise

The fabric analysis of the sediments from well 43/386 revealed a relatively wide range of preferred clay mineral orientation. The results (Fig. 82, Table 40) show slowly increasing maximum pole densities (MPD) with increasing burial depth. Weak illite/smectite (I/S) fabrics around 2m.r.d. at about 200mbsf change to moderate degrees (3.55m.r.d.) of alignment at around 950mbsf. A remarkably strong fabric for I/S (5.6m.r.d.) was observed in sample 43/36.

The samples containing enough kaolinite crystals for a HRXTG measurement confirm the trends observed for the I/S phases, although the kaolinite fabric is less well developed.

Sample	Depth [mbsf]	Temp.[°C] [†]	<2µm [%]	%I in I/S	I/S MPD [m.r.d.]	K MPD [m.r.d.]
43-4	153	5	38	<10*	2.51	2.06
43-11	254	7	59	<10*	1.93	1.69
43-14	336	9	64	<10*	2.86	-
43-28	505	12	67	<10*	2.89	-
42-32	563	13	31	<10*	3.32	-
43-36	647	15	74	<10*	5.6	5.35
43-50	820	18	85	<10*	3.7	-
43-54	859	19	67	<10*	-	2.75
43-55	867	19	71	<10*	3.64	-
43-65	959	21	73	<10*	3.55	3.19

Table 40 HRXTG results for the Central Bermuda Rise. (†) Based on information from ODP Leg 172; (*) the low temperatures prohibited any significant smectite-to-illite conversion; MPD = maximum pole density; I/S = Illite/Smectite; K = Kaolinite.

The pole figures displayed in Fig. 82 show remarkably circular contour lines which points to a very well defined direction of preferred orientation. In this sample set, this direction was found to match the bedding planes almost perfectly.

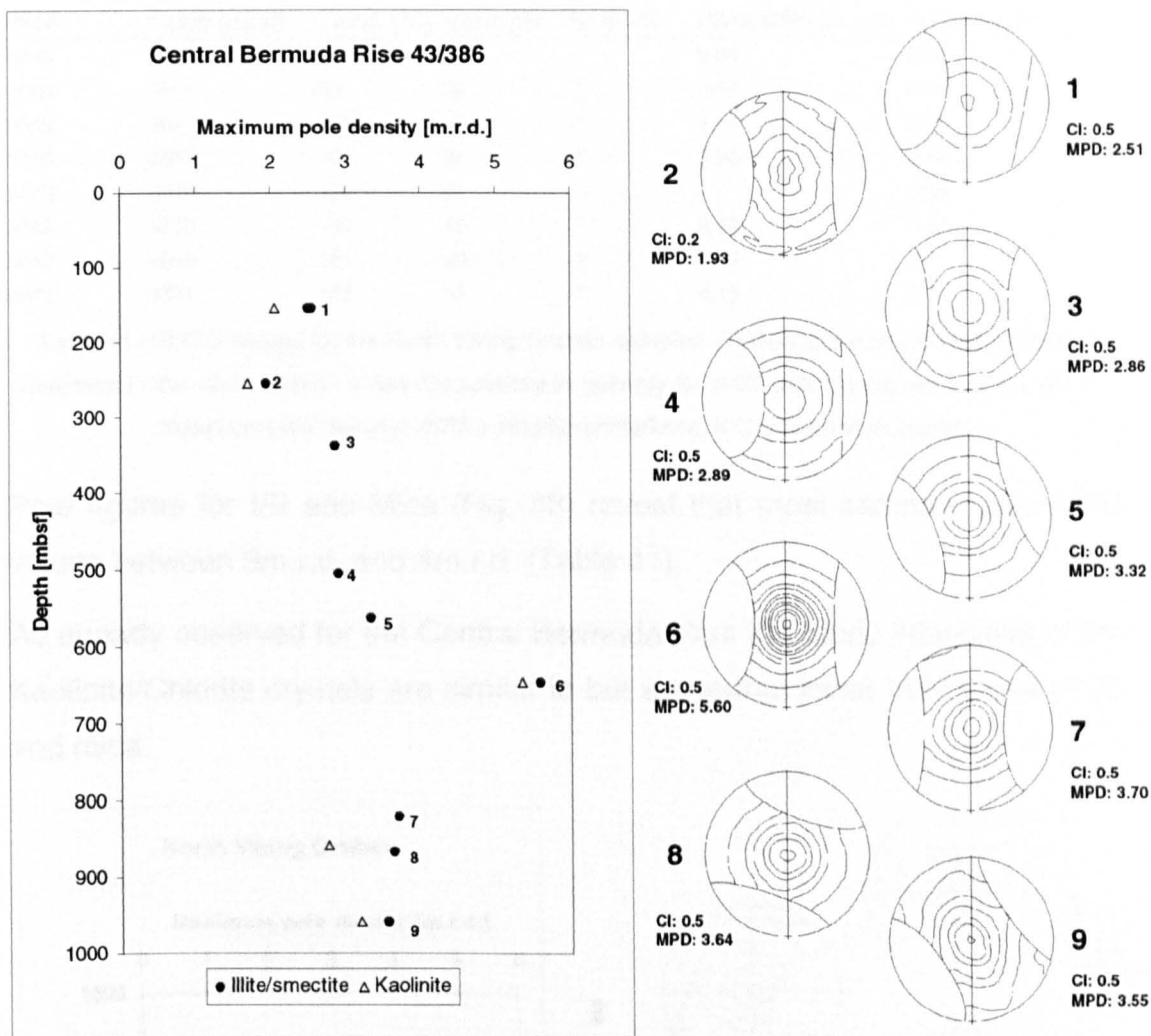


Fig. 82 The preferred orientation of clay minerals in a well (DSDP 43/386) drilled into the Central Bermuda Rise. • = value for the maximum pole density (MPD in [m.r.d.]) of illite/smectite 001 crystal surfaces; Δ = MPD value for Kaolinite; CI = contour interval [m.r.d.]. The pole figures (I/S phases) were rotated into the direction of the maximum intensity, which in the case of 43/386 is parallel/subparallel to the bedding plane.

7.9.2 North Viking Graben

The majority of samples from the North Viking Graben show moderate degrees of preferred orientation for I/S, illite/mica and kaolinite/chlorite. However, in contrast to the Central Bermuda Rise no general trend towards higher maximum pole densities with increasing burial depth can be observed (Fig. 83).

Well	Depth [mbsf]	Temp. [°C]	<2µm [%]	%I in I/S	I/S/M MPD [m.r.d.]	K/C MPD [m.r.d.]
NVG	1908	76	13	-*	3.68	3.34
NVG	2311	90	22	-*	3.08	2.62
NVG	2671	103	38	-*	3.71	3.78
NVG	2687	104	31	-*	3.34	2.85
NVG	3410	130	21	-*	-	2.59
NVG	3700	140	19	-*	2.63	2.57
NVG	4000	151	20	-*	3.16	2.7
NVG	4331	163	41	-*	4.19	3.11

Table 41 HRXTG results for the North Viking Graben samples. (*) Due to the dominance of detrital illite/mica in the <2µm fraction it was not possible to quantify %I in I/S with the applied method; MPD = maximum pole density; I/S/M = Illite/Smectite/Mica; K/C = Kaolinite/Chlorite.

Pole figures for I/S and Mica (Fig. 83) reveal that most samples yield MPD values between 3m.r.d. and 4m.r.d. (Table 41).

As already observed for the Central Bermuda Rise the fabric intensities of the Kaolinite/Chlorite crystals are similar to but somewhat lower than those of I/S and mica.

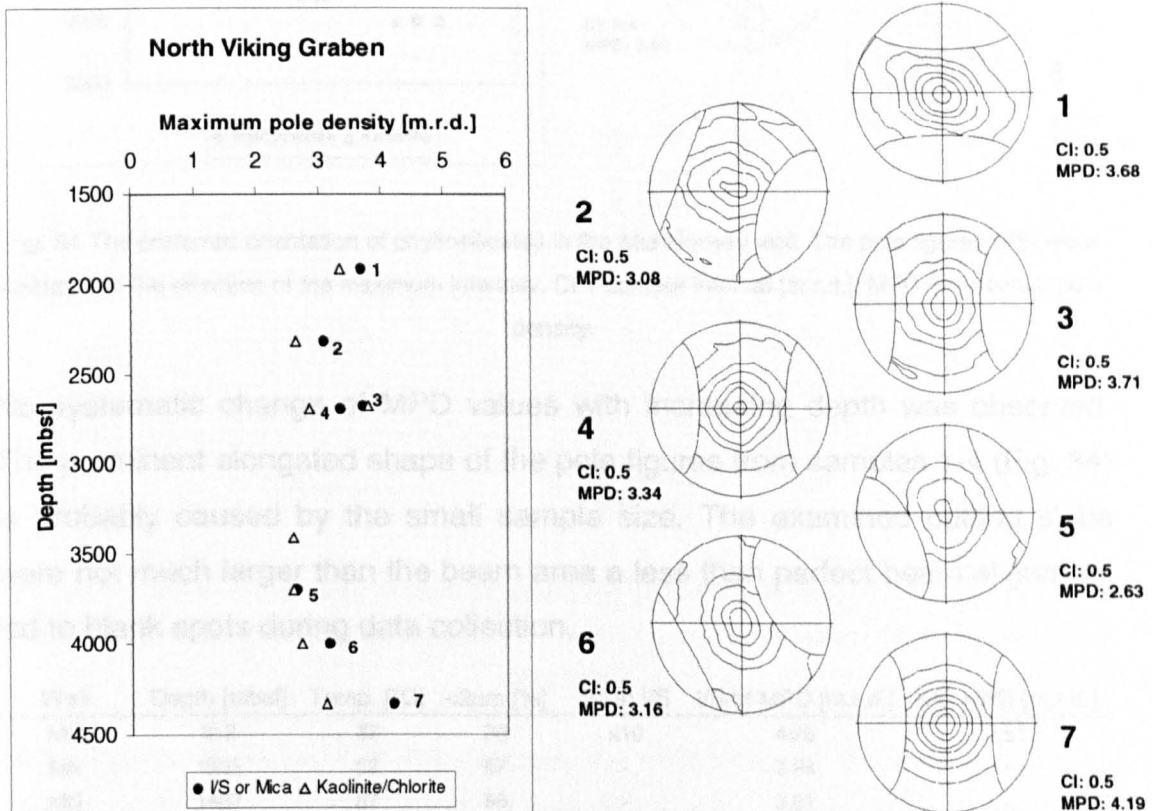


Fig. 83 The preferred orientation of phyllosilicates in the North Viking Graben. The pole figures (I/S & Mica) were rotated into the direction of the maximum intensity. CI = contour interval [m.r.d.]; MPD = maximum pole density.

7.9.3 Mid-Norway

The results of the HRXTG analysis of 5 cutting samples from a Mid-Norway well are displayed in Fig. 82 and Table 42. Maximum pole densities reveal that the examined phyllosilicates (I/S, illite/mica and kaolinite/chlorite) show moderate to strong degrees of alignment.

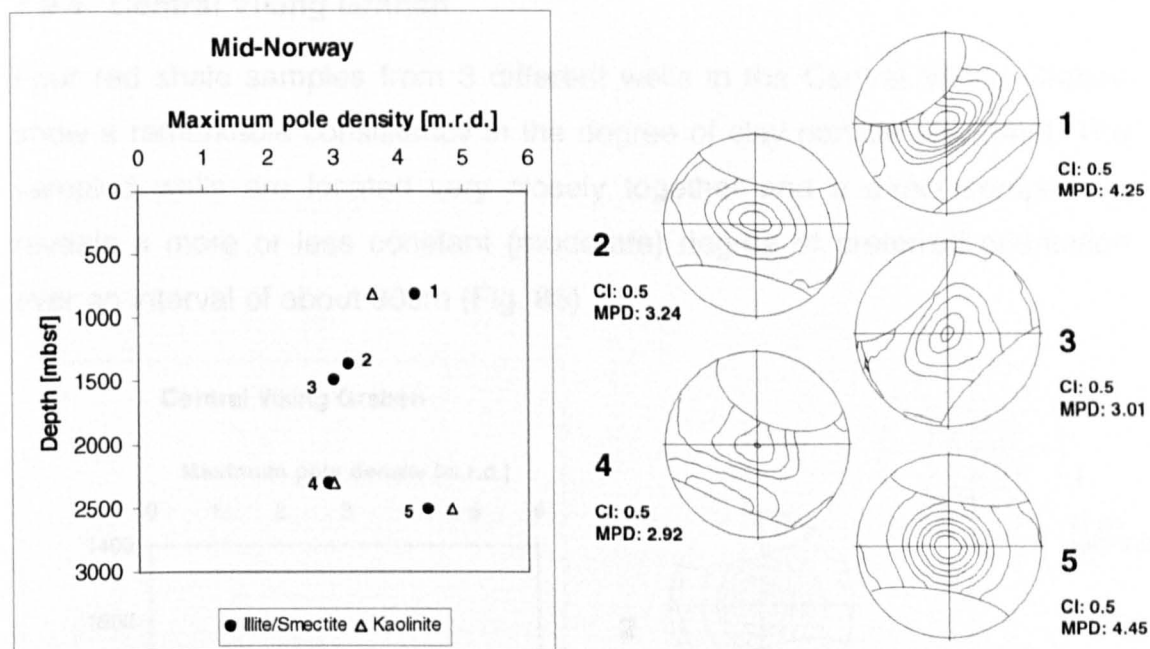


Fig. 84 The preferred orientation of phyllosilicates in the Mid-Norway well. The pole figures (I/S) were rotated into the direction of the maximum intensity. CI = contour interval [m.r.d.]; MPD = maximum pole density.

No systematic change of MPD values with increasing depth was observed. The prominent elongated shape of the pole figures from samples 1-4 (Fig. 84) is probably caused by the small sample size. The examined cutting slabs were not much larger than the beam area a less than perfect beam alignment led to blank spots during data collection.

Well	Depth [mbsf]	Temp. [°C]	<2 μ m [%]	%I in I/S	I/S/M MPD [m.r.d.]	K/C MPD [m.r.d.]
MN	812	32	33	≤10	4.25	3.61
MN	1362	52	67	-	3.24	-
MN	1487	57	58	-	3.01	-
MN	2301	86	51	≤10	2.92	2.99
MN	2499	93	59	-	4.45	4.81

Table 42 HRXTG results for the Mid-Norway well. MPD = maximum pole density; I/S/M = Illite/Smectite/Mica; K/C = Kaolinite/Chlorite.

Measurements of the orientation of kaolinite were possible in 3 of the 5 samples. The determined degree of alignment reflects in general the observations made for the I/S/M phases (Fig. 84). However, in contrast to the Central Bermuda Rise and the North Viking Graben, the MPD values of kaolinite are not generally lower than those from I/S/M.

7.9.4 Central Viking Graben

Four red shale samples from 3 different wells in the Central Viking Graben show a remarkable consistency in the degree of clay particle alignment. The sampled wells are located very closely together and a direct comparison reveals a more or less constant (moderate) degree of preferred orientation over an interval of about 300m (Fig. 85).

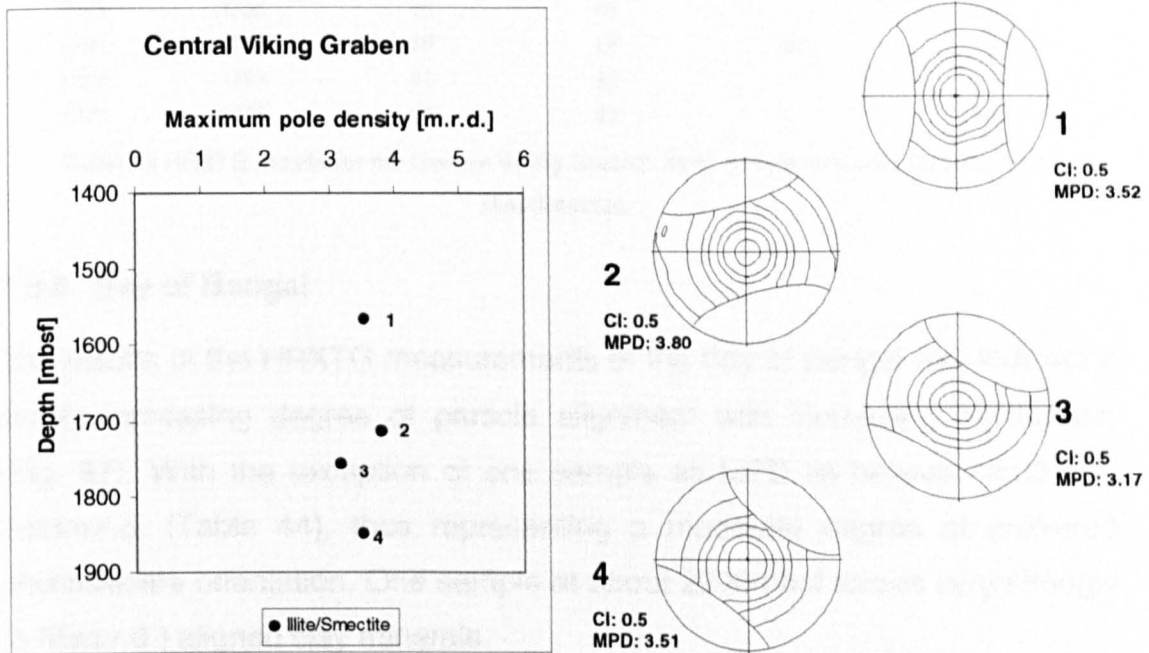


Fig. 85 The preferred orientation of phyllosilicates in the Central Viking Graben. The pole figures (I/S) were rotated into the direction of the maximum intensity. CI = contour interval [m.r.d.]; MPD = maximum pole density.

Pole figures shown in Fig. 85 indicate the uniformity of the HRXTG results. Extremely low signals for kaolinite prohibited further measurements (Fig. 86).

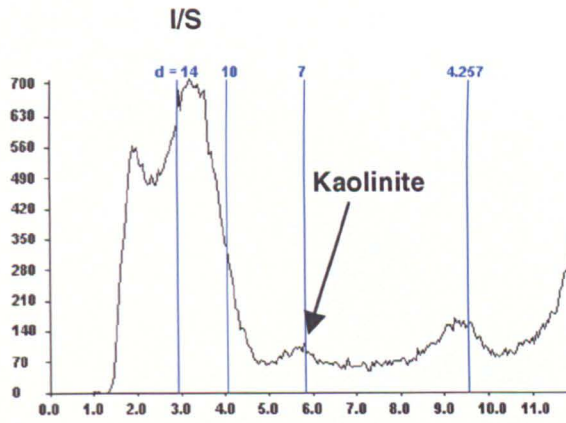


Fig. 86 2-Theta scan of a sample from the Central Viking Graben. The very low signal for the 7Å phase (Kaolinite) prohibited a HRXTG measurement for this mineral; I/S = Illite/Smectite.

Well	Depth [mbsf]	Temp. [°C]	<2µm [%]	%I in I/S	I/S MPD [m.r.d.]
CVG	1565	73	85	-	3.52
CVG	1711	79	58	30	3.8
CVG	1754	81	82	-	3.17
CVG	1848	85	65	-	3.51

Table 43 HRXTG results for the Central Viking Graben. MPD = maximum pole density; I/S = Illite/Smectite.

7.9.5 Bay of Bengal

The results of the HRXTG measurements of the Bay of Bengal well indicate a slowly increasing degree of particle alignment with increasing overburden (Fig. 87). With the exception of one sample all MPD lie between 3.03 and 3.83m.r.d. (Table 44), thus representing a moderate degree of preferred phyllosilicate orientation. One sample at about 2200mbsf shows very strongly (5.56m.r.d.) aligned clay minerals.

Well	Depth [mbsf]	Temp. [°C]	<2µm	%I in I/S	I/S MPD [m.r.d.]	K MPD [m.r.d.]
BB	1270	56	35	.*	3.03	2.63
BB	2030	83	30	.*	3.62	3.26
BB	2310	93	28	.*	5.56	4.52
BB	3305	129	26	.*	3.83	3.4
BB	3495	136	-	.*	3.3	3.08

Table 44 HRXTG results for the Bay of Bengal well. (.) Not sufficiently enough sample material; MPD = maximum pole density; I/S/M = Illite/Smectite; K = Kaolinite.

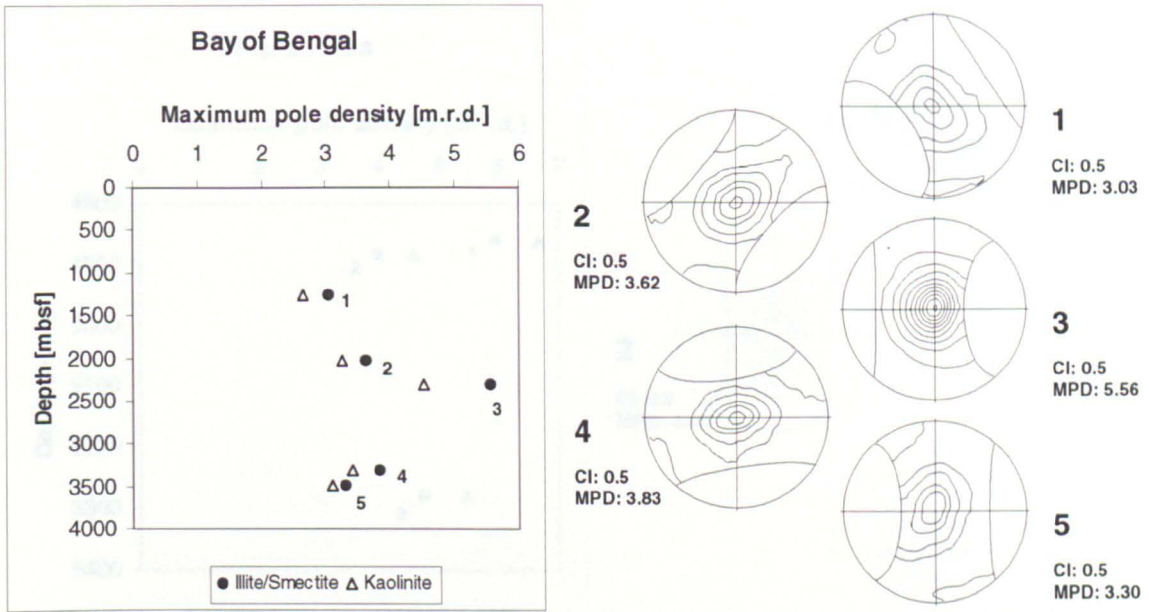


Fig. 87 The preferred orientation of phyllosilicates in a Bay of Bengal well. The pole figures (I/S) were rotated into the direction of the maximum intensity. CI = contour interval [m.r.d.]; MPD = maximum pole density.

As observed in several other wells, MPD values for the kaolinite crystals are lower than those of I/S, but display a similar trend. (Table 44).

7.9.6 Caspian Sea

The sampled shale sections were limited to an interval between 4863mbsf and 5280mbsf (Fig. 88). Three of the four samples contained a clay mineral fabric intense enough to be analyzed by HRXTG. Maximum pole densities of the I/S phases represent strong to very strong degrees of preferred orientation (4.0m.r.d. to 5.97m.r.d.).

Well	Depth [mbsf]	Temp. [°C]	<2µm [%]	%I in I/S	I/S MPD [m.r.d.]	K/C MPD [m.r.d.]
CS	4863	124	53	-	5.97	6.66
CS	4887	124	43	-	4	4.56
CS	5280	134	26	20-30	4.73	5.45

Table 45 HRXTG results for the Caspian Sea samples. MPD = maximum pole density; I/S = Illite/Smectite; K/C = Kaolinite/Chlorite.

In contrast to most other wells the kaolinite/chlorite crystals in the Caspian Sea samples are better aligned than those of the illite/smectite phases (Fig. 88, Table 45).

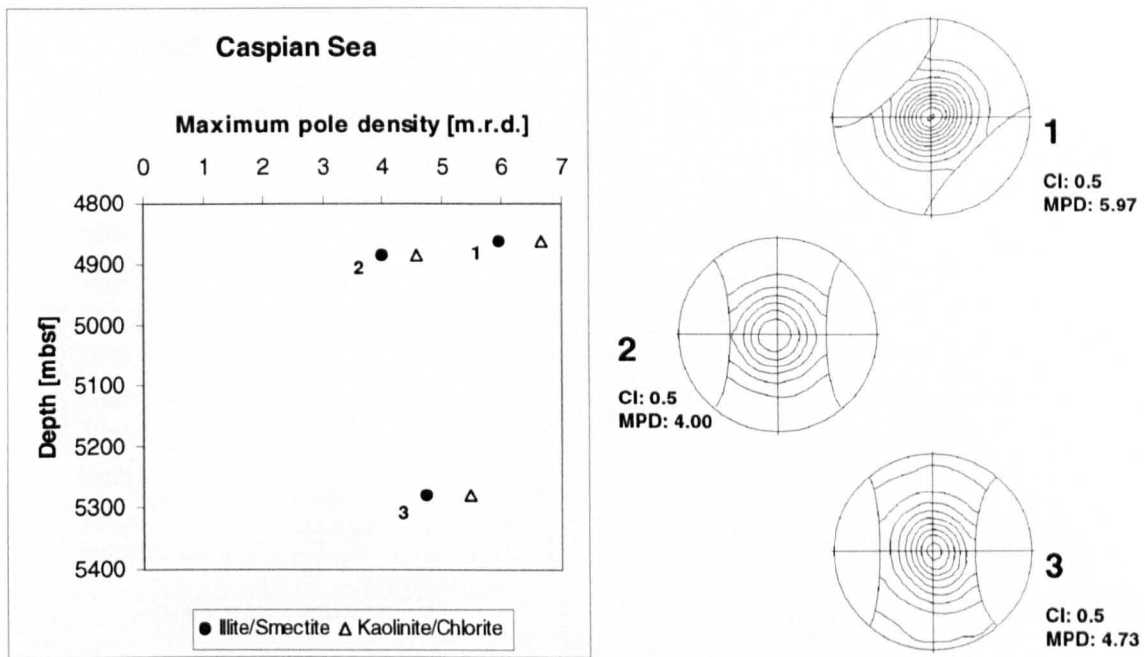


Fig. 88 The preferred orientation of phyllosilicates in the Caspian Sea well. The pole figures (I/S) were rotated into the direction of the maximum intensity. CI = contour interval [m.r.d.]; MPD = maximum pole density.

7.9.7 Gulf of Mexico: Panis, Ikon & Diva

A comparison of the results obtained from HRXTG for all three deep water Gulf of Mexico wells reveals that weakly aligned clay minerals prevail in this region (Fig. 89 to Fig. 91). Samples comprised of clay minerals with very weak (<2m.r.d.) or moderate (3-4m.r.d.) maximum pole intensities were found independent of burial depth in all three wells (Table 46). The degree of preferred orientation for the kaolinite/chlorite phases is generally similar but somewhat lower than that of illite/smectite (Fig. 89 to Fig. 91).

A systematic difference between the phyllosilicate alignment of the much shallower and colder Panis samples and those of Ikon and Diva was not observed.

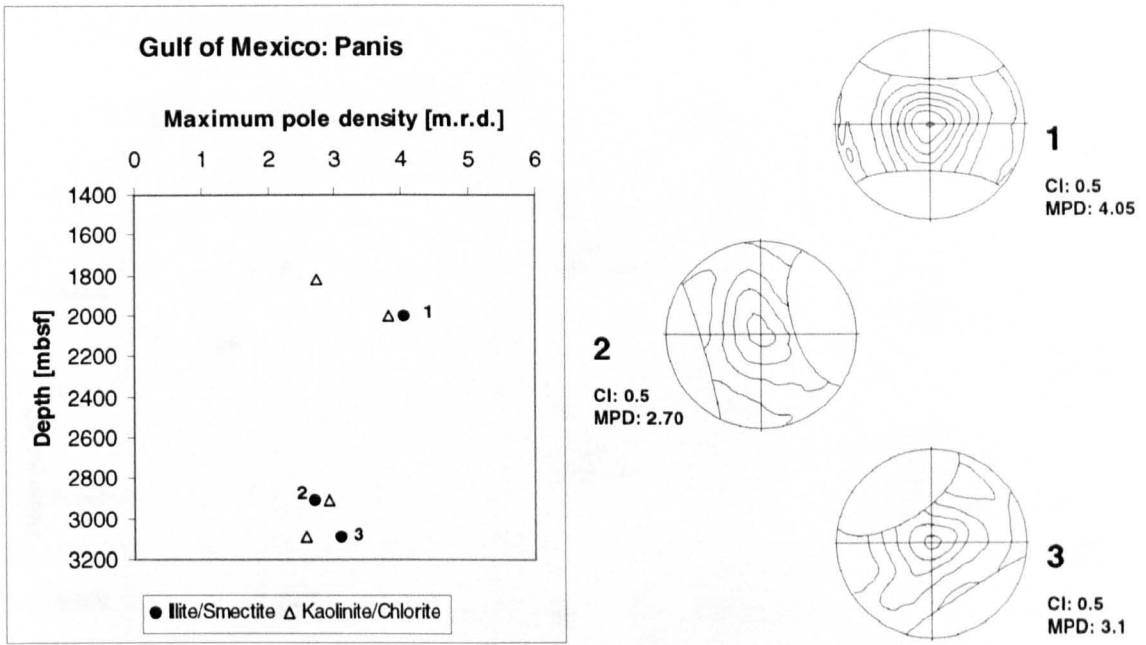


Fig. 89 The preferred orientation of phyllosilicates in the deep water Gulf of Mexico: PANIS. The pole figures (I/S) were rotated into the direction of the maximum intensity. CI = contour interval [m.r.d.]; MPD = maximum pole density.

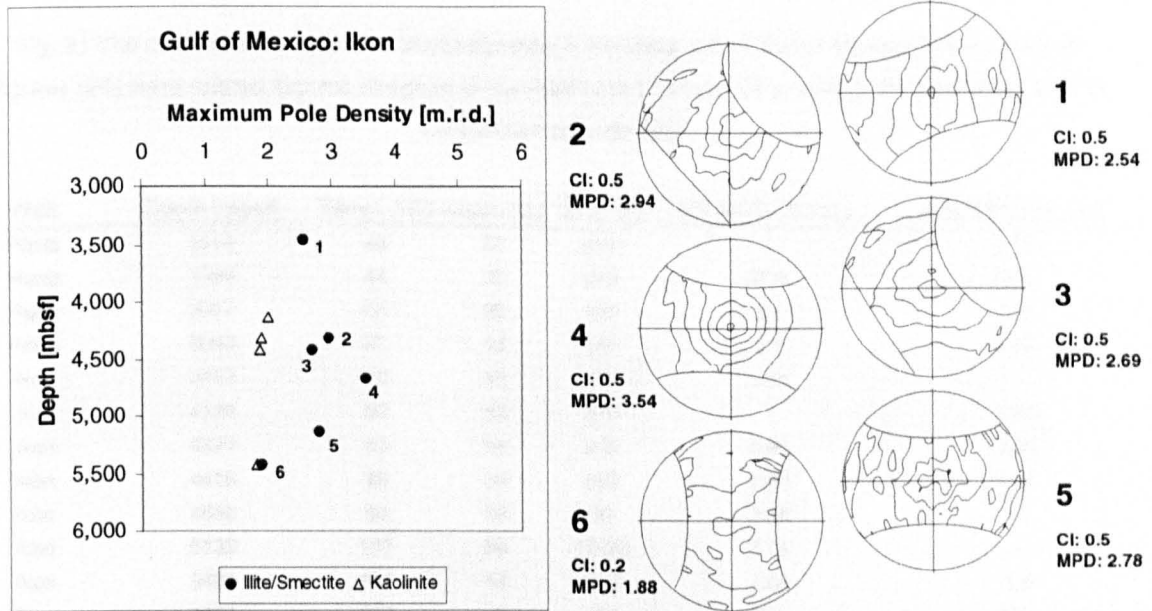


Fig. 90 The preferred orientation of phyllosilicates in the deep water Gulf of Mexico: IKON. The pole figures (I/S) were rotated into the direction of the maximum intensity. CI = contour interval [m.r.d.]; MPD = maximum pole density.

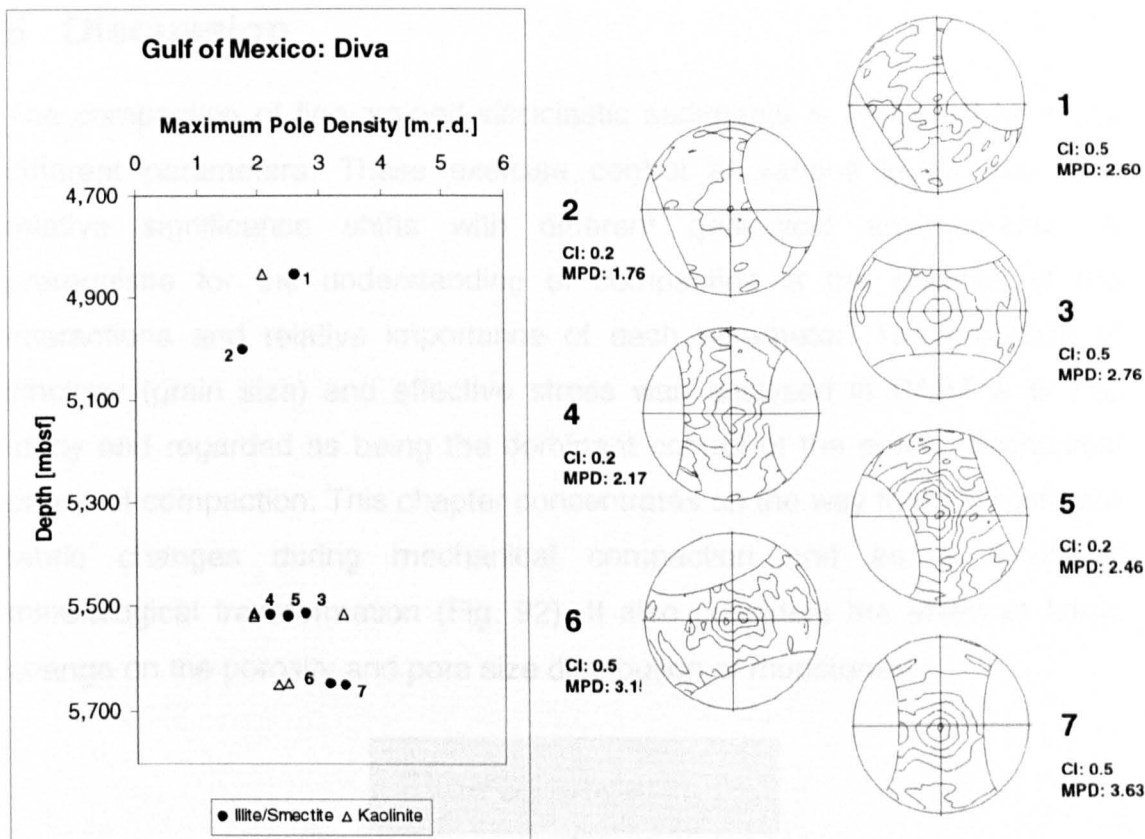


Fig. 91 The preferred orientation of phyllosilicates in the deep water Gulf of Mexico: DIVA. The pole figures (I/S) were rotated into the direction of the maximum intensity. CI = contour interval [m.r.d.]; MPD = maximum pole density.

Well	Depth [mbsf]	Temp. [°C]	<2µm [%]	%I in I/S	I/S MPD [m.r.d.]	K/C MPD [m.r.d.]
Panis	1816	40	41	≤10	-	2.73
Panis	1999	44	39	≤10	4.05	3.8
Panis	2907	64	39	≤10	2.7	2.9
Panis	3090	67	44	≤10	3.1	2.57
Ikon	3453	76	48	≤10	2.54	-
Ikon	4128	90	46	≤10	-	1.99
Ikon	4321	93	52	≤10	2.94	1.88
Ikon	4418	95	39	≤10	2.69	1.87
Ikon	4660	99	39	30	3.54	-
Ikon	5133	107	56	10-20	2.78	-
Ikon	5420	111	44	≤10	1.88	1.8
Diva	4855	117	36	≤10	2.6	2.08
Diva	5001	120	49	≤10	1.74	-
Diva	5511	128	37	40	2.76	1.92
Diva	5516	128	33	40	2.17	3.36
Diva	5518	128	60	40-50	2.46	1.91
Diva	5647	130	22	70	3.15	2.47
Diva	5649	130	38	80	3.41	2.32

Table 46 HRXTG results for the Gulf of Mexico wells. MPD = maximum pole density; I/S = Illite/Smectite; K/C = Kaolinite/Chlorite.

8 Discussion

The compaction of fine-grained siliciclastic sediments is controlled by many different parameters. These exercise control at various levels and their relative significance shifts with different geological environments. A prerequisite for the understanding of compaction is the analysis of the interactions and relative importance of each parameter. The influence of lithology (grain size) and effective stress was analyzed in PART A of this study and regarded as being the dominant control of the purely mechanical phase of compaction. This chapter concentrates on the way that phyllosilicate fabric changes during mechanical compaction and as a result of mineralogical transformation (Fig. 92). It also considers the effect of fabric change on the porosity and pore size distribution of mudstones.

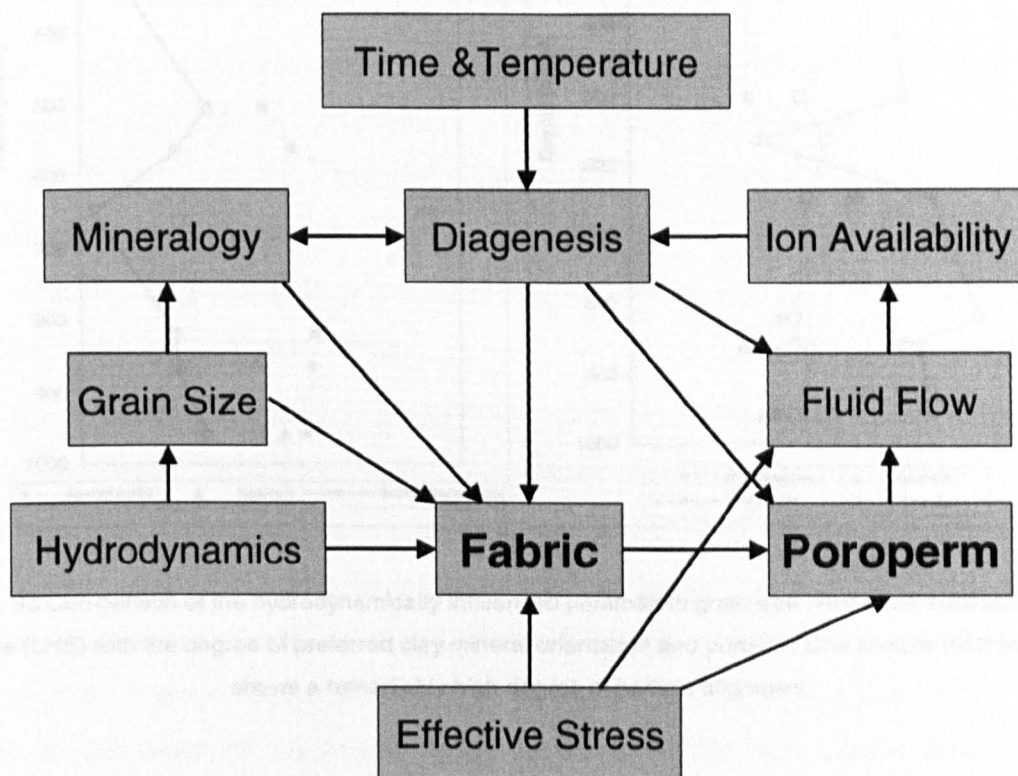


Fig. 92 The interaction of the parameters influential on mudstone fabric and poroperm.

8.1 Hydrodynamics and the depositional environment

The extensive analytical database provided by DSDP allowed a detailed investigation of the influence of the sedimentary environment on the clay

mineral fabric of well 43/386 (Central Bermuda Rise). Palaeontologically well constrained ages as well as a good understanding of the depositional history at the drill site (Tucholke et al. 1975) made it possible to compare porosity and sedimentation rate with the results of the grain size, mineralogy and fabric analyses undertaken in this study.

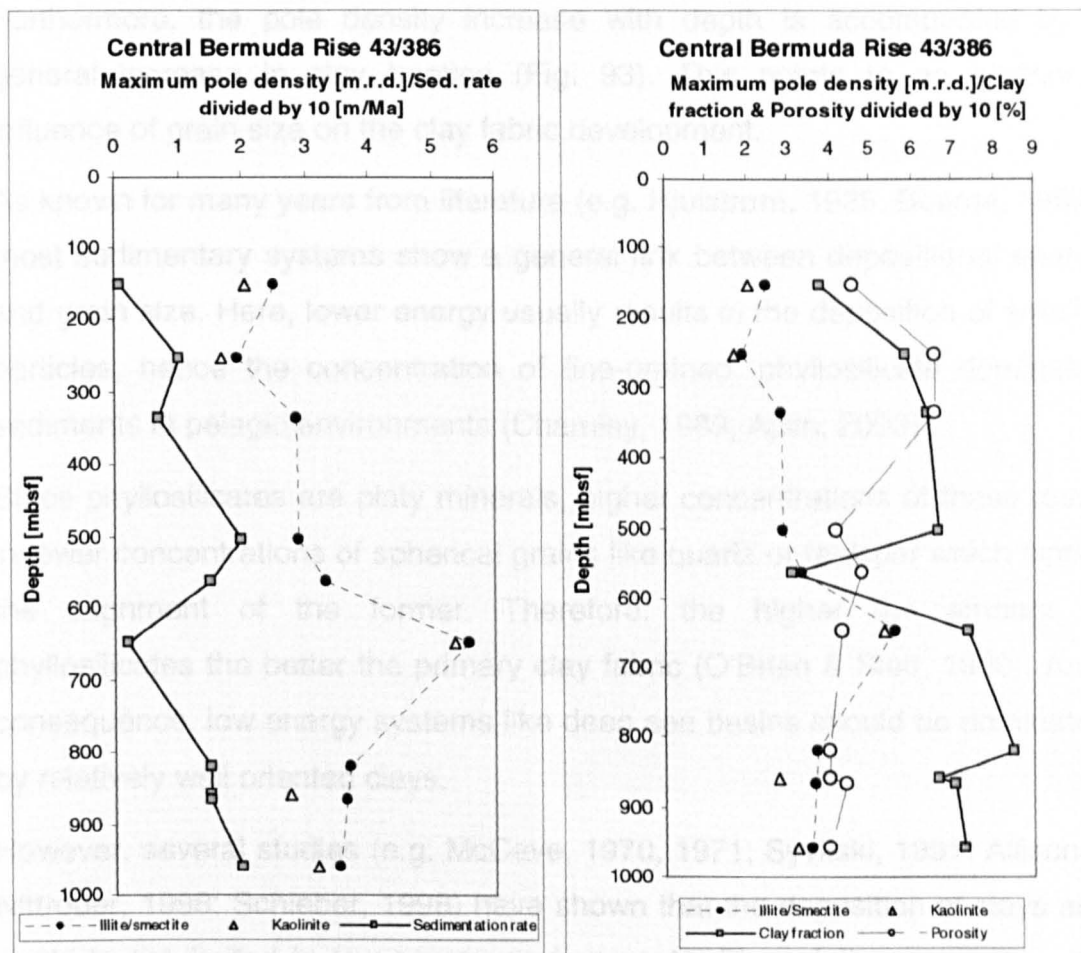


Fig. 93 Comparison of the hydrodynamically influenced parameters grain size (RHS) and sedimentation rate (LHS) with the degree of preferred clay mineral orientation and porosity. One sample (646.8mbsf) shows a remarkably high degree of particle alignment.

Sedimentation rates at site 43/386 range from extremely low (2m/Ma) to low (25m/Ma) and reflect the deep sea environment (Fig. 93). The pole densities show moderate (2-3m.r.d.) to high (>5m.r.d.) values. The negative relationship between sedimentation rate and clay mineral orientation is striking (Fig. 93) and highlights the strong influence of hydrodynamic effects in this deep water, low sedimentation rate environment. Relative changes in

sedimentation rate over time (the deepest samples is of Early Albian age (~105 Ma)) always resulted in changing degrees of clay particle alignment. Lower sedimentation rates led to higher fabric intensities and vice versa. This observation clearly points to a hydrodynamically controlled initial alignment of clay particles.

Furthermore, the pole density increase with depth is accompanied by a general increase in clay fraction (Fig. 93). This points to an additional influence of grain size on the clay fabric development.

As known for many years from literature (e.g. Hjulstrøm, 1935; Bouma, 1962), most sedimentary systems show a general link between depositional energy and grain size. Here, lower energy usually results in the deposition of smaller particles, hence the concentration of fine-grained, phyllosilicate dominated sediments in pelagic environments (Chamley, 1989; Aplin, 2000).

Since phyllosilicates are platy minerals, higher concentrations of these result in lower concentrations of spherical grains like quartz or feldspar which hinder the alignment of the former. Therefore, the higher the amount of phyllosilicates the better the primary clay fabric (O'Brien & Slatt, 1990). As a consequence, low energy systems like deep sea basins should be dominated by relatively well oriented clays.

However, several studies (e.g. McCave, 1970, 1971; Syvitski, 1991; Allison & Nittrouer, 1998; Schieber, 1998) have shown that the deposition of clays and muds is not limited to low-energy environments. Flocculation can cause the deposition of heavier silt- to sand-sized aggregates of clay particles where single grains would stay in suspension (Chamley, 1989; Kranck (1991) and references therein; Syvitski, 1991). In addition, Joseph et al. (1998) illustrated that in the case of sediment drifts higher energies not necessarily mean poorer particle alignment. They found that faster currents are able to align sediment particles more effectively than slower currents.

Flocculation as well as other physicochemical processes can form various "non-aligned" clay microstructures which prevent an initial preferred orientation (e.g. Rieke & Chilingarian, 1974; O'Brien & Slatt, 1990; Bennett et al., 1991; O'Brien & Pietraszek-Mattner, 1998). These phenomena explain

Tribble et al.'s (1992) SEM observations from the Barbados Convergent Margin, where several mud and mudstone samples showed no or only poor alignment of clay particles until depths of at least 600mbsf.

In addition to these primary factors there are various bioorganic, biomechanical or biophysical mechanisms (e.g. bioturbation or organic gas generation, Bennett et al., 1991) which prevent the preservation of initial sedimentary clay fabrics prior to lithification.

In the light of all these processes, it is quite remarkable that in the case of the Central Bermuda Rise well sedimentation rate (and to a lower extent grain size) seems to be a sufficient proxy for relative changes in initial clay particle alignment.

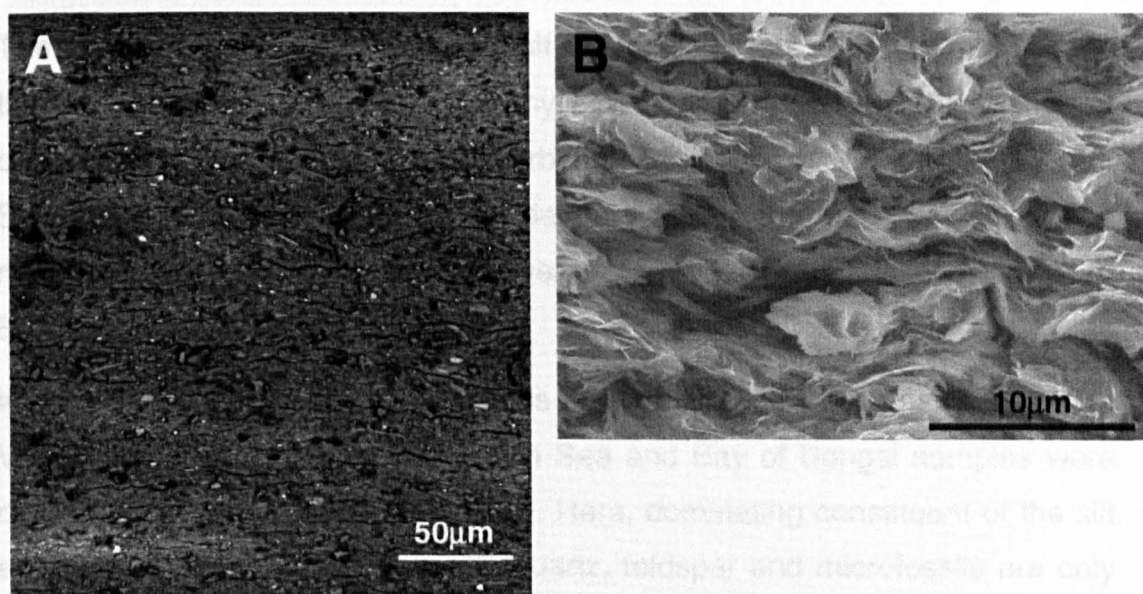


Fig. 94 Backscatter Scanning Electron Micrograph (BSEM, A) and Scanning Electron Micrograph (SEM, B) of sample 43/386-36 (646.8mbsf). Both images show the dominance of platy minerals (smectite, illite, kaolinite) in this red clay sample. The images are oriented subparallel to the bedding plane and reveal the extreme degree of clay particle alignment.

For one sample from well 43/386 an unusually high degree of preferred orientation (5.6m.r.d., Fig. 93) was detected. This red clay was deposited at a very low sedimentation rate of 2m/Ma (Tucholke et al., 1975). XRD, EDX as well as grain size analyses confirmed that not only are 74% of the particles smaller than 2µm (Fig. 93), but also that most of these are comprised of phyllosilicates (smectite, illite & kaolinite). It seems to be a consequence of

these rare conditions that initial fabric intensities were created which are more typical of deeply buried shales (Fig. 125).

8.2 Grain size and mineralogy

As mentioned before, sediments with high concentrations of lath shaped minerals (phyllosilicates) seem to have better primary clay fabrics than sediments with high contents of spherical grains. In the present study, the combination of SEM/BSEM, grain size and XRD data revealed distinct patterns in the relationship between fabric (HRXTG) and particle assemblage. Here, the main focus was put on the mineral composition of the silt grains (2-63 μ m), since this fraction seems to have a significant control on the alignment of the remaining phyllosilicates.

The analysis of samples from the Gulf of Mexico revealed that in most cases the clay fraction is dominated by phyllosilicates whereas the silt fraction is comprised of quartz, feldspar and carbonates/microfossils (Fig. 95 & Fig. 96). Significant amounts of silt-sized detrital mica were not observed. The measured pole densities are relatively low, even at depths of more than 5000mbsf.

In contrast, the grain size distributions and mineral assemblages of the North Viking Graben, Mid-Norway, Caspian Sea and Bay of Bengal samples were distinctly different (Fig. 97 - Fig. 103). Here, dominating constituent of the silt and sand fraction is detrital mica. Quartz, feldspar and microfossils are only abundant in the largest grain sizes (Fig. 97, Fig. 100 & Fig. 103). The large quantities of silt-sized phyllosilicates are often aligned subparallel to the bedding plane and create a noticeable "mica fabric" (Fig. 102). It can be assumed that it is these micas which generate the high fabric intensities determined by HRXTG. These readings might accurately reflect the general fabric of many samples, but BSEM analyses reveal (Fig. 98 & Fig. 103) that most of the fine-grained (<5 μ m) mica particles show no preferred orientation.

A further feature of samples with high detrital mica contents was revealed by the analysis of a fine sandstone sample from the North Viking Graben. This sample showed a clear macroscopic fissility and analysis by BSEM revealed a high content of biotite and muscovite (Fig. 100 & Fig. 101). The rare

concentration of these large phyllosilicates resulted in a distinct stacking of mica crystals (Fig. 101) and produced a fissility uncommon for sand-sized sediments. Since most other fine sandstones do not contain enough clay minerals to produce a detectable phyllosilicate fabric the pole densities determined by HRXTG were unexpectedly high.

Although fundamentally different with respect to grain size, samples from the Central Viking Graben, Caspian Sea (4887mbsf & 5280mbsf) and deeper (>600mbsf) Central Bermuda Rise showed degrees of phyllosilicate alignment very similar to those of the mica-rich sandstone. The resemblance of the determined fabrics can be attributed to the predominance of lath-shaped minerals in these samples. Silt- to sand-sized micas dominate in the former two whereas fine-grained clay minerals prevail the latter.

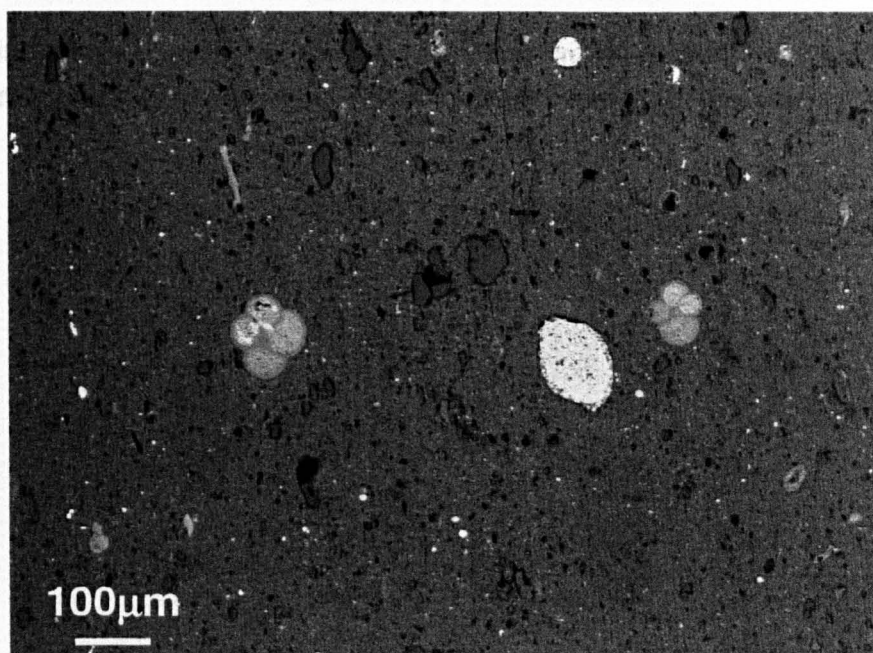


Fig. 95 BSEM image of a mudstone core sample from 5001mbsf (Diva). The clay fraction of this sample is 49%. Larger particles are primarily comprised of quartz, feldspar and microfossil material. Silt- and sand-sized detrital mica is rare.

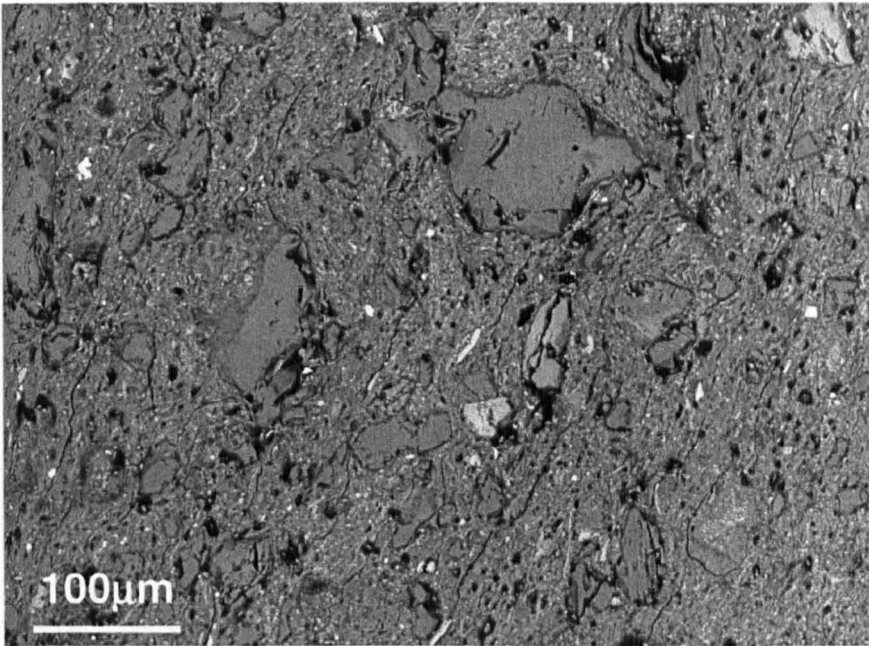


Fig. 96 BSEM image of a siltstone (33% <math><2\mu\text{m}</math>) core sample from 5516mbsf (Diva). The amount of silt- and sand-sized particles is greater than in Fig. 95. However, the matrix is dominated by clay minerals and large phyllosilicates are rare.



Fig. 97 BSEM image of a shallow (1270mbsf), fine silt (35% <math><2\mu\text{m}</math>) sample from the Bay of Bengal. The overall alignment of the phyllosilicates in this silty matrix is relatively weak (3.03m.r.d. for illite/mica). Qz = quartz; KFp = K-Feldspar.



Fig. 98 BSEM image of the same Bay of Bengal sample as in Fig. 97. This magnification illustrates the lack of preferred orientation for most of the fine-grained ($<5\mu\text{m}$) mica particles.

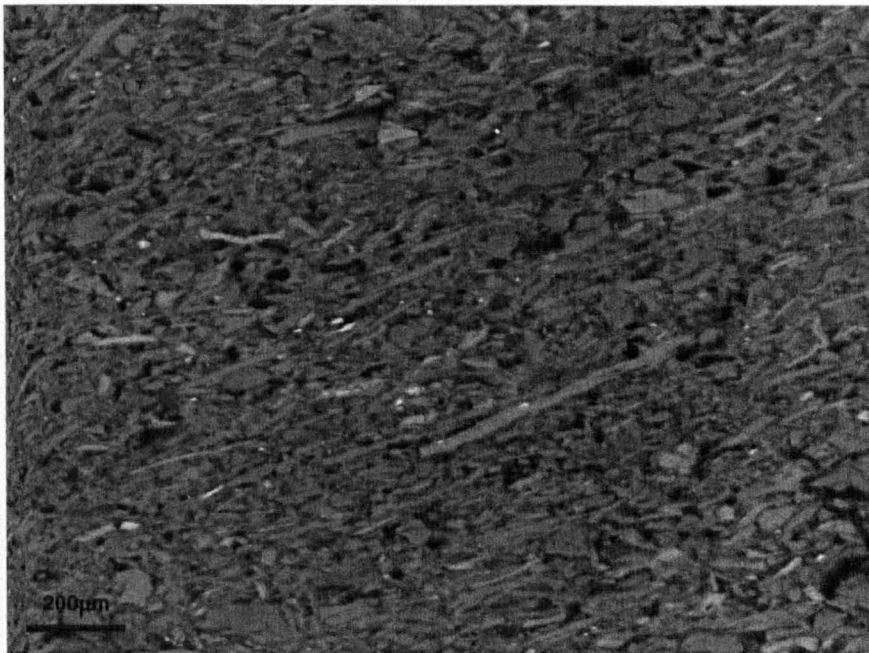


Fig. 99 BSEM image of a deeper (2310mbsf) siltstone (28% $<2\mu\text{m}$) from the Bay of Bengal. The mineral matrix consists mainly of platy minerals (mica) which are much better aligned (5.56m.r.d.) than those of the 1290mbsf sample (Fig. 98).

The measured pore density for this mica is 3.86m²/g.

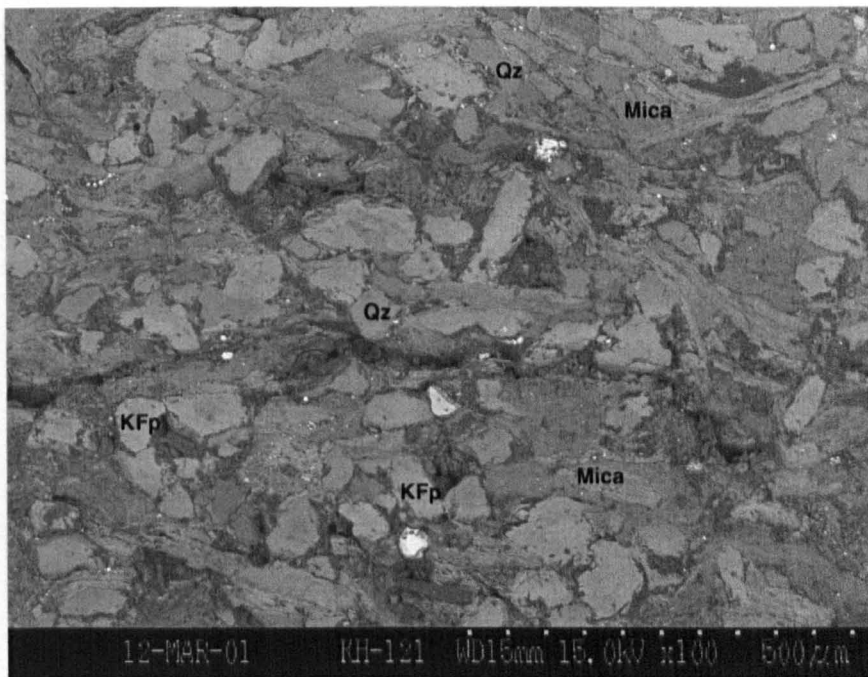


Fig. 100 BSEM image of a fine-grained sandstone (13% $<2\mu\text{m}$) from the North Viking Graben. This sample was taken at 1908mbsf and shows no obvious preferred phyllosilicate orientation at this magnification.

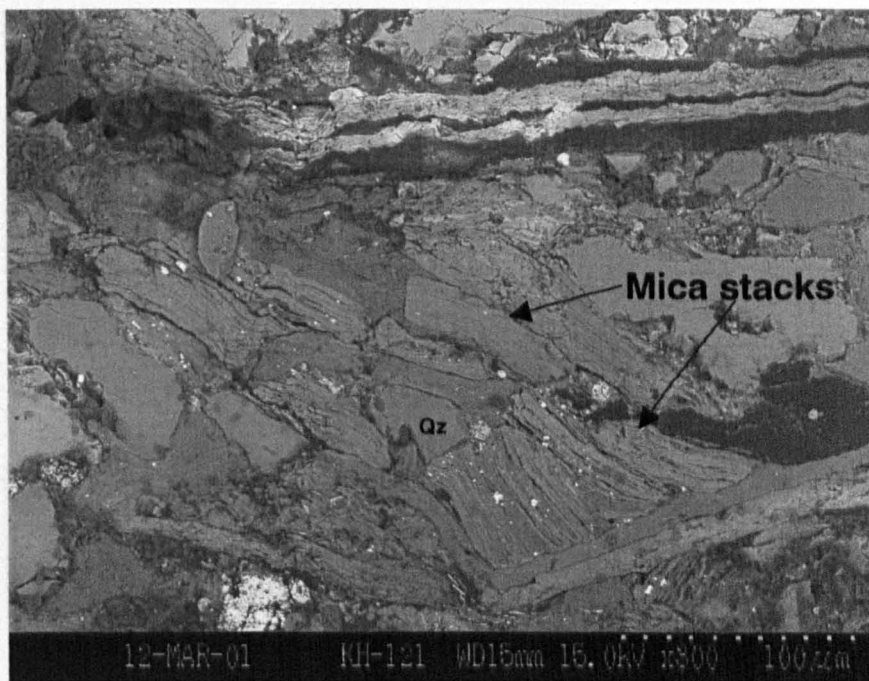


Fig. 101 Higher magnification BSEM image of the same sample as displayed in Fig. 100. The high content of silt to sand sized mica (muscovite & biotite) grains led to a stacking of these platy minerals. The measured pole density for illite/mica is 3.68m.r.d.

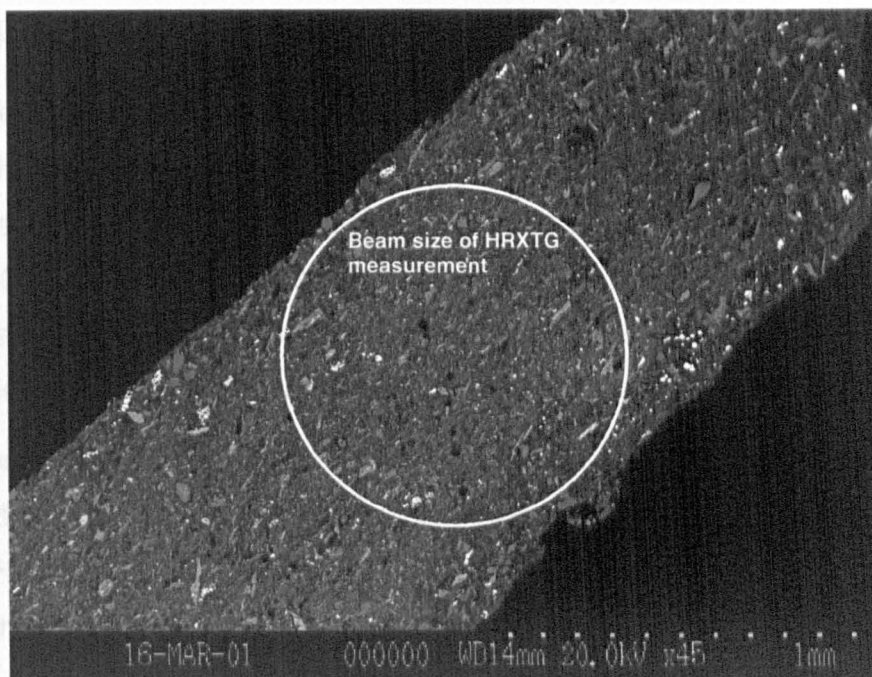


Fig. 102 BSEM image of a cutting sample (812mbsf) from the Mid-Norway well. The bright prolate minerals (mica) reveal the good degree of alignment (4.25m.r.d.) of the silt/sand fraction in this siltstone (33% <math>< 2\mu\text{m}</math>).

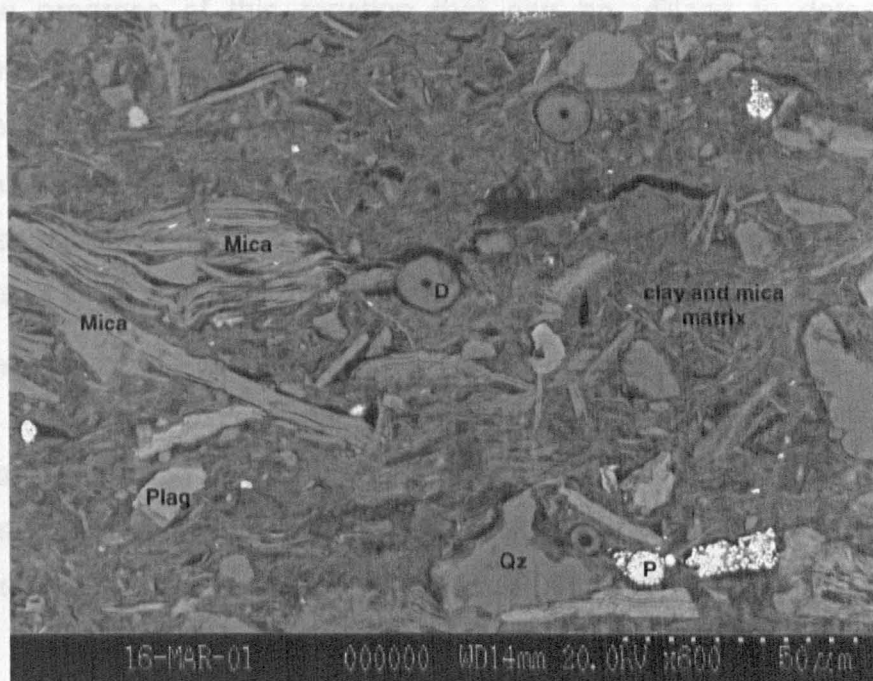
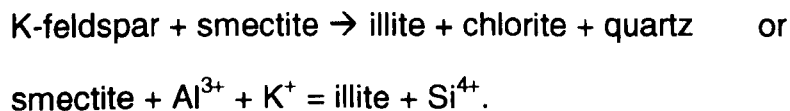


Fig. 103 This BSEM image of the same sample as in Fig. 102 illustrates that the fine-grained matrix of this siltstone is dominated by poorly oriented clay and mica grains. Qz = quartz; Plag = plagioclase; D = diatom; P = framboidal pyrite.

8.3 Clay mineral diagenesis

It is known from previous studies that clay mineral diagenesis significantly alters the fabric and mineralogy of mudstones (e.g. Perry & Hower, 1970; Hower et al., 1976; Oertel & Curtis, 1972; Curtis et al., 1980; Kisch, 1983; Ho et al., 1995; van der Pluijm et al. 1998; Jacob et al. 2000). In order to be able to systematically compare these alterations with changes in the physical properties it is important to determine the diagenetic grade of a mudstone.

Many previous studies (Dunoyer de Segonzac, 1970; Perry & Hower, 1970; Reynolds & Hower, 1970; Hower et al., 1976; Ahn & Peacor, 1986; Pollastro, 1992; Hillier et al., 1995; Drief & Nieto, 2000) have shown that in most sedimentary basins there is a diagenetic transition from smectite to mixed-layered illite/smectite to illite according to the reaction:



It is the progress of this reaction that can be utilized to determine the diagenetic grade of a mudstone. The most practicable way to accomplish this is by analyzing the separated clay fraction (<2 μm) by X-ray diffraction (Moore & Reynolds, 1997). This method enables the determination of the percentage of diagenetically generated illite in mixed-layered illite/smectite. Here, higher amounts of illite point to higher diagenetic grades.

The influence of the various parameters that control the transition of smectite to illite have been widely studied (e.g. Essene & Peacor, 1995). Besides temperature (Freed & Peacor (1989) and references therein), these parameters are mainly time (e.g. Kisch, 1983, Srodon & Eberl, 1984; Velde & Espitalie, 1989; Velde, 1995; Cuadros & Linares, 1996), pressure (e.g. Srodon & Eberl, 1984; Colton-Bradley, 1987; Buryakovsky et al., 1995), potassium availability (e.g. Hower et al., 1976; Srodon & Eberl, 1984; Pearce et al., 1991; Moore & Reynolds, 1997) and pore fluid chemistry (e.g. Blank & Seifert, 1976; Roberson & Lahann, 1981; Pearce et al., 1991; Drief & Nieto, 2000). The general kinetics of the reaction were discussed by Velde &

Vasseur (1992), Cuadros & Linares (1996 and references therein) and Elliott & Matisoff (1996).

The results of the XRD analysis in this study revealed that of all examined silt- and mudstones only the deeper samples from the Gulf of Mexico (Ikon & Diva) show a gradual increase of illite in I/S (Fig. 104 & Fig. 105). The first change in illite content was observed in a cutting sample of Ikon at a depth of 4660mbsf and an in situ temperature of about 100°C. The first increase of illite in Diva was determined at 5511mbsf (128°C).

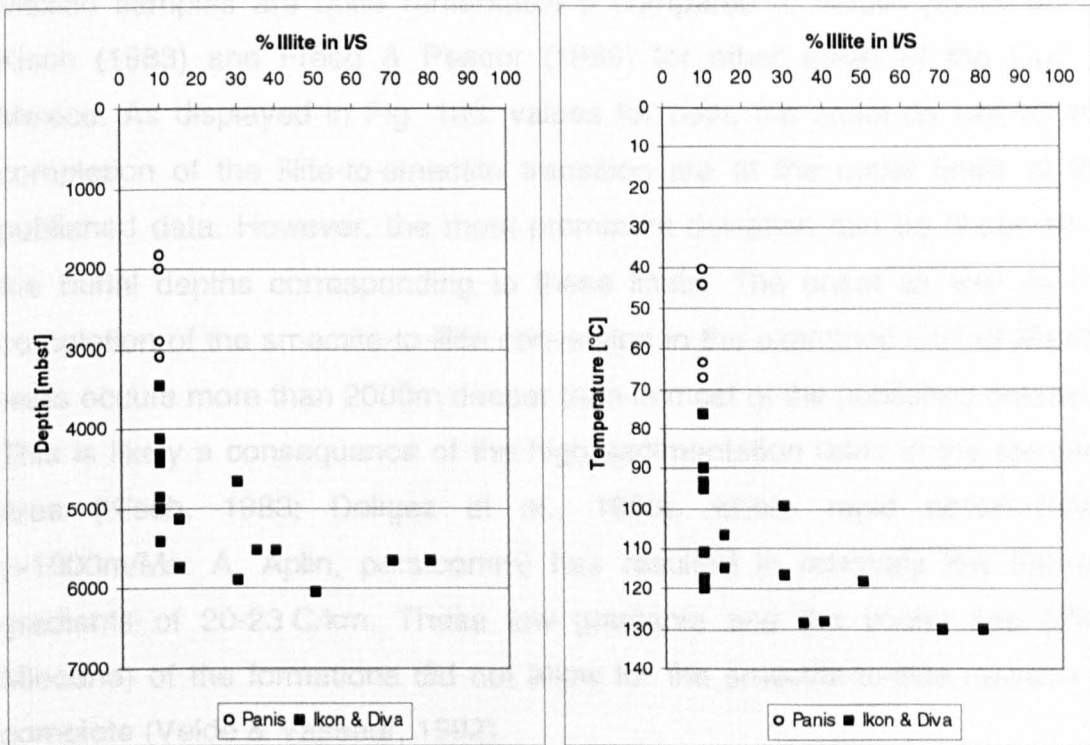


Fig. 104 The relationship between illite content in I/S and burial depth (lhs) and in situ temperature (rhs) for the deep water Gulf of Mexico samples.

The maximum percentage of illite in I/S was measured for a Diva sample which was taken from 5649mbsf. The in situ temperature was determined as 130°C, the illite content as about 80%. Although some samples from Ikon are from greater depths than those from Diva, differences in the thermal gradient (Diva: 23°C/km; Ikon: 20°C/km) resulted in higher maximum temperatures for the latter. The highest content of illite in I/S observed for Ikon was about 50% at 6041mbsf.

The maximum measurement of 80% illite in I/S for the Diva sample resembles a value often regarded as the completion value for the smectite-to-illite transition (Kisch, 1983; Freed & Peacor, 1989). Srodon & Eberl (1984) as well as Moore & Reynolds (1997) report that the illite content in I/S in the Gulf of Mexico rarely exceeds 80%. They argue that at this stage most of the available potassium to feed this reaction is consumed, an observation which is in agreement with the results of Hower et al.'s (1976) study.

The temperature/diagenetic grade relationships observed for the Gulf of Mexico samples are quite remarkable if compared to values published by Kisch (1983) and Freed & Peacor (1989) for other areas of the Gulf of Mexico. As displayed in Fig. 106, values for both, the onset as well as the completion of the illite-to-smectite transition are at the upper limits of the published data. However, the most prominent deviation can be observed in the burial depths corresponding to these limits. The onset as well as the completion of the smectite-to-illite conversion in the examined Gulf of Mexico wells occurs more than 2000m deeper than in most of the published datasets. This is likely a consequence of the high sedimentation rates in the sampled area (Kisch, 1983; Doligez et al., 1986), where rapid accumulation (>1000m/Ma; A. Aplin, pers.comm) has resulted in relatively low thermal gradients of 20-23 C/km. These low gradients and the young age (Pliocene) of the formations did not allow for the smectite-to-illite reaction to complete (Velde & Vasseur, 1992).

In addition, the lowered thermal gradient also leads to a shift in the pore pressure/temperature relationship, which causes higher pressures at lower temperatures and may hinder the dehydration of smectite prior to the conversion into illite (Kisch, 1983; van Groos & Guggenheim, 1984; Buryakovsky et al., 1995). The often present overpressures due to disequilibrium compaction (Swarbrick & Osborne, 1998) might further contribute to this effect (Buryakovsky et al., 1995).

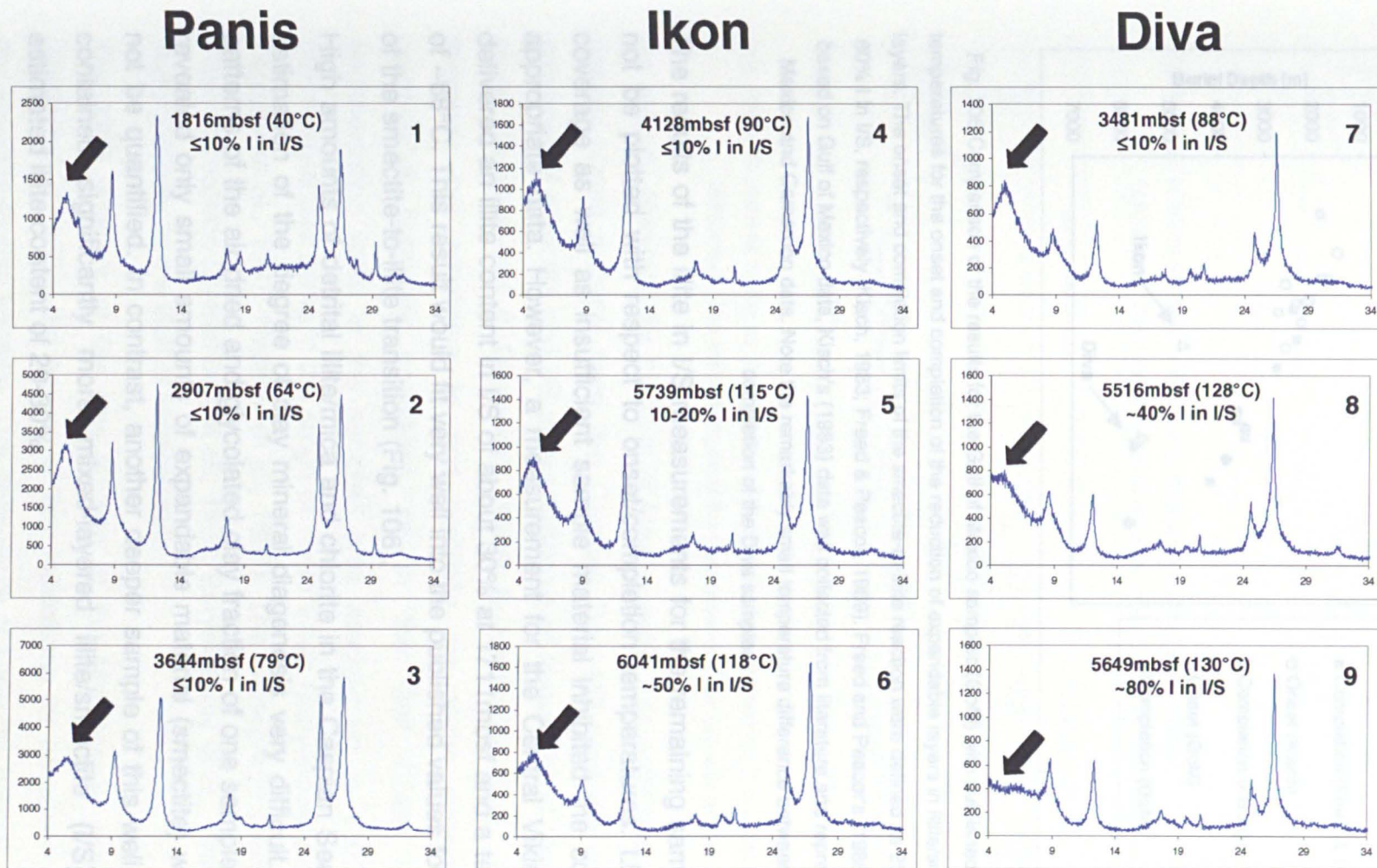


Fig. 105 XRD traces from the Gulf of Mexico sample set. The arrows mark the position of the smectite 001 peak. All Panis samples (1-3) as well the shallow samples from Ikon & Diva (4 & 7) show no indication for a progress of the smectite-to-illite conversion. Only the deeper samples from Ikon & Diva (5,6,8,9) show a gradual decrease in smectite and increase in diagenetic illite.

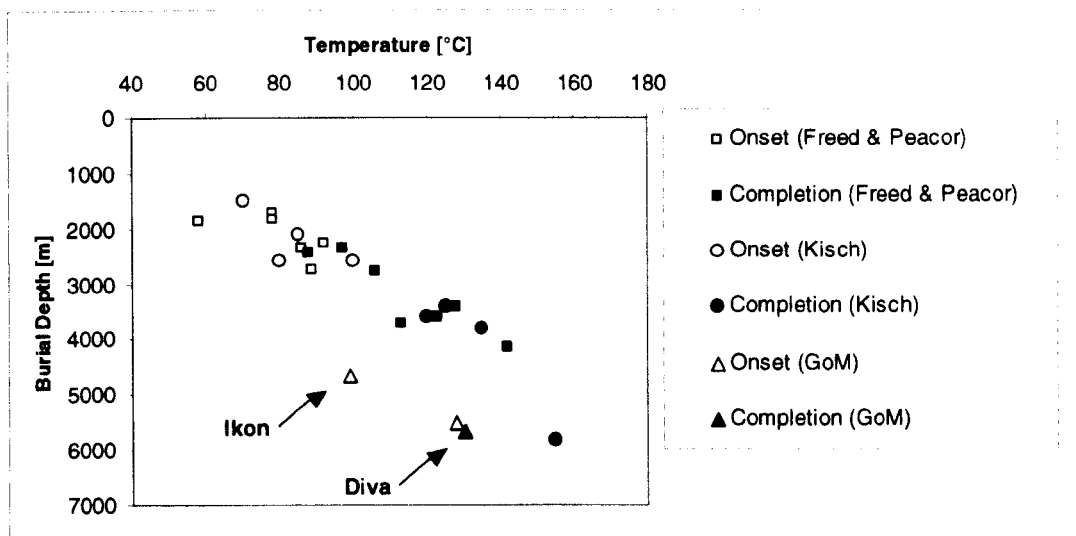


Fig. 106 Comparison of the results for the Gulf of Mexico samples (GoM) with published depths and temperatures for the onset and completion of the reduction of expandable layers in illite/smectite mixed-layers. The onset and completion limits of the smectite-to-illite reaction were defined as 25% I in I/S and 80% I in I/S, respectively (Kisch, 1983; Freed & Peacor, 1989). Freed and Peacor's (1989) data are all based on Gulf of Mexico data, Kisch's (1983) data was collected from literature and represents Gulf of Mexico and Cameroon data. Note the remarkably small temperature difference between onset and completion of the Diva samples.

The results of the illite in I/S measurements for the remaining samples could not be plotted with respect to onset/completion temperatures. Limited well coverage as well as insufficient sample material inhibited the collection of appropriate data. However, a measurement for the Central Viking Graben delivered an illite content in I/S of about 30% at 1711mbsf and a temperature of ~68°C. This result would fit very well into the published values for the onset of the smectite-to-illite transition (Fig. 106).

High amounts of detrital illite/mica and chlorite in the Caspian Sea made an estimation of the degree of clay mineral diagenesis very difficult. The XRD patterns of the air dried and glycolated clay fraction of one sample (Fig. 107) revealed only small amounts of expandable material (smectite) which could not be quantified. In contrast, another deeper sample of this well (Fig. 108) contained significantly more mixed-layered illite/smectite (I/S) with an estimated illite content of 20-30%.

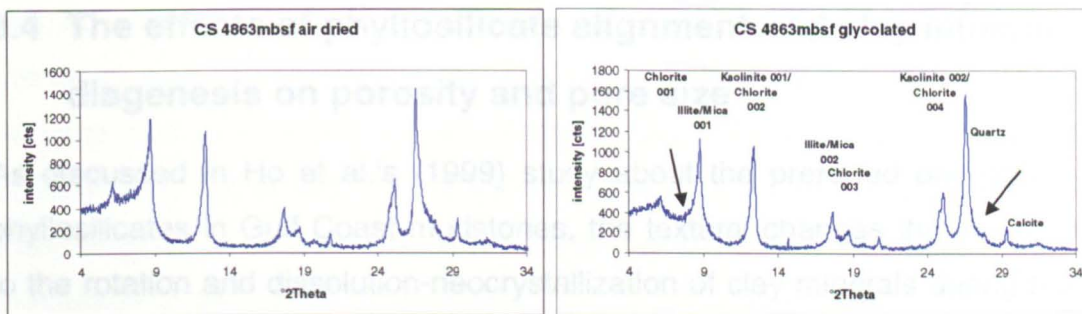


Fig. 107 XRD patterns for the air dried (lhs) and glycolated (rhs) clay fraction of a Caspian Sea sample (4863mbsf). The main changes of the glycolation are marked with arrows.

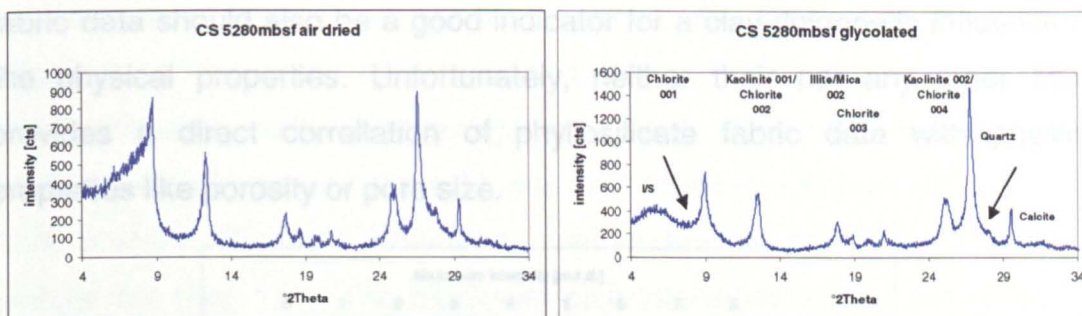


Fig. 108 XRD patterns for the air dried (lhs) and glycolated (rhs) clay fraction of a Caspian Sea sample (5280mbsf). The main changes of the glycolation are marked with arrows.

As already observed for the Gulf of Mexico wells, it is quite remarkable that deeply buried material from the Caspian Sea still contains considerable amounts of smectite and I/S at temperatures of about 135°C (data from this study; Buryakovsky & Djevanshir, 1986; Buryakovsky et al., 1995). It is therefore not surprising to find basically the same depositional and geothermal boundary conditions as in the Gulf Coast wells. The sedimentation rates in the sampled area reached up to 1300m/Ma, the thermal gradient being in the range of 16-25°C/km (Buryakovsky et al., 1995; Tagiyev et al., 1997; Nadirov et al., 1997). The widespread overpressure in these formations (Bredehoeft et al., 1988; Buryakovsky et al., 1995) is also a feature similar to the Gulf of Mexico wells.

The XRD analysis of the clay fraction of the Mid-Norway samples (812-2499mbsf, 32-93°C) did not reveal any indications for an advanced level of the smectite-to-illite transition. The dominance of kaolinite, detrital chlorite and detrital illite/mica significantly hindered the quantification of %I in I/S.

8.4 The effects of phyllosilicate alignment and clay mineral diagenesis on porosity and pore size

As discussed in Ho et al.'s (1999) study about the preferred orientation of phyllosilicates in Gulf Coast mudstones, the textural changes that occur due to the rotation and dissolution-neocrystallization of clay minerals during burial should have a significant impact on physical properties like porosity and permeability. Since Ho et al. (1999) showed that the textural changes are strongest close to and during the smectite-to-illite transformation (Fig. 109), fabric data should also be a good indicator for a clay-diagenetic influence on the physical properties. Unfortunately, neither their nor any other study provides a direct correlation of phyllosilicate fabric data with physical properties like porosity or pore size.

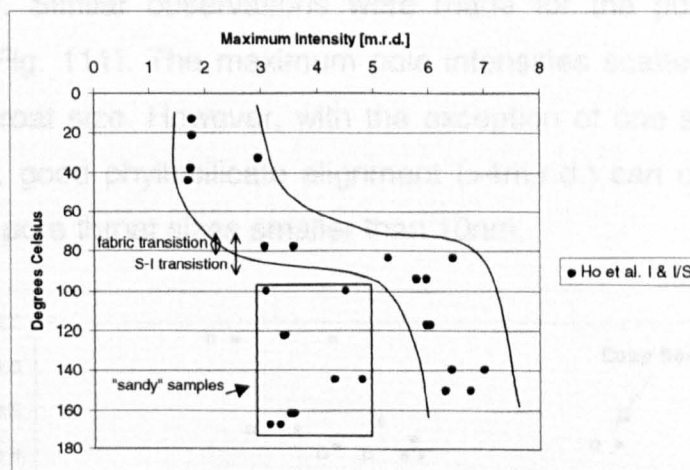


Fig. 109 HRXTG data from Ho et al. (1999). Maximum pole intensities are plotted against in situ formation temperature assuming a thermal gradient of 37 C/km and a surface temperature of 10 C. The box marks samples which were described as showing larger concentrations of detrital quartz grains.

As shown in Part A of this study, during the purely mechanical part of compaction the porosity of a mudstones is mainly controlled by its lithology (grain size) and the governing effective stress. As a consequence of different burial histories, these stresses occur at different formation temperatures and geological ages. Due to the kinetics of the smectite-to-illite reaction (Velde & Vasseur, 1992; Cuadros & Linares, 1996) this means that clay mineral diagenesis affects sedimentary rocks at different stages of mechanical compaction.

In order to examine the influence of non-mechanical processes on compaction it is necessary to establish whether changes in mudstone porosity and pore size can be related to both changes of the measured phyllosilicate fabric and the diagenetic grade. It is also of great interest whether grain size has a significant control on the impact of non-mechanical processes on mudstone compaction.

8.4.1 General correlation of the phyllosilicate fabric with porosity, pore size and grain size

In this study, no general relation between the degree of phyllosilicate alignment and porosity was revealed by the HRXTG measurements (Fig. 110). However, with the exception of one deep sea sample, good phyllosilicate alignment ($>4\text{m.r.d.}$) was only found in samples with less than 15% porosity. Similar observations were made for the pore sizes of the sample set (Fig. 111). The maximum pole intensities scatter widely for any given pore throat size. However, with the exception of one sample from the Caspian Sea, good phyllosilicate alignment ($>4\text{m.r.d.}$) can only be found in samples with pore throat sizes smaller than 10nm.

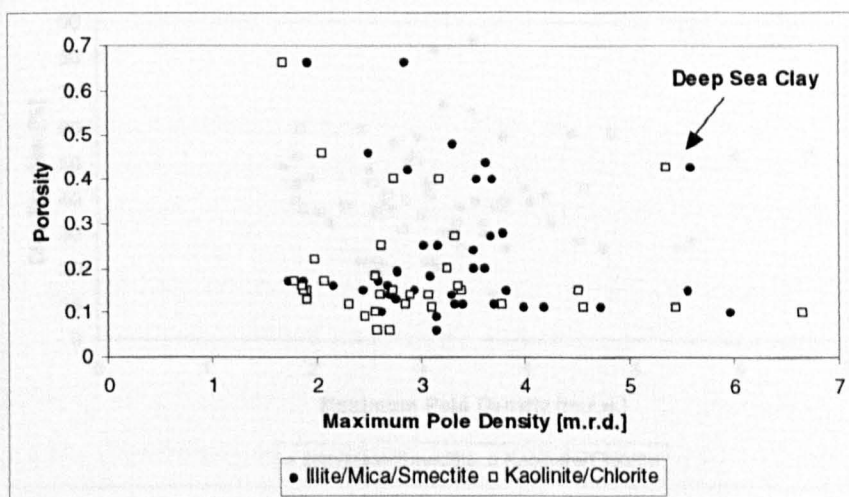


Fig. 110 Plot of the measured maximum pole densities against porosity. Note that porosity data for the Mid-Norway well was not available.

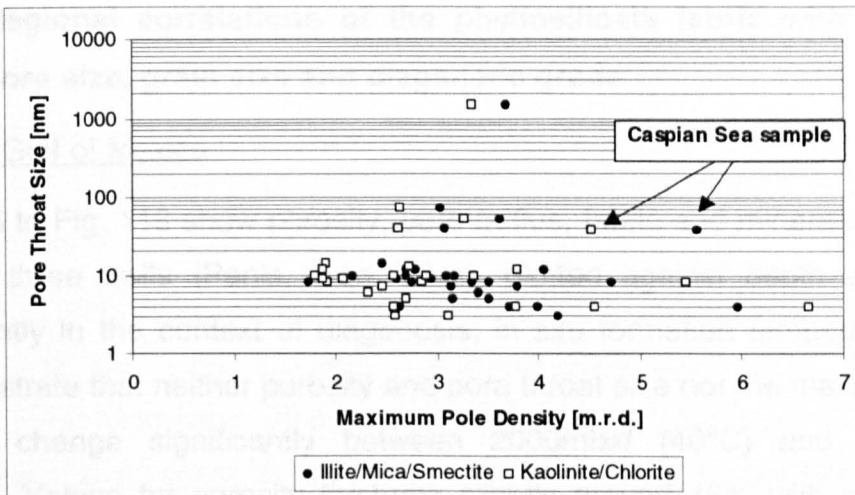


Fig. 111 Comparison of the mode or mean pore throat sizes with the maximum pole densities. Pore size data was limited to the samples listed in Table 37.

In addition, the correlation of maximum pole density and clay fraction in Fig. 112 revealed that there is no obvious connection between the two parameters. These results confirm earlier observations (this chapter), where the granulometrical composition of the silt fraction was more significant for the primary phyllosilicate fabric than the overall grain size.

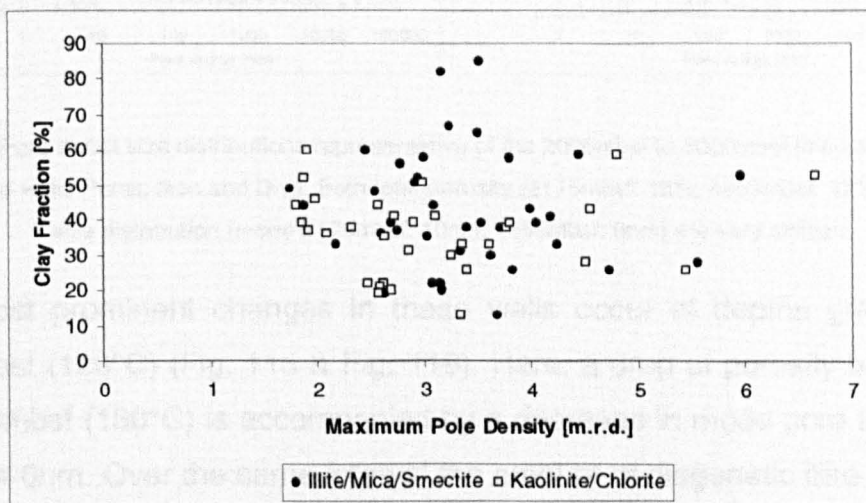


Fig. 112 Plot of the measured maximum pole densities against clay fraction.

8.4.2 Regional correlations of the phyllosilicate fabric with porosity, pore size, grain size and diagenetic grade

8.4.2.1 Gulf of Mexico

Fig. 115 to Fig. 118 show porosity, pore radius, fabric and mineralogical data for the three wells (Panis, Ikon, Diva), plotted against depth and, more importantly in the context of diagenesis, in situ formation temperature. The data illustrate that neither porosity and pore throat size nor the maximum pole density change significantly between 2000mbsf (40°C) and 5000mbsf (120°C). Values for porosity fluctuate slightly around 15% with mode pore throat sizes around 10nm (Fig. 113). The maximum pole densities in this interval hardly exceed 3.0m.r.d. X-ray diffraction analyses reveals that significant clay mineral recrystallization is absent in this interval.

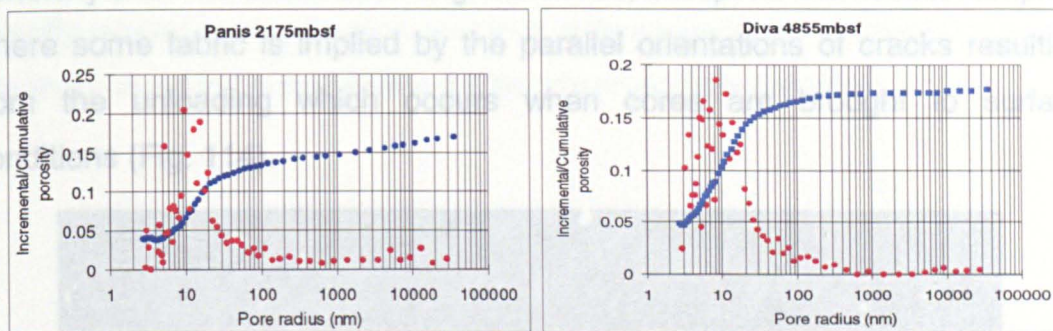


Fig. 113 Pore throat size distributions representative of the 2000mbsf to 5000mbsf interval of the Gulf of Mexico wells Panis, Ikon and Diva. Both total porosity (2175mbsf: 15%, 4855mbsf: 17%) and pore size distribution (mode 2175mbsf: 10nm, 4855mbsf: 9nm) are very similar.

The most prominent changes in these wells occur at depths greater than 5000mbsf (120°C) (Fig. 115 & Fig. 116). Here, a drop of porosity below 10% at 5649mbsf (130°C) is accompanied by a decrease in mode pore throat size to about 6nm. Over the same interval the amount of diagenetic illite (% illite in I/S) increases to 80%.

Most dramatic are these changes in the deepest (hottest) core samples from Diva (5511mbsf-5649mbsf; 128°C-130°C). Within 140m porosity drops by 25%_{rel} and illite in I/S increases by 40% (Fig. 117 & Fig. 118). A comparison of porosity with diagenetic illite and clay fraction (Fig. 119) reveals that these parameters are weakly correlated in this interval. Although consistent with the

predictions of the mechanical compaction model, the correlation between clay fraction and porosity is weaker than that between illitization and porosity. A similar observation was made for the relation between pore throat size, clay fraction and illitization (Fig. 120). In both cases, diagenesis is of slightly greater influence than lithology.

Changes in the degree of phyllosilicate alignment are much less prominent (Fig. 115 to Fig. 118). Maximum pole densities range from very weak (<2m.r.d.) to moderate (3-4m.r.d.) and, even in samples which have undergone the smectite to illite transition (5647mbsf & 5649mbsf), never reach the values of 5-6m.r.d. measured by Ho et al. (1999) in lower temperature samples from the coastal Gulf of Mexico section (Fig. 121). These results are qualitatively consistent with the BSEM images. These generally show no evidence of aligned fabrics, except for the hottest samples, where some fabric is implied by the parallel orientations of cracks resulting from the unloading which occurs when cores are brought to surface conditions (Fig. 114).

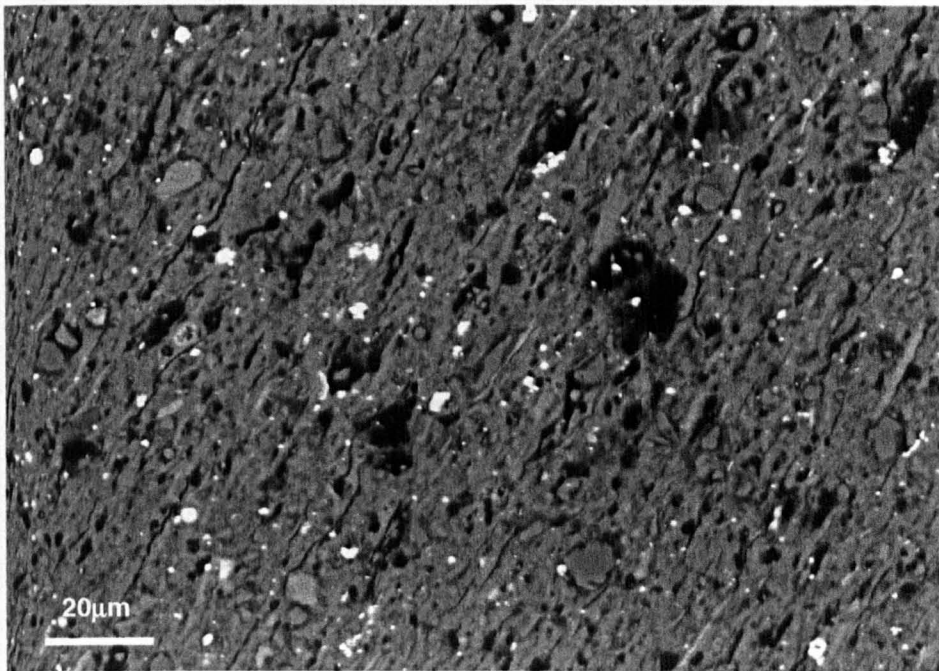


Fig. 114 BSEM image of a mudstone from Diva (5649mbsf). This sample showed the highest degree of alignment (3.41m.r.d.) of all GoM cores samples. The prevailing phyllosilicate fabric is highlighted by unloading cracks (black) and subparallel aligned detrital mica grains (bright grey).

The difference between the pole densities for the Gulf of Mexico in this study and those from Ho et al.'s (1999) study are likely related to two observations. Firstly, different burial histories provided a different kinetic background for the illitization in both regions. The samples from Ho et al.'s (1999) study are in general more diagenetically mature since a smaller formation thickness and higher thermal gradient allowed for a more intense recrystallisation of the clay minerals. Secondly, Ho et al. (1999) observed that the fabric intensities are much lower in samples rich in detrital quartz grains (Fig. 109). Unfortunately, no further information about the grain size of their samples set is available. Since, some of the samples from this study have pole densities similar to those of the "sandy" samples from Ho et al. (1999) it is not clear whether the different results were caused by significant differences in the analyzed lithologies. However, as shown earlier, phyllosilicate fabric in general is not directly related to clay fraction and thus differences in the diagenetic maturity are more likely to be the reason for the observed pole densities.

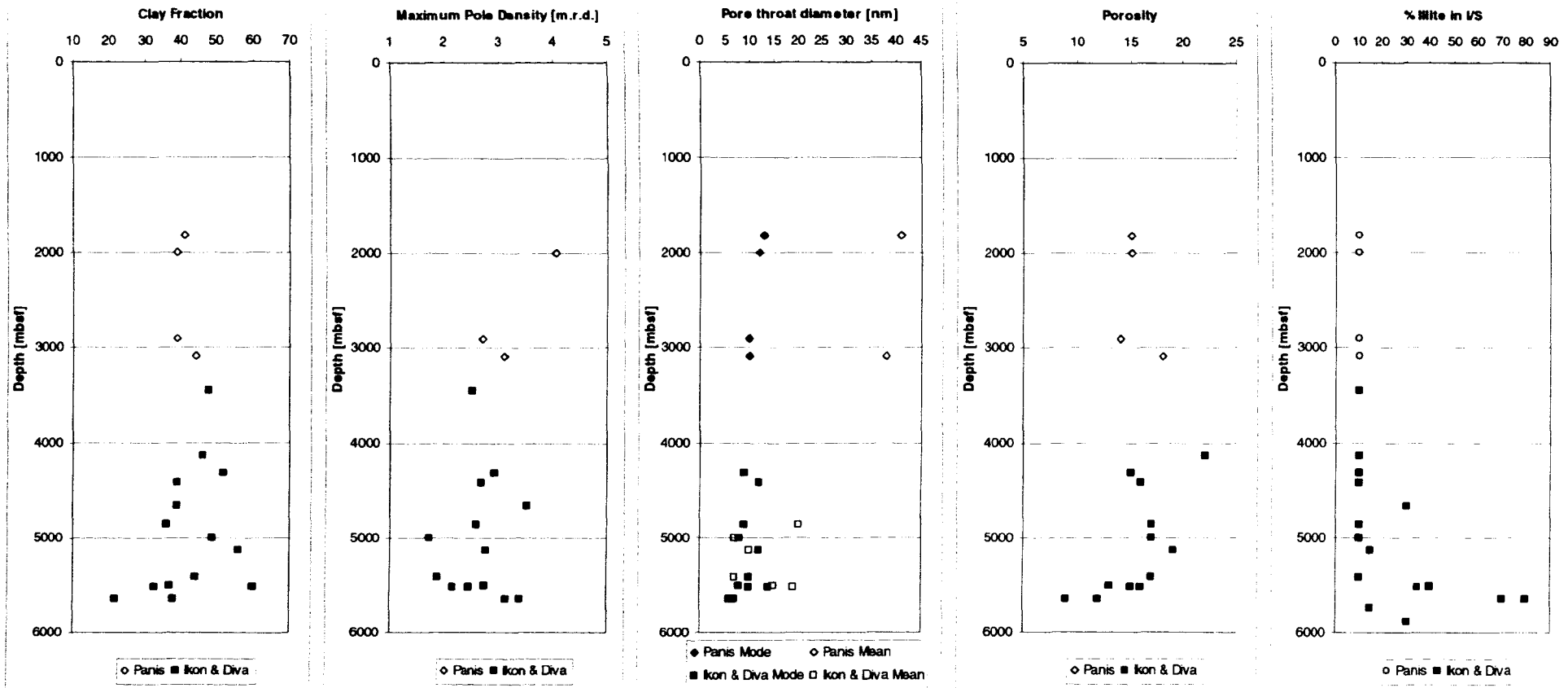


Fig. 115 A comparison of the physical and diagenetic properties of the three deep water Gulf of Mexico wells. The different parameters are plotted against burial depth (mbsf). The maximum pole densities reflect values for I/S.

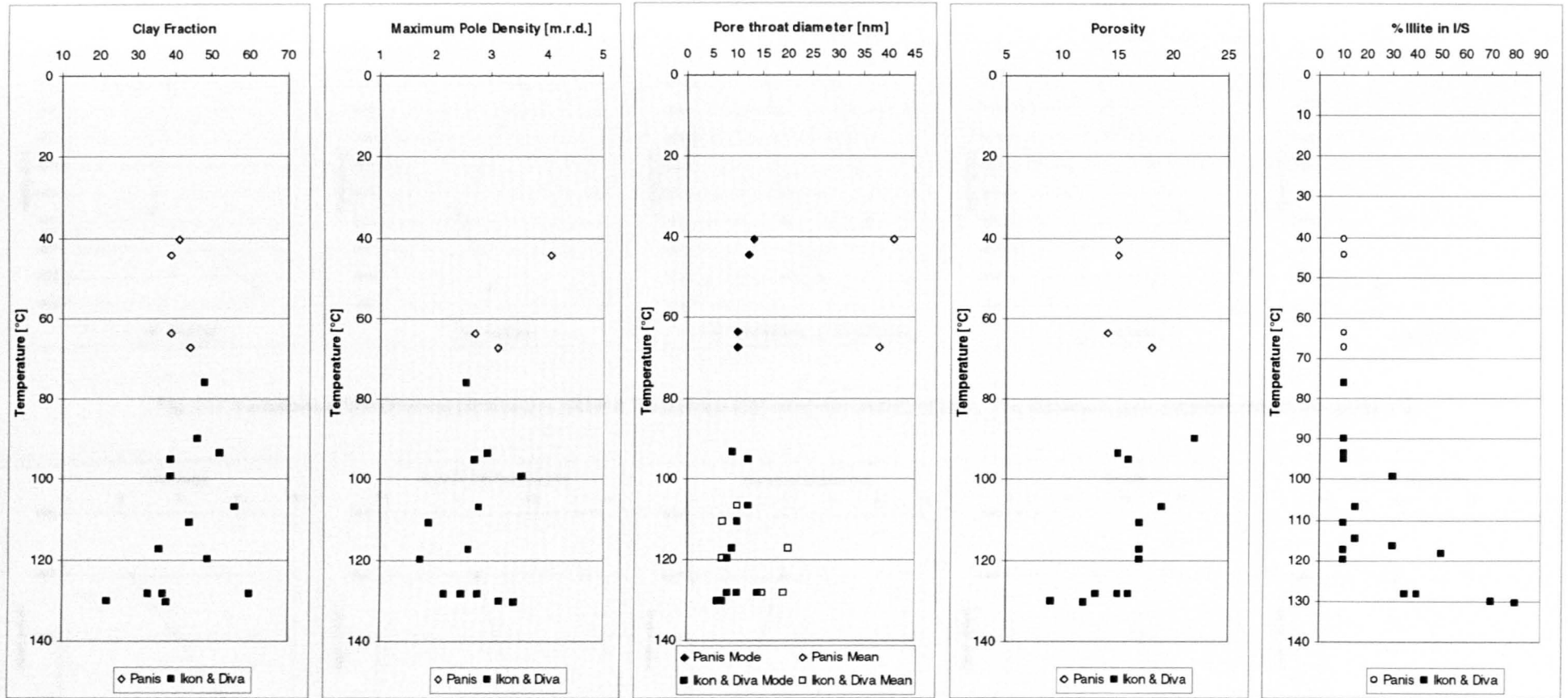


Fig. 116 A comparison of the physical and diagenetic properties of the three deep water Gulf of Mexico wells. The different parameters are plotted against temperature. The maximum pole densities reflect values for I/S.

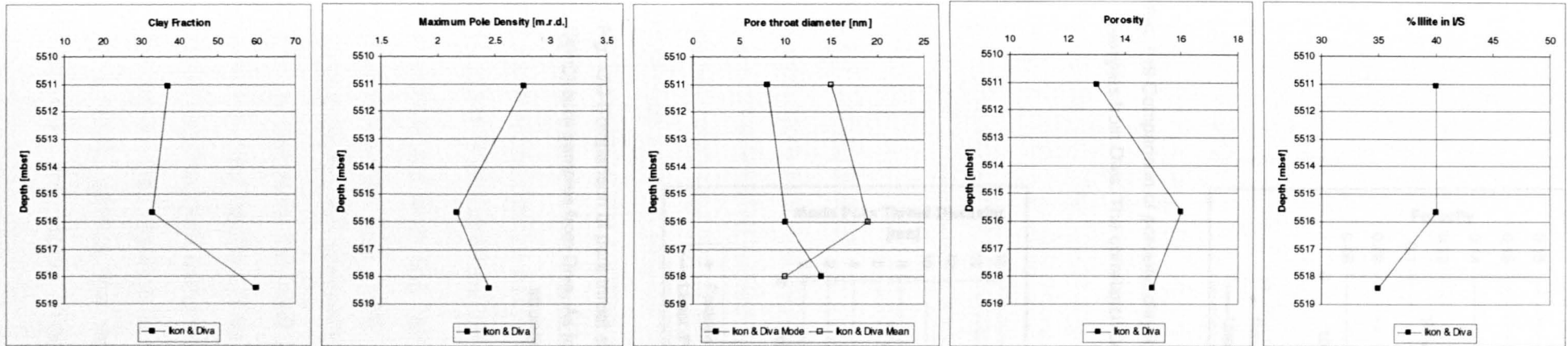


Fig. 117 Variations of the physical parameters within a 7m interval (551mbsf-5518mbsf) of Ikon. The maximum pole densities reflect values for I/S.

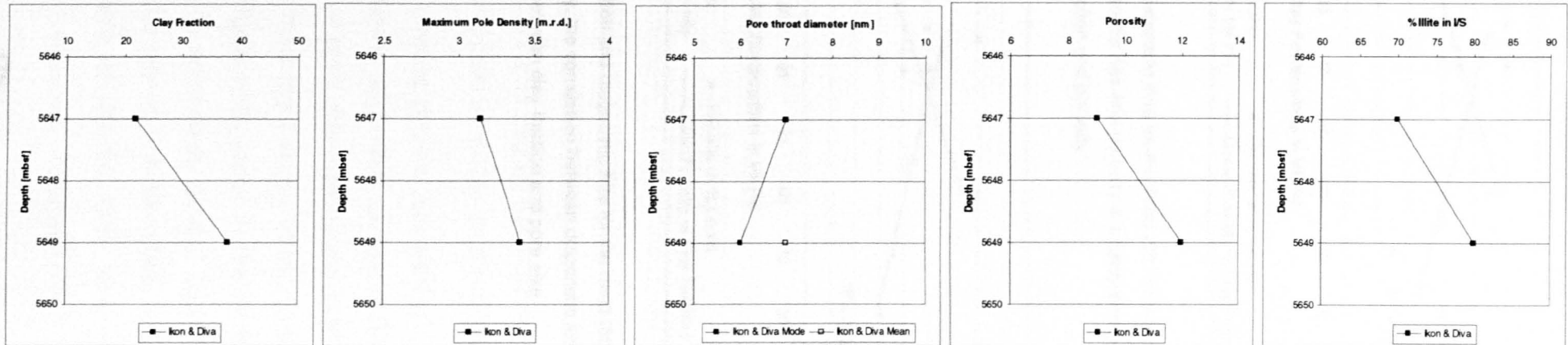


Fig. 118 Variations of the physical parameters within a 2m interval (5646mbsf-5650mbsf) of Ikon. The maximum pole densities reflect values for I/S.

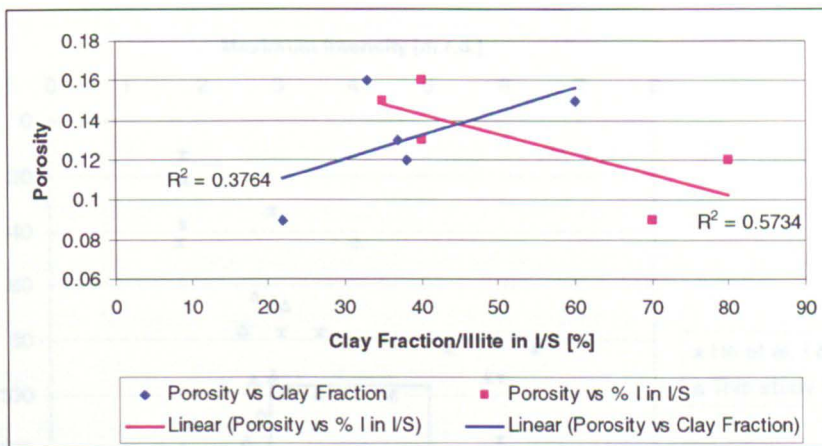


Fig. 119 Comparison of porosity, clay fraction and diagenetic illite for the deep (5511mbsf-549mbsf, 128°C-130°C) core samples from Diva. The correlation between diagenetic illite and porosity is slightly stronger than that between clay fraction and porosity.

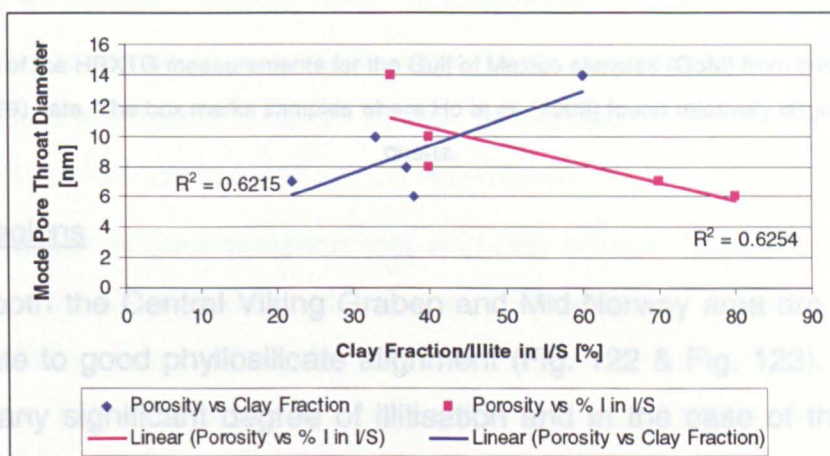


Fig. 120 Comparison of pore throat size, clay fraction and diagenetic illite for the deep (5511mbsf-549mbsf, 128°C-130°C) core samples from Diva. As for the porosity, the correlation between diagenetic illite and pore size is slightly stronger than that between clay fraction and pore size.

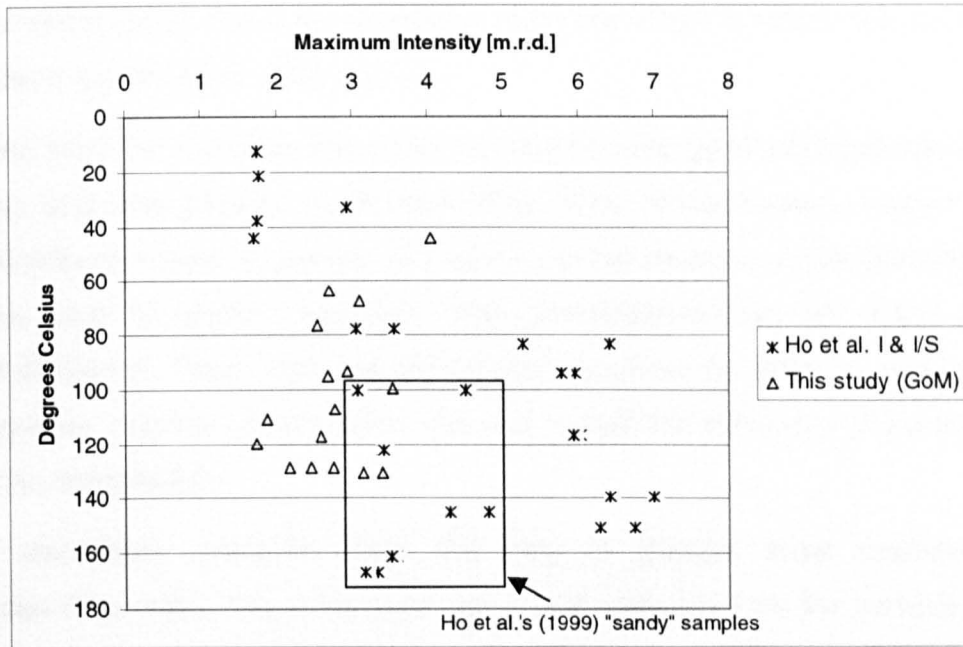


Fig. 121 The results of the HRXTG measurements for the Gulf of Mexico samples (GoM) from this study in comparison with Ho et al.'s (1999) data. The box marks samples where Ho et al. (1999) found relatively larger amounts of detrital quartz.

8.4.2.2 Other regions

Samples from both the Central Viking Graben and Mid-Norway area are fine-grained and show a moderate to good phyllosilicate alignment (Fig. 122 & Fig. 123). Neither of these wells revealed any significant degree of illitisation and in the case of the Central Viking Graben no relation between fabric and porosity or pore size distribution (see Appendix) was observed. Clay fraction and phyllosilicate alignment are also not related in either of the wells. However, the shallowest sample from the Mid-Norway well was very rich in silt- and sand-sized detrital mica, which created a so-called "mica fabric" (Fig. 101). Relatively large stack of this crystals led to increased pole densities for this sample (Fig. 123).

The sample set from the North Viking Graben shows very similar characteristics to that from Mid-Norway (Fig. 124). The observed alignment of phyllosilicates is moderate to good and shows no relation to porosity or pore size distribution (see Appendix). The main difference between this well and those from the Central Viking Graben and Mid-Norway area is the clay fraction. The latter is significantly lower in the North Viking Graben and explains the frequent occurrence of silt- to sand-sized detrital mica (Fig. 100). It is these grains again that resulted in some of the higher pole densities. In addition to frequently causing mica fabrics the large amounts of detrital mica also masked any ongoing illitisation in the North Viking Graben samples. Although XRD traces revealed the

presence of expandable material (smectite) even the $<2\mu\text{m}$ fraction was too rich in detrital mica to allow a quantification of illite in I/S.

The samples from the Caspian Sea show a good to very good phyllosilicate alignment for both coarse and fine-grained mudstones (Fig. 125). Nevertheless, neither porosity nor pore size distribution (see Appendix) are related to the maximum pole densities. Similar to most of the Gulf of Mexico samples, high temperatures did not result in significant degrees of illitisation. Thus, any clay diagenetic influence on fabric or porosity should be limited. However, the low porosities in this well reveal the efficiency of purely mechanical processes on compaction.

With one exception, samples from the Bay of Bengal have moderately aligned phyllosilicates (Fig. 126). The measured very good alignment for the sample at 2310mbsf is again related to silt-sized detrital mica. A systematic relationship between fabric and porosity or pore size distribution (see Appendix) was not observed. Clay fraction is not related to phyllosilicate fabric. Due to a lack of sample material the progress of the smectite-to-illite transformation could not be determined.

The strong correlation of sedimentation rate and clay mineral alignment observed for the deep sea clays of the Central Bermuda Rise is not reflected in the total porosity of these sediments (Fig. 127). Here, neither clay fraction nor phyllosilicate alignment are related to porosity. However, Fig. 127 reveals that very good degrees of phyllosilicate alignment can be reached in shallow and clay diagenetically unaffected deep sea formations.

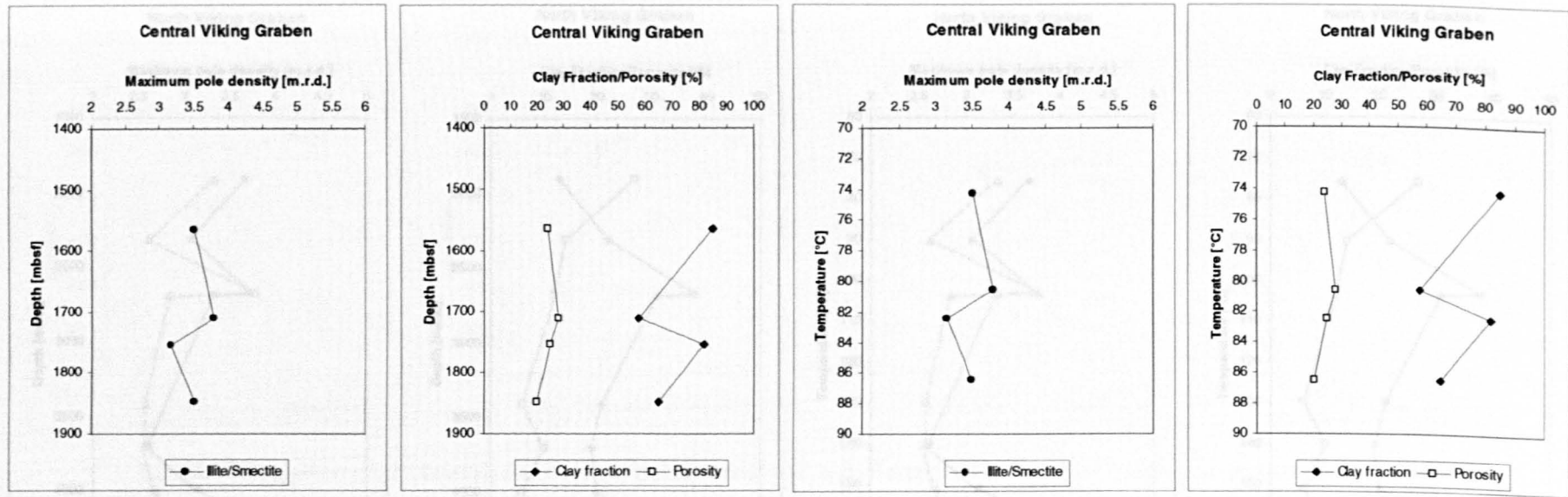


Fig. 122 A comparison of the observed degree of phyllosilicate alignment with changes in lithology (clay fraction) and porosity: Central Viking Graben.

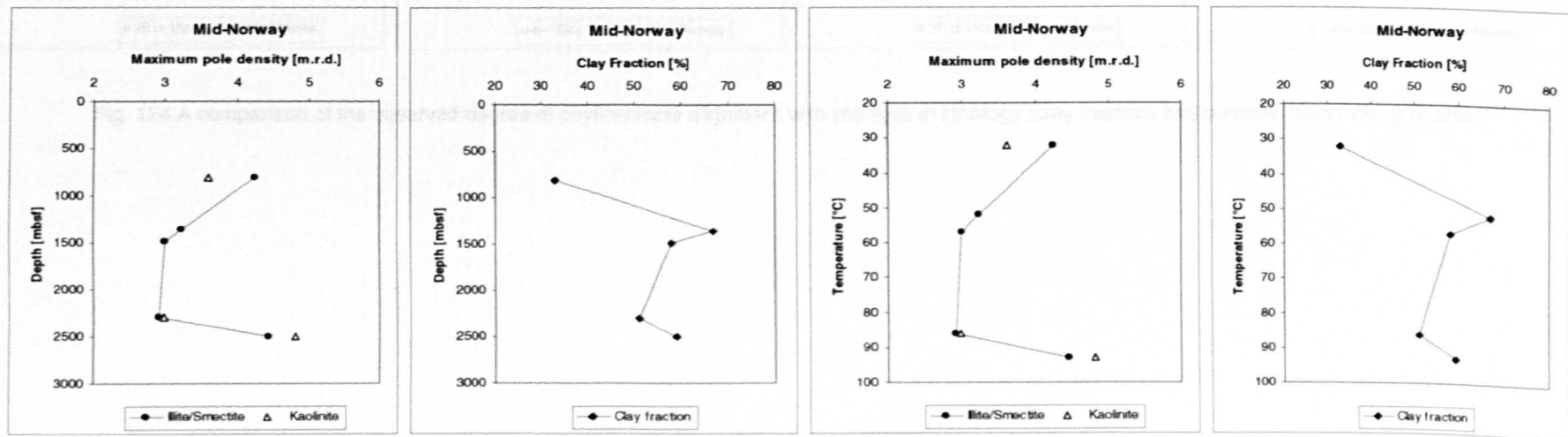


Fig. 123 A comparison of the observed degree of phyllosilicate alignment with changes in lithology (clay fraction): Mid-Norway.

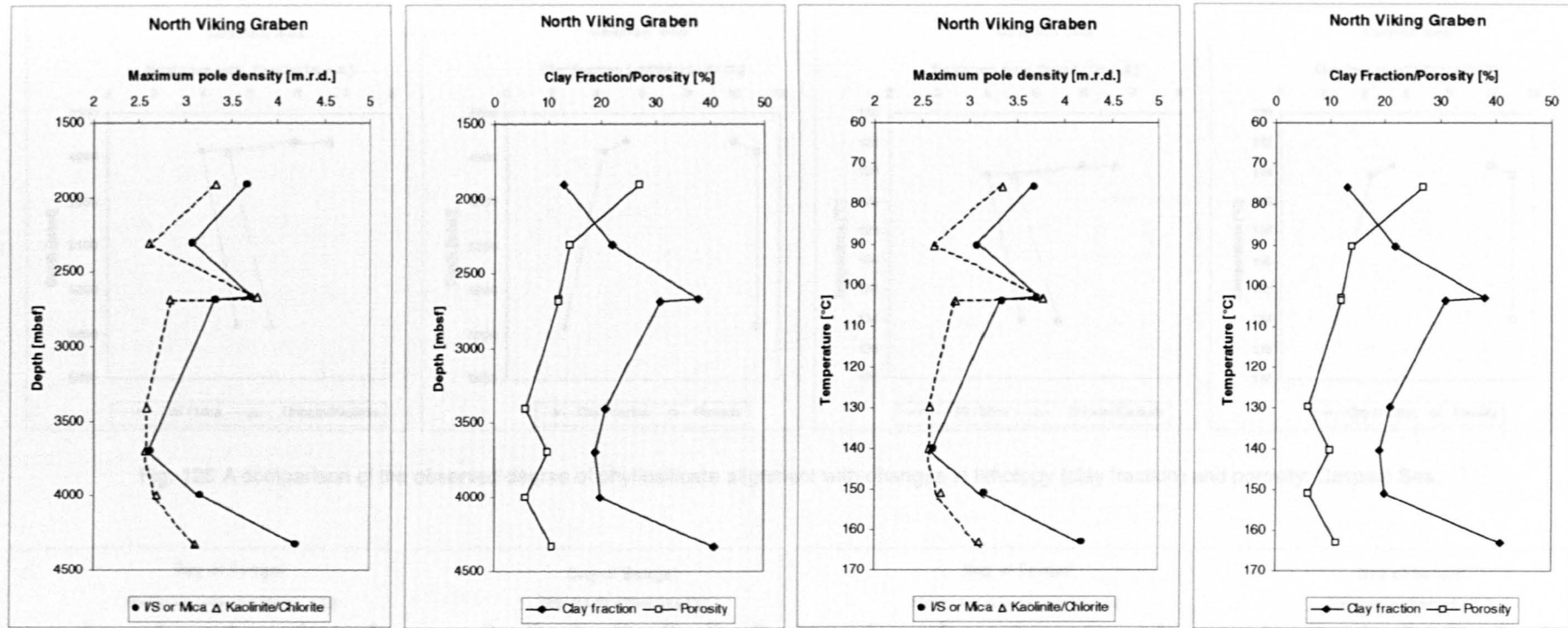


Fig. 124 A comparison of the observed degree of phyllosilicate alignment with changes in lithology (clay fraction) and porosity: North Viking Graben.

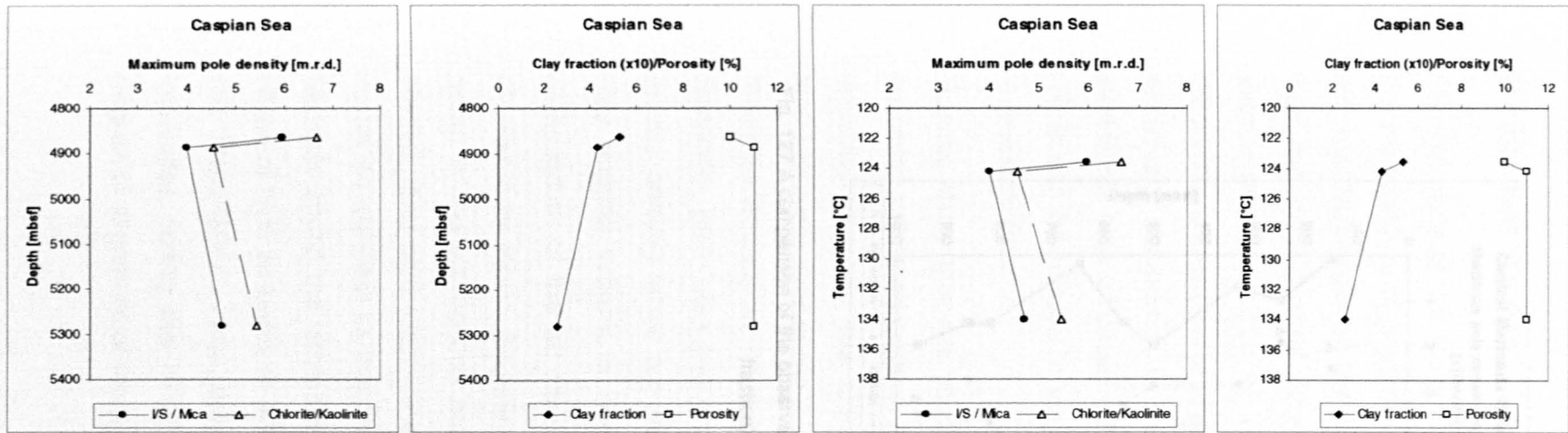


Fig. 125 A comparison of the observed degree of phyllosilicate alignment with changes in lithology (clay fraction) and porosity: Caspian Sea.

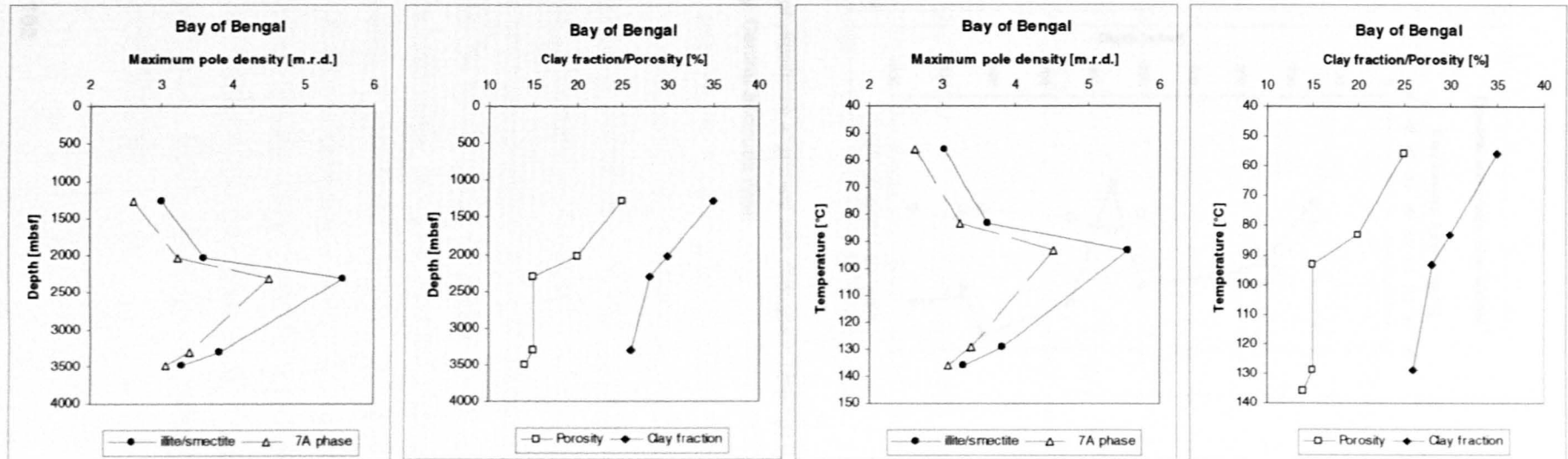


Fig. 126 A comparison of the observed degree of phyllosilicate alignment with changes in lithology (clay fraction) and porosity: Bay of Bengal.

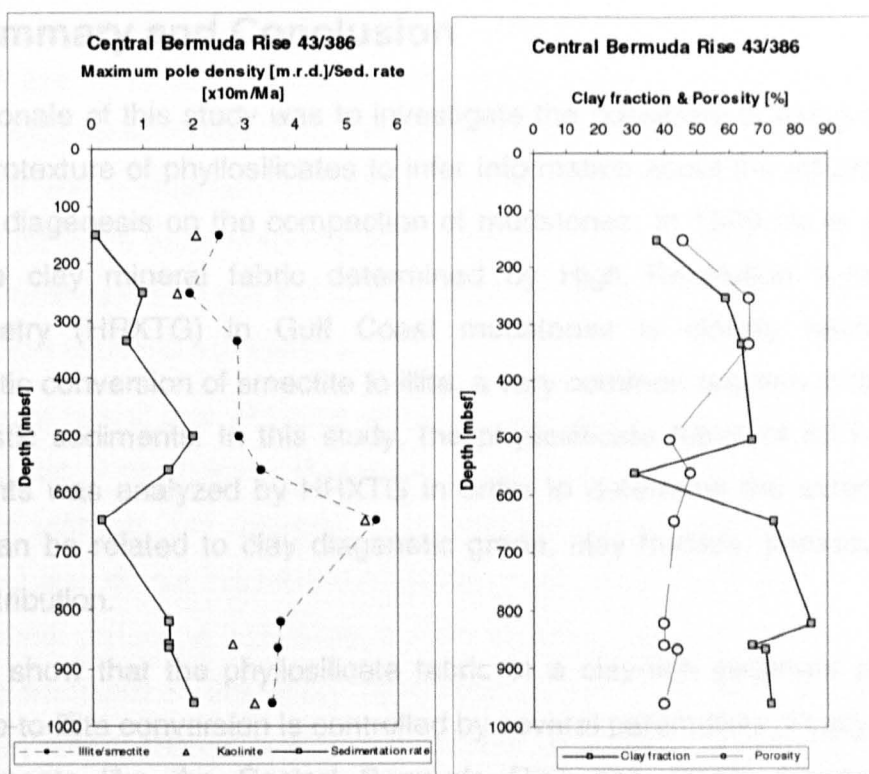


Fig. 127 A comparison of the observed degree of phyllosilicate alignment with changes in lithology (clay fraction) and porosity: Central Bermuda Rise.

9 Summary and Conclusion

The rationale of this study was to investigate the possibility of using changes in the microtexture of phyllosilicates to infer information about the influence of clay mineral diagenesis on the compaction of mudstones. In 1999 Ho et al. showed that the clay mineral fabric determined by High Resolution X-ray Texture Goniometry (HRXTG) in Gulf Coast mudstones is closely related to the diagenetic conversion of smectite to illite, a very common reaction in fine-grained siliciclastic sediments. In this study, the phyllosilicate fabric of 83 fine-grained sediments was analyzed by HRXTG in order to determine the extent to which fabric can be related to clay diagenetic grade, clay fraction, porosity and pore size distribution.

Results show that the phyllosilicate fabric of a clay-rich sediment prior to the smectite-to-illite conversion is controlled by several parameters. Firstly, deep sea environments like the Central Bermuda Rise can create situations where hydrodynamic processes control the degree of clay mineral alignment. Here, lower sedimentation rates clearly led to initially better aligned clay particles. Secondly, grain size and grain shape seem to have a complex control not only on the primary fabric but also on the reorientation of phyllosilicates. Since the clay fraction ($<2\mu\text{m}$) is dominated by platy minerals it is the granulometric composition of the silt fraction ($2\mu\text{m}$ - $63\mu\text{m}$) which is significant for the overall phyllosilicate fabric. Samples with high amounts of lath shaped minerals (clay & mica) in the silt fraction not only show better degrees of alignment at earlier stages, they also seem to improve the alignment more rapidly with increasing burial. In contrast to this, higher amounts of spherical minerals like quartz or feldspar inhibit the development of a strong phyllosilicate fabric. An additional effect of high amounts of silt- to sand-sized detrital mica is what is termed here the "mica fabric". Here, larger stacks of detrital mica can lead to higher fabric intensities during the HRXTG measurements, which often do not reflect the degree of alignment of the majority of phyllosilicates.

Since the main aim of this investigation was to reveal how alterations of the phyllosilicate fabric and clay diagenetic grade relate to porosity and pore size, several wells were chosen where in situ temperatures cover the levels typical for the onset and completion of the smectite-to-illite conversion. The main focus was put on three wells from the Gulf of Mexico (GoM), since Ho et al.'s (1999) study concentrated on the same area and the sample availability was sufficient to cover the critical temperatures.

The results reveal that although similar in age and temperature, samples from the GoM are of much lower diagenetic grade than those from Ho et al.'s (1999) study. In addition, the degrees of phyllosilicate alignment are not only much lower, but also do not increase substantially with diagenetic grade. A comparison of the burial history of both case studies showed that high sedimentation rates and low heatflows in this study have retarded the smectite-to-illite conversion. Thus, any fabric change due to clay mineral diagenesis was inhibited. Only for the very deepest and hottest samples of Diva the transformation of smectite into illite has just started. The analysis of the remaining wells delivered similar results. In most cases the clay diagenetic grades were either too low or undetectable to reveal any influence on the phyllosilicate fabric.

A systematic relationship between porosity or pore size distribution and phyllosilicate fabric was not observed. However, the very deepest samples of the GoM showed some indications for a decrease in porosity and pore size parallel to an increase in pore density and diagenetic grade.

In general, it was revealed that purely mechanical processes are sufficient to reduce mudstone porosity and modal pore throat sizes to values of 10% and less than 8nm, respectively. It was also shown that high burial depths (>5000mbsf) do not necessarily result in mudstones with well aligned phyllosilicates.

10 Final Conclusions

In general, the results of this study support the mechanical compaction models previously published by Skempton (1970), Burland (1990) and Yang & Aplin, (submitted). Grain size (clay fraction) seems to be the single most important lithological control on the purely mechanical compaction of fine-grained, siliciclastic sediments. However, the previously observed positive correlation between nannofossil content and porosity (e.g. Bryant & Rack, 1990; Kraemer et al., 2000) was also confirmed. This has important implications for investigations similar to the compaction study of Dugan & Flemings (2000a/b) on the New Jersey Continental Margin. Here, differences in the porosity and permeability of fossil-poor and fossil-rich sediments can have significant implications for the prediction of pore pressures based on sedimentation-compaction models.

The analysis by HRXTG revealed that prior to the diagenetic conversion of smectite into illite the phyllosilicate fabric of fine-grained sediments is mainly controlled by hydrodynamic (sedimentation rate) and granulometric parameters (grain size and shape distribution of the silt fraction). A comparison with Ho et al.'s (1999) study also suggests that in sediments where the smectite-to-illite conversion has significantly progressed, the duration of the illitisation (i.e. recrystallisation) is of major importance for the development of a preferred phyllosilicate orientation. Nevertheless, a systematic relationship between porosity or pore size distribution and phyllosilicate fabric was observed neither for sediments prior to nor within the smectite-to-illite conversion.

In general, it was shown that purely mechanical processes are sufficient to reduce mudstone porosity and modal pore throat sizes to values of 10% and less than 8nm, respectively. Furthermore, it was revealed that high burial depths (>5000mbsf) do not necessarily result in mudstones with well aligned phyllosilicates.

11 Future Work

The basic controls on the purely mechanical compaction of mudstones are reasonably well understood, at least from a practical, petroleum geological perspective. The influence of grain sorting and fossil material on the pore size distributions should be examined further, since these have a significant impact on the permeability of fine-grained sediments. Regarding the quantification of the phyllosilicate fabric of mudstones by HRXTG, this study has shown that much more work is necessary to establish whether this technique can be used to quantify changes in the physical properties due to diagenetic processes. In addition, besides its use as an indicator for non-mechanical compaction, more work is needed on the influence of changes in the phyllosilicate fabric on other petrophysical properties such as permeability, sonic velocity or mechanical strength. Suggested further work is described below:

1. A methodology should be developed to characterize the grain sorting of the silt fraction in fine-grained sediments. This could either be done by a better calibration of the applied Sedigraph™ method or by using optical methods such as the computer aided image analysis of scanning electron micrographs. The results should help to explain why fine-grained sediments with similar clay fractions can have different porosities and permeabilities at the same effective stress.
2. An integrated study to understand the mechanical compaction of fine-grained, fossil-rich siliciclastic sediments. Several case studies should be used to quantify the influence of fossil material in clay-rich sediments on physical properties like porosity, pore size distribution and permeability. This could help to better constrain traditional mechanical compaction models in marine environments with changing sedimentary facies.

3. More combined studies of the phyllosilicate fabric and physical properties of mudstone sequences where the completion of the smectite-to-illite conversion is reached. In these studies both High Resolution X-ray Texture Goniometry (HRXTG) and transmission electron microscopy (TEM) should be applied to obtain a detailed understanding of the fabric changes during clay mineral diagenesis. These analyses should then be compared to alterations of the porosity and pore size distribution of these sediments.

4. A study about the influence of changing phyllosilicate fabrics on the hydraulic and acoustic properties of fine-grained sediments. Since an increase in the preferred orientation of phyllosilicates results in an increase in the textural heterogeneity of a sediment, the implications for directed permeability and sonic velocity should be significant. The results of this research should not only help to predict the fluid flow in sedimentary basins but also to locate clay mineral diagenesis in seismic or sonic surveys.

References

- AHN, J.H., PEACOR, D.R. (1986) Transmission and analytical electron microscopy of the smectite-to-illite transition. *Clays and Clay Minerals*, 34, 2, 165-179.
- ALLISON, M.A., NITTROUER, C.A. (1998) Identifying accretionary mud shorefaces in the geologic record: insights from the modern Amazon dispersal system. In Schieber, J., Zimmerle, W., Sethi, P.S. (eds.) *Shales and Mudstones I: Basin studies, Sedimentology, and Paleontology*. E. Schweizerbart'sche Verlagsbuchhandlung Stuttgart, 147-161.
- APLIN, A. C.; YUNLAI YANG; HANSEN, S. (1995) Assessment of beta, the compression coefficient of mudstones and its relationship with detailed lithology - *Marine and Petroleum Geology*, 12, No 8, 955-963.
- APLIN, A.C. (2000) Mineralogy of modern marine sediments: A geochemical framework. In Vaughan, D.J. & Wogelius, R.A. (eds.) *European Mineralogical Union Notes on Mineralogy: Volume 2 Environmental Mineralogy*. Eotvos University Press, Budapest. 4, 125-172.
- APLIN, A.C., FLEET, A.J., MACQUAKER, J.H.S. (eds.) (1999) *Muds and mudstones: physical and fluidflow properties*. Geol. Soc. Spec. Publ., 158, 1-9.
- ATHY, L.F. (1930) Density, porosity, and compaction of sedimentary rocks. *AAPG Bulletin*, 14, 1-24.
- ATWATER, G.I., MILLER, E.E. (1965) The effect of decrease in porosity with depth on future development of oil and gas reserves in south Louisiana. *AAPG Bulletin*, 49, 334.
- AUDET, D.M., MCCONNELL, J.D.C. (1992) Forward modeling of porosity and pore pressure evolution in sedimentary basins. *Basin Res.*, 4, 147-162.
- AUSTIN, J.A., CHRISTIE-BLICK, J., MALONE, M.J. AND SHIPBOARD SCIENTIFIC PARTY (1998) *Proceedings of the Ocean Drilling Program Initial Reports*. 174A, College Station, TX.

- AUSTIN, J.A., JR., CHRISTIE-BLICK, N., MALONE, M.J., ET AL. (1998) Proceedings of the Ocean Drilling Program, Initial Reports, Vol. 174A.
- BAKER, D.W., WENK, H.R., CHRISTIE, J.M. (1969) X-ray analysis of preferred orientation in fine-grained quartz aggregates. *J. Geol.*, 77, 144-172.
- BALDWIN, B., BUTLER, C.O. (1985) Compaction curves. *AAPG Bulletin*, 69, 4, 622-626.
- BARKER, P., DALZIEL, W.D. AND SHIPBOARD SCIENTIFIC PARTY (1974) Initial Reports of the Deep Sea Drilling Project. 36, College Station, TX.
- BATHURST, R.G.C. (1975) Diagenesis on the Sea Floor. In *Carbonate Sediments and their diagenesis. Developments in sedimentology*, 12, 361-413.
- BENNET, R.H., O'BRIEN, N.R., HULBERT, H. (1991) Determinants of Clay and Shale Microfabric Signatures: Processes and Mechanisms. In Bennett, R.H., Bryant, W.R., Hulbert, M.H. (eds.) *Microstructure of Fine-Grained Sediments*. Springer Verlag, 5-33.
- BJØRKUM, P.A. (1996) How important is pressure in causing dissolution of quartz in sandstones? *Journal of Sedimentary research*, 66, 1, 147-154.
- BLANK, P., SEIFERT, W. (1976) Zur Untersuchung diagenetischer Tonmineralbildungen und deren experimentelle Modellierung. *Z. angew. Geologie*, 22, 560-564.
- BLUM, P., XU, J., DONTIREDDY, S. (1996) Geotechnical properties of Pleistocene sediments from the New Jersey Upper Continental Slope. In: Mountain, G.S., Miller, K.G., Blum, P., Poag, C.W., Twichell, D.C. (Eds.), *Proceedings of the Ocean Drilling Program Scientific Results 150*. Ocean Drilling Program, College Station, TX, 377-384.
- BOLTON, A., MALTMAN, A. (1998) Fluid-flow pathways in actively deforming sediments: the role of pore fluid pressures and volume change. *Marine and Petroleum Geology*, 15, 281-297.

- BOULTON, G.S., DOBBIE, K.E. (1993) Consolidation of sediments by glaciers: relations between sediment geotechnics, soft-bed glacier dynamics and subglacial ground-water flow. *Journal of Glaciology*, 39, 131, 26-44.
- BOUMA, A.H. (1962) *Sedimentology of some flysch deposits. A graphic approach to facies interpretation.* Elsevier Publ. Co., Amsterdam.
- BOWLES, F.A., BRYANT, W.R., WALLIN, C. (1969) Microstructure of unconsolidated and consolidated marine sediments. *Journal of Sedimentary Petrology*, 39, 4, 1546-1551.
- BOYCE, R.E. (1976) Leg 33, Definitions and laboratory techniques of compressional sound velocity parameters and wet-water content, wet-bulk density and porosity parameters by gravimetric and gamma attenuation techniques. In Schlanger, S.O., Jackson, E.D., et al. (eds.) *Initial Reports of the Deep Sea Drilling Project*, 33, 931-958.
- BOYCE, R.E. (1984) Methods for laboratory-measured physical properties. In Hay, W.W., Sibuet, J.C., et al. (eds.) *Initial Reports of the Deep Sea Drilling project*, 75, 1179-1187.
- BREDEHOEFT, J.D., DJEVANSHIR, R.D., BELITZ, K.R. (1988) Lateral fluid flow in a compacting sand-shale sequence: South Caspian Basin. *AAPG Bulletin*, 72, 416-424.
- BRITISH STANDARDS 1377, part 6 (1990) *Method of Test for Soils for Civil Engineering Purpose.* London: British Standard Institution.
- BRITISH STANDARDS 733. part 2 (1987) *Pyknometers. Part 2. Methods for calibration and use of pyknometers.* London: British Standard Institution.
- BRYANT, W.R., BENNETT, R.H., BURKETT, B.J., RACK, F.R. (1990) The fabric of a consolidating clayey sediment column, ODP site 697. *Proc., scientific results, ODP, Leg 113, Weddell Sea, Antarctica*, 225-237.
- BRYANT, W.R., RACK, F.R. (1990) 17. Consolidation characteristics of Weddel Sea sediments: results of ODP Leg 113. In Barker, P.F., Kennet, J.P. et al. (eds.) *Proceedings of the Ocean Drilling Program, Scientific Results*, Vol. 113, 211-223.

- BURLAND, J. B. (1990) On the compressibility and shear strength of natural clays. *Geotechnique*, 40, No 3, 329-378.
- BURYAKOVSKY, L.A., DJEVANSHIR, R.D (1986) Interaction of clay mineral transformation with thermobaric conditions at depth. *Geochem. Int.*, 23, 8, 99-106.
- BURYAKOVSKY, L.A., DJEVANSHIR, R.D., CHILINGAR, G.V. (1995) Abnormally-high formation pressures in Azerbaijan and the South Caspian Basin (as related to smectite ↔ illite transformation during diagenesis and catagenesis). *Journal of Petroleum Science and Engineering*, 13, 203-218.
- CARR, S. (1999) The micromorphology of Last Glaciation Maximum sediments in the southern North Sea. *Catena*, 35, 123-145.
- CASAGRANDE, A. (1936) The determination of the pre-consolidation load and its practical significance, *Proc. 1st Int. Conf. Soil Mech. Found. Eng.*, 3, (D-33), 60-64.
- CHAIKA, C., DVORKIN, J. (2000) Porosity reduction during diagenesis of diatomaceous rocks. *AAPG Bulletin*, 84, 8, 1173-1184.
- CHAIKA, C., WILLIAMS, L.A. (2001) Density and Mineralogy variations as a function of porosity in Miocene Monterey Formation oil and gas reservoirs in California. *AAPG Bulletin*, 85, 1, 149-167.
- CHAMLEY, H. (1989) *Clay Sedimentology*. Springer-Verlag Berlin Heidelberg.
- CHEN, Q., NUR, A. (1991) Critical concentration models for the mechanical and acoustic properties of porous rocks and sediments. *Eos*, 72, 438.
- CLARKE, B.G., CHEN, C.C., AFLAKI, E. (1998) Intrinsic compression and swelling properties of a glacial till. *Quarterly Journal of Engineering Geology*, 31, 235-246.
- COCHRAN, J.R., STOW, D.A.V. AND SHIPBOARD SCIENTIFIC PARTY (1988) *Proceedings of the Ocean Drilling Program Initial Reports*. 116, College Station, TX.

- COLTON-BRADLEY, V.A. (1987) Role of pressure in smectite dehydration – effects on geopressure and smectite-to-illite transformation. AAPG Bulletin, 71, 11, 1414-1427.
- COMPTON, J.S. (1991) Porosity reduction and burial history of siliceous rocks from the Monterey and Siquoc Formations, Point Pedernales area, California. Geol. Soc. Amer. Bull., 103, 625-636.
- CONGER, P.S. (1942) Accumulation of diatomaceous deposits. Journal of Sedimentary Petrology, 12, 55-66.
- CRAIG, R. F. (1997): Soil Mechanics. 6. edition - E & FN SPON, Chapman & Hall, 485 p..
- CRAWFORD, C.B., BOZOUK, M. (1990) Thirty years of secondary consolidation in sensitive marine clay. Canadian Geotechnical Journal, 27, 315-319.
- CUADROS, J., LINARES, J. (1996) Experimental kinetic study of the smectite-to-illite transformation. Geochimica et Cosmochimica Acta, 60, 3, 439-453.
- CURTIS, C.D., LIPSHIE, S.R., OERTEL, G., PEARSON, M.J. (1980) Clay orientation in some Upper Carboniferous mudrocks, its relationship to quartz content and some inferences about fissility, porosity and compactional history. Sedimentology, 27, 333-339.
- DAVIES, T.A., LUYENDYK, B.P. AND SHIPBOARD SCIENTIFIC PARTY (1972) Initial Reports of the Deep Sea Drilling Project. 26, College Station, TX.
- DELAGE, P., TESSIER, D., MARCEL-AUDIGUIER, M. (1982) Use of the Cryoscan apparatus for observation of freeze-fractured planes of a sensitive Quebec clay in scanning electron microscopy. Can. Geotech., J., 19, 111-114.
- DELAGE, P.; LEFEBVRE, G. (1984) Study of a sensitive Champlain Clay and its evolution during consolidation. Can. Geotech. J., 21, 21-35.
- DEWHURST, D.N., APLIN, A.C., SARDA, J.P. (1999b) Influence of clay fraction on pore-scale properties and hydraulic conductivity of experimentally compacted mudstones. Journal of Geophysical Research, 104, No.B14, 29261-29274.

- DEWHURST, D.N., APLIN, A.C., SARDA, J.P., YANG, Y. (1998) Compaction-driven evolution of poroperm in natural mudstones: an experimental study. *Journal of Geophysical Research*, 103, 651-661.
- DEWHURST, D.N., APLIN, A.C., YANG, Y. (1999a) Permeability and fluid flow in natural mudstones. In: Aplin, A.C., Fleet, A.J. and Macquaker, J.H.S. (eds.) *Muds and Mudstones: Physical and Fluid Flow Properties*. Geological Society Special Publication 158, 23-43.
- DOLIGEZ, B., BESSIS, F., BURRUS, J., UNGERER, P., CHENET, P.Y. (1986) Integrated numerical simulation of the sedimentation heat transfer, hydrocarbon formation and fluid migration in a sedimentary basin: The THEMIS Model. In Burrus, J. (ed.) *Thermal modeling in sedimentary basins*. Editions Technip Paris, 173-195.
- DRIEF, A., NIETO, F. (2000) Chemical composition of smectites in clastic sediments. Implications for the smectite-illite transformation. *Clay Minerals*, 35, 665-678.
- DUGAN, B., FLEMINGS, P.B. (2000a) Overpressure and Fluid Flow in the New Jersey Continental Slope: Implications for Slope Failure and Cold Seeps. *Science*, 289, 288-291.
- DUGAN, B., FLEMINGS, P.B. (2000b) The New Jersey margin: compaction and fluid flow. *Journal of Geochemical exploration*, 69-70, 477-481.
- DUNOYER DE SEGONZAC, G. (1970) The Transformation of Clay Minerals during Diagenesis and Low-Grade Metamorphism: A Review. *Sedimentology*, 15, 281-346.
- DZEVANSHIR, R.D., BURYAKOVSKIY, L.A., CHLINGARIAN, G.V. (1986) Simple quantitative evaluation of porosity of argillaceous sediments at various depths of burial. *Sedimentary Geology*, 46, 169-175.
- ELLIOTT, W.C., MATISOFF, G. (1996) Evaluation of kinetic models for the smectite to illite transformation. *Clays and Clay Minerals*, 44, 1, 77-87.
- ELLOUZ-ZIMMERMANN, N., MASCLE, J. (2001) Introduction to papers resulting from a conference organized by the French research group "GDR Marges". *Marine and Petroleum Geology*, 443-444.

- ESSENE, E.J., PEACOR, D.R. (1995) Clay mineral thermometry – a critical perspective. *Clays and Clay Minerals*, 43, 5, 540-553.
- FABRICIUS, I.L. (2000) 10. Interpretation of burial history and rebound from loading experiments and occurrence of microstylolites in mixed sediments of Caribbean sites 999 and 1001. In Leckie, R.M., Sigurdsson, H., Acton, G.D., Draper, G. (eds.) *Proceedings of the Ocean Drilling Program, Scientific Results*, 165, 177-190.
- FREED, R.L., PEACOR, D.R. (1989) Variability in temperature of the smectite/illite reaction in Gulf Coast sediments. *Clay Minerals*, 24, 171-180.
- FÜCHTBAUER, H. (1967) Influence of different types of diagenesis on sandstone porosity: 7th World Petroleum Congress Proceedings, 2, 353-369.
- FÜCHTBAUER, H. (1979) Die Sandsteindiagenese im Spiegel der neueren Literatur. *Geologische Rundschau*, 68, 3, 1125-1151.
- FÜCHTBAUER, H. (ed.) (1988) *Sediment-Petrologie Teil II: Sedimente und Sedimentgesteine*. E. Schweizerbart'sche Verlagsbuchhandlung, Stuttgart.
- GALLOWAY, W.E. (1974) Deposition and diagenetic alteration of sandstone in Northeast Pacific arc-related basins: Implications for graywacke genesis. *Geol. Soc. Amer. Bull.*, 85, 379-390.
- GALLOWAY, W.E.; GARBER, J.L.; LIU, X.; SLOAN, B.J. (1993) Sequence stratigraphic and depositional framework of the Cenozoic fill, Central and Northern North Sea Basin. In Parker, J.R. (ed.) *Petroleum Geology of Northwest Europe: Proceedings of the 4th Conference*, The Geological Society London, 33-43.
- GARRISON, R.E., KENNEDY, W.J. (1977) Origin of solution seams and flaser structures in the Upper Cretaceous chalks of southern England. *Sed. Geol.*, 19, 107-137.
- GERBER, R.E., HOWARD, K. (2000) Recharge through a regional till aquitard: three-dimensional flow model water balance approach. *Ground Water*, 38, 3, 410-422.

- GIBSON, R.E., ENGLAND, G.L., HUSSEY, M.J.L. (1967) The theory of one-dimensional consolidation of saturated clays. I. Finite nonlinear consolidation of thin homogenous layers. *Geotechnique*, 17, 3, 261-273.
- GIBSON, R.E., SCHIFFMAN, R.L.O., CARGILL, K.W. (1981) The theory of one-dimensional consolidation of saturated clays. II. Finite nonlinear consolidation of thick homogenous layers. *Canadian Geotechnical Journal*, 18, 280-293.
- GILES, M.R., INDRELID, S.L., JAMES, D.M.D. (1998) Compaction – the great unknown in basin modeling. In Dueppenbecker, S.J. & Iliffe, J.E. (eds.) *Basin Modeling: Practice and Progress*. Geological Society, London, Special Publication, 141, 15-43.
- GILLOT, J.E. (1973) Methods of sample preparation for microstructural analysis of soil. *Soil microscopy. Proceedings, 4th International Working-Meeting on soil micromorphology*, Kingston, 143-164.
- GRADSTEIN, F.; BACKSTRÖM, S. (1996) Cenozoic biostratigraphy and palaeobathymetry, northern North sea and Haltenbanken. *Norsk Geologisk Tidsskrift*, 76, 3-32.
- GRAULS, D. (1999) Overpressures: causal mechanisms, conventional and hydromechanical approaches. *Oil & Gas Science and Technology – Rev. IFP*, 54, 6, 667-678.
- GREGERSEN, U. (1997) The depositional significance of 3-D seismic attributes in the Upper Cenozoic of the Central North Sea. *Petroleum Geoscience*, 3, 291-304.
- GREGERSEN, U. (1998) Upper Cenozoic channels and fans on 3D seismic data in the northern Norwegian North Sea. *Petroleum Geoscience*, 4, 67-80.
- GRIFFITHS, F.J.; JOSHI, R.C. (1990) Clay fabric response to consolidation. *Applied Clay Science*, 5, 37-66.
- HAMILTON, E.L. (1976) Variations of density and porosity with depth in deep sea sediments. *Journal of Sedimentary Petrology*, 46, 2, 280-300.

- Hansen, S. (1996a) A compaction trend for Cretaceous and Tertiary shales on the Norwegian Shelf based on sonic transit times. *Petroleum Geosciences*, 2, 159-166.
- HANSEN, S. (1996b) Quantification of net uplift and erosion on the Norwegian Shelf south of 66 N from sonic transit times of shale. *Norsk Geologisk Tidsskrift*, 76, 245-252.
- HENRIKSEN, S., VORREN, T.O. (1996) Late Cenozoic sedimentation and uplift history on the mid-Norwegian continental shelf. *Global and Planetary Change*, 12, 171-199.
- HERMANRUD, C.L., WENSAAS, L., TEIGE, G.M.G., VIK, H.M., NORDGARD BOLAS, HANSEN, S. (1998) Shale porosities from well logs on Haltenbanken (offshore mid-Norway) show no influence of overpressuring – Law, B.E., Ulmishek, G.F., Slavin, V.I. (eds.): *Abnormal pressures in hydrocarbon environments*; AAPG Memoir 70, 65-85.
- HILLIER, S., MATYAS, J., MATTER, A., VASSEUR, G. (1995) Illite/smectite diagenesis and its variable correlation with vitrinite reflectance in the Pannonian Basin. *Clays and Clay Minerals*, 43, 2, 174-183.
- HJULSTRØM, F. (1955) Transportation of debris by moving water. In Trask, P.D. (ed.) *Recent marine sediments*. SEPM Spec. Publ., 4, 5-31.
- HO, N.C., PEACOR, D.R., VAN DER PLUIJM, B.A. (1995) Reorientation of phyllosilicates in the mudstone-to-slate transition at Lehigh Gap, Pennsylvania. *Journal of Structural Geology*, 17, No.3, 345-356.
- HO, N.C. (1996) X-Ray Pole Figure Analysis. Software developed at the Geological Department, University of Michigan, USA.
- HO, N.C., PEACOR, D.R., VAN DER PLUIJM, B.A. (1996) Contrasting roles of detrital and authigenic phyllosilicates during slaty cleavage development. *Journal of Structural Geology*, 18, No.5, 615-623.
- HO, N.C., PEACOR, D.R., VAN DER PLUIJM, B.A. (1999) Preferred orientation of phyllosilicates in Gulf Coast mudstones and relation to the smectite-to-illite transition. *Clays and Clay Minerals*, 47, No.4, 495-504.

- HO, N.C., VAN DER PLUIJM, B.A., PEACOR, D.R. (2001) Static recrystallisation and preferred orientation of phyllosilicates: Michigamme Formation, northern Michigan. *Journal of Structural geology*, 23, 887-893.
- HOLEYWELL, R.C., TULLIS, T.E. (1975) Mineral reorientation and slaty cleavage in the Martinburg Formation, Lehigh Gap, Pennsylvania. *GSA Bulletin*, 86, 1296-1304.
- HOLLANDER, N.B. (1984) Geohistory and hydrocarbon evaluation of the Haltenbank area. In Norwegian Petroleum Society (ed.) *Petroleum Geology of the North European Margin*, Graham & Trotman, 383-388.
- HOLTEDAHL, H. (1993) Marine geology of the Norwegian continental margin. *Nor. geol. undes. Special Publication 6*, 1-150.
- HORSRUD, P., SØNSTEBØ, E.F., BØE, R. (1998) Mechanical and petrophysical properties of North Sea shales. *Int. J. Rock Mech. Min. Sci.*, 35, 8, 1009-1020.
- HOSSAIN, D. (1996) Direct and indirect permeability of fissured till. *Geotechnical Testing Journal*, 191-202.
- HOUSEKNECHT, D.W. (1987) Assessing the relative importance of compaction processes and cementation to reduction of porosity in sandstones. *AAPG Bulletin*, 71, 6, 633-642.
- HOWER, J.; ESLINGER, E.V.; HOWER, M.E.; PERRY, E.A. (1976) Mechanism of burial metamorphism of argillaceous sediment: 1. Mineralogical and chemical evidence. *Geological Society of America Bulletin*, 87, 725-737.
- HUENE, R. VON, NASU, N. AND SHIPBOARD SCIENTIFIC PARTY (1977) *Initial Reports of the Deep Sea Drilling Project*. 57, College Station, TX.
- ISAACS, C.M. (1981) Porosity reduction during diagenesis of the Monterey Formation, Santa Barbara coastal area, California. In Garrison, R.E. & Douglas, R.G. (eds.) *The Monterey Formation and related siliceous rocks of California*. Soc. Econ. Paleont. Mineral. Pacif. Section, 257-271.

- ISSLER, D.R. (1992) A new approach to shale compaction and stratigraphic restoration, Beaufort-Mackenzie Basin and Mackenzie Corridor, Northern Canada In: AAPG Bulletin, 76., N 8, 1170-1189.
- JACOB, G., KISCH, H.J., VAN DER PLUIJM, B.A. (2000) The relationship of phyllosilicate orientation, X-ray diffraction intensity ratios, and c/b fissility ratios in metasedimentary rocks of the Helvetic zone of the Swiss Alps and the Caledonides of Jaemtland, central western Sweden. *Journal of Structural Geology*, 22, 245-258.
- JADGOZINSKI, H. (1949) Eindimensionale Fehlordnung in Kristallen und ihr Einfluss auf die Röntgeninterferenzen. I. Berechnung des Fehlorderungsgrades aus den Röntgenintensitäten: *Acta Crystallogr.*, 2, 201-207.
- JONES, M. (1994) Mechanical principles of sediment deformation. In: Maltman, A. (ed.) *The geological deformation of sediments*. Chapman & Hall, 37-71.
- JORDT, H.; FALEIDE, J.I.; BJORLYKKE, K.; IBRAHIM, M.T. (1995) Cenozoic sequence stratigraphy of the central and northern North Sea Basin: tectonic development, sediment distribution and provenance areas. *Marine and Petroleum Geology*, 12, 8, 845-879.
- JOSEPH, L.H., REA, D.K., VAN DER PLUIJM, B.A. (1998) Use of grain size and magnetic fabric analyses to distinguish among depositional environments. *Paleoceanography*, 13, 5, 491-501.
- KABBAJ, M., TAVENAS, F., LEROUEIL, S. (1988) In situ and laboratory stress-strain relationships. *Geotechnique* 38, 1, 83-100.
- KATSUBE, T.J., MUDFORD, B.S., BEST, M.E. (1991) Petrophysical characteristics of shales from the Scotian shelf. *Geophysics*, 56, 1681-1689.
- KISCH, H.J. (1983) Mineralogy and petrology of burial diagenesis (burial metamorphism) and incipient metamorphism in clastic rocks. In Larsen, G., Chilingar, G.V. (eds.) *Developments in Sedimentology 25B: Diagenesis in Sediments and Sedimentary Rocks II*, Elsevier, 289-493.

- KRAEMER, L.M., OWEN, R.M., DICKENS, G.R. (2000) 23. Lithology of the upper gas hydrate zone, Blake Outer Ridge: a link between diatoms, porosity, and gas hydrate. In Paull, C.K., Matsumoto, R., Wallace, P.J., Dillon, W.P. (eds.) Proceedings of the Ocean Drilling Program, Scientific Results, 164, 229-236.
- KRANCK, K (1991) Interparticle grain size relationships resulting from flocculation. In In Bennett, R.H., Bryant, W.R., Hulbert, M.H. (eds.) Microstructure of Fine-Grained Sediments. Springer Verlag, 125-130.
- KUENEN, P.H. (1950) Marine Geology. Wiley, New York.
- KVILHAUG, T., ROALDSET, E. (1998) Rock mechanical characterization of an offshore mudrock from Haltenbanken, Mid-Norway. Rock Mechanics and Rock Engineering, 31, 2, 95-115.
- LAMBECK, K., YOKOYAMA, Y., JOHNSTON, P., PURCELL, A. (2000) Global ice volumes at the Last Glacial Maximum and early Lateglacial. Earth and Planetary Science Letters, 181, 513-527.
- LANGE, C.B.; BERGER, W.H.; LIN, H.L.; WEFER, G. (1999) The early Matuyama diatom maximum off SW Africa, Benguela Current System ODP Leg 175. Marine Geology, 161, 93-114.
- LEE, J.H., AHN, J.H., PEACOR, D.R. (1985) Textures in layered silicates: progressive changes through diagenesis and low-temperature metamorphism. Journal of Sedimentary Petrology, 55, No.4, 532-540.
- LEE, J.H., PEACOR, D.R., LEWIS, D.D., WINTSCH, R.P. (1986) Evidence for syntectonic crystallization for the mudstone to slate transition at Lehigh Gap, Pennsylvania, USA. Journal of Structural Geology, 8, No.7, 767-780.
- LI, G.; PEACOR, D.R.; MERRIMAN, R.J.; ROBERTS, B. (1994) The diagenetic to low-grade metamorphic evolution of matrix white micas in the system muscovite-paragonite in a mudrock from central Wales, United Kingdom. Clays and Clay Minerals, 42, 4, 369-381.
- LIND, B.B (1999) The influence of grain-size and sediment sorting on the hydraulic conductivity of some Swedish tills. GFF, 121, 107-111.

- LIPSHIE, S.R., OERTEL, G., CHRISTIE, J.M. (1976) Measurement of preferred orientation of phyllosilicates in schists. *Tectonophysics*, 34, 91-99.
- LUO, M., BAKER, M.R., LEMONE, D.V. (1994) Distribution and generation of the overpressure system: Easter Delaware Basin, Western Texas and Southern New Mexico. *AAPG Bulletin*, 78, 9, 1386-1405.
- LUO, X., VASSEUR, G., POUYA, A., LAMOUREUX-VAR, V., POLIOKAOV, A. (1998) Elastoplastic deformation of porous media applied to the modeling of compaction at basin scale. *Marine and Petroleum Geology*, 15, 145-162.
- LUTJEHARMS, J.R.E., VALENTINE, H.R. (1987) Water types and volumetric considerations of the south-east Atlantic upwelling regime. *S. Af. J. Mar. Sci.*, 5, 63-71.
- MACDONALD, I.R., CALLENDER, W.R., GABRIELLE, S.G., GUINASSO, JR N.L., REILLY, J.F., BROOKS, J.M. (1990) Gulf of Mexico hydrocarbon seep communities: VI. Patterns in community structure and habitat. *Geo-Marine Letters*, 10, 4, 244-252.
- MAGARA, K. (1978) *Compaction and fluid migration, practical petroleum geology*. Elsevier Scientific Publishing Company.
- MANGERUD, J., JANSEN, E., LANDVIK, J.Y. (1996) Late Cenozoic history of the Scandinavian and Barents Sea ice sheets. *Global and Planetary Change*, 12, 11-26.
- MANN, D.M., MACKENZIE, A.S. (1990) Prediction of pore fluid pressures in sedimentary basins. *Marine and Petroleum Geology*, 7, 2, 55-65.
- MASUDA, H., PEACOR, D.R., DONG, H. (2001) Transmission electron microscopy study of conversion of smectite to illite in mudstones of the Nankai Trough: contrast with coeval bentonites. *Clay and Clay Minerals*, 49, 2, 109-118.
- MCCAVE, I.N. (1970) Deposition of fine-grained sediment from tidal currents. *J. Geophys. Res.*, 75, 4151-4159.

- MCCAVE, I.N. (1971) Wave effectiveness at the seabed and its relationship to bedforms and deposition of mud. *Journal of Sedimentary Petrology*, 41, 89-96.
- MEADE, R.H. (1961) X-ray diffractometer methods for measuring preferred orientation in clays. US Geological Survey Prof. Paper 424B, 273-276.
- MEADE, R.H. (1963) Factors influencing pore volume in fine-grained sediments. *Sedimentology*, 2, 235-242.
- MEADE, R.H. (1966) Factors influencing the early stages of the compaction of clays and sands – review. *Journal of Sedimentary Petrology*, 36, 4, 1085-1101.
- MERRIMAN, R.J., PEACOR, D.R. (1999) Very low-grade metapelites: mineralogy, microfabrics and measuring reaction progress. In Frey, M., Robinson, D. (eds.) *Low-Grade Metamorphism*. Blackwell Science Ltd, UK, 10-60.
- MERRIMAN, R.J., ROBERTS, B., PEACOR, D.R. (1990) A transmission electron microscope study of white mica crystallite size distribution in a mudstone to slate transitional sequence, North Wales, UK. *Contrib. Mineral. Petrol.*, 106, 27-40.
- MOORE, D.M., REYNOLDS, R.C. JR (1997) X-ray diffraction and the identification and analysis of clay minerals 2nd Edition. Oxford University Press, Oxford, New York.
- MOUNTAIN, G.S., MILLER, K.G., BLUM, P., AND SHIPBOARD SCIENTIFIC PARTY (1994) *Proceedings of the Ocean Drilling Program Initial Reports*. 150, College Station, TX.
- MUNRO-STASIUK, M.J.(2000) Evidence for repeated hydraulic lifting of a stagnant ice mass. *Journal of Sedimentary Research*, 70, 1, 94-106.
- NADIROV, R.S., TAGIYEV, M.F., BAGIROV, E.B., LERCHE, I. (1997) Flexural plate subsidence, sedimentation rates, and structural development of the super-deep South Caspian Basin. *Marine and Petroleum Geology*, 14, 4, 383-400.

- NEUZIL, C.E. (1994) How permeable are clays and shales? *Water resources Research*, 30, 2, 145-150.
- NOBES, D.C., MURRAY, R.W., KURAMOTO, S., PISCIOTTO, K.A., HOLLER, P. (1992) Impact of silica diagenesis on physical property variations. In Pisciotta, K.A., Ingle, J.C., von Breyman, M.T., Barron, J. (eds.) *Proceedings of the Ocean Drilling Program, Scientific Results*, 127/128, 3-31.
- NOBES, D.C., VILLINGER, H., DAVIS, E.E., LAW, L.K. (1986) Estimation of marine sediment bulk physical properties at depth from seafloor geophysical measurements. *Journal of Geophysical Research*, 91, B14, 14033-14043.
- O'BRIEN, N.R. (1970) The fabric of shale – an electron microscope study. *Sedimentology*, 15, 229-246.
- O'BRIEN, N.R. (1987) The effects of bioturbation on the fabric of shale. *Journal of Sedimentary Petrology*, 57, 449-455.
- O'BRIEN, N.R., PIETRASZEK-MATTNER, S. (1998) Origin of the fabric of laminated fine-grained glaciomarine deposits. *Journal of Sedimentary Research*, 68, 5, 832-840.
- O'BRIEN, N.R., SLATT, R.M. (1990) *Argillaceous Rock Atlas*, Springer-Verlag, New York.
- ODP TAMU (2001) Leg Summaries (100-158): Leg 150. http://www-odp.tamu.edu/sciops/Leg_Summaries/Legs_141-158/Leg150.html
- OERTEL, G. (1970) Deformation of a slaty, lapillar tuff in the Lake District, England. *GSA Bulletin*, 81, 1173-1188.
- OERTEL, G. (1983) The relationship of strain and preferred orientation of phyllosilicate grains in rocks – a review. *Tectonophysics*, 100, 413-447.
- OERTEL, G., CURTIS, C.D. (1972) Clay-ironstone concretion preserving fabrics due to progressive compaction. *GSA Bulletin*, 83, 2597-2606.
- OERTEL, G., ENGELDER, T., EVANS, K. (1989) A comparison of the strain of crinoid columnals with that of their enclosing silty and shaly matrix on the

- Appalachian Plateau, New York. *Journal of Structural Geology*, 11, No.8, 975-993.
- OSBORNE, M.J., SWARBRICK, R.E. (1997) Mechanisms for generating overpressure in sedimentary basins: A Re-evaluation. *AAPG Bulletin*, 81, 1023-1041.
- PAGE, R.H., WENK, H.R. (1979) Phyllosilicate alteration of plagioclase studied by transmission electron microscopy. *Geology*, 7, 393-397.
- PEARCE, R.B., CLAYTON, T., KEMP, E.S. (1991) Illitisation and organic maturity in Silurian sediments from the Southern Uplands of Scotland. *Clay Minerals*, 26, 199-210.
- PEARSON, F.J. (1999) What is the porosity of a mudrock? In: Aplin, A.C., Fleet, A.J. and Macquaker, J.H.S. (eds.) *Muds and Mudstones: Physical and Fluid Flow Properties*. Geological Society Special Publication 158, 9-21.
- PERRY, E., HOWER, J. (1970) Burial diagenesis in Gulf Coast pelitic sediments. *Clays and Clay Minerals*, 18, 165-177.
- PETTIJOHN, F.J. (1975) *Sedimentary Rocks 3rd Edition*. Harper & Row, New York.
- POLLASTRO, R.M. (1992) Clay minerals as geothermometers – indicators of thermal maturity for hydrocarbon exploration. *USGS Bulletin* 2007, 61-65.
- POTTER, P.E. (1998) Shale-rich Basins: Controls and Origin. In Schieber, J., Zimmerle, W., Sethi, P.S. (eds.) *Shales and Mudstones I: Basin studies, Sedimentology, and Paleontology*. E. Schweizerbart'sche Verlagsbuchhandlung Stuttgart, 21-33.
- POTTER, P.E., MAYNARD, J.B., PRYOR, W.A. (1980) *Sedimentology of Shale*. Springer Verlag, New York.
- RACK, F.R., PALMER-JULSON, A. (1992) Sediment microfabric and physical properties record of late Neogene Polar Front migration, Site 751. Proc., scientific results, ODP, Leg 120, central Kerguelen Plateau, 179-205.

- RAMM, M., BJØRLYKKE, K. (1994) Porosity/depth trends in reservoir sandstones: assessing the quantitative effects of varying pore-pressure, temperature history and mineralogy, Norwegian Shelf data. *Clay Minerals*, 29, 475-490.
- RAMSAY, J.G., HUBER, M.I. (1983) The technique of modern structural geology. Volume I: Strain analysis. Academic Press, London.
- REA, D.K., HOVAN, S.A. (1995) Grain size distribution and depositional processes of the mineral component of abyssal sediments: lessons from the North Pacific. *Paleoceanography*, 10, 2, 251-258.
- REYNOLD, R.C. JR., HOWER, J. (1970) The nature of interlayering in mixed-layer illite-montmorillonite. *Clays and Clay Minerals*, 18, 25-36.
- REYNOLDS, R.C. JR. (1985) NEWMOD[®] a Computer Program for the Calculation of One-Dimensional Diffraction Patterns of Mixed-Layered Clays: R.C. Reynolds, Jr. 8 Brook Rd., Hanover, NH.
- RIDER, M.H. (1996) The geological interpretation of well logs. Second Edition, Whittles Publishing, 280 p.
- RIEKE, H.H.; CHILINGARIAN, G.V. (1974) Compaction of argillaceous sediments. *Developments in Sedimentology* 16, Elsevier.
- RIIS, F., FJELDSKAAR, W. (1992) On the magnitude of the Late Tertiary and Quaternary erosion and its significance for the uplift of Scandinavia and the Barents Sea. In Larsen, R.M.; Brække, H.; Larsen, B.T.; Talleraas, E. (eds.): *Structural and Tectonic Modeling and its Applications for Petroleum Geology*. Norwegian Petroleum Society, NPF Special Publication 1, Amsterdam, 163-185.
- ROBERSON, H.E., LAHANN, R.W. (1981) Smectite to illite conversion rates: effects of solution chemistry. *Clays and Clay Minerals*, 29, 129-135.
- ROKOENGEN, K., RØNNINGSLAND, T.M. (1983) Shallow bedrock geology and Quaternary thickness in the Norwegian sector of the North Sea between 60°30'N and 62°N. *Norsk Geologisk Tidsskrift*, 63, 83-102.

- SCHIEBER, J. (1998) Deposition of mudstones and shales: overview, problems and challenges. In Schieber, J., Zimmerle, W., Sethi, P.S. (eds.) Shales and Mudstones I: Basin studies, Sedimentology, and Paleontology. E. Schweizerbart'sche Verlagsbuchhandlung Stuttgart, 131-146.
- SCHIEBER, J., KRINSLEY, D., RICIPUTI, L. (2000) Diagenetic origin of quartz silt in mudstones and implications for silica cycling. *Nature*, 406, 981-985.
- SCHIEBER, J., ZIMMERLE, W. (1998) The history and promise of shale research. In Schieber, J., Zimmerle, W., Sethi, P.S. (eds.) Shales and Mudstones I: Basin studies, Sedimentology, and Paleontology. E. Schweizerbart'sche Verlagsbuchhandlung Stuttgart, 1-10.
- SCHMERTMANN, J. (1991) The Mechanical Aging of Soils. *Journal of Geotechnical Engineering*, Vol.117, No. 9, pp 1288-1329.
- SCHNEIDER, F., BOUTECA, M., VASSEUR, G. (1994) Validity of the porosity/effective-stress concept in sedimentary basin modeling. *First Break*, 12, 6, 312-326.
- SCLATER, J.G., CHRISTIE, P.A.F. (1980) Continental stretching: an explanation of the post-mid-cretaceous subsidence of the Central North Sea basin. *Journal of Geophysical Research*, 85, B7, 3711-3739.
- SEARS, S.O. (1984) Porcelaneous cement and micro porosity in California Miocene turbidites - origin and effect on reservoir properties (Los Angeles Basin). *Journal of Sedimentary Petrology* 54, 159-169.
- SINTUBIN, M. (1994) Clay fabrics in relation to the burial history of shales. *Sedimentology*, 41, 1161-1169.
- SKEMPTON, A. W. (1970) The consolidation of clays by gravitational compaction. *Q. Jl geol. Lond.*, 125, 373-411.
- SMITH, J.E. (1971) The dynamics of shale compaction and evolution of pore pressure. *Math. Geol.*, 3, 239-263.
- SRODON, J., EBERL, D.D. (1984) Illite. In Bailey, S.W. (ed.) *Micas, Reviews in Mineralogy*, Min. Soc. of Am., Washington, D.C., Vol. 13, 495-544.

- STEIGER, R.P., LEUNG, P.K. (1988) Quantitative determination of the mechanical properties of shales. Proc. 63rd Ann. Conf. and Exh., Paper SPE 18024, Houston Texas.
- SUETNOVA, E., VASSEUR, G. (2000) 1-D modeling rock compaction in sedimentary basins using a visco-elastic rheology. *Earth and Planetary Science Letters*, 178, 373-383.
- SWARBRICK, R.E., OSBORNE, M.J. (1998) Mechanisms that generate abnormal pressures: An overview. In Law, B.E., Ulmishek, G.F., Slavin, V.I. (eds.) *Abnormal pressures in hydrocarbon environments*. AAPG Memoir 70, 13-34.
- SWARBRICK, R.E., OSBORNE, M.J., GRUNBERGER, D., YARDLEY, G.S., MACLEOD, G., APLIN, A.C., LARTER, S.R., KNIGHT, I., AULD, H.A. (2000) Integrated study of the Judy Field (Block 30/7a) – an overpressured Central North Sea oil/gas field. *Marine and Petroleum Geology*, 17, 993-1010.
- SYVITSKI, J.P.M. (1991) The changing microfabric of suspended particle matter – the fluvial to marine transition: flocculation, agglomeration, and pelletization. In Bennett, R.H., Bryant, W.R., Hulbert, M.H. (eds.) *Microstructure of Fine-Grained Sediments*. Springer Verlag, 131-137.
- TADA, R., SIEVER, R. (1989) Pressure solution during diagenesis. *Ann. Rev. Earth Planet. Sci.*, 17, 89-118.
- TAGIYEV, M.F., NADIROV, R.S., BAGIROV, E.B., LERCHE, I. (1997) Geohistory, thermal history and hydrocarbon generation history of the north-west South Caspian Basin. *Marine and Petroleum Geology*, 14, 4, 363-382.
- TAMAKI, K., PISCIOTTO, K., ALLAN, J. AND SHIPBOARD SCIENTIFIC PARTY (1990) *Proceedings of the Ocean Drilling Program Initial Reports*. 127, College Station, TX.
- TAYLOR, D. W. (1948) *Fundamentals of soil mechanics*. Wiley, New York.
- TERZAGHI, K. (1921) Die physikalischen Grundlagen des technisch-geologischen Gutachtens. *Zeitschrift des Österreichischen Ingenieurs und Architekten Verein*, September Issue, Table V.

- TOVEY, P., WONG, K.Y. (1973) The preparation of soils and other geological materials for the scanning electron microscope. Proceedings, International Symposium on Soil Structure, Gothenburg, 59-67.
- TRIBBLE, J.S.; MACKENZIE, F.T.; URMOS, J.; O'BRIEN, D.K.; MANGHANI, M.H. (1992) Effects of biogenic silica on acoustic and physical properties of clay-rich marine sediments. AAPG Bulletin, 76, 6, 792-804.
- TUCHOLKE, B.E., VOGT, P.R. AND SHIPBOARD SCIENTIFIC PARTY (1975) Initial Reports of the Deep Sea Drilling Project. 43, College Station, TX.
- TULACZYK, S., KAMB, B., ENGELHARDT, H.F. (2001) Estimates of effective stress beneath a modern West Antarctic ice stream from till preconsolidation and void ratio. Boreas, 30, 101-114.
- TURNER, F.J., WEISS, L.E. (1963) Structural Analysis of metamorphic tectonites. McGraw-Hill, New York.
- VAN DER PLUIJM, B.A., HO, N. & PEACOR, D.R. (1994). High-resolution X-ray texture goniometry. Journal of Structural Geology, 16, 1029-1032.
- VAN DER PLUIJM, B.A., HO, N.C., PEACOR, D.R., MERRIMAN, R.J. (1998) Contradictions of slate formation resolved?. Nature, 392, 348.
- VAN DER PLUIJM, B.A., KAARS-SIJPENSTEIJN, C.H. (1984) Chlorite-mica aggregates: morphology, orientation, development and bearing on cleavage formation in very-low-grade rocks. Journal of Structural Geology, 6, No.4, 399-407.
- VAN GROOS, A.F.K., GUGGENHEIM, S. (1984) The effect of pressure on the dehydration reaction of interlayer water in Na-montmorillonite (Swy-1). American Mineralogist, 69, 872-879.
- VANDERAVEROET, P. (2000) Miocene to Pleistocene clay mineral sedimentation on the New Jersey shelf. Oceanologica Acta, 23, 1, 25-36.
- VELDE, B. (1995) Use of the smectite to illite conversion model: effects of order of magnitude. Bull. Centres Rech. Explor.-Prod. Elf Aquitaine, 19, 1, 235-242.

- VELDE, B., ESPITALIE, J. (1989) Comparison of kerogen maturation and illite/smectite composition in diagenesis. *Journal of Petroleum Geology*, 12, 1, 103-110.
- VELDE, B., VASSEUR, G. (1992) Estimation of the diagenetic smectite to illite transformation in time-temperature space. *American Mineralogist*, 77, 967-976.
- WEFER, G., BERGER, W.H., RICHTER, C. AND SHIPBOARD SCIENTIFIC PARTY (1998) *Proceedings of the Ocean Drilling Program Initial Reports*. 175, College Station, TX.
- WENK, H.R. (1985) Measurement of pole figures. In Wenk, H.R. (ed.) *Preferred orientation in deformed metals and rocks: An introduction to modern texture analysis*. Academic Press, INC., 11-48.
- WENSAAS, L.; SHAW, H.F.; GIBBSONS, K.; AAGAARD, P.; DYPVIK, H. (1994) Nature and causes of overpressuring in mudrocks of the Gullfaks area, North sea. *Clay Minerals*, 29, 439-449.
- WETZEL, A. & WIJAYANANDA, N.P. (1990) Biogenic sedimentary structures in outer Bengal Fan deposits drilled during Leg 116. In: Cochran et al. (1990) *Proceedings of the Ocean Drilling Program Scientific Results*. 116, 15-24, College Station, TX.
- WINDOM, H.L. (1976) Lithogenous material in marine sediments. In Riley, J.P. & Chester, R. (eds.) *Chemical oceanography*. London, Academic Press, 5, 103-135.
- WOOD, D.S., OERTEL, G., SINGH, J., BENNETT, H.F. (1976) Strain and anisotropy in rocks. *Philos. Trans. R. Soc. London*, 283, 27-42.
- YANG, Y., APLIN, A.C. (1997) A method for the disaggregation of mudstones. *Sedimentology*, 44, 559-562.
- YANG, Y., APLIN, A.C. (1998) Influence of lithology and compaction on the pore size distribution and modeled permeability of some mudstones from the Norwegian margin In: *Marine and Petroleum Geology*, 15, 163-175.

YANG, Y., APLIN, A.C. (submitted) Definition of porosity – effective stress relationships of fine-grained calcic sediments.

Appendix

Physical Property Data: Part A DSDP/ODP core material

Well	Sample	Depth*	σ'	ϕ	MPI ϕ	wc Lab	wc ODP	Gs	<2 μ m	TC	TOC
26/250	4	119.38	572	0.57	0.47	33	-	2.592	72	0.8	0.5
26/250	6	189.6	986	0.59	0.53	33	-	2.668	72	0.4	0.3
26/250	7	238.65	1286	0.57	0.54	34	-	2.645	74	1.0	0.3
26/250	8	295.65	1813	0.58	0.54	34	-	2.668	74	1.3	0.3
26/250	9	351.22	2220	0.43	0.39	24	-	2.613	77	0.5	0.4
26/250	10	407.3	2612	0.50	0.37	23	-	2.642	78	0.1	0.1
26/250	11	464.97	3035	0.41	0.33	22	-	2.632	75	0.2	0.1
26/250	13	571.67	3931	0.39	0.32	19	-	2.669	74	0.1	0.1
26/250	14	606.7	4141	0.34	0.34	19	-	2.642	72	0.1	0.0
26/250	17	645.71	4426	0.39	0.30	16	-	2.677	73	0.0	0.0
26/257	1	7.2	20	0.85	-	-	-	2.529	70	0.0	0.6
26/257	3	49.2	97	0.75	-	-	-	2.633	76	0.0	0.5
26/257	5	124.04	322	0.69	-	-	-	2.508	73	0.1	0.6
26/257	9	248.7	958	0.68	-	-	-	2.596	82	0.1	0.5
36/330	1	134.71	781	0.69	0.41	16	45	2.669	51	5.6	0.9
36/330	2	177.41	1077	0.54	0.52	8	30	2.754	52	6.1	1.0
36/330	6	314.55	2384	0.45	0.31	6	24	2.647	39	5.3	3.4
36/330	8	350.37	2689	0.44	0.37	10	23	2.662	62	3.2	3.2
36/330	9	377.75	2906	0.43	0.33	7	22	2.695	59	1.8	2.0
36/330	10	405.95	3234	0.47	0.34	8	24	2.695	62	1.8	1.8
36/330	11	434.8	3507	0.40	0.30	6	21	2.674	50	2.2	2.2
36/330	13	490.83	4200	0.41	0.33	4	21	2.711	40	1.4	1.4
36/330	14	519.88	4511	0.34	0.38	3	16	2.720	25	0.8	0.8
43/386	1	59.28	246	0.68	-	-	-	2.811	68	1.9	1.0
43/386	4	151.97	750	0.46	-	-	-	2.798	38	5.9	0.8
43/386	11	252.94	1493	0.66	-	-	-	2.946	59	2.4	0.7
43/386	14	335.82	2097	0.66	-	-	-	2.394	64	2.4	1.1
43/386	26	480.81	3110	0.48	0.46	16	28	2.465	41	2.2	1.0
43/386	28	502	3300	0.42	0.47	9	28	2.530	67	0.6	0.9
43/386	32	562.96	3780	0.48	0.41	16	26	2.586	31	2.0	0.9
43/386	36	646.8	4554	0.43	0.30	11	21	2.820	74	0.3	0.7
43/386	42	731.8	5344	0.43	0.40	6	24	2.763	60	0.0	0.3
43/386	50	818.22	6173	0.40	0.36	7	20	2.758	85	0.3	0.8
43/386	54	858.82	6606	0.40	0.41	11	20	2.793	67	0.4	0.9
43/386	55	865.05	6687	0.44	0.37	12	22	2.760	71	3.8	2.9
43/386	59	900.59	7019	0.39	0.39	9	19	2.740	75	1.6	1.3
43/386	65	957.37	7648	0.40	0.38	7	19	2.828	73	0.2	0.7
57/440b	8	208.2	1091	0.57	-	-	-	2.453	37	0.6	1.2
57/440b	13	257.23	1443	0.63	0.51	30	37	2.516	40	0.6	1.1
57/440b	24	358.74	2083	0.62	0.53	20	35	2.386	33	0.7	1.2
57/440b	28	399.7	2363	0.59	0.51	23	38	2.382	37	0.4	0.9
57/440b	39	502.72	2918	0.59	0.53	25	38	2.240	45	1.0	1.6
57/440b	52	624.7	3723	0.67	0.46	7	-	2.403	24	0.4	0.9
57/440b	60	702.2	4210	0.59	0.44	11	-	2.470	35	0.5	1.0
57/440b	65	748.24	4497	0.61	-	-	-	2.364	47	0.5	1.0

Physical Property Data: Part A DSDP/ODP core material (continued)

Well	Sample	Depth*	σ'	ϕ	MPI ϕ	wc Lab	wc ODP	Gs	<2 μ m	TC	TOC
116/719b	11	90.58	660	0.52	0.46	22	28	2.807	40	0.9	1.1
116/719b	14	120.12	960	0.56	0.47	22	32	2.816	42	1.0	1.2
116/719b	16	138.26	1112	0.48	0.39	18	26	2.823	45	0.6	1.2
116/719b	17	150.87	1202	0.57	0.36	20	34	2.752	60	1.2	1.8
116/719b	22	200	1573	0.53	0.37	21	30	2.789	63	1.4	1.9
116/719b	28	251.55	2002	0.52	0.45	25	29	2.767	61	1.2	1.8
116/719b	33	300.75	2411	0.50	0.43	15	27	2.802	60	0.7	1.3
116/719b	38	350.3	2822	0.58	0.43	28	34	2.734	78	0.3	0.8
116/719b	48	448.95	3746	0.47	0.43	17	24	2.801	53	0.5	0.9
127/794a	1	1.02	3	0.85	-	-	-	2.666	50	0.5	0.4
127/794a	95	80.28	317	0.81	-	-	-	2.334	49	0.8	0.6
127/794b	91	376.07	1532	0.43	0.53	32	22	2.384	46	0.4	0.4
127/794b	11	395.75	1664	0.59	0.48	26	33	2.568	40	0.6	0.6
127/794b	17	453.6	2137	0.53	-	-	-	2.579	65	1.4	1.3
127/794b	20	485.35	2396	0.51	0.47	24	27	2.586	57	1.4	1.1
150/906a	14	121.31	981	0.50	0.49	27	30	2.694	51	1.3	1.8
150/906a	31	285.6	2180	0.50	0.50	28	35	2.684	57	1.5	2.0
150/906a	33	305.05	2348	0.51	0.49	26	30	2.628	47	1.4	1.9
150/906a	41	384.53	3052	0.38	-	-	-	2.813	35	1.5	0.8
150/906a	51	481.1	3807	0.43	0.42	21	25	2.678	39	5.0	2.7
150/906a	59	554.86	4462	0.35	0.49	27	20	2.544	33	6.1	3.7
174/1072	7	51.35	507	0.49	0.48	25	26	2.781	61	1.6	0.4
174/1073	11	71.08	690	0.48	0.39	18	22	2.727	38	1.9	0.3
174/1074	17	100.21	996	0.39	0.38	17	19	2.737	29	0.5	0.3
174/1075	25	145.16	1452	0.41	0.35	16	20	2.748	31	0.6	0.5
174/1076	37	198.34	2026	0.38	0.20	15	18	2.691	37	0.7	0.6
174/1077	46	249.68	2531	0.37	0.40	17	18	2.687	18	0.4	0.5
175/1084a	12	103	336	0.77	-	-	49	2.346	50	10.9	8.0
175/1084a	17	145.8	476	0.76	-	-	62	2.334	58	12.4	7.1
175/1084a	24	201	659	0.76	-	-	48	2.500	47	8.4	3.1
175/1084a	29	250.1	837	0.75	-	-	58	2.294	59	8.8	8.4
175/1084a	34	300.1	1024	0.75	-	-	53	2.447	60	5.9	2.4
175/1084a	39	349.5	1173	0.74	-	-	66	2.066	56	3.8	3.7
175/1084a	43	389.4	1274	0.74	-	-	62	2.103	61	6.6	6.5
175/1084a	49	449.3	1496	0.74	-	-	59	2.284	64	5.4	2.9

Sample	MIP ϕ	ϕ^*	wc Lab	<2 μ m	Gs
BI	0.43	0.48	32	67	2.76
BII	0.39	0.44	27	56	2.8

Key: (*) – mbsf, σ' – effective stress [kPa], ϕ - porosity (measured by ODP), MPI ϕ - porosity (measured by mercury intrusion porosimetry), ϕ^* - porosity from water content Lab, wc Lab – water content [%] (this study), wc ODP – water content [%] (measured by ODP), Gs – grain density [g/cm³], <2 μ m – clay fraction [%], TC – total carbon [%], TOC – total organic carbon [%].

Physical Property Data: Part B

Well	Depth [mbsf]	Type	MIP ϕ	Gs	<2 μ m	TC	TOC
BB	1270	cutting	0.25	-	35	-	-
BB	2030	cutting	0.2	-	30	-	-
BB	2310	cutting	0.15	-	28	-	-
BB	3305	cutting	0.15	-	26	-	-
BB	3495	cutting	0.14	-	-	-	-
CS	4863	core	0.1	2.79	53	1.22	0.44
CS	4887	core	0.11	2.81	43	1.13	0.37
CS	5280	core	0.11	2.76	26	1.25	0.15
CS	5383	core	0.11	2.82	40	1.36	0.17
CVG	1565	core	0.24	-	85	-	-
CVG	1711	core	0.28	-	58	-	-
CVG	1754	core	0.25	-	82	-	-
CVG	1848	core	0.2	-	65	-	-
Diva	1515	cutting*	0.5	2.738	46	2.41	2.19
Diva	2392	cutting*	0.38	2.708	46	2.89	2.31
Diva	3481	cutting*	0.53	2.639	40	3.11	2.7
Diva	4477	cutting*	0.58	2.46	39	4.6	4.6
Diva	4849	cutting*	0.21	2.738	35	4.98	4.73
Diva	4855	swc	0.17	2.792	36	2.16	1.34
Diva	5001	core	0.17	2.788	49	1.06	0.524
Diva	5428	cutting*	0.5	2.625	36	6.22	5.11
Diva	5435	swc	0.14	2.783	39	1.74	0.567
Diva	5511	core	0.13	2.764	37	1.01	0.764
Diva	5516	core	0.16	2.764	33	0.915	0.465
Diva	5518	core	0.15	2.773	60	0.963	0.558
Diva	5647	core	0.09	2.726	22	1.95	0.183
Diva	5649	core	0.12	2.753	38	0.4-0.8	0.3-0.6
Diva	6906	cutting*	0.27	2.466	-	-	-
Ikon	2529	cutting*	0.36	2.779	39	4.44	3.56
Ikon	2685	cutting*	0.52	2.755	45	3.59	3.02
Ikon	2840	cutting*	0.43	2.632	19	2.94	2.26
Ikon	2986	cutting*	0.57	2.651	48	3.51	3.27
Ikon	3142	cutting*	0.41	2.678	42	3.5	3.5
Ikon	3297	cutting*	0.47	2.733	42	3.16	3.03
Ikon	3453	cutting*	0.52	2.674	48	4.21	3.66
Ikon	3599	cutting*	0.37	2.517	39	8.52	7.07
Ikon	3746	cutting*	0.4	2.628	33	5.04	3.76
Ikon	3901	cutting*	0.38	2.61	39	5.43	4.47
Ikon	4126	cutting*	0.39	2.598	42	6.57	6.35
Ikon	4128	core	0.22	2.807	46	0.905	0.303
Ikon	4321	swc	0.15	2.666	52	2.61	2.28
Ikon	4418	core	0.16	2.766	39	1.28	0.996
Ikon	4660	cutting*	0.33	2.744	39	9.12	5.19
Ikon	5133	core	0.19	2.771	56	0.88	0.569
Ikon	5282	cutting*	0.47	2.558	39	5.23	5.02
Ikon	5420	swc	0.17	2.78	44	1.72	0.881
Ikon	5739	cutting*	0.51	2.525	30	6.71	6.03
Ikon	5884	swc	0.16	2.752	40	7.82	6.43
Ikon	6041	cutting*	0.46	2.62	40	4.44	3.56

Physical Property Data: Part B (continued)

Well	Depth [mbsf]	Type	MIP ϕ	Gs	<2 μ m	TC	TOC
NVG	1908	core	0.27	2.74	13	1	1
NVG	2311	core	0.14	2.78	22	1.61	1.28
NVG	2671	core	0.12	2.75	38	1.01	0.81
NVG	2687	core	0.12	2.75	31	1.81	1.54
NVG	3410	core	0.06	2.72	21	1.61	1.28
NVG	3700	core	0.1	2.74	19	1.87	1.59
NVG	4000	core	0.06	2.73	20	0.11	0.11
NVG	4331	core	0.11	2.82	41	1.49	1.46
Panis	901	cutting	0.19	2.59	-	2.67	5.31
Panis	1444	cutting	0.2	2.60	45	0.76	2.37
Panis	1633	cutting	0.19	2.65	43	1.96	3.8
Panis	1816	cutting	0.15	2.62	41	1.60	4.38
Panis	1999	cutting	-	2.63	39	2.56	4.03
Panis	2175	cutting	0.15	2.55	-	2.36	3.87
Panis	2541	cutting	0.12	2.56	40	1.97	2.26
Panis	2724	cutting	0.17	2.67	-	2.20	2.77
Panis	2907	cutting	0.14	2.58	39	2.77	3.4
Panis	3090	cutting	0.18	2.64	44	1.38	2.11
Panis	3263	cutting	0.15	2.66	47	2.07	2.44
Panis	3370	cutting	0.16	2.63	-	1.98	2.81
Panis	3553	cutting	0.21	2.68	43	2.20	2.41
Panis	3644	cutting	0.19	2.66	-	1.95	2.55
Mid-Norway	812	cutting	-	2.63	33	-	-
Mid-Norway	1362	cutting	-	2.80	67	-	-
Mid-Norway	1487	cutting	-	2.63	58	-	-
Mid-Norway	2301	cutting	-	2.79	51	-	-
Mid-Norway	2499	cutting	-	2.76	59	-	-

Key: (*) wet (canned) cuttings, swc – side wal core, MPI ϕ - porosity (measured by mercury intrusion porosimetry), Gs – grain density [g/cm³], <2 μ m – clay fraction [%], TC – total carbon [%], TOC – total organic carbon [%].

Grain Size Data: Part A

Well	Sample	Depth [mbsf]	Grain Size [%]											
			>63 μ m	63 μ m	20 μ m	10 μ m	8 μ m	6 μ m	4 μ m	2 μ m	1 μ m	0.6 μ m	0.4 μ m	0.25 μ m
26/250	4	119.38	0.2	99.8	91.9	90.6	89.3	86.7	81.6	71.9	62.7	56.3	52.1	45.3
26/250	6	189.6	0.1	99.9	92.1	92.1	90.7	89.3	83.9	72.4	62.9	56.1	51.8	45.7
26/250	7	238.65	0.0	100.0	92.2	92.2	89.4	86.6	82.4	74.5	64.5	58.6	54.0	47.6
26/250	8	295.65	0.0	100.0	92.2	90.7	89.2	86.3	82.0	73.7	63.3	57.2	50.3	40.6
26/250	9	351.22	0.0	100.0	92.2	92.2	90.7	89.1	86.1	77.3	67.7	61.1	57.4	51.3
26/250	10	407.3	0.0	100.0	92.2	92.2	90.9	88.3	85.7	78.3	70.0	64.3	61.0	55.7
26/250	11	464.97	0.4	99.6	91.7	91.7	91.7	87.6	83.7	74.9	65.4	59.8	55.5	49.3
26/250	13	571.67	0.0	100.0	92.2	89.4	86.6	85.2	81.1	74.5	66.9	62.1	58.6	54.0
26/250	14	606.7	0.3	99.7	91.9	88.9	87.5	84.6	80.3	72.1	64.4	59.4	55.9	50.1
26/250	17	645.71	0.0	100.0	92.2	89.5	88.1	85.4	81.4	72.5	64.1	58.4	54.0	45.7
26/257	1	7.2	3.1	96.9	86.6	85.0	83.5	82.0	77.5	70.4	62.2	54.5	48.4	40.5
26/257	3	49.2	0.0	100.0	92.2	92.2	90.7	89.2	85.6	76.4	68.4	63.3	59.6	57.2
26/257	5	124.04	0.0	100.0	92.2	91.5	90.9	88.3	83.1	73.3	62.9	55.4	50.3	43.5
26/257	9	248.7	0.0	100.0	92.2	92.2	92.2	90.9	89.5	81.8	74.3	68.4	64.9	59.3
36/330	1	134.71	2.8	97.2	84.7	80.8	78.3	75.8	69.8	51.1	31.8	22.6	17.9	14.8
36/330	2	177.41	1.0	99.0	90.9	89.6	87.1	83.3	78.4	52.0	33.1	24.0	18.7	15.0
36/330	6	314.55	12.3	87.7	72.3	65.9	63.9	57.9	50.3	39.1	30.6	25.0	21.8	18.8
36/330	8	350.37	0.1	99.9	92.1	89.4	88.1	85.6	76.9	62.0	47.6	37.6	30.2	23.5
36/330	9	377.75	0.2	99.8	91.9	87.6	86.1	81.9	73.7	58.6	41.0	28.8	20.0	14.5
36/330	10	405.95	0.1	99.9	92.1	89.4	88.1	82.8	76.5	62.3	46.5	32.8	22.7	16.1
36/330	11	434.8	0.4	99.6	86.8	79.0	77.5	73.0	64.5	50.1	28.3	18.7	14.9	12.2
36/330	13	490.83	3.8	96.2	70.1	60.6	57.6	54.6	48.9	40.1	31.4	22.9	18.5	15.1
36/330	14	519.88	0.2	99.8	60.5	39.9	37.1	33.6	30.2	25.4	21.0	17.6	15.7	13.9
43/386	1	59.28	0.8	99.2	90.6	89.9	89.9	87.3	81.0	67.9	51.8	39.5	32.3	26.5
43/386	4	151.97	0.1	99.9	90.8	89.5	88.2	81.8	71.0	45.7	32.6	26.4	22.8	18.8
43/386	11	252.94	0.1	99.9	92.0	90.7	89.3	83.9	76.2	59.4	45.7	39.9	35.3	30.2
43/386	14	335.82	0.1	99.9	92.0	92.0	90.5	89.1	82.0	63.8	46.6	38.5	32.9	26.8
43/386	26	480.81	17.7	82.3	70.3	68.3	66.3	61.5	54.1	41.4	29.6	22.0	17.9	14.3
43/386	28	502	0.2	99.8	91.9	91.9	89.2	85.2	80.0	66.5	52.1	43.1	38.4	33.2
43/386	32	562.96	50.5	49.5	37.2	37.2	37.2	36.7	35.8	30.8	23.0	19.0	16.6	14.6
43/386	36	646.8	2.6	97.4	88.8	88.8	87.4	86.0	82.4	73.6	62.1	56.2	51.6	45.1
43/386	42	731.8	0.0	100.0	92.2	92.2	90.6	87.5	78.5	60.5	43.6	33.1	27.4	23.0

Grain Size Data Part A: continued

Well	Sample	Depth [mbsf]	Grain size [%]											
			>63 μ m	63 μ m	20 μ m	10 μ m	8 μ m	6 μ m	4 μ m	2 μ m	1 μ m	0.6 μ m	0.4 μ m	0.25 μ m
43/386	50	818.22	0.1	99.9	92.1	92.1	92.1	90.7	89.4	84.8	77.8	70.4	63.4	52.0
43/386	54	858.82	0.0	100.0	92.2	92.2	90.8	90.8	82.4	66.9	46.5	34.9	29.6	24.7
43/386	55	865.05	0.0	100.0	92.2	89.5	86.8	84.2	79.1	70.5	57.9	46.5	34.6	25.7
43/386	59	900.59	0.0	100.0	92.2	92.2	90.8	88.0	83.9	74.7	56.6	39.0	30.9	24.5
43/386	65	957.37	0.5	99.5	91.6	91.6	91.6	88.7	84.5	72.5	50.1	35.1	29.8	24.9
57/440b	8	208.2	13.5	86.5	75.2	68.2	64.9	57.3	49.3	37.4	26.2	19.4	13.9	9.7
57/440b	13	257.23	1.7	98.3	81.9	68.2	63.5	57.9	49.4	39.6	30.0	23.1	17.5	12.7
57/440b	24	358.74	5.5	94.5	79.2	66.8	61.5	54.4	45.1	33.3	23.2	15.8	11.0	8.2
57/440b	28	399.7	3.9	96.1	80.9	70.2	66.8	59.2	50.1	37.2	25.4	17.4	12.8	9.7
57/440b	39	502.72	0.6	99.4	90.0	81.8	77.8	71.4	60.4	45.2	28.6	17.4	12.9	9.6
57/440b	52	624.7	3.9	96.1	73.2	53.3	47.7	41.4	32.7	24.1	18.0	13.3	10.3	7.6
57/440b	60	702.2	2.0	98.0	77.2	66.9	63.2	58.4	49.4	35.4	25.8	17.6	13.1	9.6
57/440b	65	748.24	0.7	99.3	85.7	80.3	79.0	73.8	63.9	47.2	31.9	21.5	15.4	10.1
116/719	11	90.58	0.0	100.0	90.7	83.6	79.5	68.9	55.6	39.6	29.4	23.7	19.9	15.7
116/719	14	120.12	0.0	100.0	92.2	87.6	81.6	74.5	59.8	42.3	31.3	25.0	20.9	16.4
116/719	16	138.26	0.3	99.7	90.5	80.5	74.5	66.5	55.8	45.1	37.1	29.8	24.6	20.5
116/719	17	150.87	0.1	99.9	90.7	84.0	80.1	75.1	67.8	59.8	54.3	51.2	48.1	44.1
116/719	22	200	0.1	99.9	92.0	87.3	84.3	81.3	74.0	63.0	52.8	44.6	37.1	28.3
116/719	28	251.55	0.0	100.0	92.2	92.2	89.5	85.6	76.9	60.7	47.3	41.6	37.2	32.1
116/719	33	300.75	0.0	100.0	92.2	92.2	91.5	88.0	79.7	59.7	45.5	37.6	31.3	23.9
116/719	38	350.3	0.0	100.0	92.2	92.2	92.2	89.5	86.7	77.6	67.7	59.5	53.0	43.8
116/719	48	448.95	0.0	100.0	92.2	92.2	89.3	82.1	71.3	52.9	39.1	34.3	29.8	26.4
127/794a	1	1.02	0.9	99.1	91.0	81.1	78.4	71.7	64.1	50.1	38.7	29.5	22.9	17.1
127/794a	95	80.28	3.8	96.2	84.4	76.2	73.5	69.6	62.0	49.3	37.0	27.9	22.3	16.5
127/794b	91	376.07	1.0	99.0	80.6	74.5	73.3	68.6	61.8	46.4	33.0	25.9	21.6	17.7
127/794b	11	395.75	0.0	100.0	92.2	90.7	87.8	82.1	70.0	49.5	30.6	17.9	12.0	8.1
127/794b	17	453.6	0.0	100.0	92.2	92.2	90.9	88.3	80.6	65.2	46.4	31.3	26.7	13.5
127/794b	20	485.35	0.4	99.6	91.6	87.5	84.9	80.9	73.3	57.0	40.7	28.5	19.6	13.3
150/906a	14	121.31	3.9	96.1	76.2	69.7	68.4	64.7	61.1	50.7	40.3	33.7	27.6	22.0
150/906a	31	285.6	0.3	99.7	90.5	85.4	81.6	76.6	69.5	57.3	47.2	38.0	29.7	20.9
150/906a	33	305.05	1.2	98.8	80.4	70.9	67.4	64.1	56.6	46.6	35.8	28.6	22.1	17.5
150/906a	41	384.53	8.5	91.5	76.5	69.6	66.3	62.0	53.8	34.8	22.2	18.4	16.6	14.8
150/906a	51	481.1	5.6	94.4	68.9	63.1	60.9	56.5	50.3	38.8	28.7	22.0	17.3	13.1

Grain Size Data Part A: continued

Well	Sample	Depth [mbsf]	Grain size [%]											
			>63 μ m	63 μ m	20 μ m	10 μ m	8 μ m	6 μ m	4 μ m	2 μ m	1 μ m	0.6 μ m	0.4 μ m	0.25 μ m
150/906a	59	554.86	2.0	98.0	76.3	66.3	62.8	57.1	47.4	33.2	22.0	17.8	15.2	12.8
174/1072a	7	51.35	0.0	100.0	92.2	89.2	86.3	83.4	75.1	60.9	45.9	35.7	29.2	22.6
174/1072a	11	71.08	1.9	98.1	80.6	66.5	61.2	56.1	48.9	37.8	30.0	24.6	20.4	16.6
174/1072a	17	100.21	20.6	79.4	48.8	42.3	41.3	38.2	35.2	28.8	23.7	19.8	16.9	14.1
174/1072a	25	145.16	15.6	84.4	57.3	24.9	44.3	41.9	37.3	30.8	25.5	21.8	19.5	16.8
174/1072a	37	198.34	12.6	87.4	66.8	60.1	56.9	52.7	45.7	34.0	26.1	20.4	17.2	13.0
174/1072a	46	249.68	52.1	47.9	32.3	29.7	28.9	26.5	22.7	18.5	14.6	11.7	10.0	8.0
175/1084a	12	103	0.4	99.6	91.7	88.7	85.8	78.7	67.8	49.6	30.4	19.7	14.7	11.0
175/1084a	17	145.8	0.5	99.5	91.6	88.5	85.5	81.0	73.8	57.9	33.4	18.7	13.1	10.0
175/1084a	24	201	0.1	99.9	92.0	89.4	86.8	81.6	69.4	46.9	28.4	18.5	14.2	10.8
175/1084a	29	250.1	0.2	99.8	91.9	90.5	89.2	83.7	75.9	59.1	41.3	28.9	21.9	15.8
175/1084a	34	300.1	0.4	99.6	91.7	91.0	90.3	86.1	76.5	60.3	40.8	27.3	20.4	15.6
175/1084a	39	349.5	0.1	99.9	92.0	92.0	90.5	87.6	80.5	55.9	34.7	21.8	17.4	14.6
175/1084a	43	389.4	0.1	99.9	92.0	90.5	88.1	84.4	77.0	60.7	41.8	27.0	21.1	17.3
175/1084a	49	449.3	0.0	100.0	92.2	92.2	91.4	87.4	81.3	62.8	40.9	25.0	18.4	14.0

Grain Size Data: Part B

Well	Depth [mbsf]	Grain Size [%]											
		>63 μ m	63 μ m	20 μ m	10 μ m	8 μ m	6 μ m	4 μ m	2 μ m	1 μ m	0.6 μ m	0.4 μ m	0.25 μ m
Panis	1444	1.2	98.8	96.4	70.1	67.4	62.1	55.8	45.2	35.6	28.9	22.8	13.8
Panis	2541	4.1	95.9	86.2	62.4	59.8	55.9	48.6	39.6	32.4	27.6	24.1	19.1
Panis	2907	8.2	91.8	76.3	56.3	54.3	50.4	45.7	38.7	32.9	28.4	25.5	21.4
Panis	3090	1.5	98.5	91.7	70.1	65.4	60.9	52.3	44.4	39.4	34.7	30.2	23.1
Panis	3263	2.6	97.4	87.8	67.2	64.1	61.1	56.7	47.1	39.5	33.6	28.2	22.3
Panis	1633	1.1	98.9	94.9	74.5	69.9	64.2	55.6	42.9	33.4	27.9	24.2	18.8
Panis	1816	0.7	99.3	81.9	70.6	67.0	61.2	53.5	41.5	30.8	25.3	20.9	16.9
Panis	1999	1.9	98.1	88.0	66.5	62.7	56.7	50.9	39.3	29.9	24.8	20.9	16.6
Panis	3553	1.2	98.8	76.8	64.1	62.6	56.7	52.5	43.2	35.9	31.4	27.2	22.3

Well	Depth [mbsf]	Grain Size [%]											
		>63 μ m	63 μ m	20 μ m	10 μ m	8 μ m	6 μ m	4 μ m	2 μ m	1 μ m	0.6 μ m	0.4 μ m	0.25 μ m
Diva	1515	0.2	99.8	93.2	68.8	66.3	61.4	55.5	45.6	34.7	28.5	22.9	17.0
Diva	2392	1.4	98.6	90.9	69.9	67.0	62.7	57.2	45.7	36.5	31.2	26.3	20.9
Diva	3481	2.8	97.2	83.9	60.7	58.5	55.3	50.1	40.5	31.8	27.8	28.6	21.2
Diva	4477	1.3	98.7	79.3	66.5	62.1	57.9	49.8	38.8	30.6	23.2	19.9	13.9
Diva	4849	6.3	93.7	62.9	54.8	51.9	49.1	43.7	35.3	26.4	20.4	16.2	12.9
Diva	4855	4.0	96.0	71.5	58.6	56.1	52.6	46.9	36.4	25.4	17.6	13.5	10.4
Diva	5001	1.9	98.1	92.8	77.0	75.6	73.0	66.5	48.7	29.0	19.4	13.9	11.5
Diva	5428	3.7	96.3	68.0	57.0	54.9	50.8	45.0	36.1	28.8	22.9	18.2	12.9
Diva	5435	11.3	88.7	92.2	65.9	63.4	59.7	52.6	38.6	25.0	16.7	12.7	9.8
Diva	5511	8.5	91.5	72.3	63.7	60.2	56.7	50.2	37.2	23.7	16.0	11.7	9.0
Diva	5516	16.2	83.8	54.7	49.9	48.3	45.3	42.4	32.8	22.2	16.1	12.4	9.2
Diva	5518	1.1	98.9	81.2	76.6	73.6	70.7	66.4	59.5	53.0	46.8	41.0	33.5
Diva	5647	44.7	55.3	87.5	33.9	32.8	30.6	28.4	22.4	16.2	12.2	9.4	6.8
Diva	5649	0.0	100.0	83.2	68.8	64.3	58.9	50.6	38.5	26.4	19.5	15.1	12.3

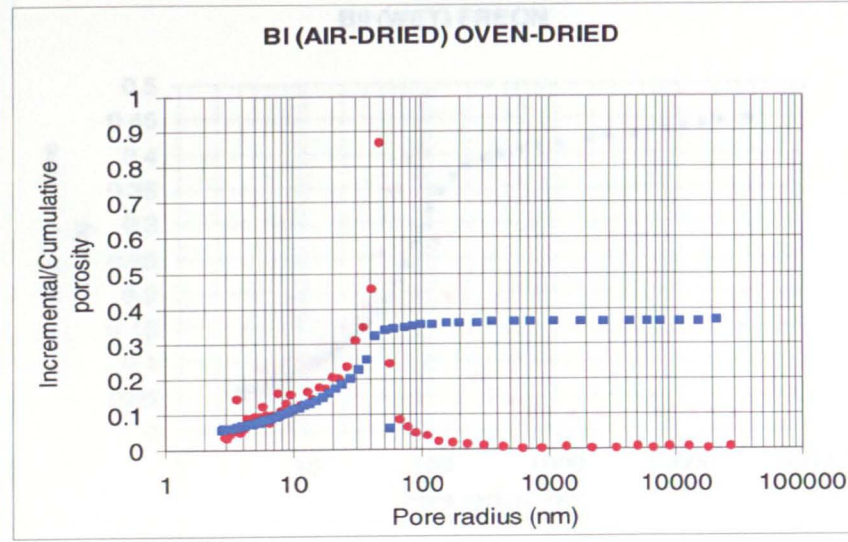
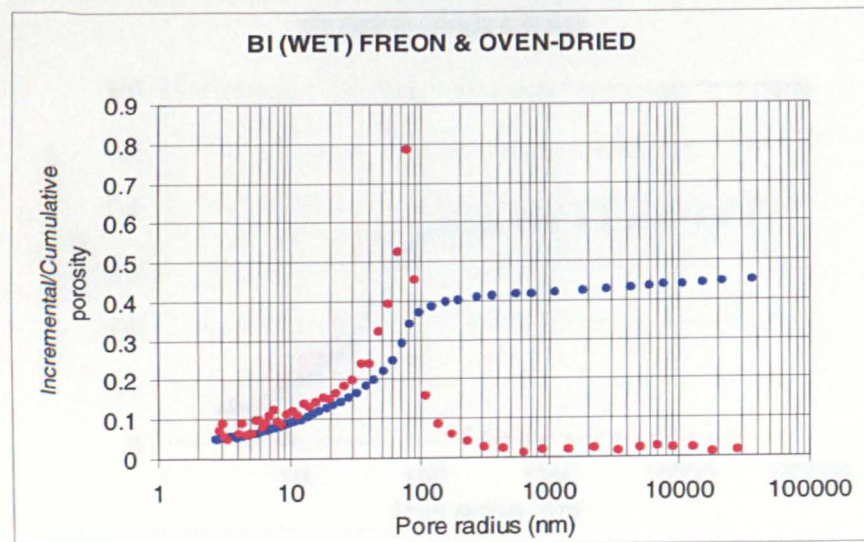
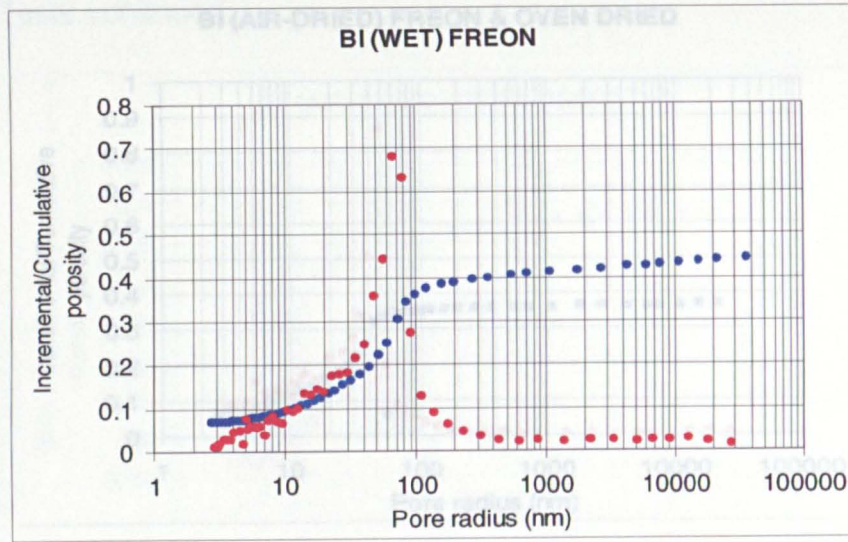
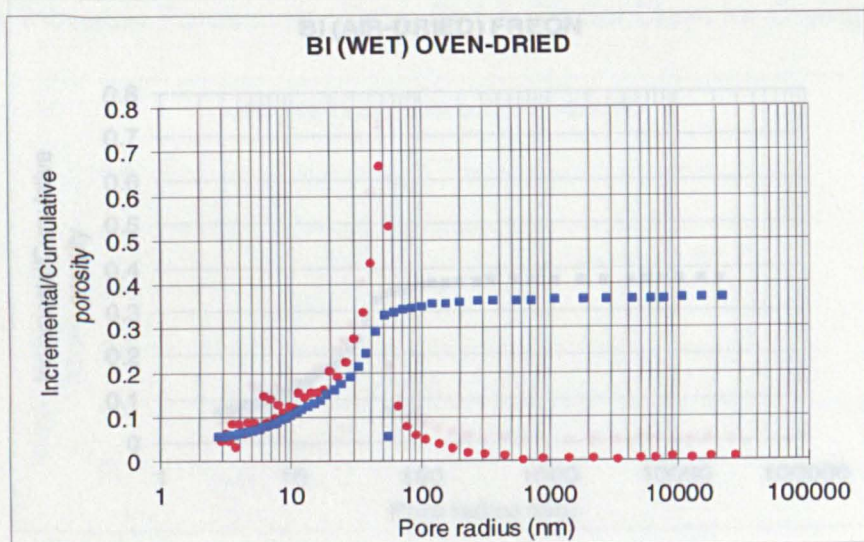
Grain Size Data Part B: continued

Well	Depth [mbsf]	Grain Size [%]											
		>63mic	63 μ m	20 μ m	10 μ m	8 μ m	6 μ m	4 μ m	2 μ m	1 μ m	0.6 μ m	0.4 μ m	0.25 μ m
Ikona	2529	7.7	92.3	76.8	56.7	54.7	50.8	46.1	38.9	33.2	28.6	25.7	21.5
Ikona	2685	0.4	99.6	92.4	69.5	66.8	60.2	55.1	44.5	35.9	31.0	24.6	18.2
Ikona	2840	9.5	90.5	50.8	29.9	29.2	26.4	23.7	18.8	15.9	14.3	12.7	10.8
Ikona	2986	4.7	95.3	89.7	68.5	67.2	62.3	58.6	48.4	40.0	34.2	30.6	25.5
Ikona	3142	1.2	98.8	77.2	64.9	61.4	58.0	51.4	42.3	34.8	30.5	27.3	21.9
Ikona	3297	5.0	95.0	85.1	62.3	59.2	54.8	50.5	42.4	34.9	30.3	27.1	21.0
Ikona	3453	0.8	99.2	83.0	73.7	70.7	64.9	59.4	47.7	37.3	31.0	26.1	21.6
Ikona	3599	11.5	88.5	68.0	58.9	55.1	52.7	48.1	39.3	32.3	27.7	24.3	17.9
Ikona	3746	18.4	81.6	58.5	49.5	47.4	44.2	39.2	32.7	25.9	22.7	19.8	17.0
Ikona	3901	0.6	99.4	72.7	59.2	56.0	51.9	46.0	37.8	30.3	25.8	22.2	17.6
Ikona	4126	8.2	91.8	89.6	63.3	60.7	56.8	50.7	41.5	34.2	28.4	24.0	15.3
Ikona	4128	0.3	99.7	85.2	74.2	72.7	66.8	61.1	45.6	31.1	23.5	18.4	13.8
Ikona	4321	0.8	99.2	86.1	74.8	73.3	68.7	62.9	51.9	37.3	25.8	18.7	13.2
Ikona	4418	0.5	99.5	83.6	71.7	66.1	60.7	50.5	39.0	28.9	22.6	17.0	12.1
Ikona	4660	0.3	99.7	87.5	64.0	59.7	54.4	48.5	39.2	30.9	24.9	20.7	15.1
Ikona	5133	0.3	99.7	88.3	79.7	78.0	73.1	68.4	56.4	38.1	25.0	18.5	12.1
Ikona	5282	12.2	87.8	64.7	56.8	53.5	50.4	46.3	38.7	32.5	26.8	23.1	18.2
Ikona	5420	0.4	99.6	86.2	74.1	70.8	66.0	58.3	44.4	28.9	19.0	13.9	9.4
Ikona	5739	3.7	96.3	58.0	47.9	45.0	41.3	36.9	30.3	23.6	18.9	15.8	12.3
Ikona	5884	4.8	95.2	68.4	56.8	54.1	52.7	47.5	37.8	26.2	19.7	14.8	11.2
Ikona	6041	4.1	95.9	76.2	65.0	60.8	56.8	49.9	40.0	31.1	25.3	20.6	15.2

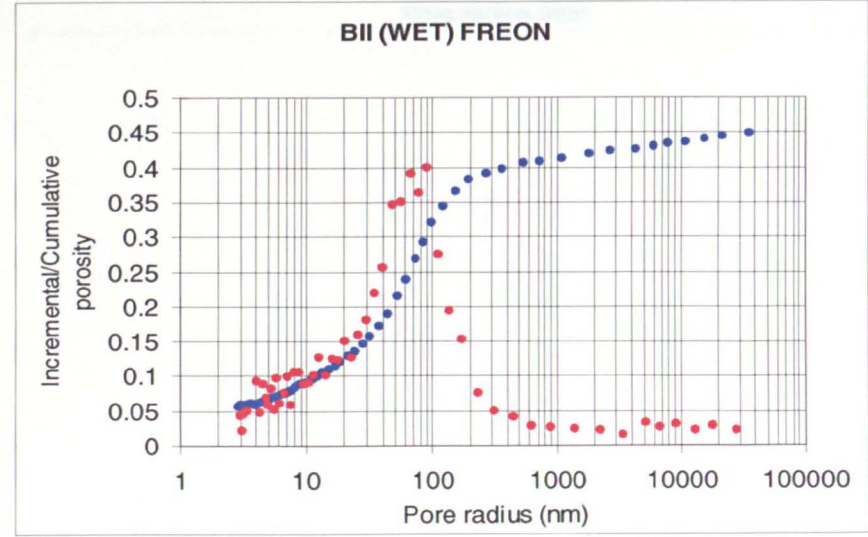
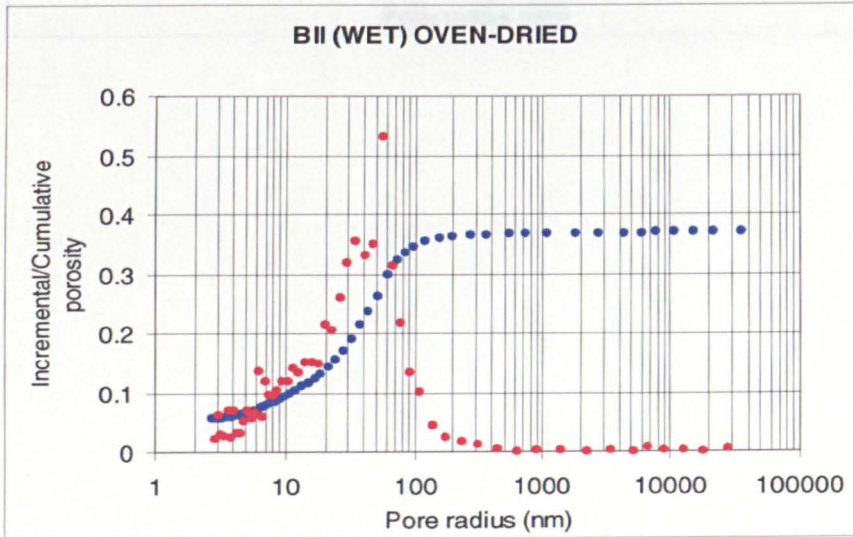
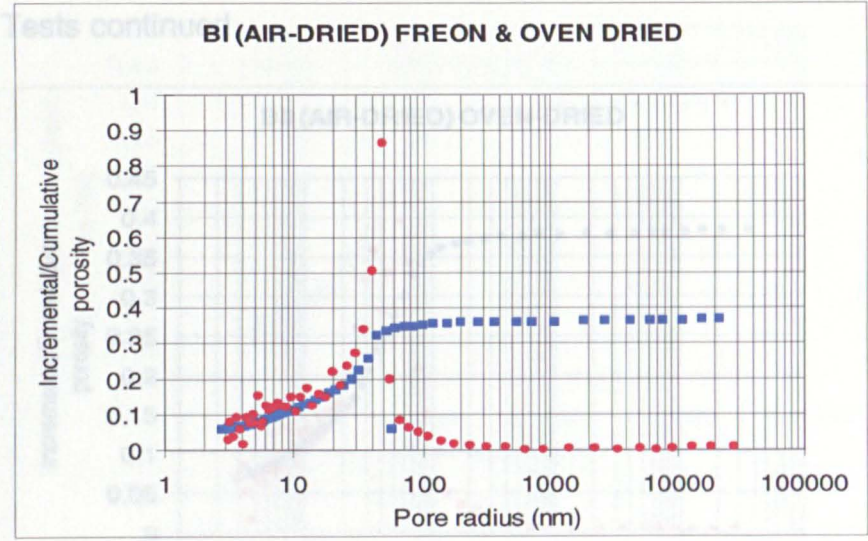
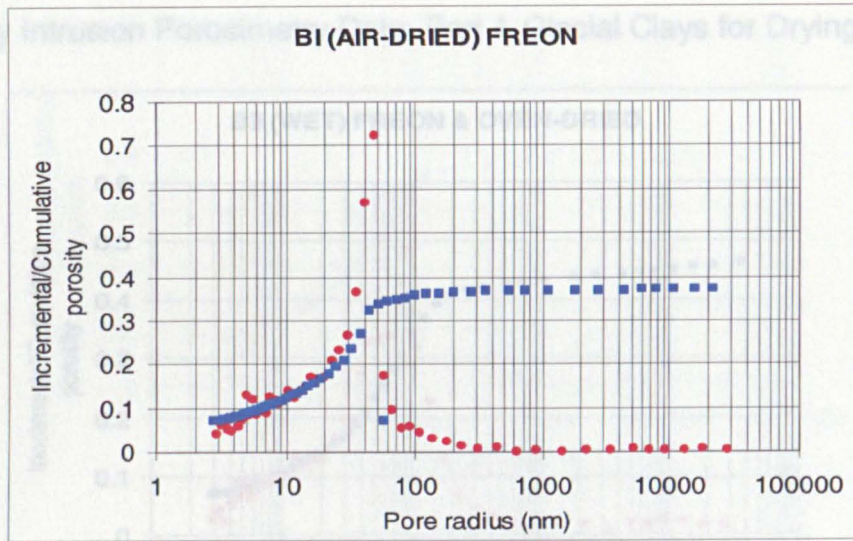
Grain Size Data Part B: continued

Well	Depth [mbsf]	Grain Size [%]											
		>63 μ m	63 μ m	20 μ m	10 μ m	8 μ m	6 μ m	4 μ m	2 μ m	1 μ m	0.6 μ m	0.4 μ m	0.25 μ m
BB	1270	1.4	98.6	98.6	74.9	66.4	58.3	45.9	34.9	25.3	18.6	14.1	6.7
BB	2030	0.0	100.0	86.5	73.8	67.0	57.4	45.6	30.3	21.7	16.1	12.7	9.6
BB	2310	0.3	99.7	85.2	64.7	57.3	48.6	36.0	22.8	13.1	8.7	6.4	5.6
BB	3305	0.9	99.1	84.7	68.2	62.7	51.4	39.4	25.9	16.7	12.2	10.1	8.2
NVG	1908	33.8	66.2	34.5	27.7	25.7	23.4	19.3	13.7	9.9	8.3	7.2	6.5
NVG	2311	23.8	76.2	55.3	48.4	46.2	41.9	34.0	22.4	14.7	11.4	9.8	9.1
NVG	2671	22.1	77.9	53.7	47.5	46.0	43.8	38.9	31.7	24.0	17.8	15.0	11.5
NVG	2687	4.5	95.5	80.4	65.7	61.5	57.4	49.7	38.2	28.0	21.2	16.3	12.0
NVG	3410	16.6	83.4	54.2	42.1	37.6	34.8	28.2	21.0	15.7	12.9	11.1	9.4
NVG	3700	0.4	99.6	70.7	43.2	37.9	32.4	25.6	19.4	15.1	12.8	11.8	10.2
NVG	4000	22.3	77.7	36.1	29.1	27.9	26.8	23.7	19.7	15.8	13.6	12.3	10.7
NVG	4331	0.7	99.3	80.1	68.7		58.9		40.5				
CVG	1565	7.8	92.2	92.2	92.2	92.2	92.2	90.9	85.1	74.1	62.6	53.6	39.4
CVG	1711	7.8	92.2	92.2	90.9	90.9	90.9	88.3	76.4	56.7	43.0	33.0	24.2
CVG	1754	7.8	92.2	92.2	92.2	92.2	92.2	90.9	83.2	70.0	58.9	49.6	37.6
CVG	1848	7.8	92.2	90.9	89.6	87.0	87.0	80.7	65.4	45.8	33.0	24.9	19.1
MN	812	7	93	74	59	54	50	42	33	25	19	16	12
MN	1362	2	98	88	85	84	81	77	67	56	49	44	34
MN	1487	1	99	89	83	80	77	70	58	46	35	28	22
MN	2301	10	90	76	70	69	66	60	51	41	36	30	23
MN	2499	1	99	90	89	86	84	76	59	42	29	22	16
CS	4863	0.1	99.9	98.6	90.8	88.2	85.6	75.8	52.6	28.6	17.5	12.9	10.2
CS	4887	0.0	100.0	92.2	90.9	87.0	79.5	67.7	43.0	23.5	15.1	11.8	9.2
CS	5280	0.0	100.0	72.3	45.8	42.1	36.8	31.8	26.4	20.1	16.3	14.0	11.3
CS	5383	0.0	100.0	90.9	87.0	83.2	75.8	64.3	40.3	22.1	15.1	11.8	9.2

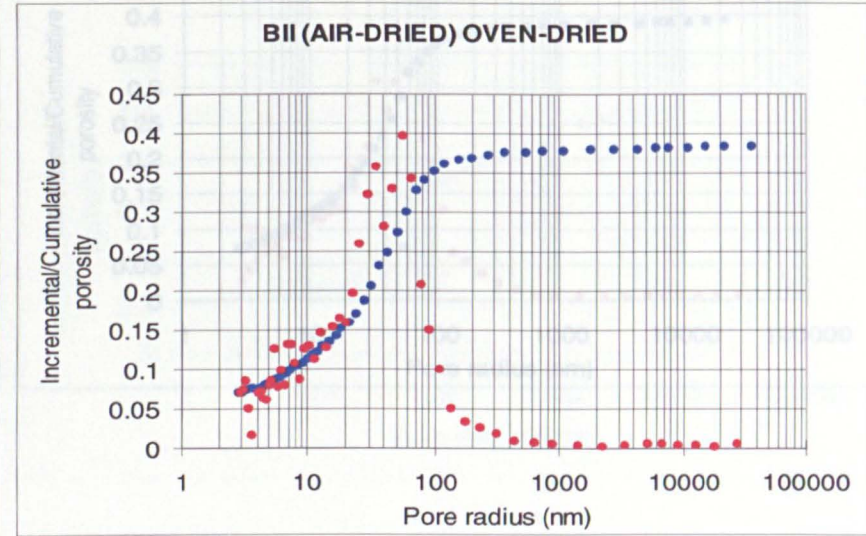
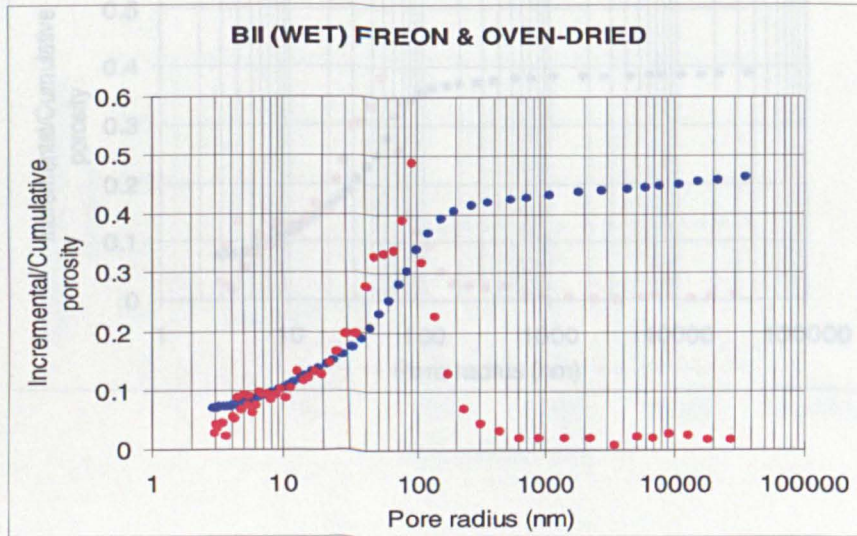
Mercury Intrusion Porosimetry Data: Part A Glacial Clays for Drying Tests



Mercury Intrusion Porosimetry Data: Part A Glacial Clays for Drying Tests continued

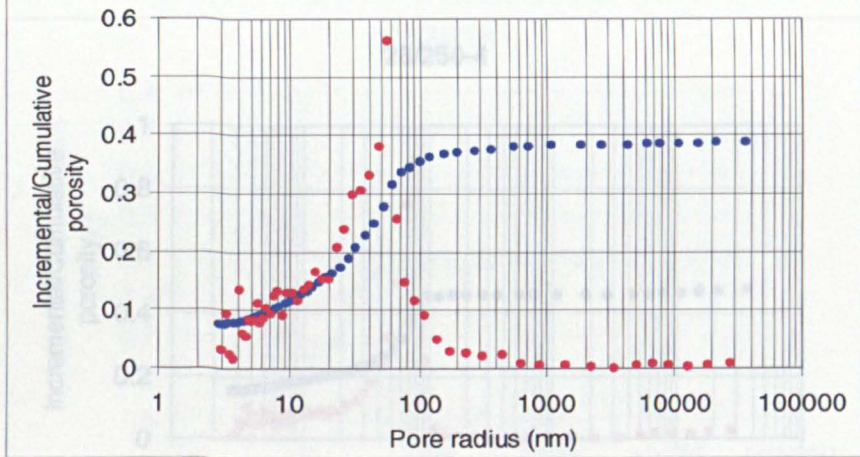


Mercury Intrusion Porosimetry Data: Part A Glacial Clays for Drying Tests continued

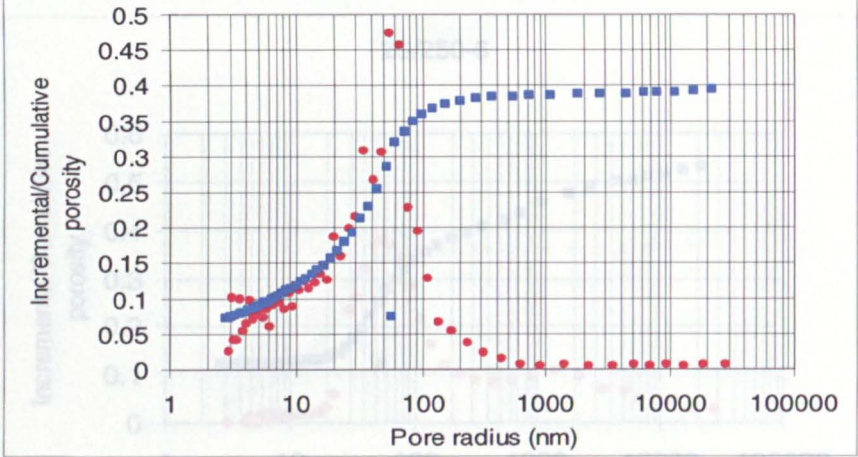


Mercury Intrusion Porosimetry Part A DSDP/ODP

BII (AIR-DRIED) FREON



BII (AIR-DRIED) FREON & OVEN-DRIED



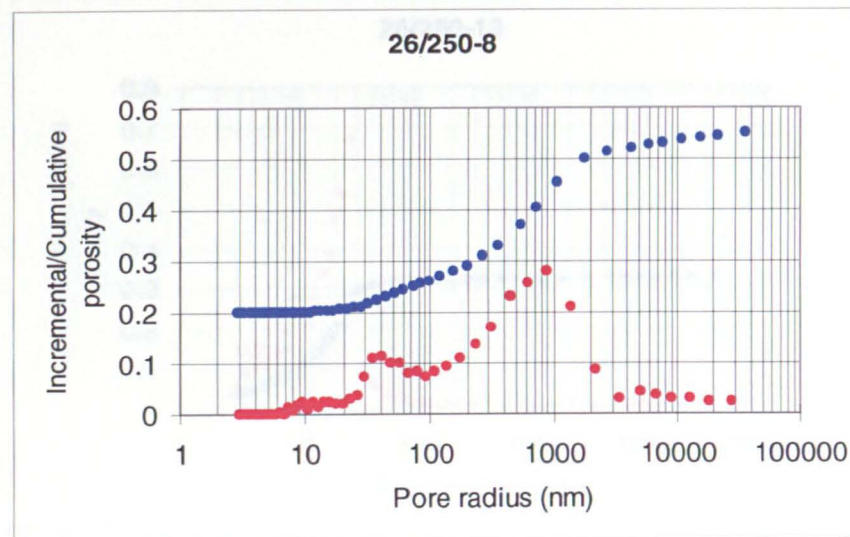
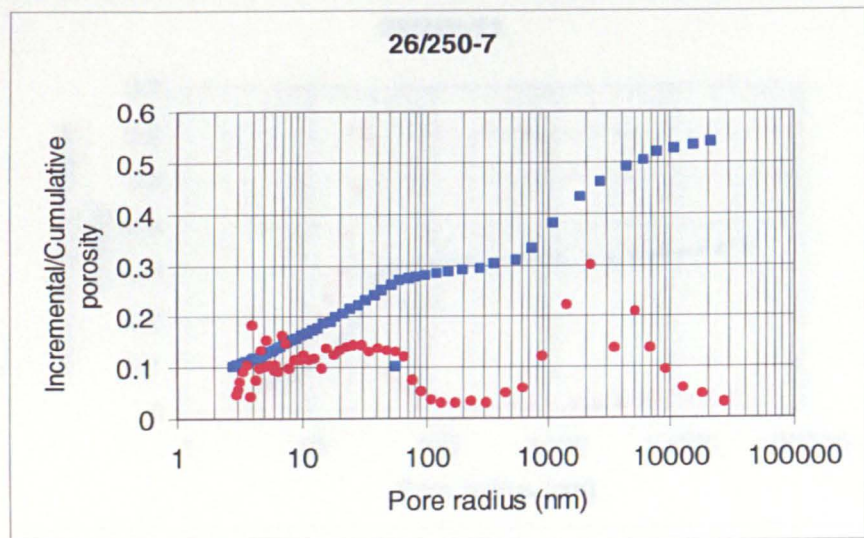
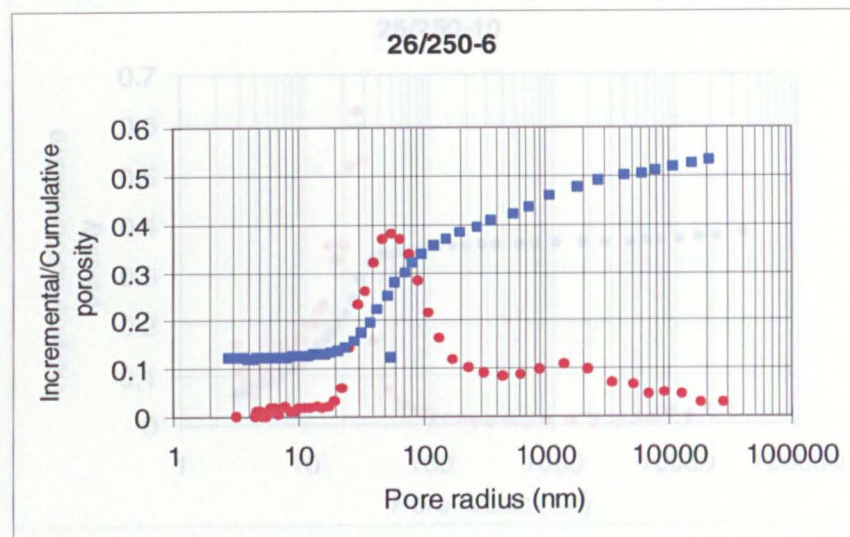
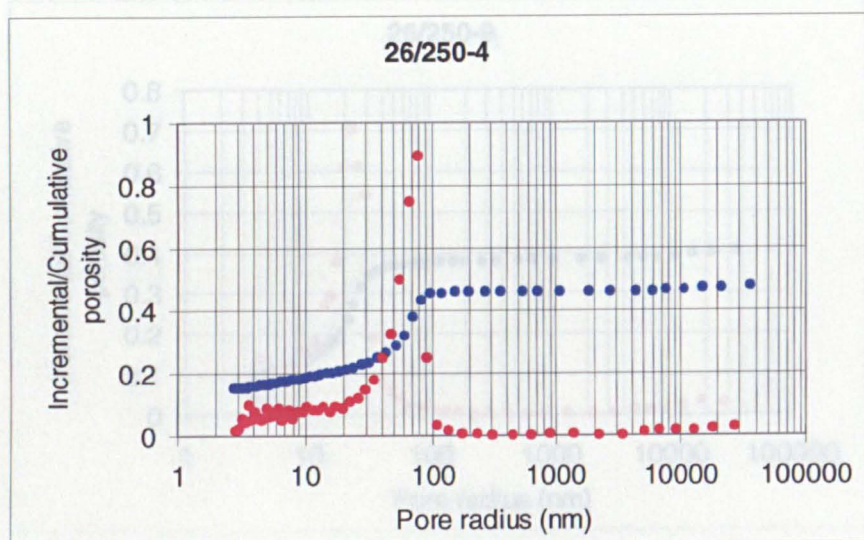
26220-7



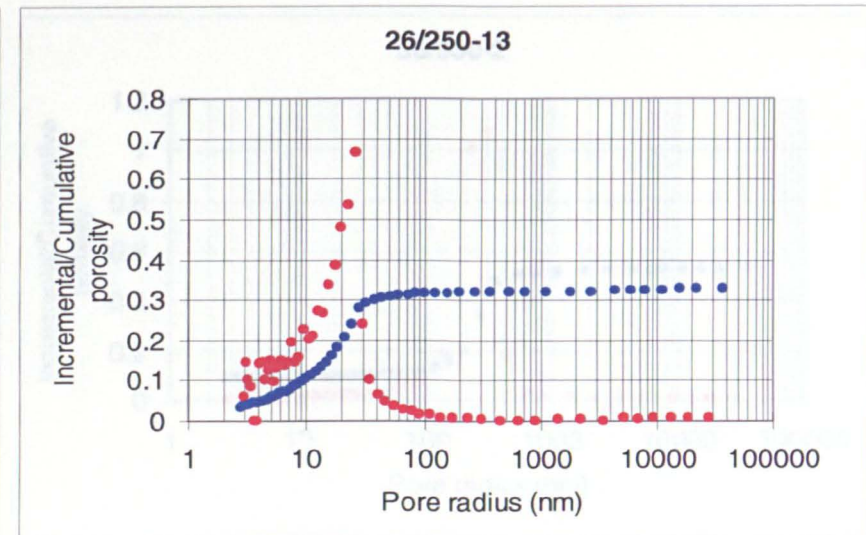
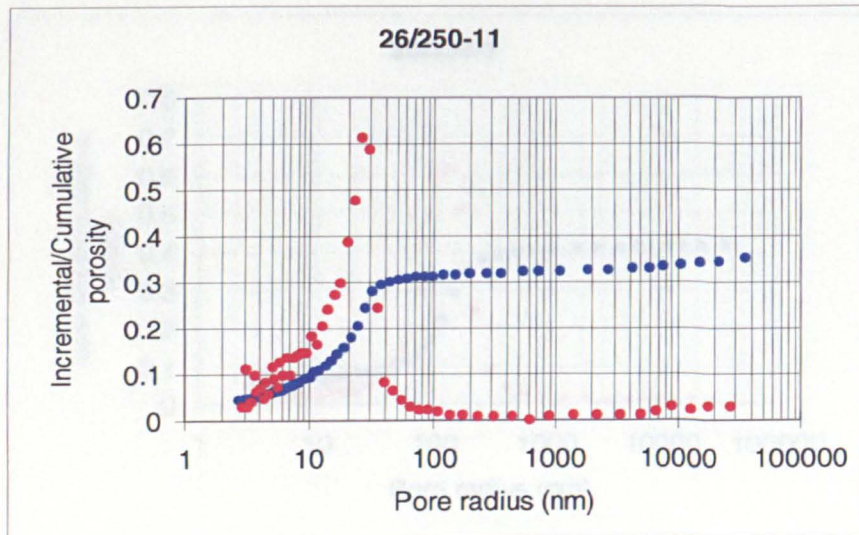
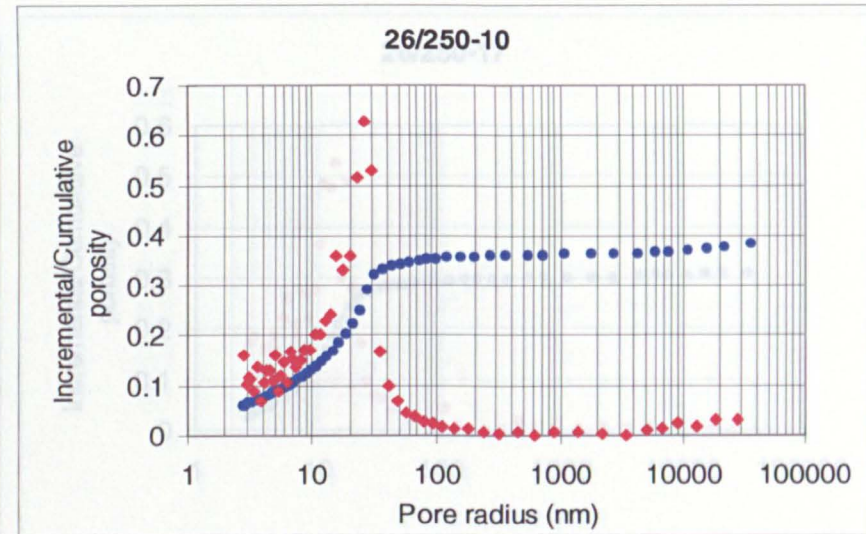
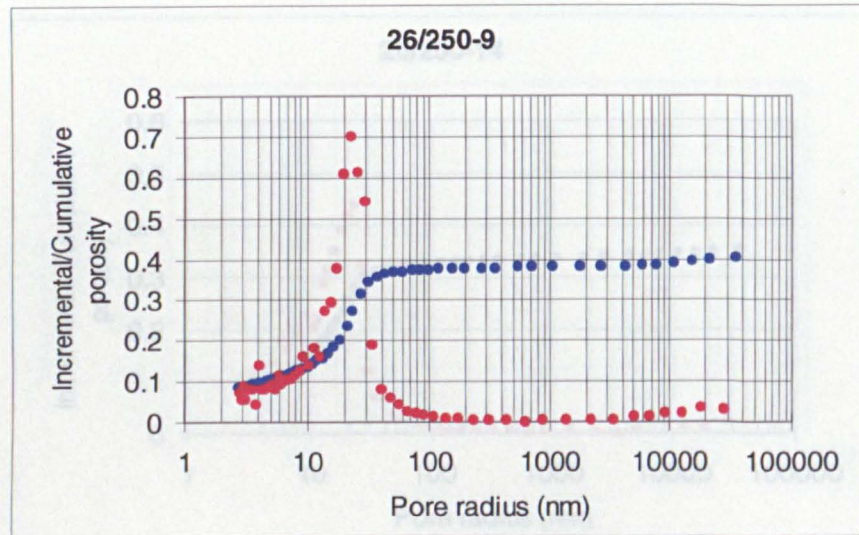
26220-6



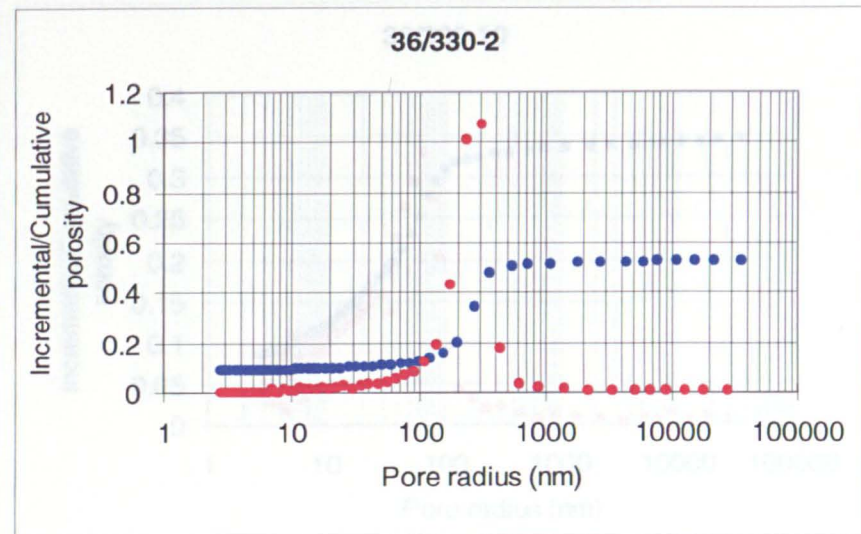
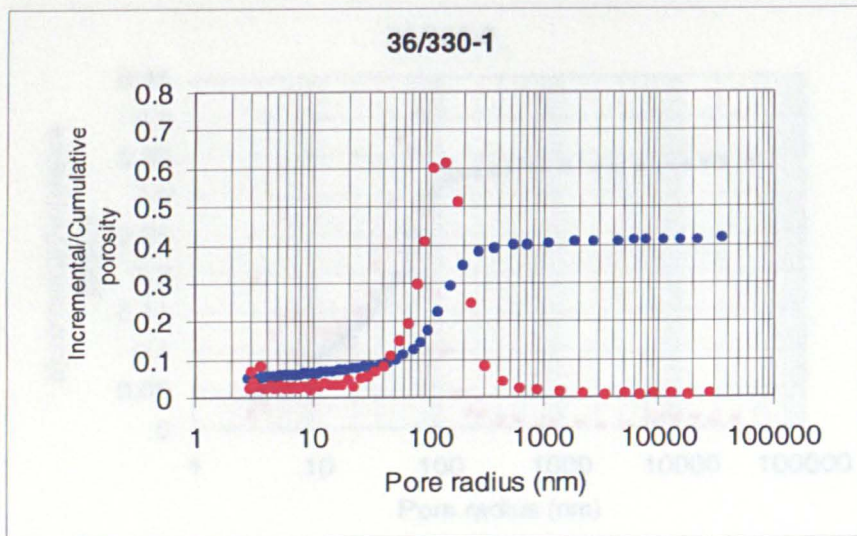
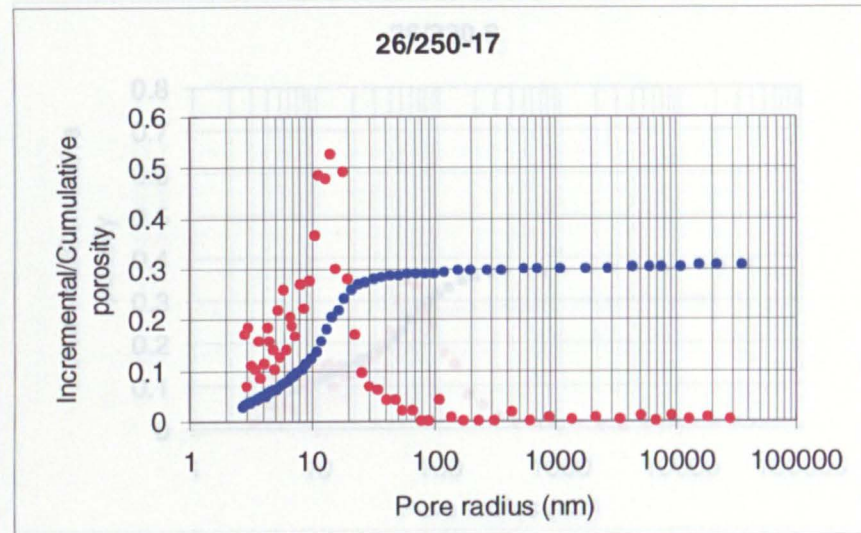
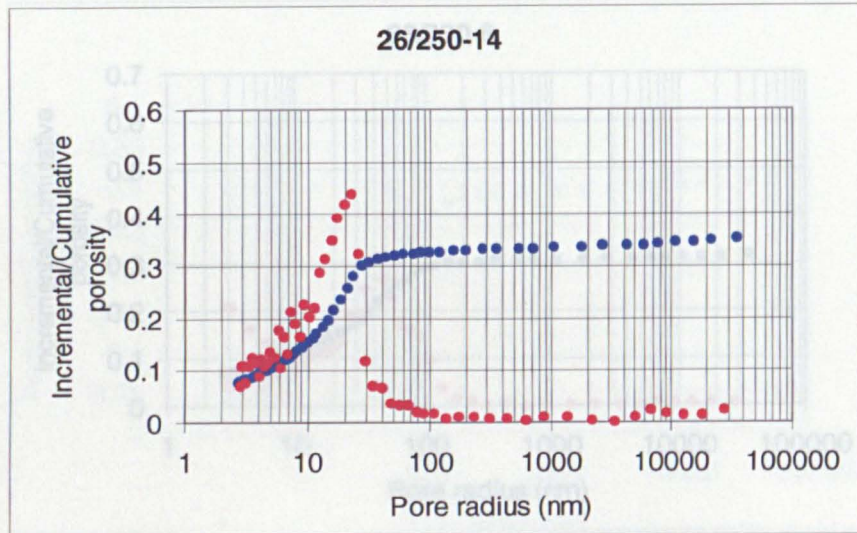
Mercury Intrusion Porosimetry Data: Part A DSDP/ODP



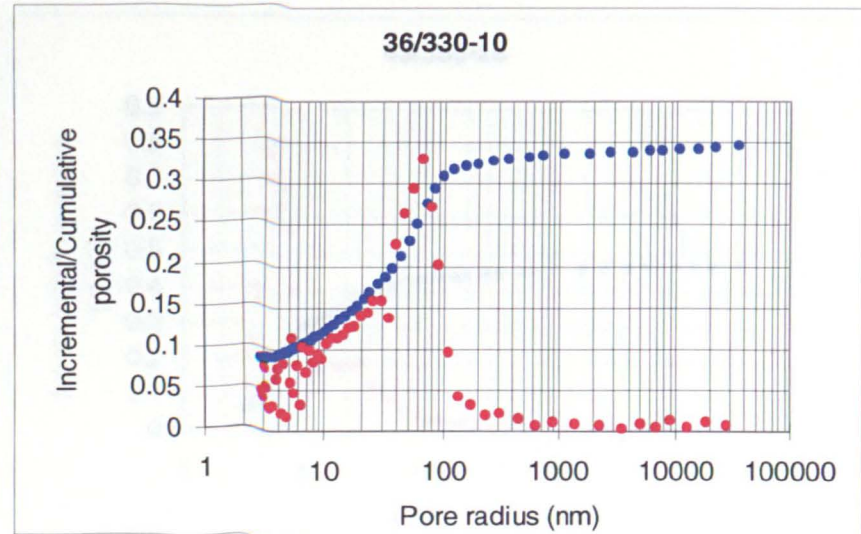
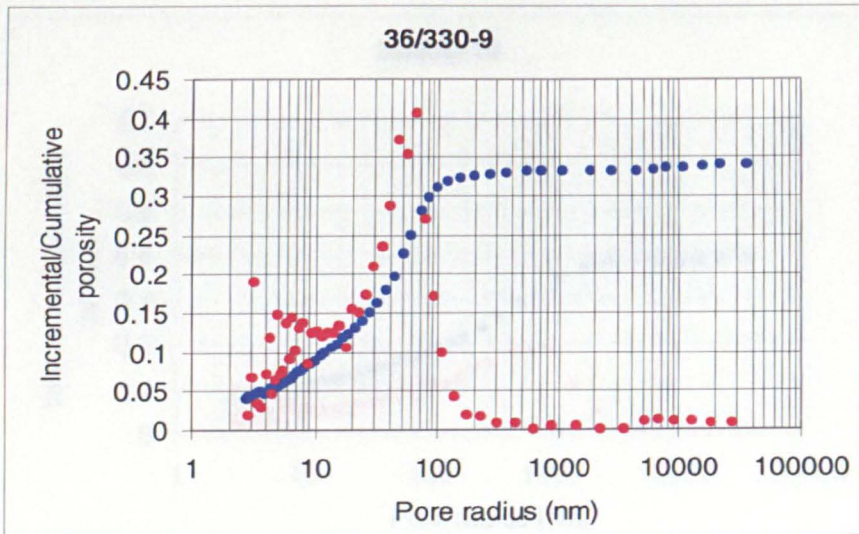
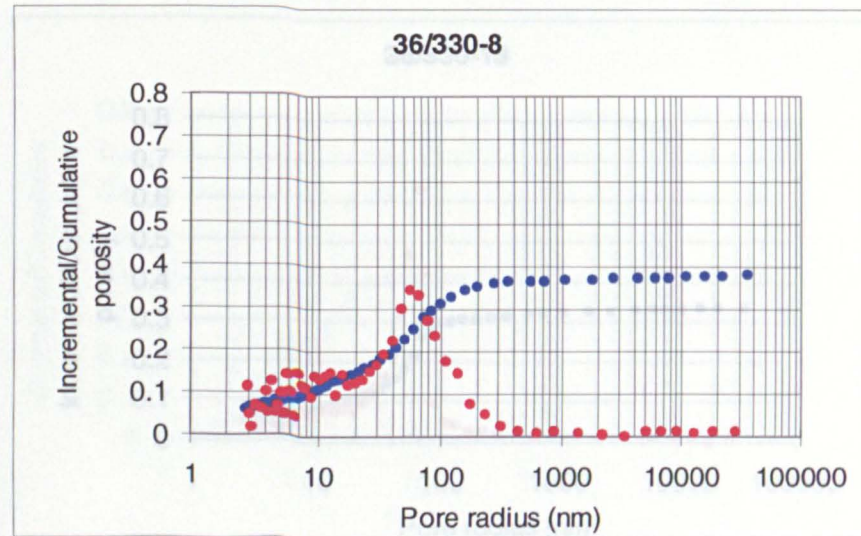
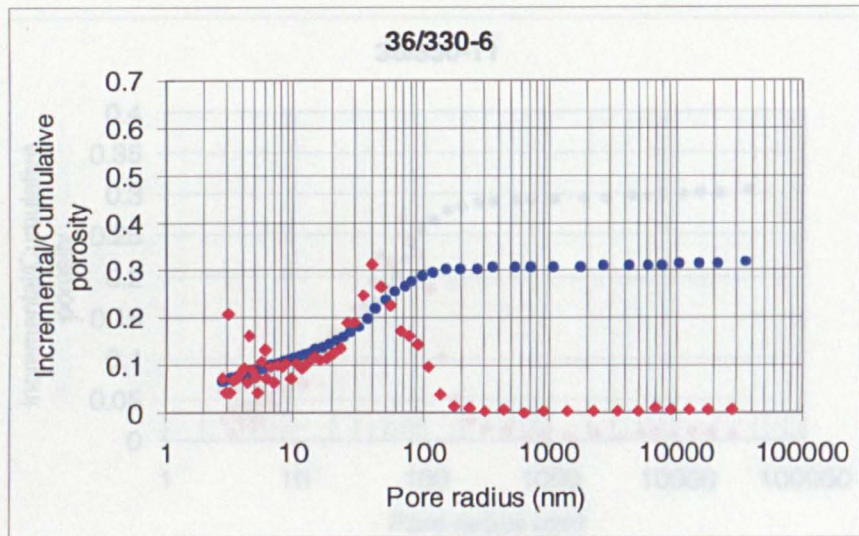
Mercury Intrusion Porosimetry Data: Part A DSDP/ODP continued



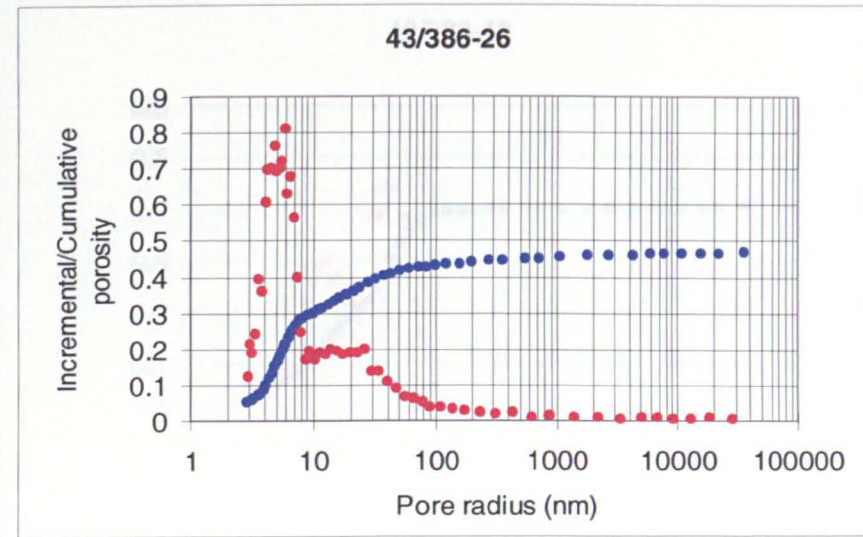
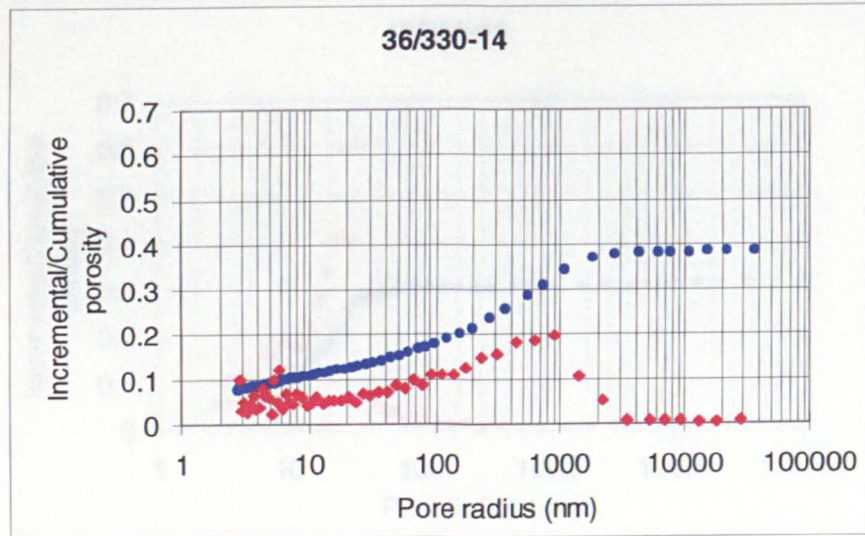
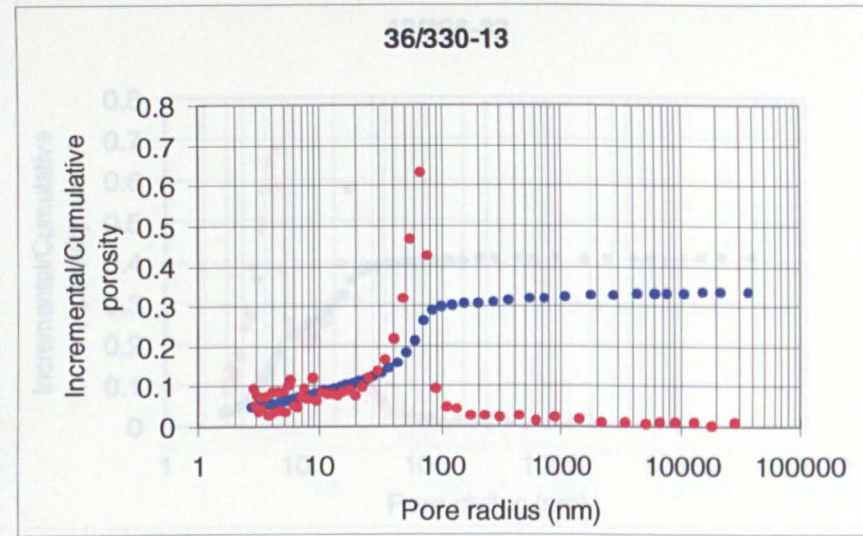
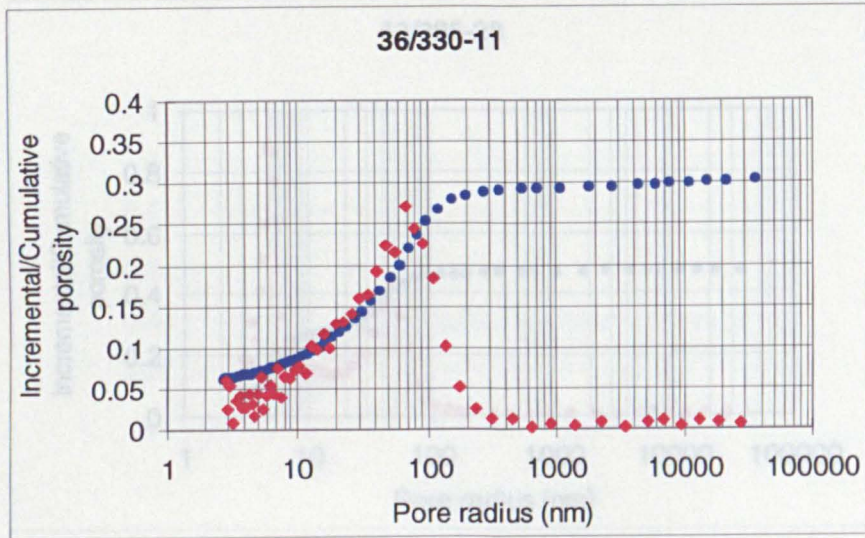
Mercury Intrusion Porosimetry Data: Part A DSDP/ODP continued



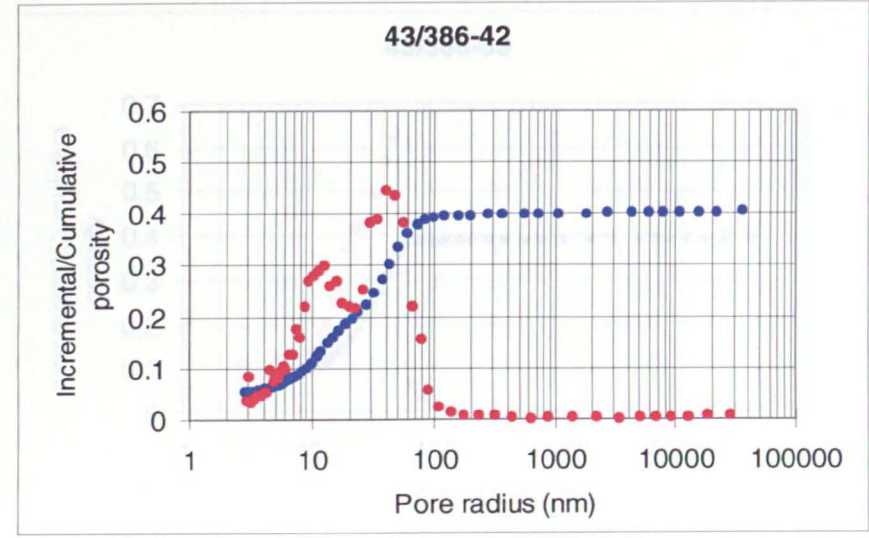
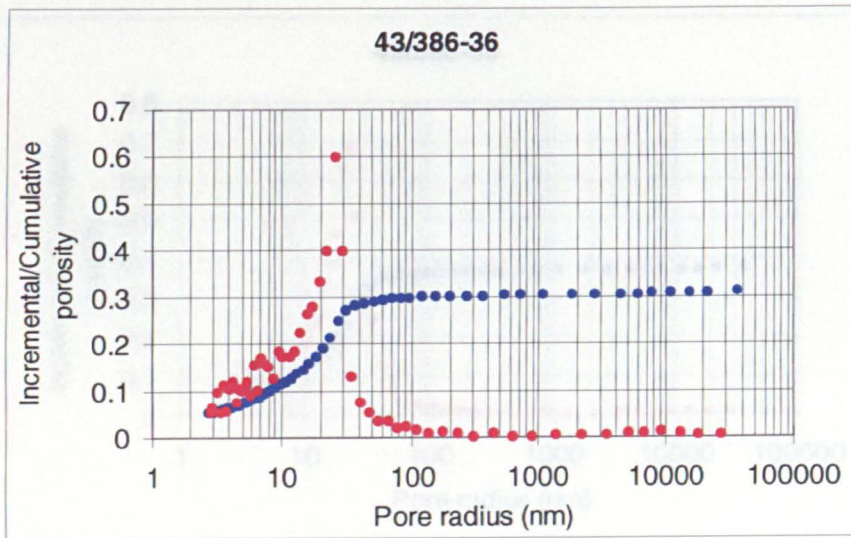
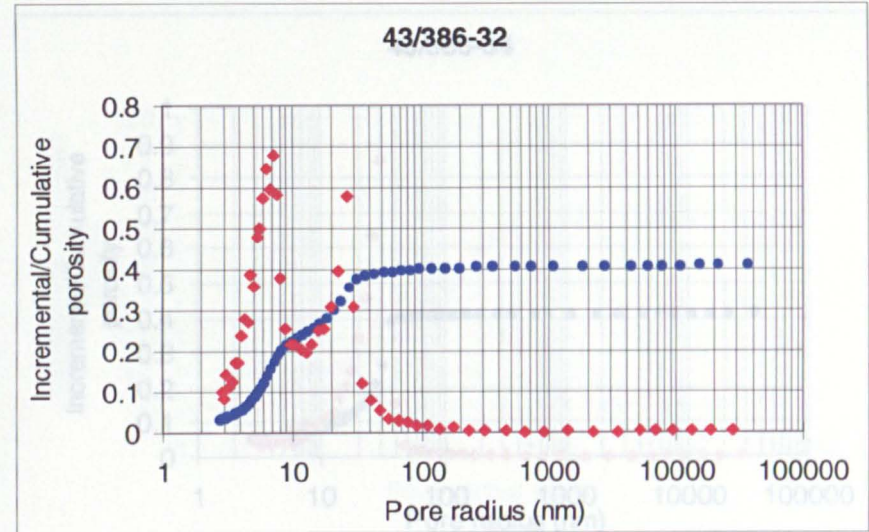
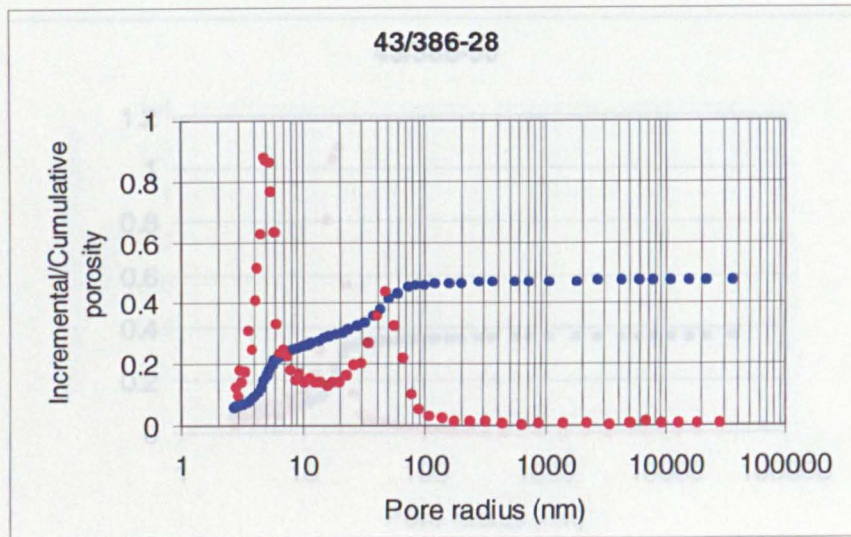
Mercury Intrusion Porosimetry Data: Part A DSDP/ODP continued



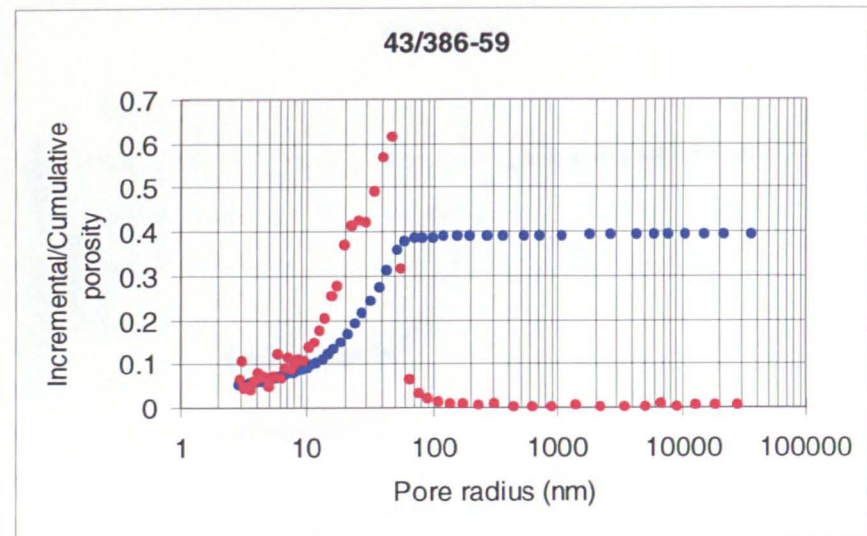
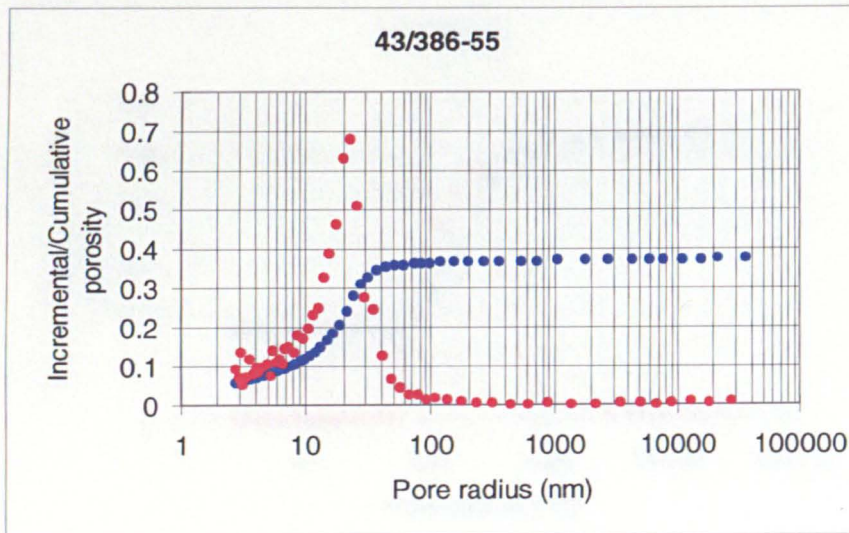
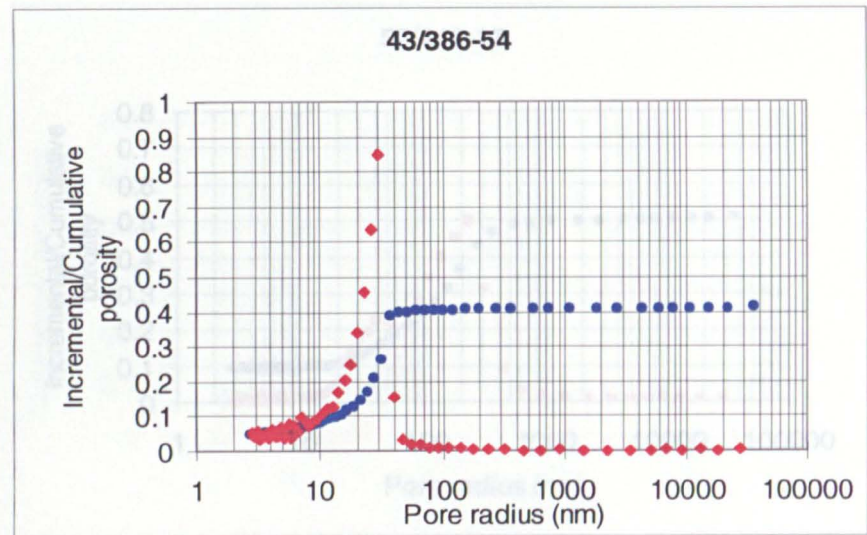
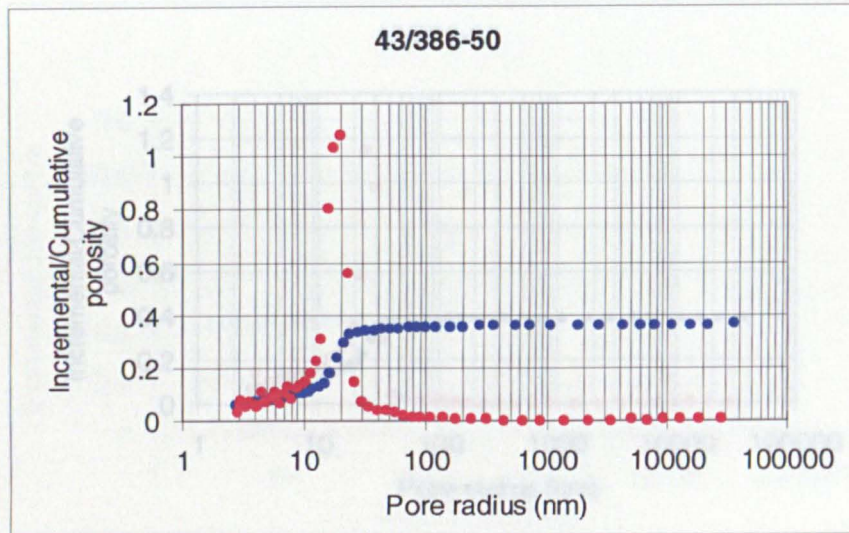
Mercury Intrusion Porosimetry Data: Part A DSDP/ODP continued



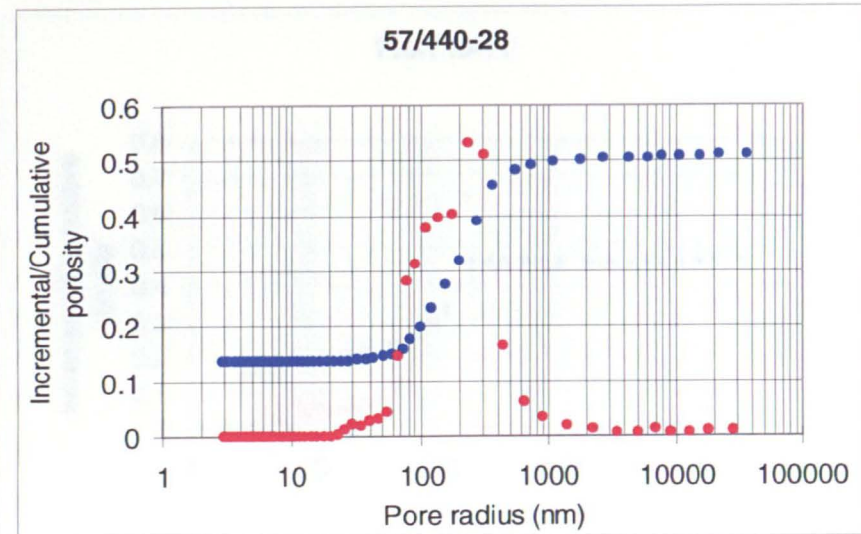
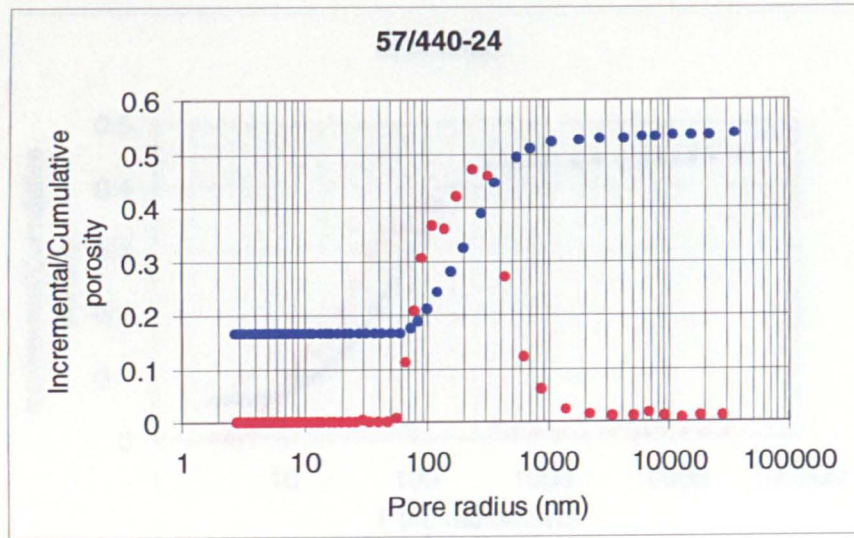
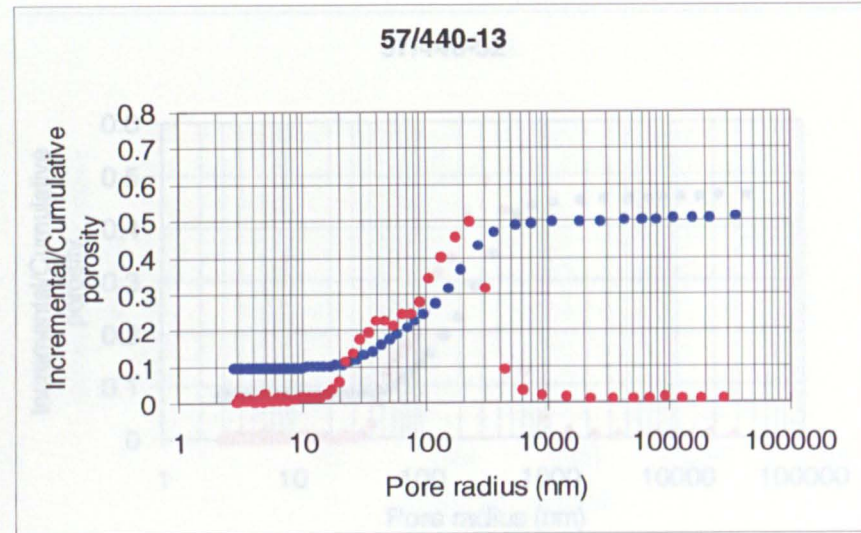
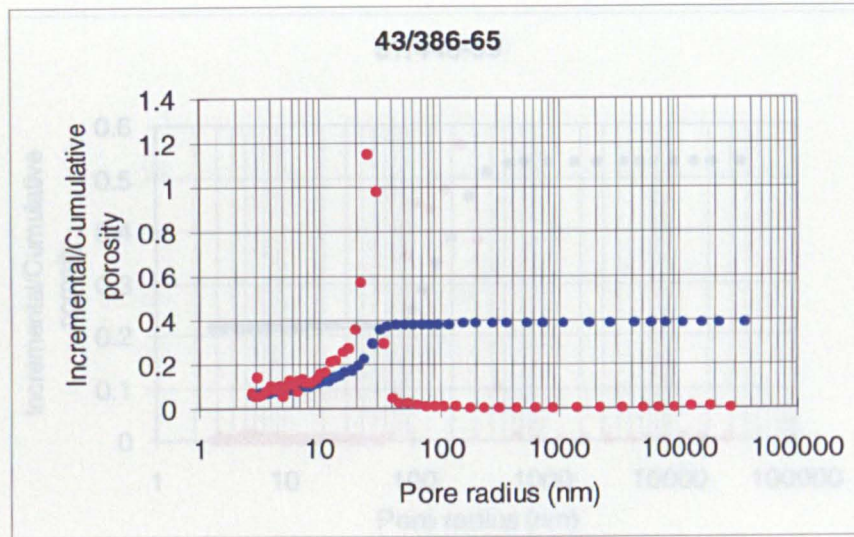
Mercury Intrusion Porosimetry Data: Part A DSDP/ODP continued



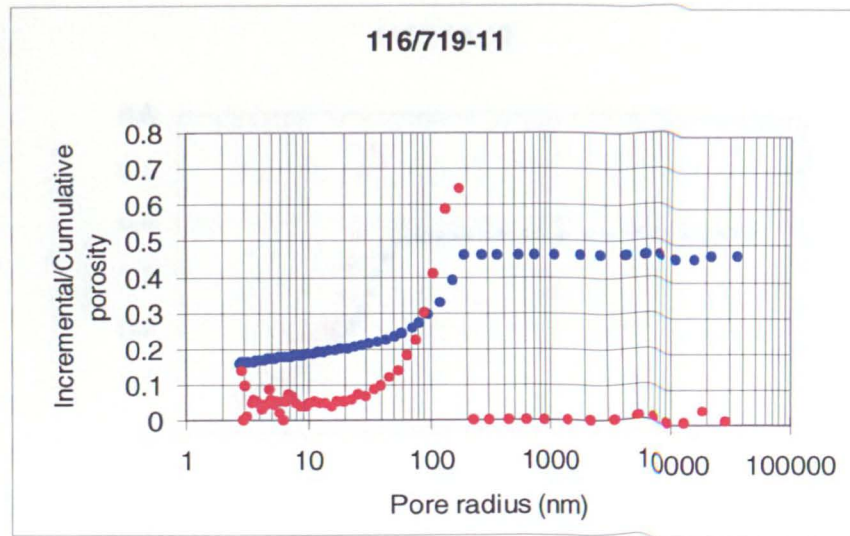
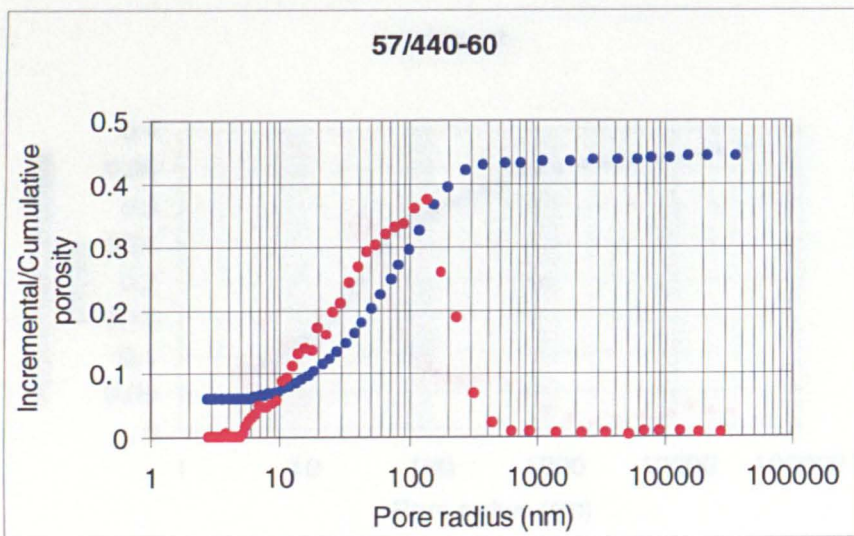
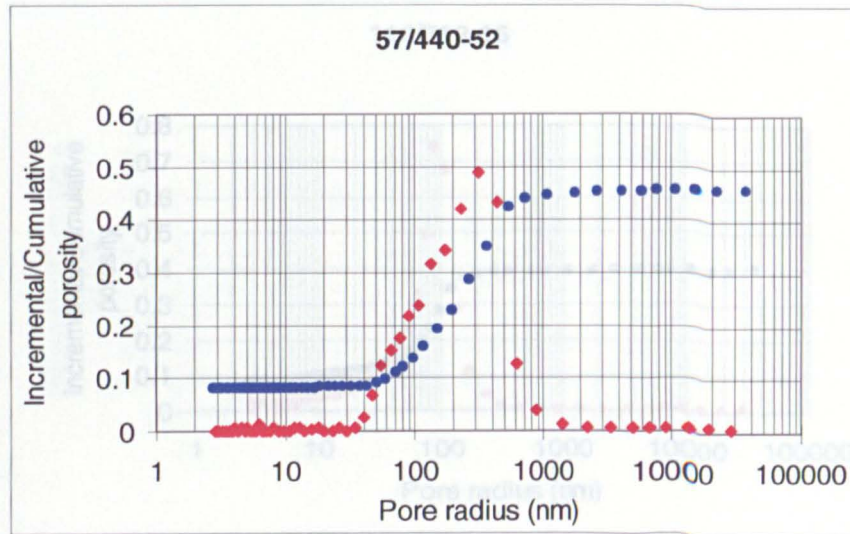
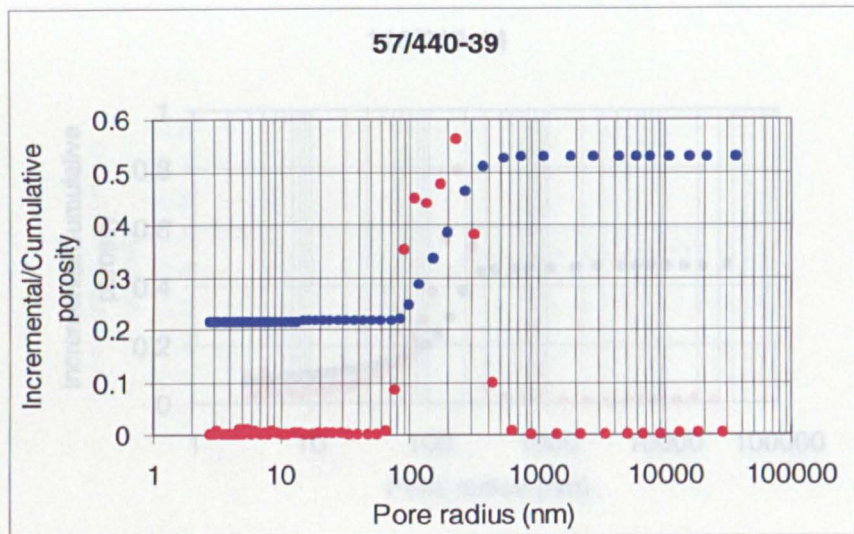
Mercury Intrusion Porosimetry Data: Part A DSDP/ODP continued



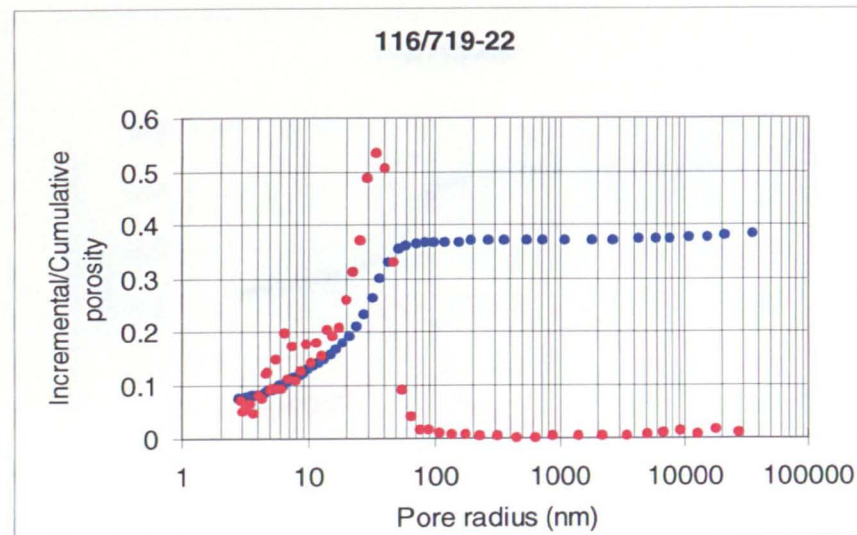
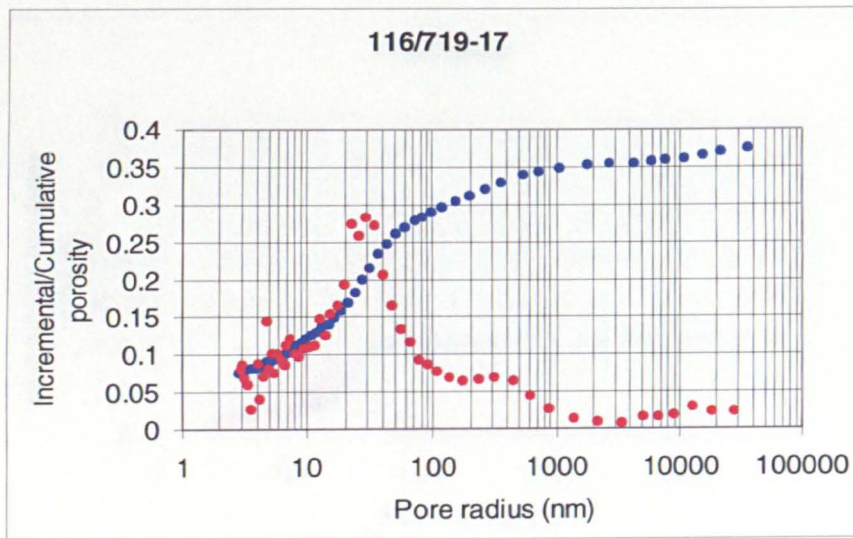
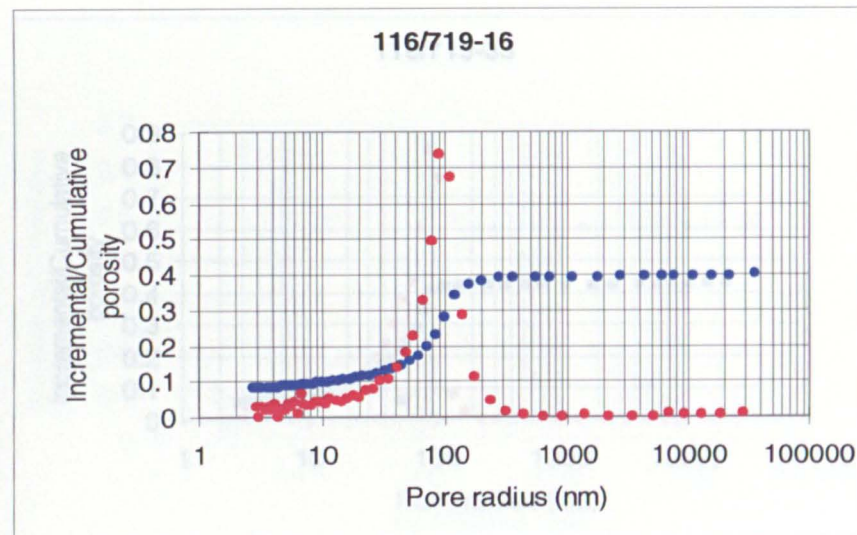
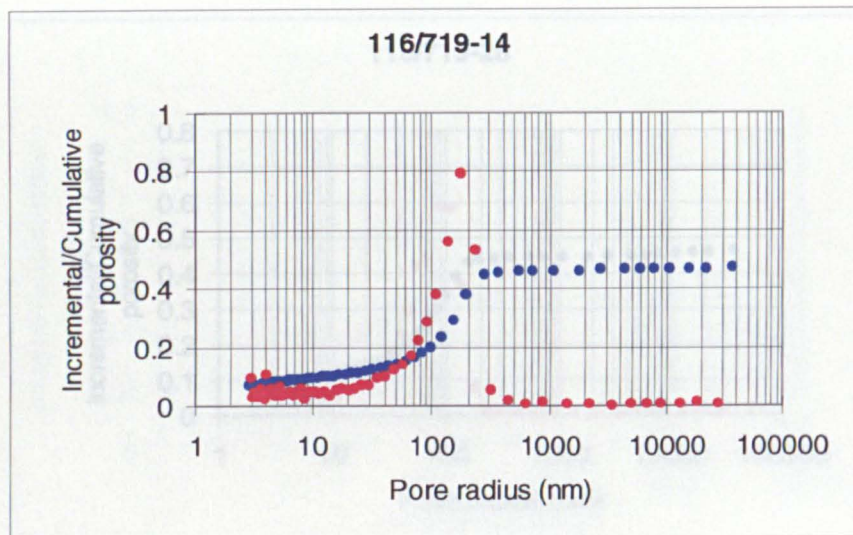
Mercury Intrusion Porosimetry Data: Part A DSDP/ODP continued



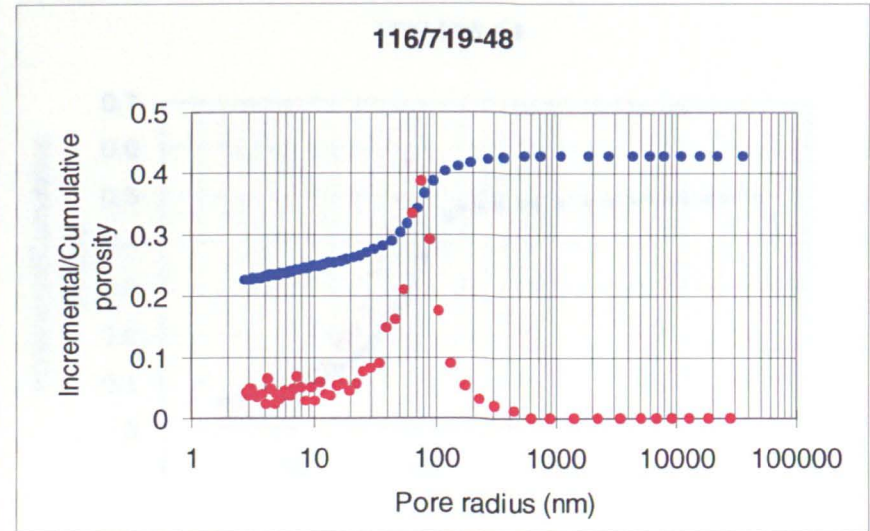
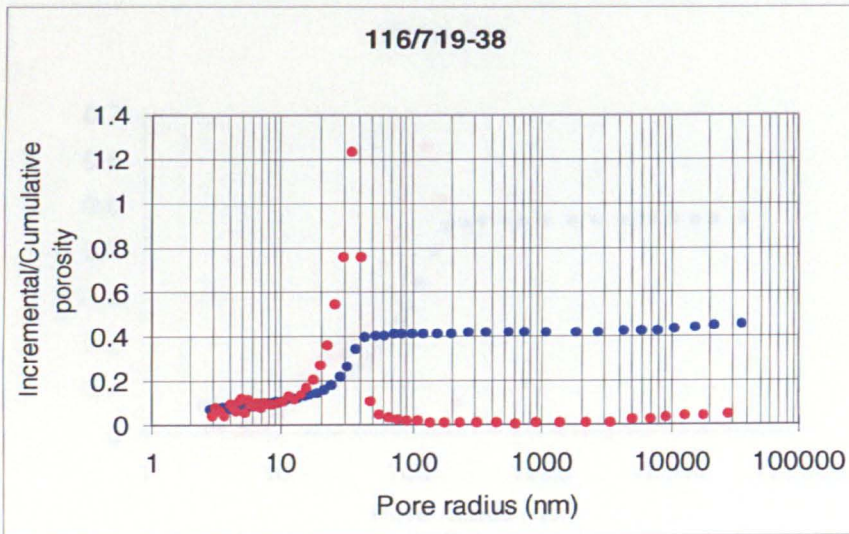
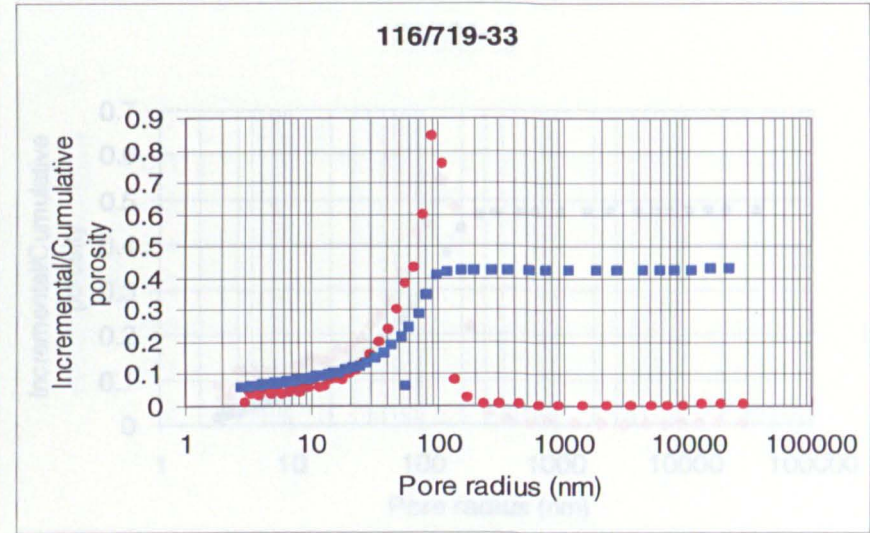
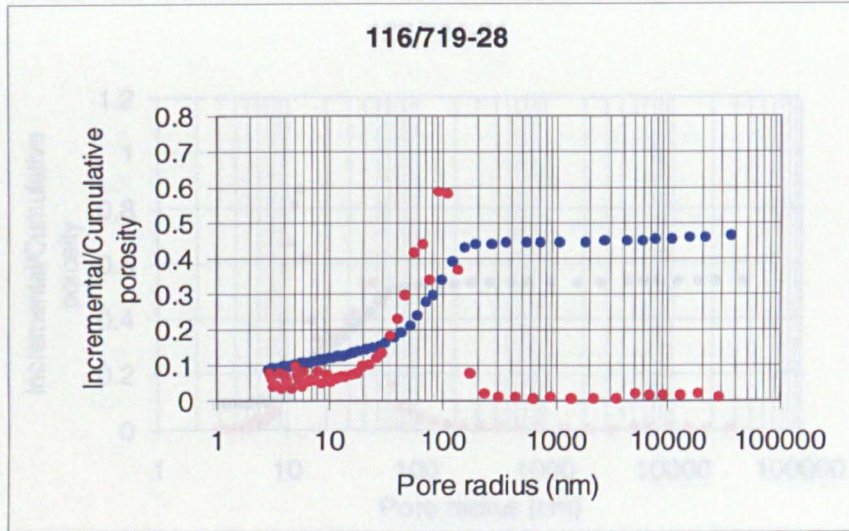
Mercury Intrusion Porosimetry Data: Part A DSDP/ODP continued



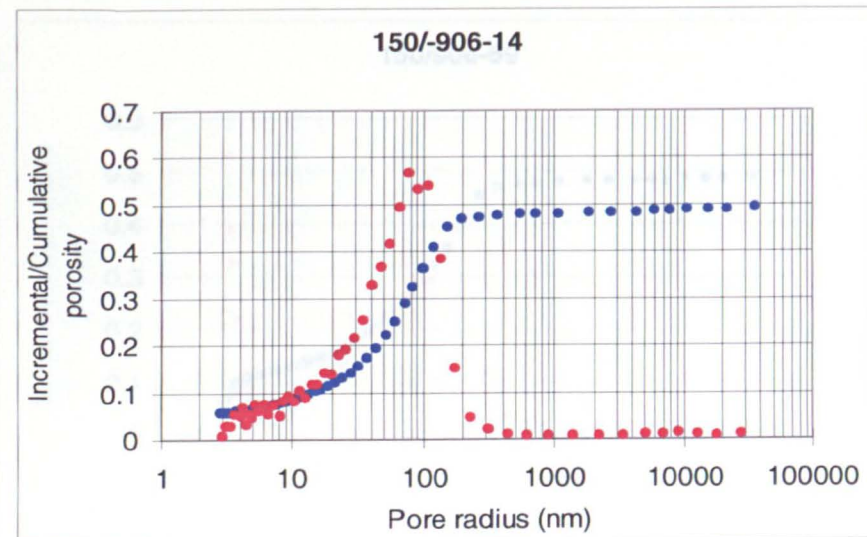
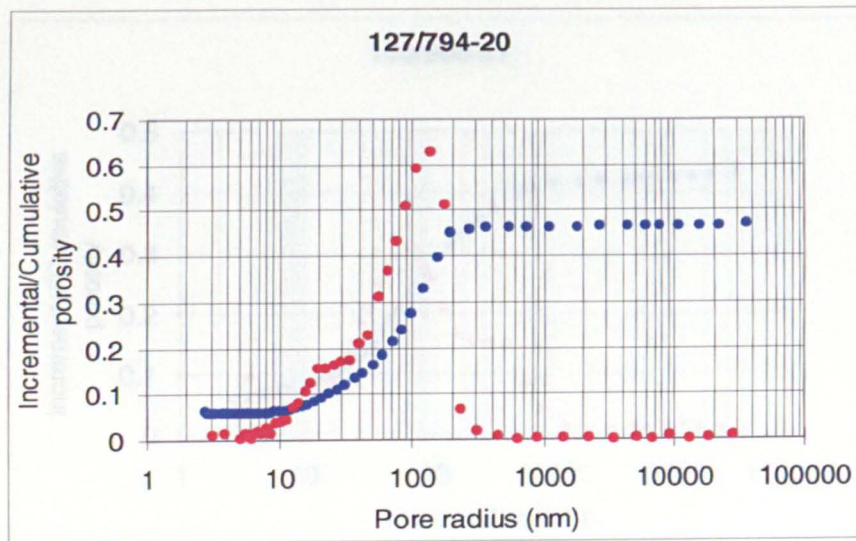
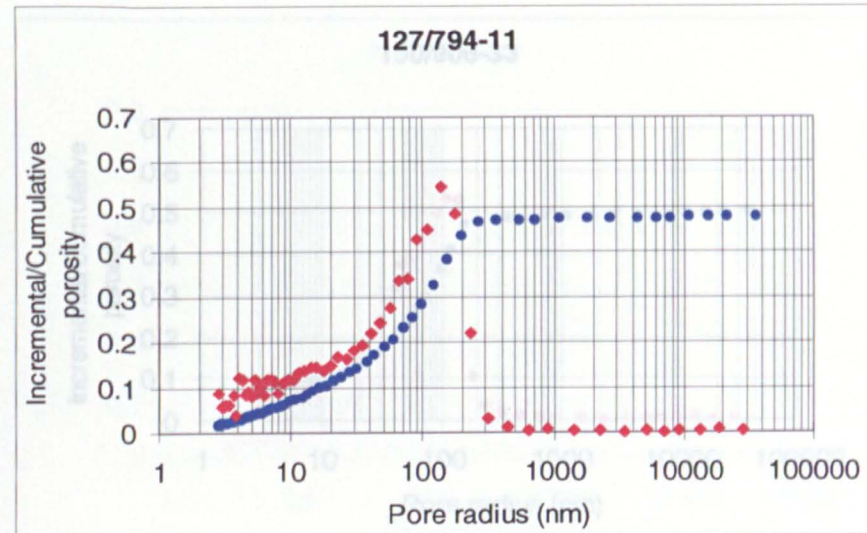
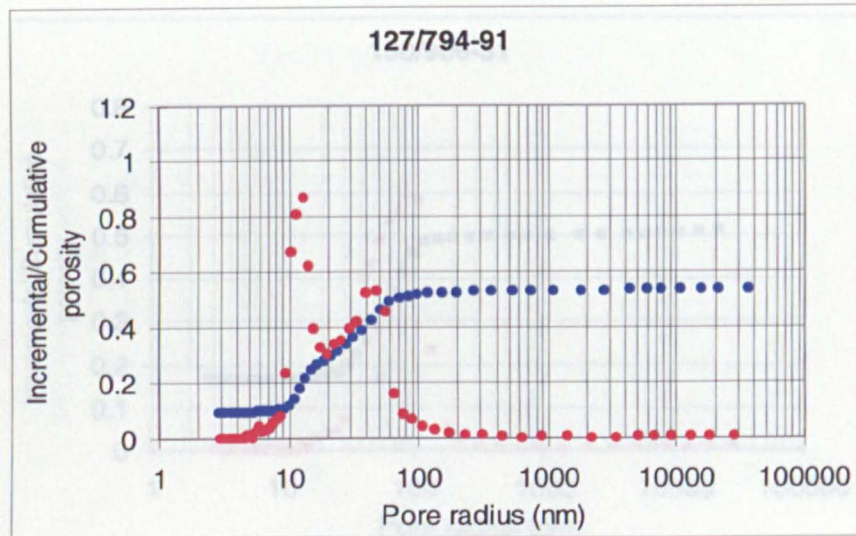
Mercury Intrusion Porosimetry Data: Part A DSDP/ODP continued



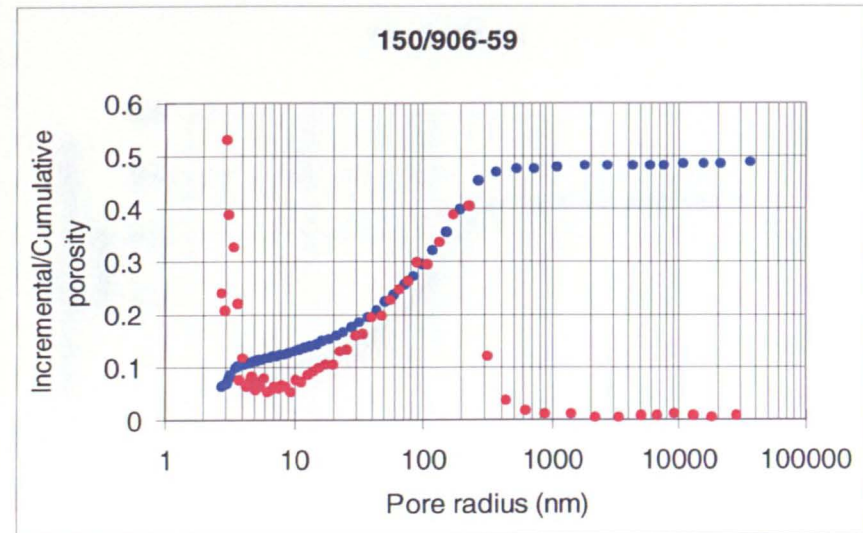
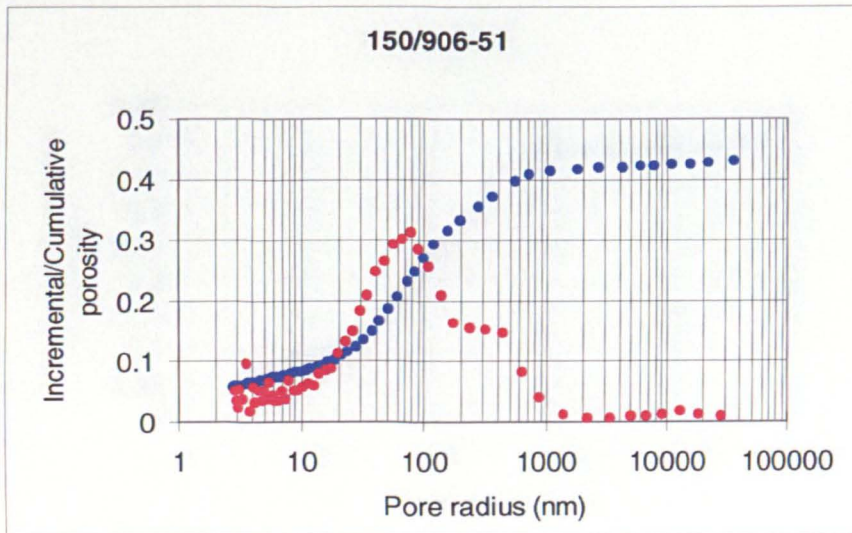
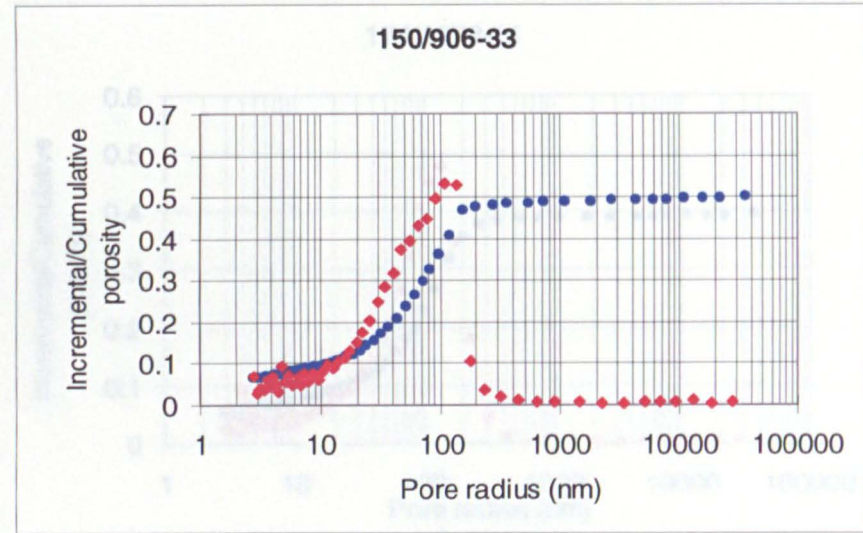
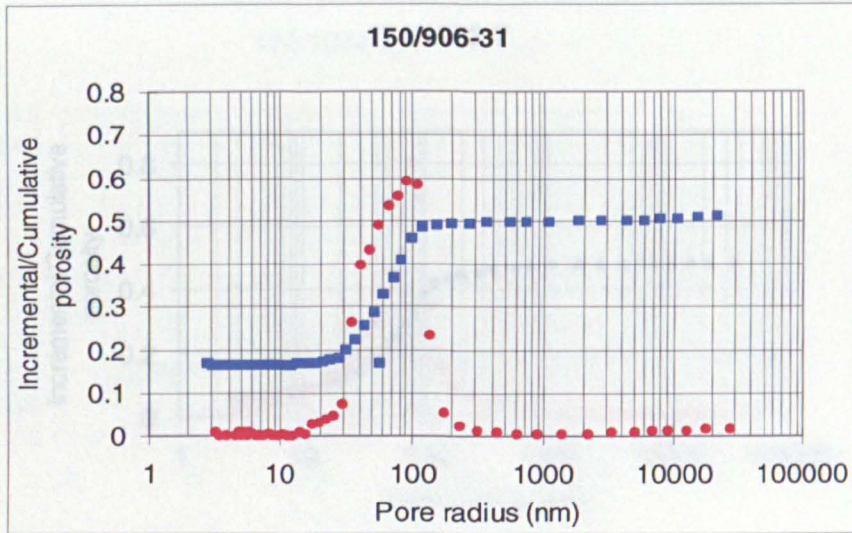
Mercury Intrusion Porosimetry Data: Part A DSDP/ODP continued



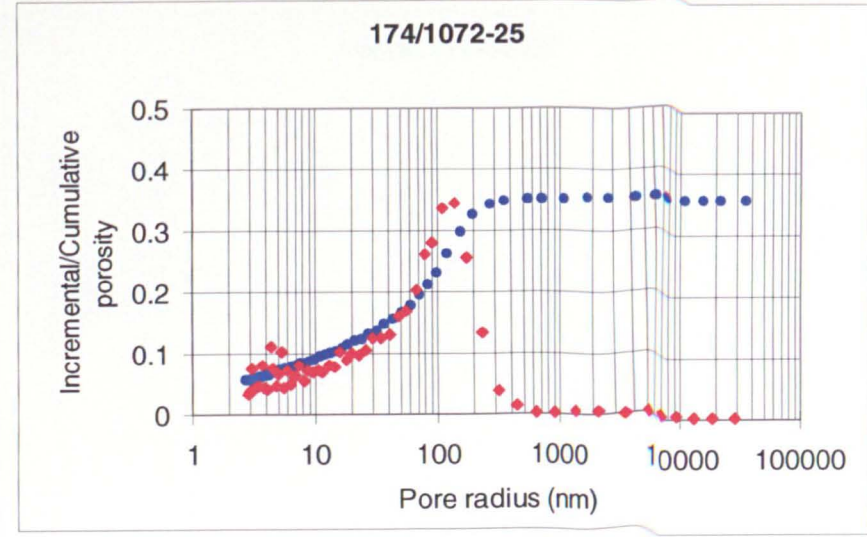
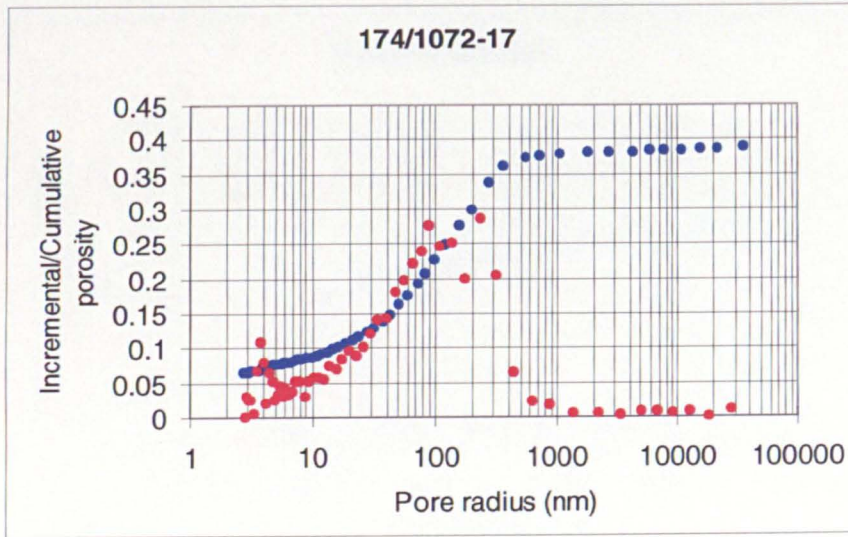
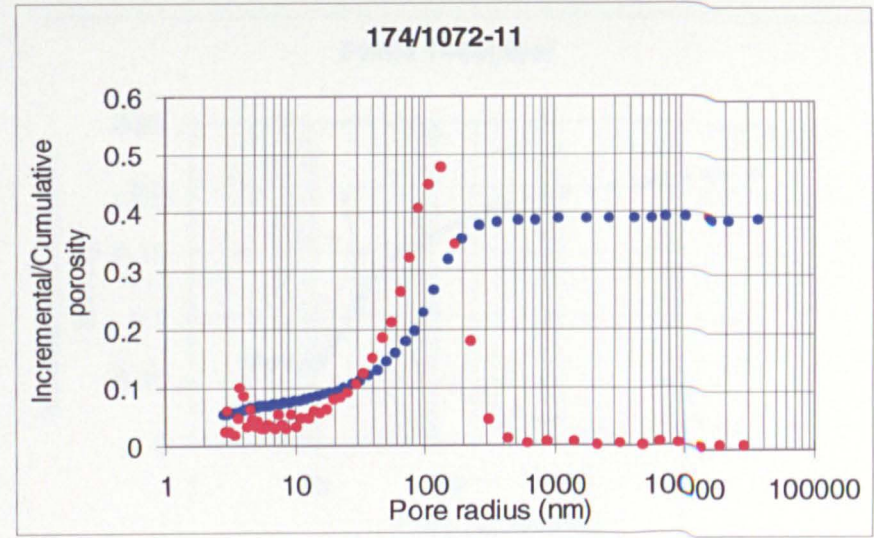
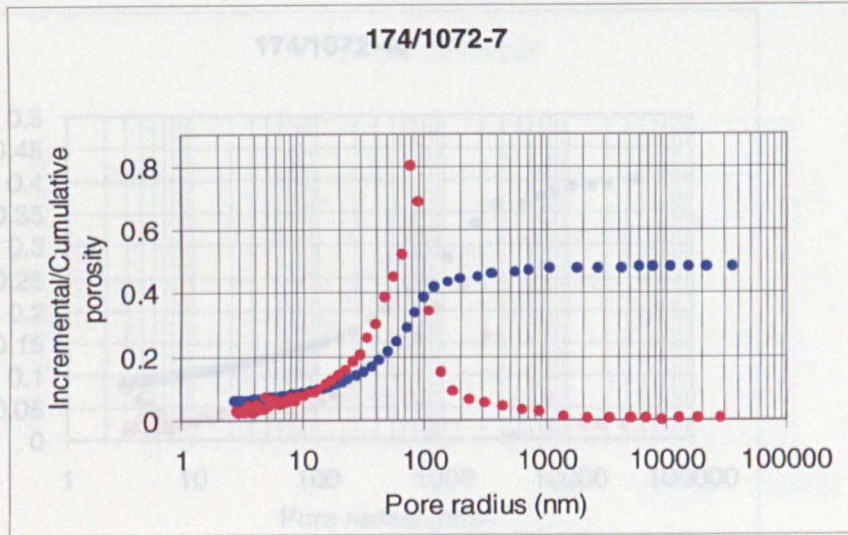
Mercury Intrusion Porosimetry Data: Part A DSDP/ODP continued



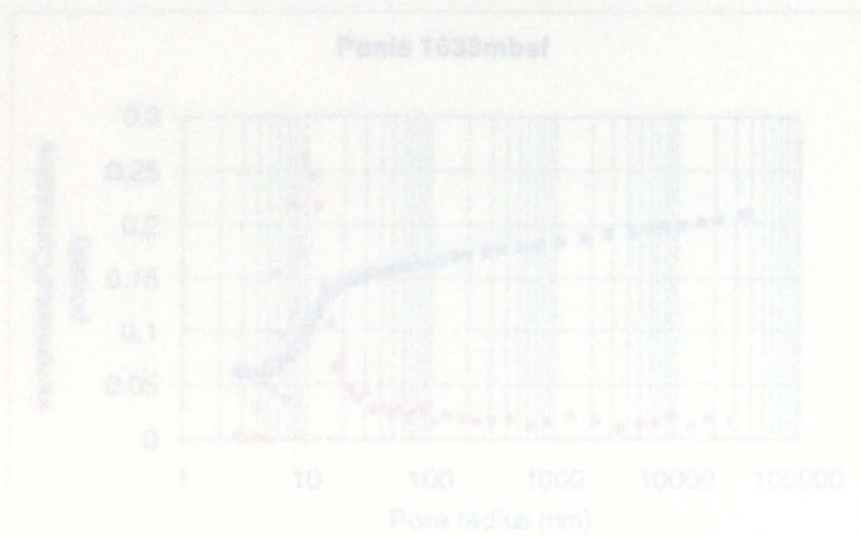
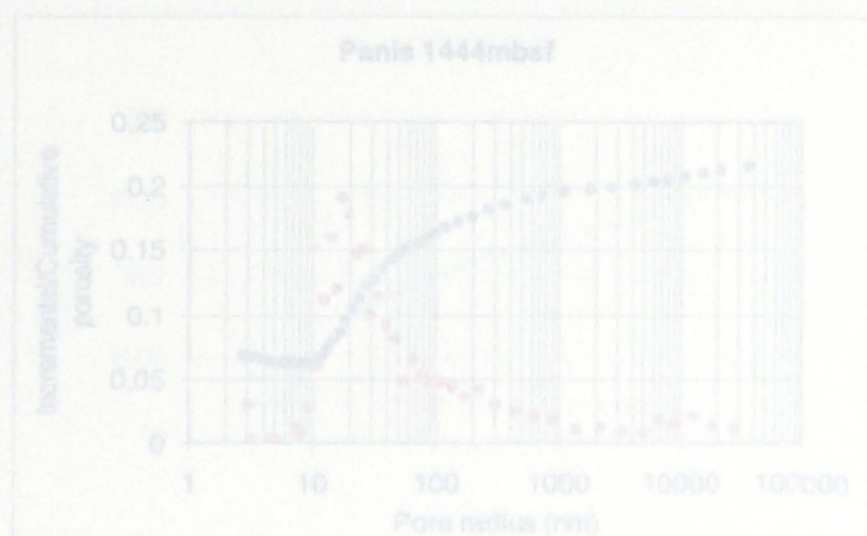
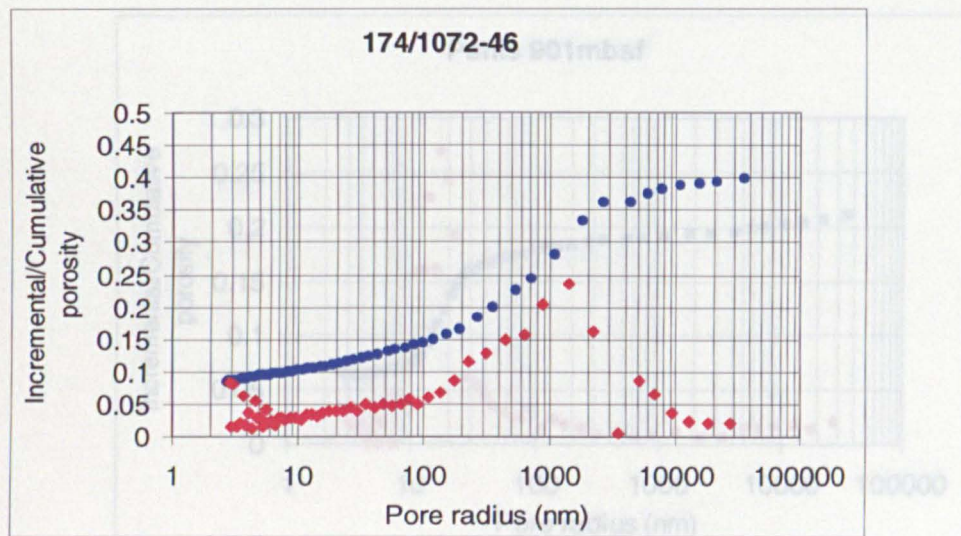
Mercury Intrusion Porosimetry Data: Part A DSDP/ODP continued



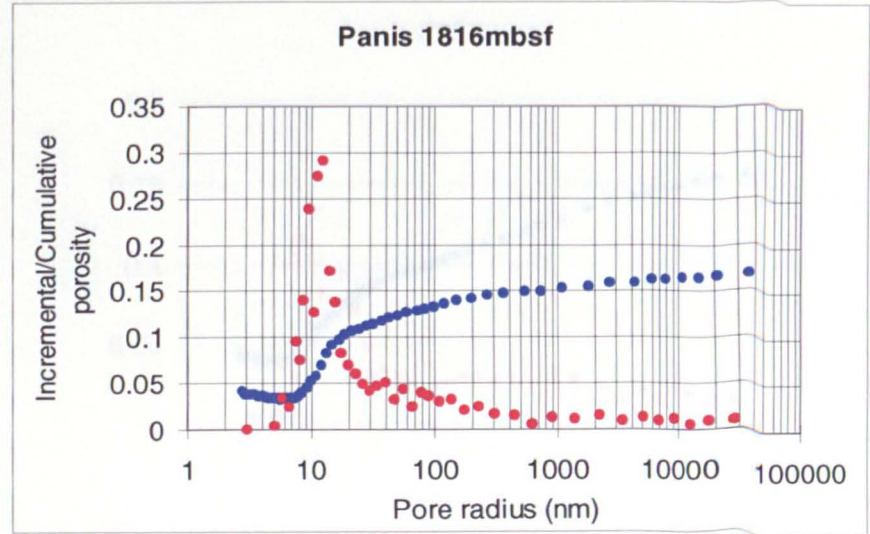
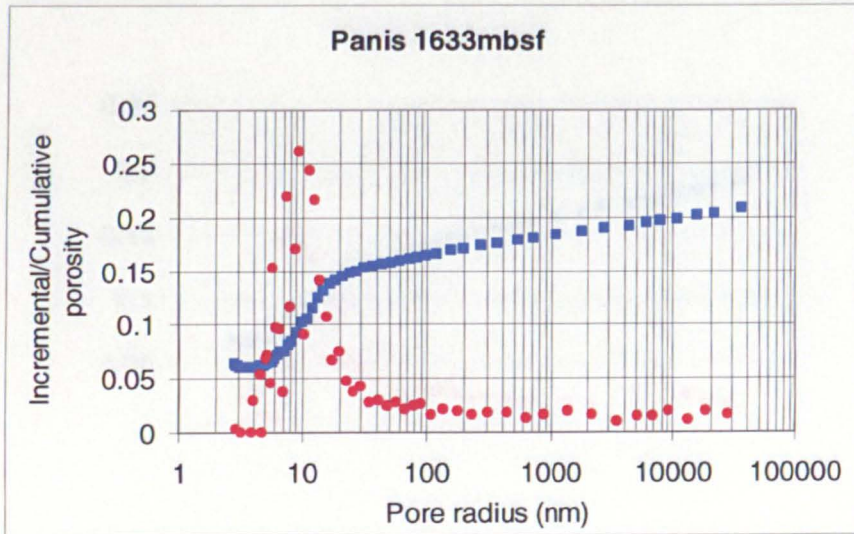
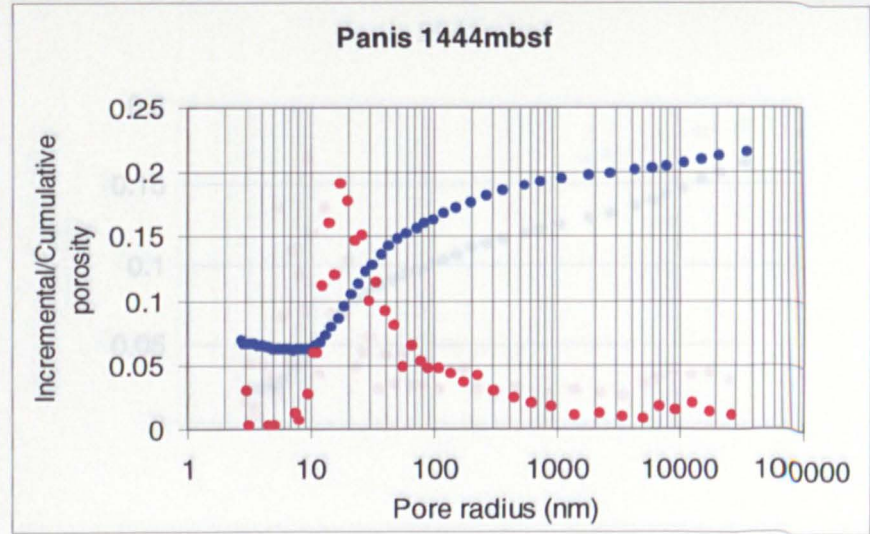
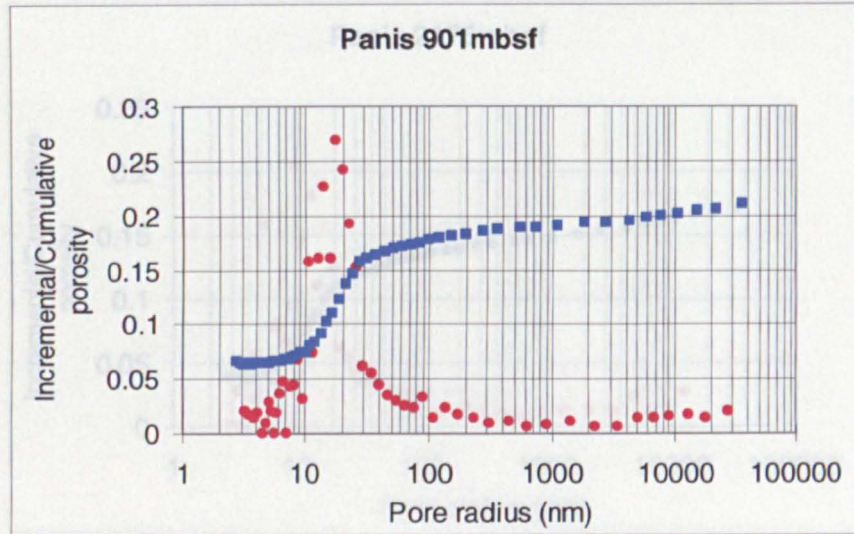
Mercury Intrusion Porosimetry Data: Part A DSDP/ODP continued



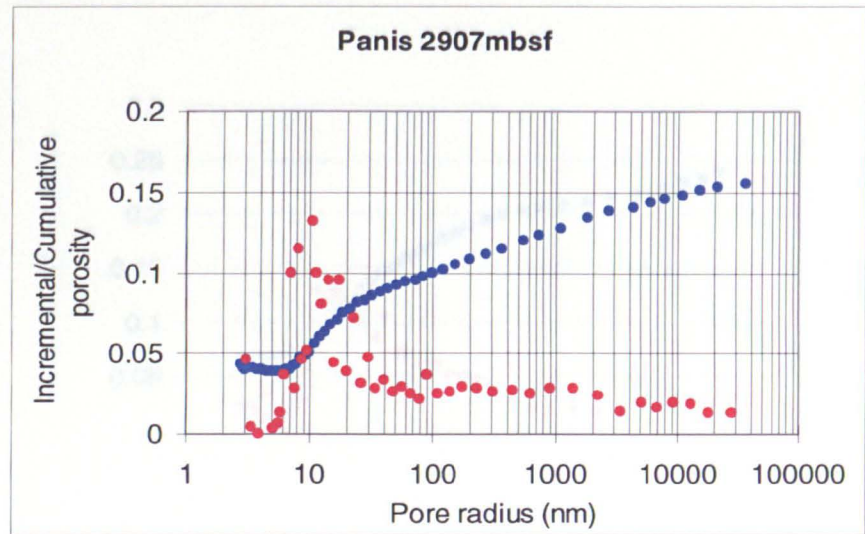
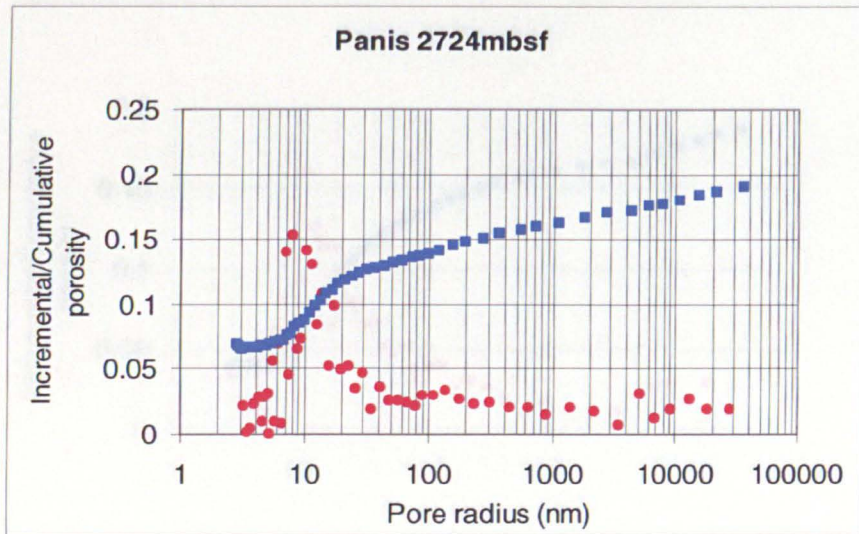
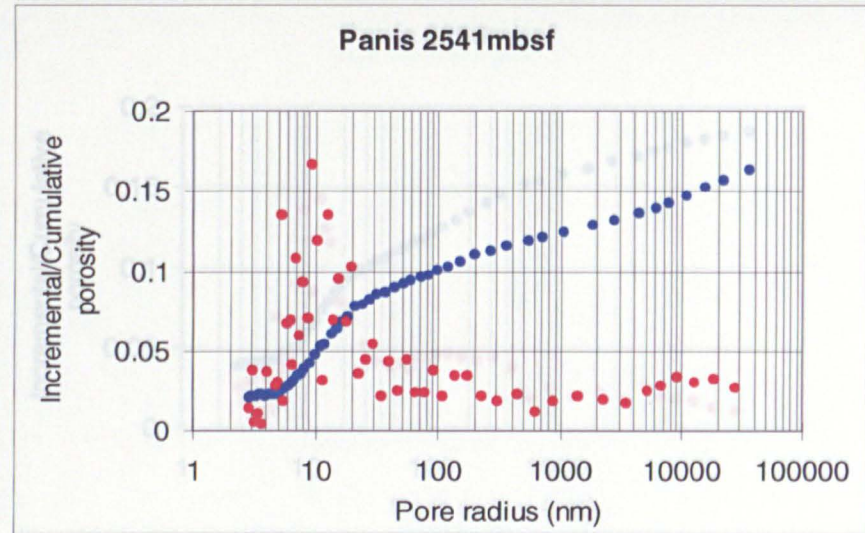
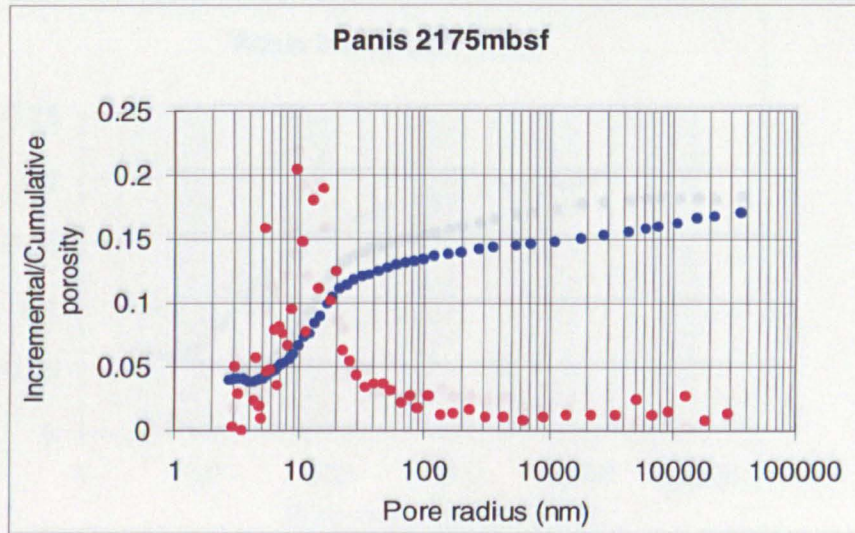
Mercury Intrusion Porosimetry Data: Part A DSDP/ODP continued



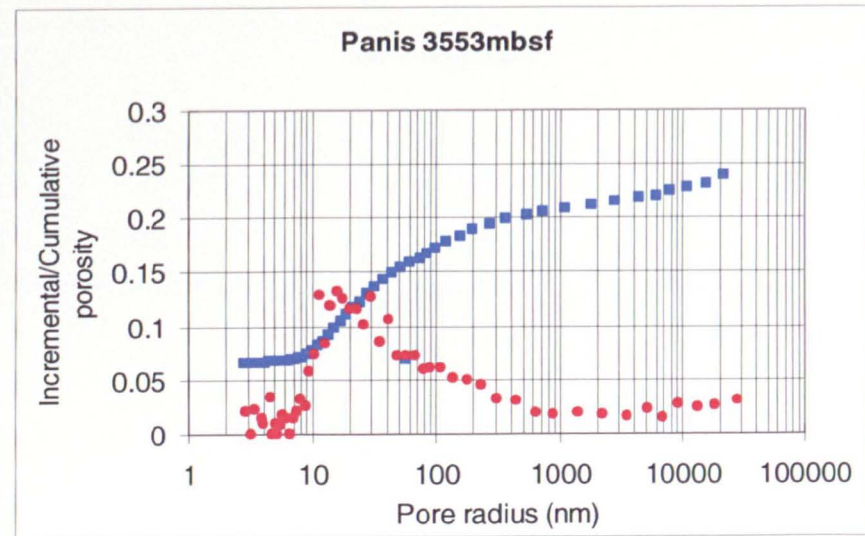
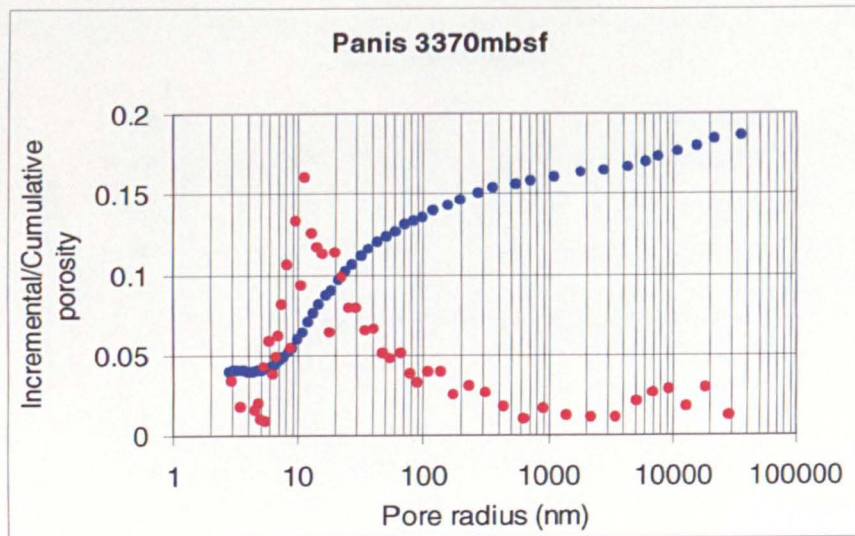
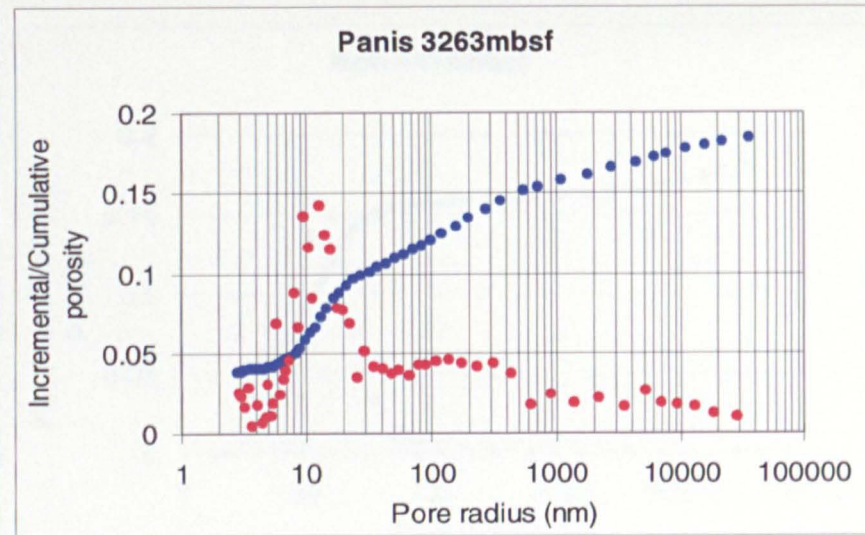
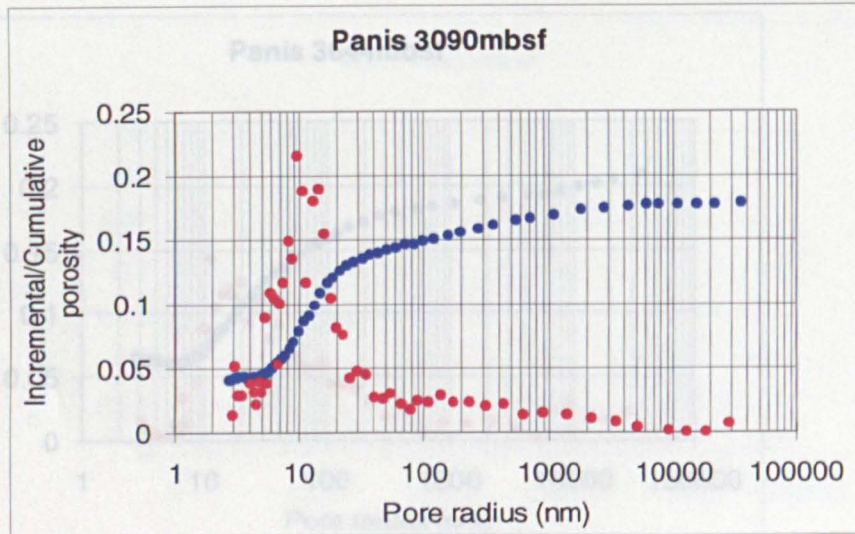
Mercury Intrusion Porosimetry Data: Part B Panis (cuttings)



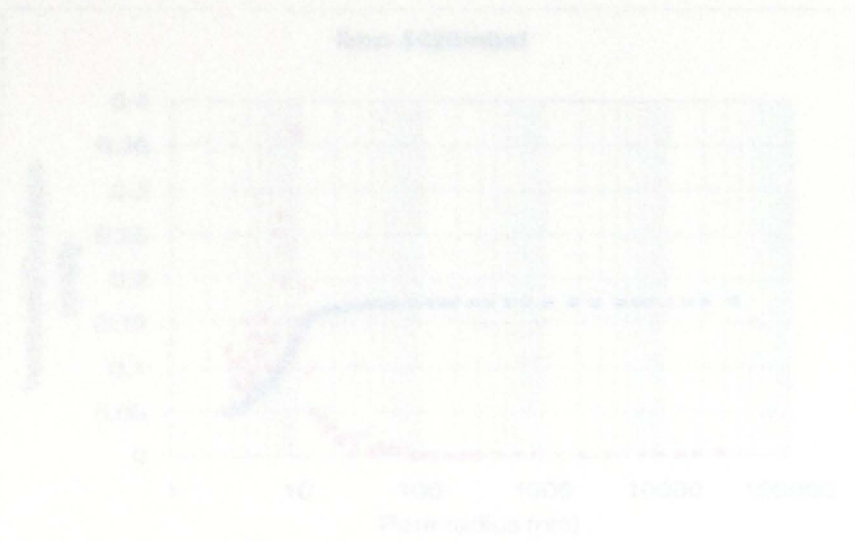
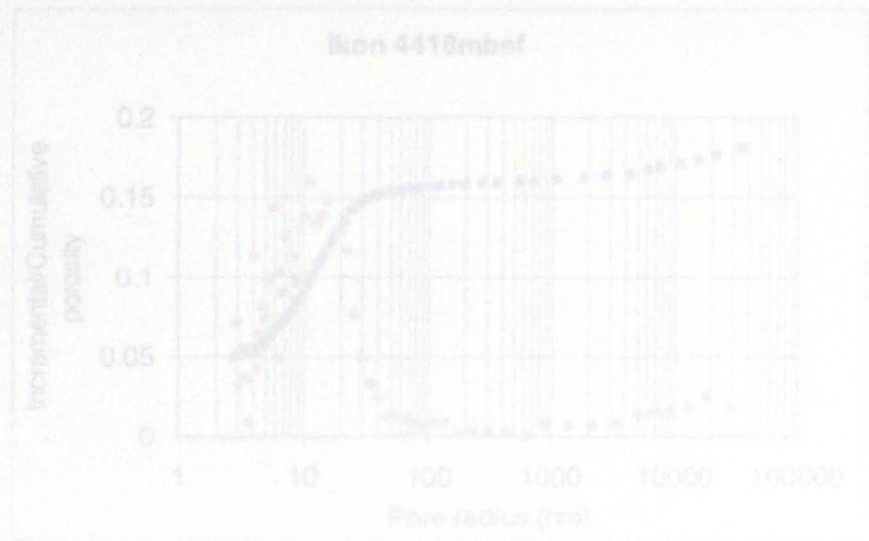
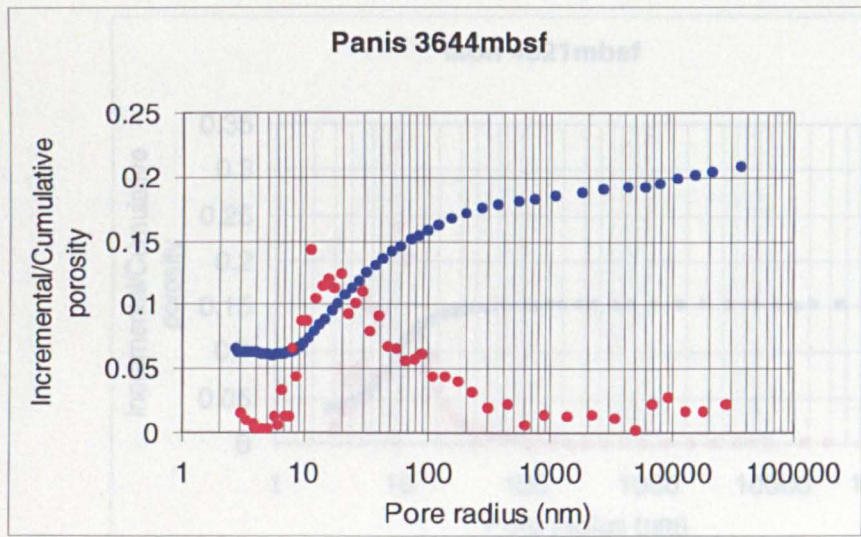
Mercury Intrusion Porosimetry Data: Part B Panis (cuttings) continued



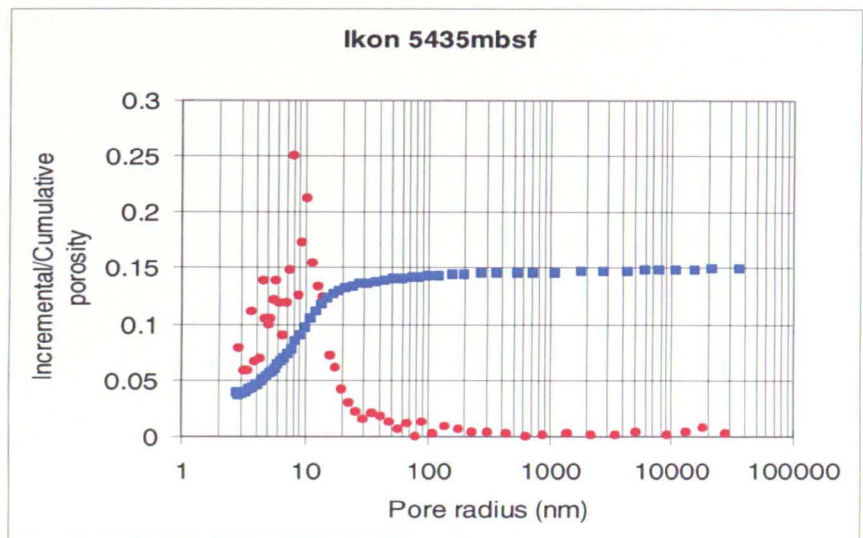
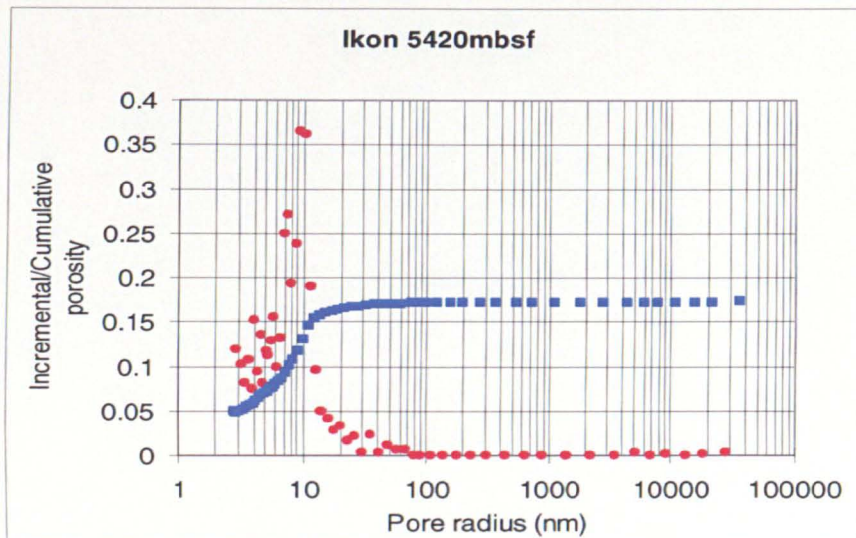
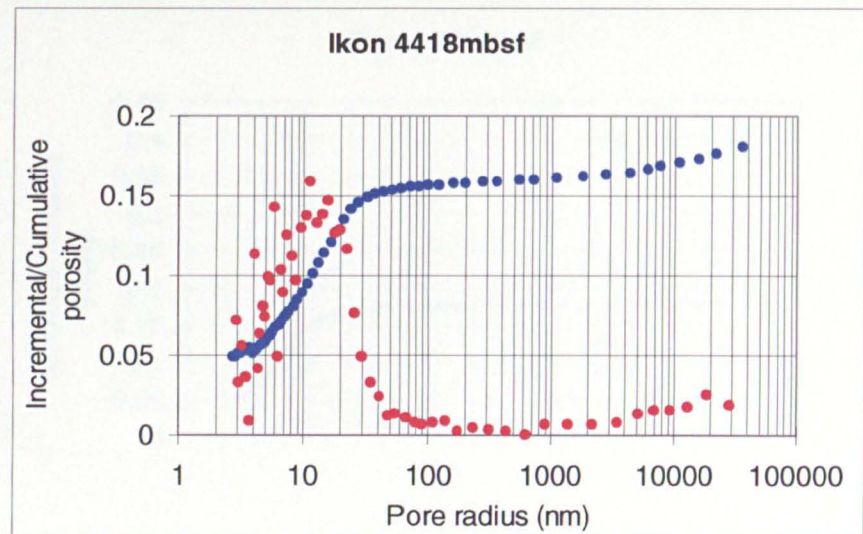
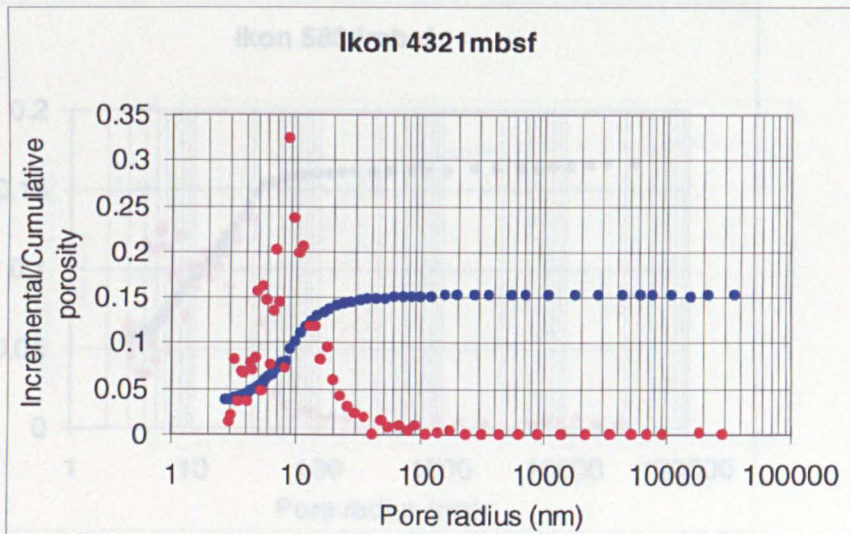
Mercury Intrusion Porosimetry Data: Part B Panis (cuttings) continued



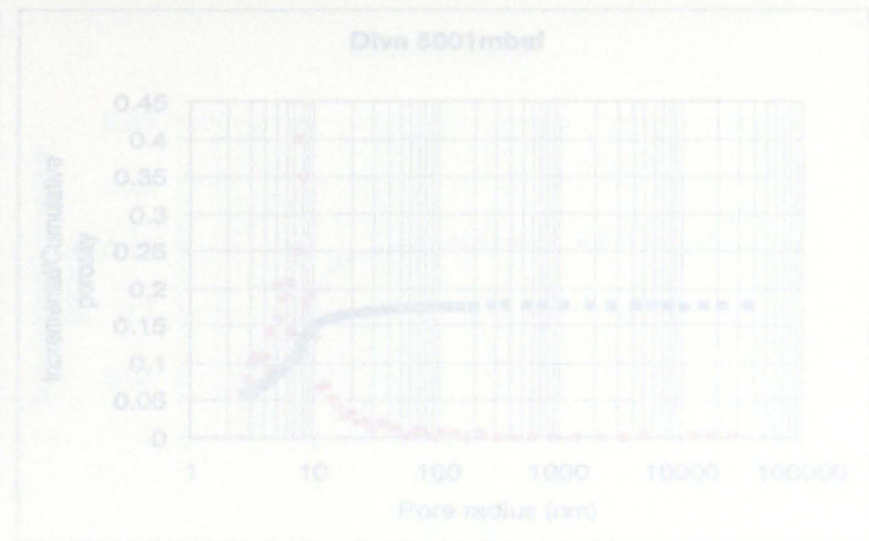
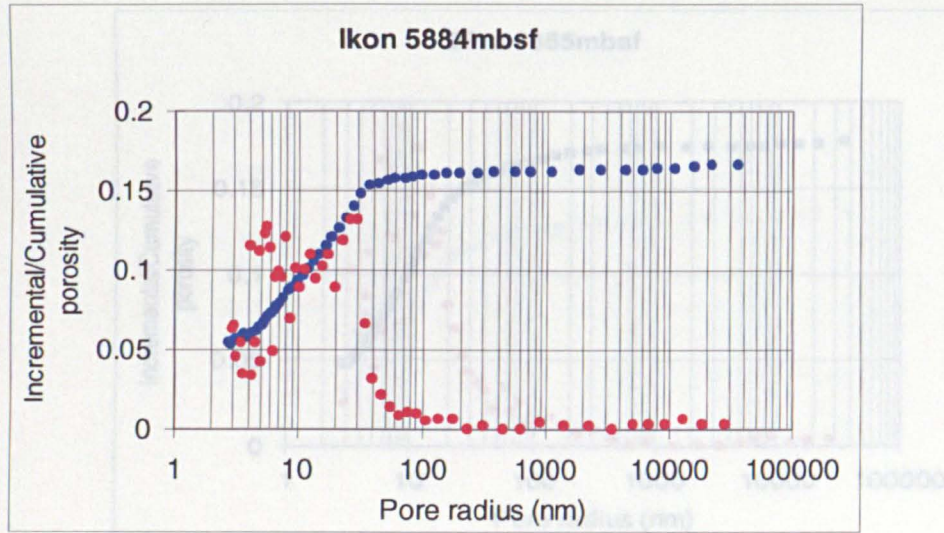
Mercury Intrusion Porosimetry Data: Part B Panis (cuttings) continued (samples)



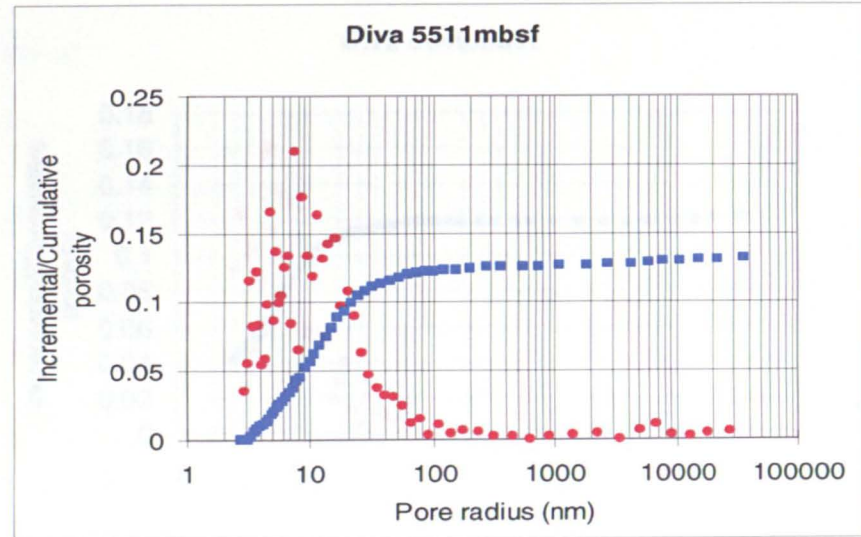
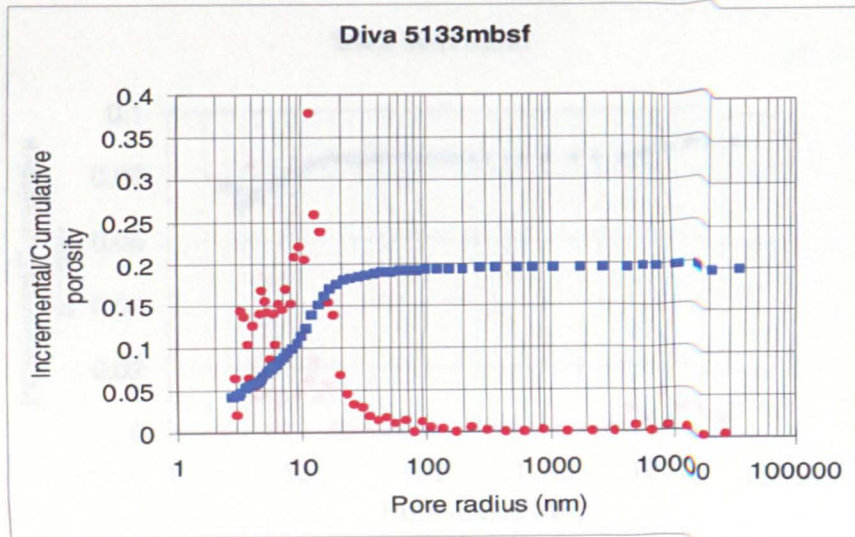
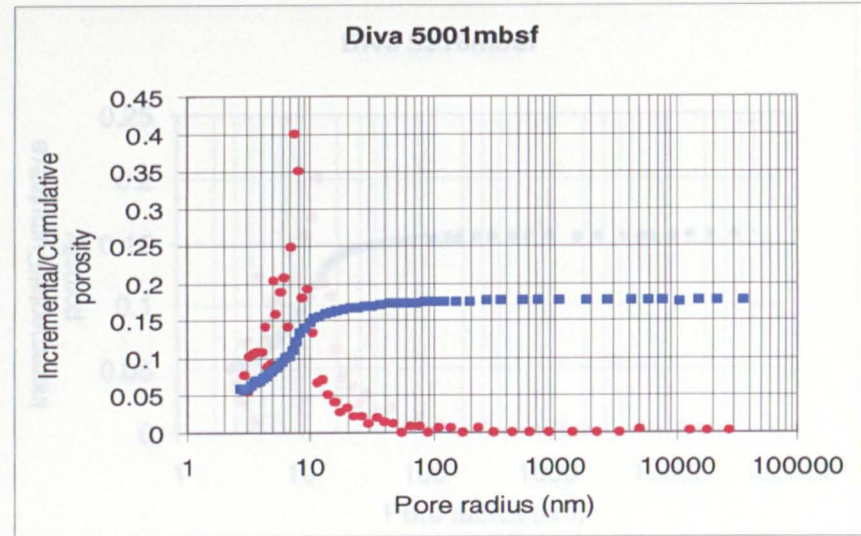
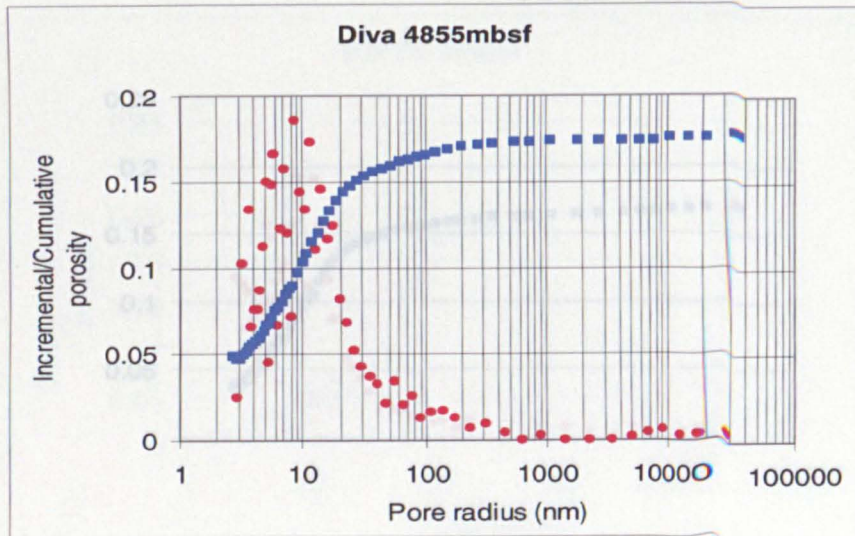
Mercury Intrusion Porosimetry Data: Part B Ikon (core samples)



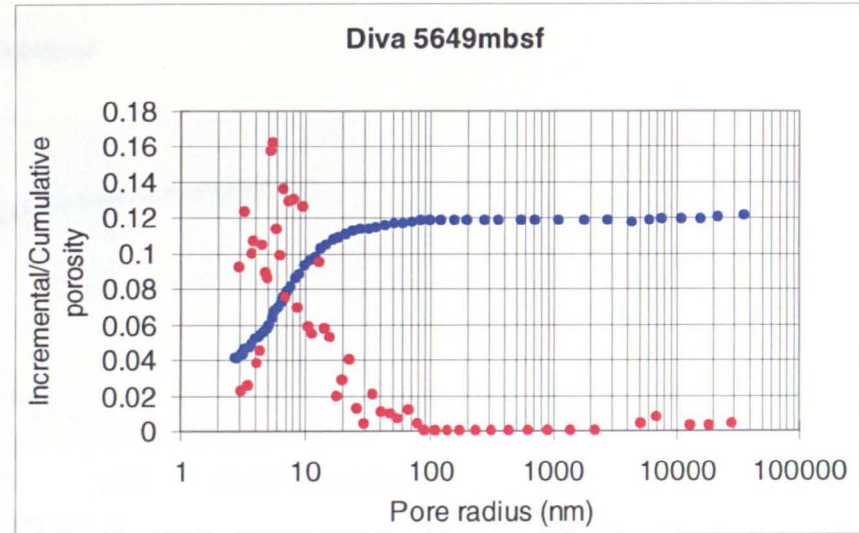
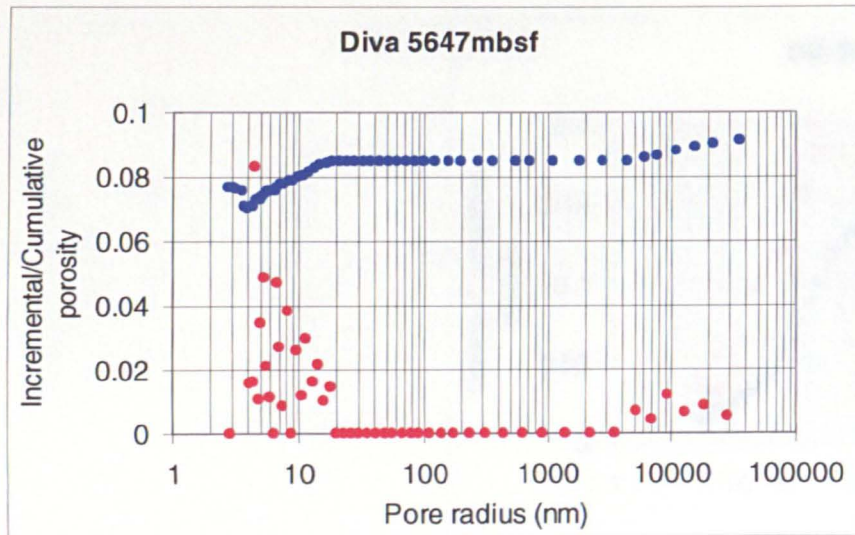
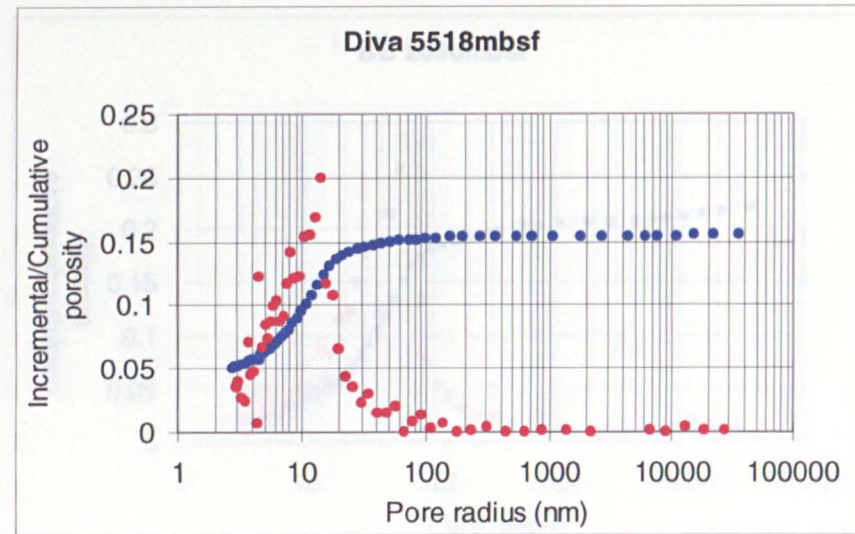
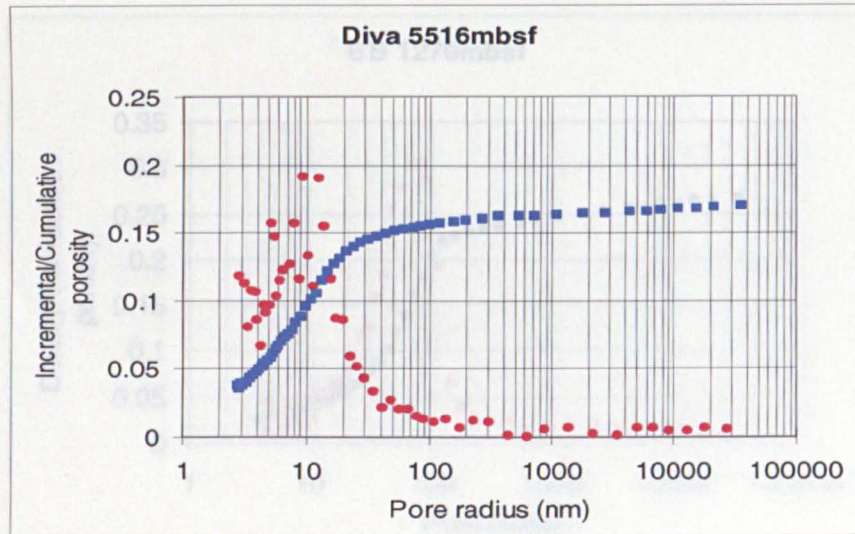
Mercury Intrusion Porosimetry Data: Part B Ikon (core samples) continued



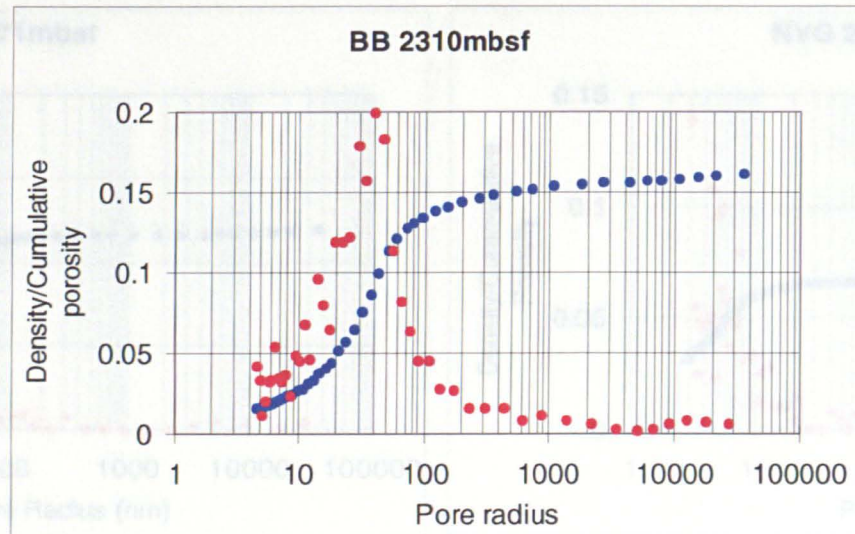
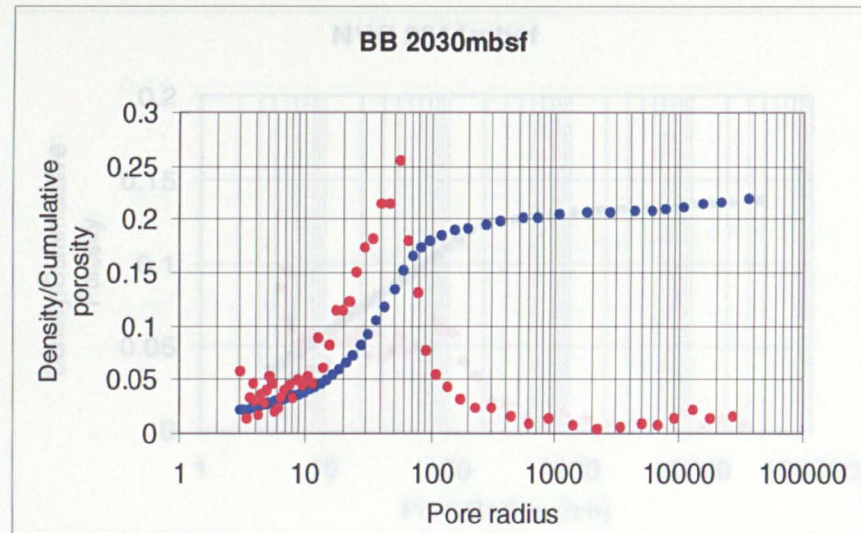
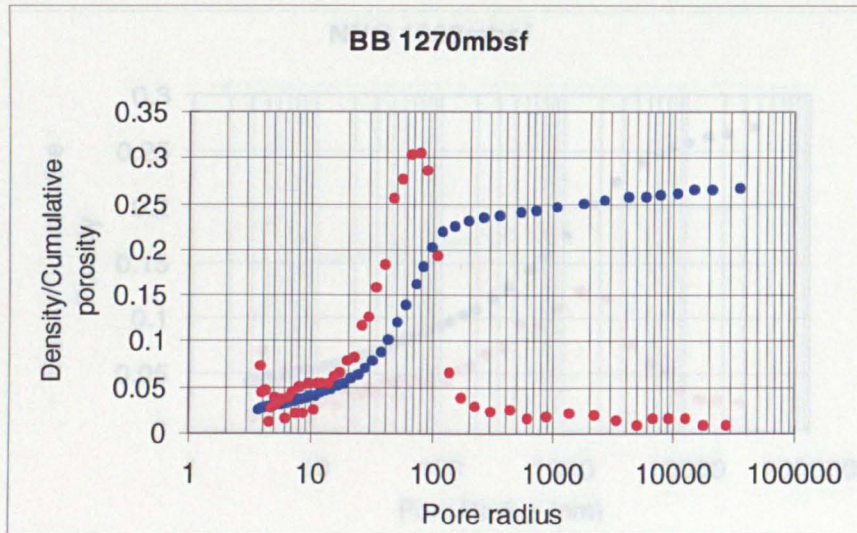
Mercury Intrusion Porosimetry Data: Part B Diva (core samples)



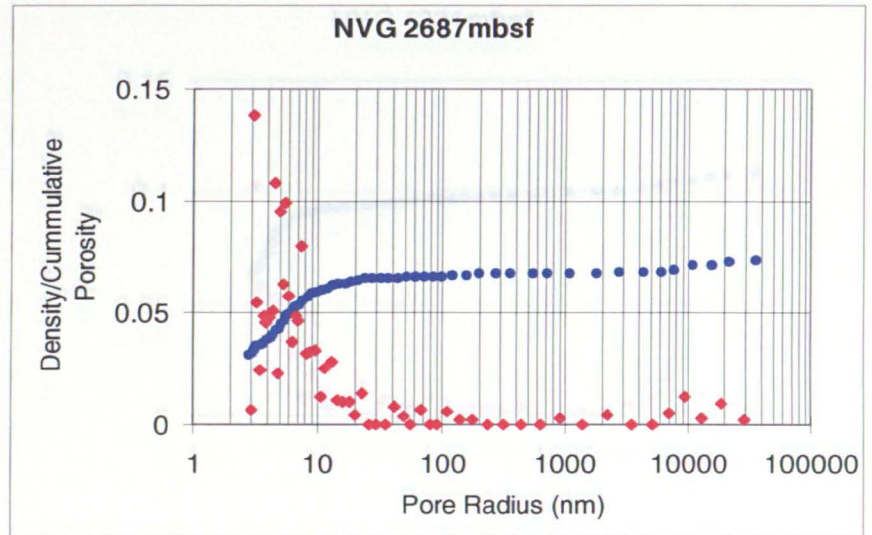
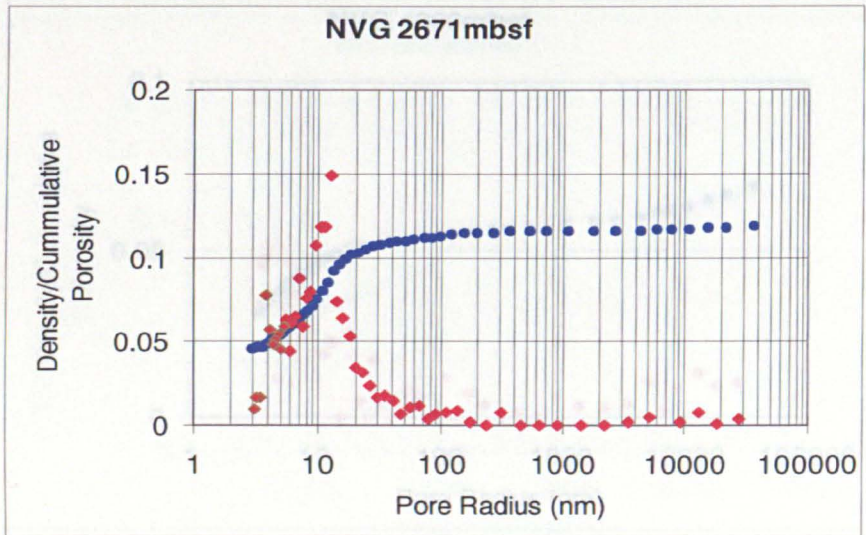
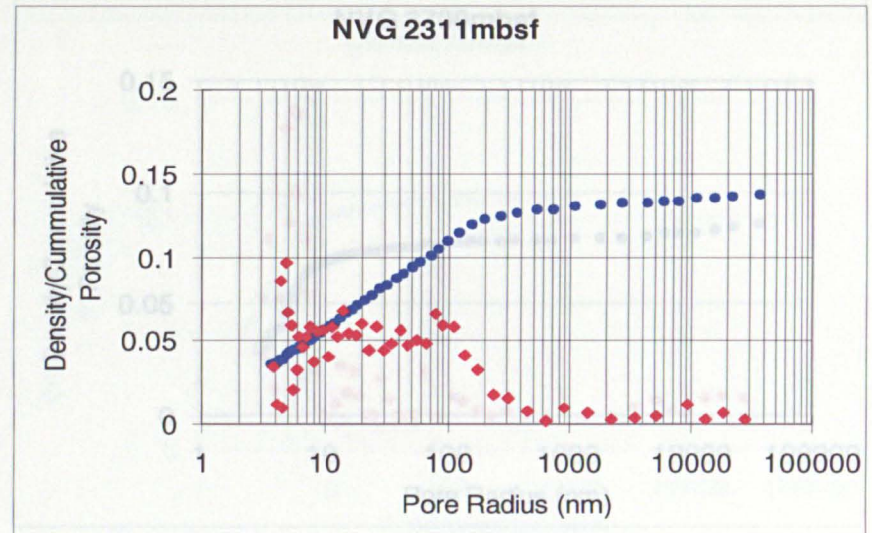
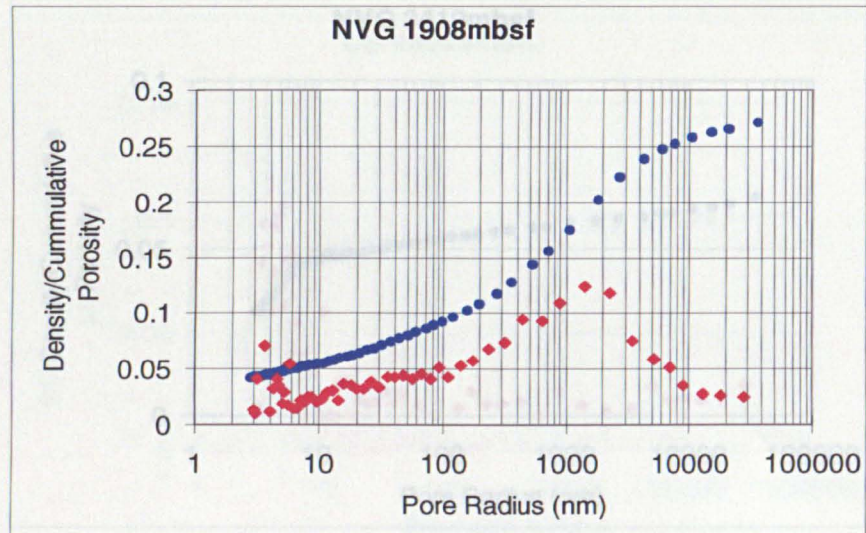
Mercury Intrusion Porosimetry Data: Part B Diva (core samples) continued



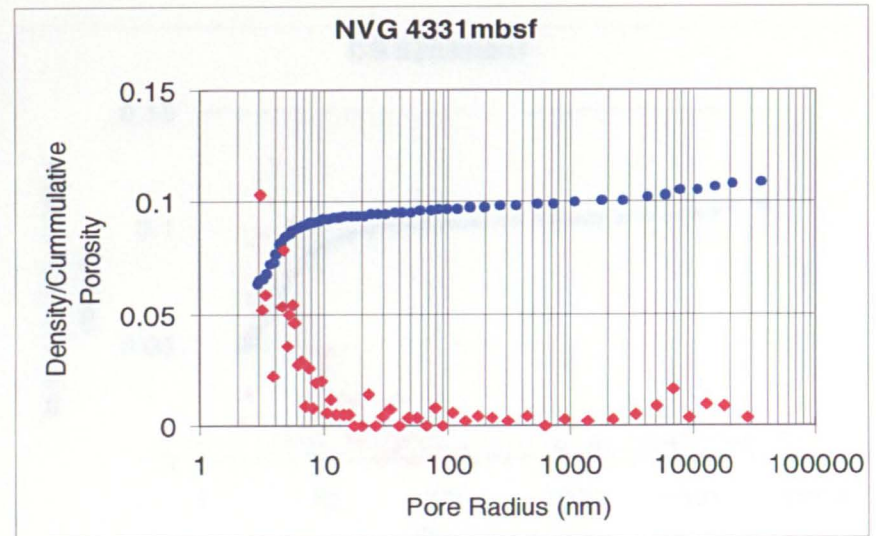
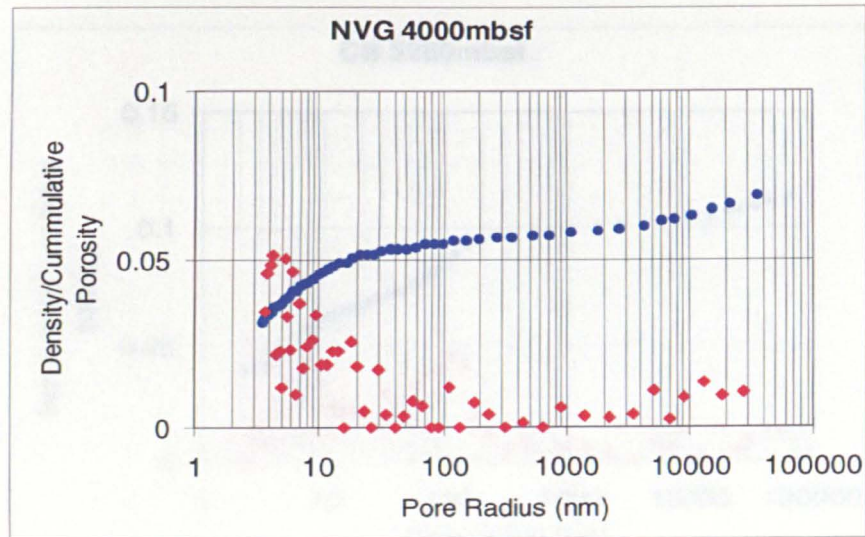
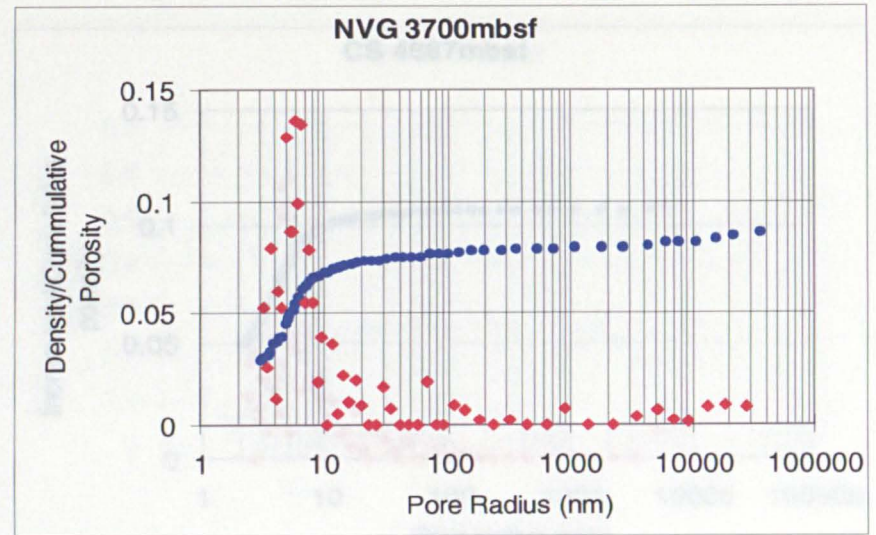
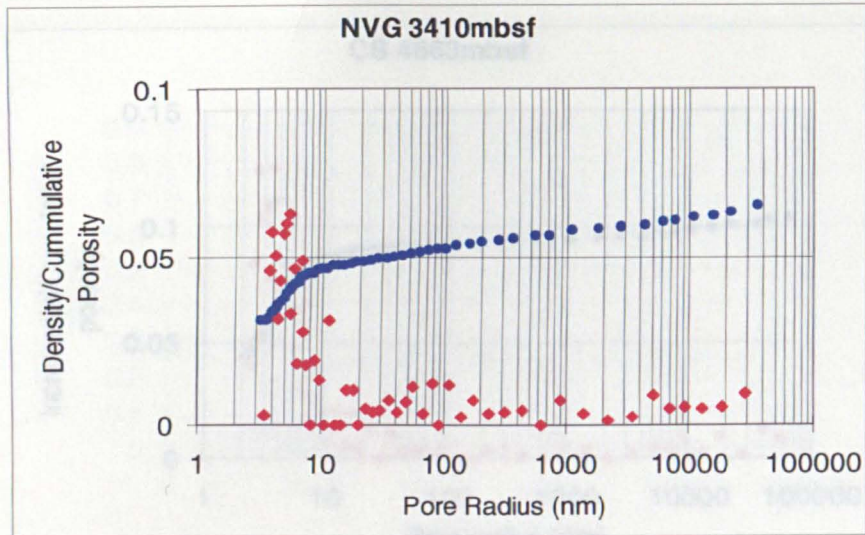
Mercury Intrusion Porosimetry Data: Part B Bay of Bengal (cuttings)



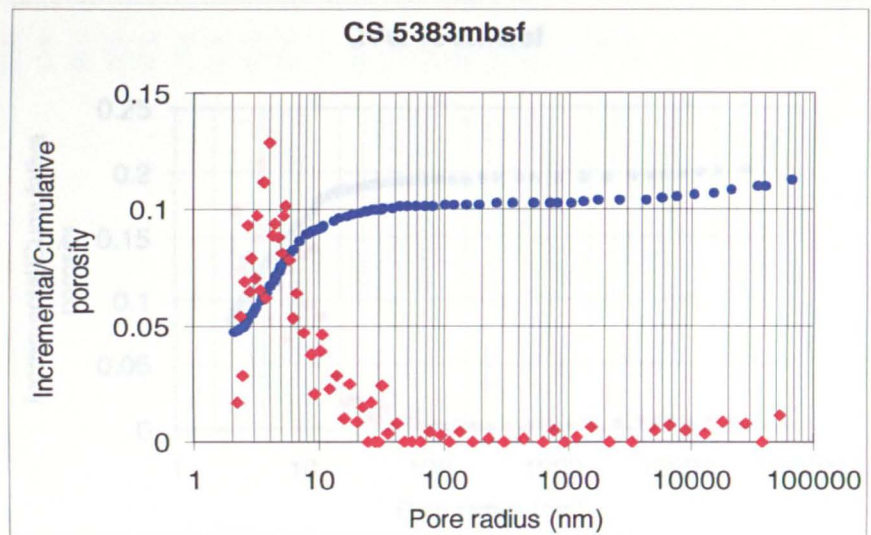
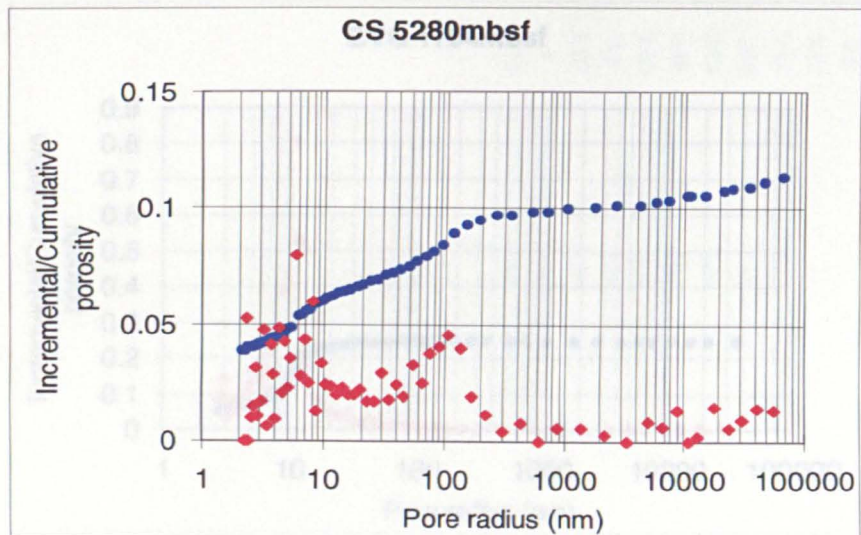
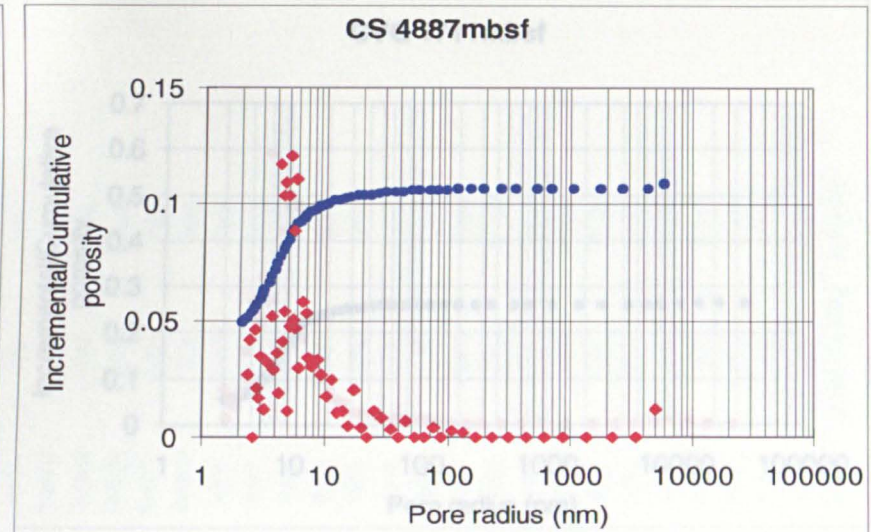
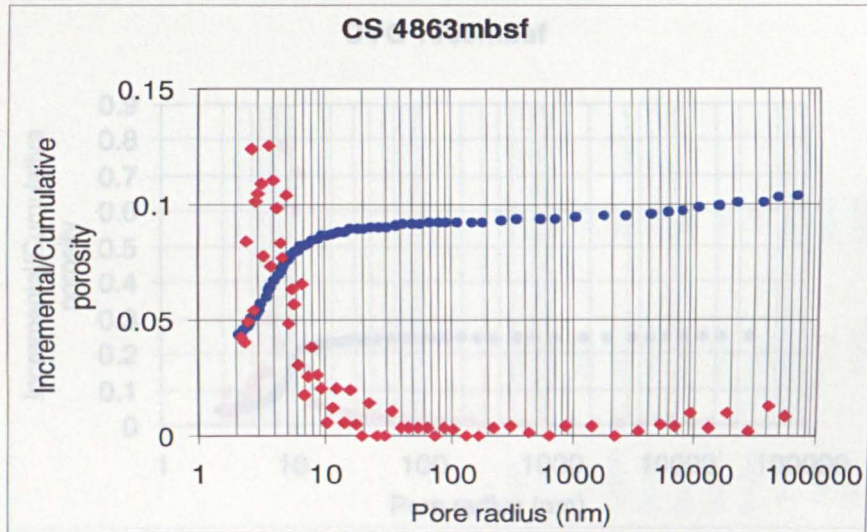
Mercury Intrusion Porosimetry Data: Part B North Viking Graben (core)



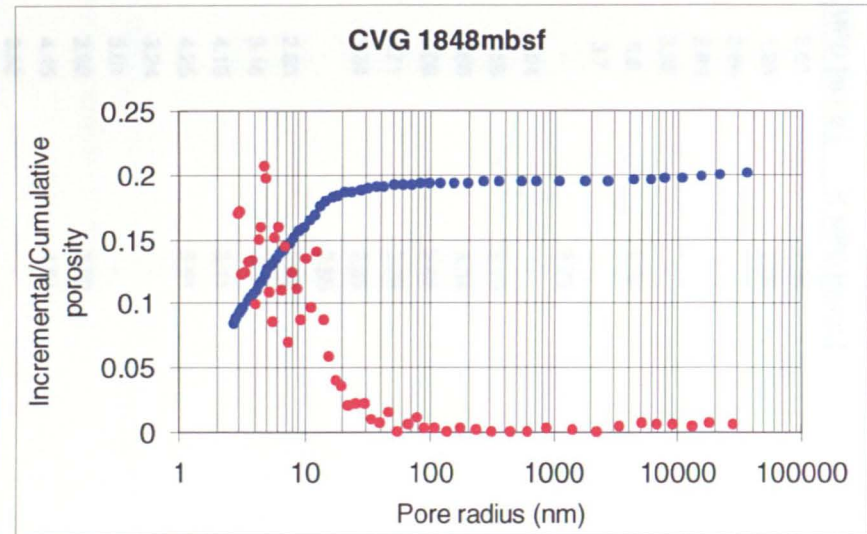
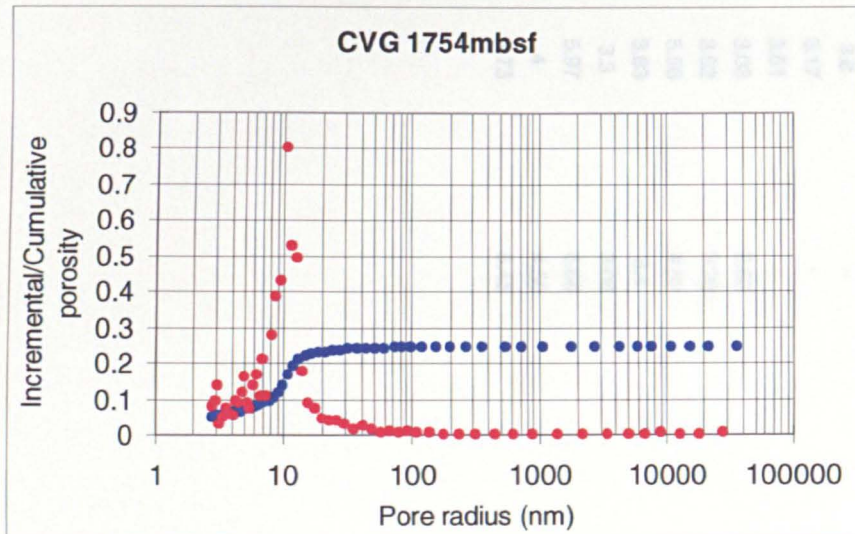
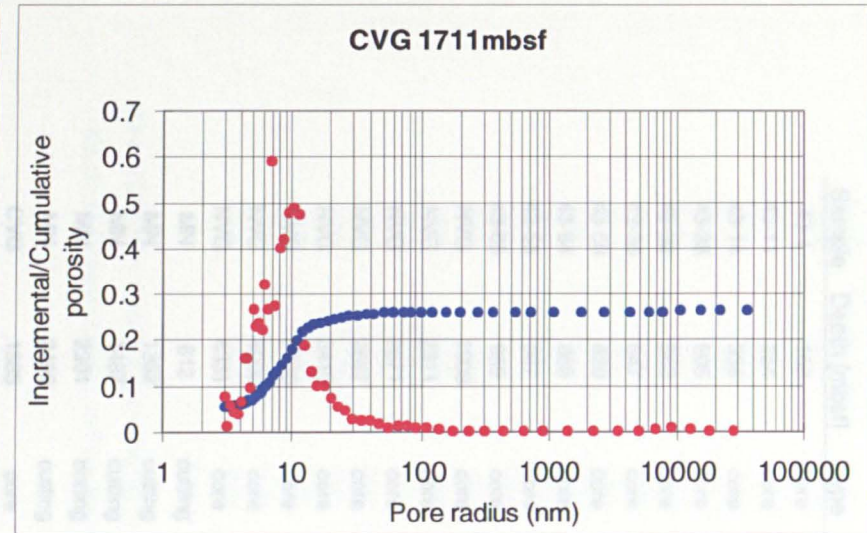
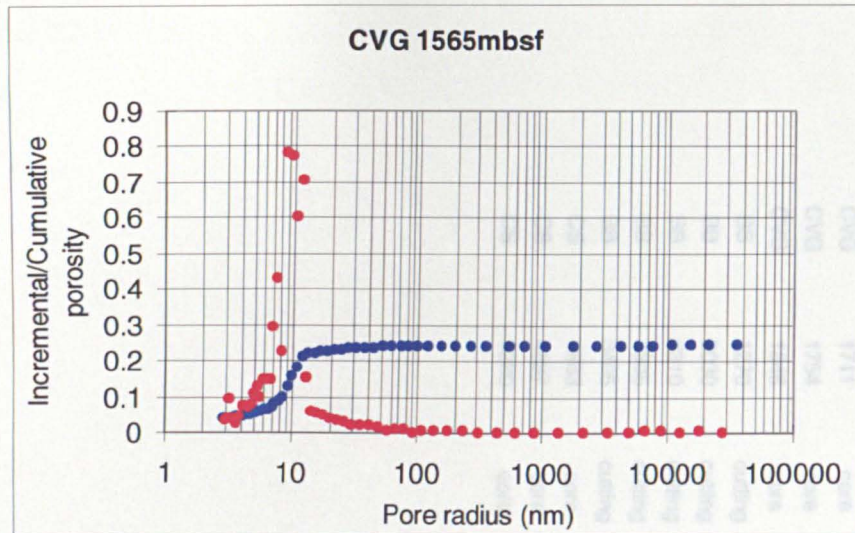
Mercury Intrusion Porosimetry Data: Part B North Viking Graben (core) continued



Mercury Intrusion Porosimetry Data: Part B Caspian Sea (core)



Mercury Intrusion Porosimetry Data: Part B Central Viking Graben (core)



HRXTG Data Part B

Sample	Depth [mbsf]	Type	I/S MPD [m.r.d.]	K MPD [m.r.d.]
43-4	153	core	2.51	2.06
43-11	254	core	1.93	1.69
43-14	336	core	2.86	-
43-28	505	core	2.89	-
42-32	563	core	3.32	-
43-36	647	core	5.6	5.35
43-50	820	core	3.7	-
43-54	859	core	-	2.75
43-55	867	core	3.64	-
43-65	959	core	3.55	3.19
NVG	1908	core	3.68	3.34
NVG	2311	core	3.08	2.62
NVG	2671	core	3.71	3.78
NVG	2687	core	3.34	2.85
NVG	3410	core	-	2.59
NVG	3700	core	2.63	2.57
NVG	4000	core	3.16	2.7
NVG	4331	core	4.19	3.11
MN	812	cutting	4.25	3.61
MN	1362	cutting	3.24	-
MN	1487	cutting	3.01	-
MN	2301	cutting	2.92	2.99
MN	2499	cutting	4.45	4.81
CVG	1565	core	3.52	-
CVG	1711	core	3.8	-
CVG	1754	core	3.17	-
CVG	1848	core	3.51	-
BB	1270	cutting	3.03	2.63
BB	2030	cutting	3.62	3.26
BB	2310	cutting	5.56	4.52
BB	3305	cutting	3.83	3.4
BB	3495	cutting	3.3	3.08
CS	4863	core	5.97	6.66
CS	4887	core	4	4.56
CS	5280	core	4.73	5.45

HRXTG Data Part B (continued)

Well	Depth [mbsf]	Type	I/S MPD [m.r.d.]	K/C MPD [m.r.d.]
Panis	1816	cutting	-	2.73
Panis	1999	cutting	4.05	3.8
Panis	2907	cutting	2.7	2.9
Panis	3090	cutting	3.1	2.57
Ikon	3453	cutting	2.54	-
Ikon	4128	core	-	1.99
Ikon	4321	swc	2.94	1.88
Ikon	4418	core	2.69	1.87
Ikon	4660	cutting	3.54	-
Ikon	5133	core	2.78	-
Ikon	5420	swc	1.88	1.8
Diva	4855	swc	2.6	2.08
Diva	5001	core	1.74	-
Diva	5511	core	2.76	1.92
Diva	5516	core	2.17	3.36
Diva	5518	core	2.46	1.91
Diva	5647	core	3.15	2.47
Diva	5649	core	3.41	2.32

Key: I/S MPD – Illite/Smectite Maximum Pole Density in mean random distribution, ; K/C MPD
– Kaolinite/Chlorite Maximum Pole Density in mean random distribution.